C-A/AP/142
March 2004

eRHIC

Zeroth-Order Design Report

BNL
L. Ahrens, D. Anderson, M. Bai, J. Beebe-Wang, I. Ben-Zvi, M. Blaskiewicz, J.M. Brennan, R. Calaga, X. Chang, E.D. Courant, A. Deshpande, A. Fedotov, W. Fischer, H. Hahn, J. Kewisch, V. Litvinenko, W.W. MacKay, C. Montag, S. Ozaki, B. Parker, S. Peggs, T. Roser, A. Ruggiero, B. Surrow, S. Tepikian, D. Trbojevic, V. Yakimenko, S.Y. Zhang

MIT-Bates
W. Franklin, W. Graves, R. Milner, C. Tschalaer, J. van der Laan, D. Wang, F. Wang, A. Zolfaghari and T. Zwart

BINP
A.V. Otboev, Yu.M. Shatunov

DESY
D.P. Barber

Editors: M. Farkhondeh (MIT-Bates) and V. Ptitsyn (BNL)

Zeroth-Order Design Report: eRHIC
Executive Summary

The scientific case and the scope of a high energy electron-ion collider with high luminosity to study the fundamental structure of matter using the deep inelastic scattering has been discussed in the nuclear physics communities around the world for the past few years. A collider at BNL which adds a new, 10 GeV/c, high intensity polarized electron/positron beam to the existing Relativistic Heavy Ion Collider (RHIC) complex, called "eRHIC", was first presented to NSAC in 2001. NSAC supported this idea enthusiastically and encouraged rapid R&D towards realizing such facility. Since then eRHIC has successfully gone through multiple BNL internal and NSAC sub-panel reviews. It has recently appeared on the list of 28 scientific projects supported by the US Department of Energy Twenty-Year Science Facility Plan.

This report, the eRHIC Zeroth-Order Design Report (ZDR), is the first detailed document reporting studies on the accelerator and the interaction region of this collider. The ZDR results from several months of studies performed jointly by BNL and MIT-Bates, with close collaboration with scientists from BINP (Novosibirsk) and DESY (Hamburg). The principal goals of these studies are to develop an initial design for eRHIC, to investigate accelerator physics issues most important for its design, and to evaluate the luminosities that could be achieved in such a collider if it were to be built in the near future with minimal R&D. Secondary goals include identifying specific accelerator aspects needing varying levels of R&D, which would lead to significantly higher luminosities. It is assumed that the time scale for realizing eRHIC is short enough, that at least one if not two experiments at RHIC are still taking data in an upgraded RHICII collider, using upgraded RHIC detectors. Those experiments and eRHIC would share one of the hadron beams in RHIC.

RHIC proton and heavy ion beams can be stored at design energies of 250 GeV and 100 GeV per nucleon, but they can also be stored at lower energies. eRHIC will provide collisions with variable center-of-mass energies, with longitudinal and/or transverse polarization in the interaction region (IR) for both electron and hadron beams. The main design option for eRHIC presented in the report is based on the construction of a 10 GeV electron/positron storage ring, adjacent to either the 12 or 4 o'clock collision point of RHIC, intersecting with one of the RHIC hadron beams. The electron beam energy will be variable down to ~5 GeV with minimal loss in luminosity and in polarization for collisions. The electron beam injector system will consist of linacs and recirculators fed by a polarized electron source. The study suggests that an e-p collision luminosity of 4×10^{32} $cm^{-2}s^{-1}$ can be achieved for the high-energy mode (10 GeV on 250 GeV), if the electron beam facility is designed using today's established state-of-the-art reliable accelerator technology, without an extensive R&D program. For the electron-gold ions collisions (10 GeV on 100 GeV/u), the same design results in a luminosity of about 4×10^{30} $cm^{-2}s^{-1}$. The potential to go to significantly higher luminosities by increasing the electron beam intensity will be explored in the future. A polarized positron beam of 10 GeV energy and high intensity will also be possible, using the process of self-polarization due to synchrotron radiation in the ring to build up the beam polarization.

eRHIC requires some modifications of the RHIC hadron rings. Most important among them are

a) the addition of electron cooling system, to achieve and maintain small beam emittances (this is also required for the RHICII upgrade plans), and
b) increasing the number of bunches in each ring from 120 to 360, consistent with the RF frequency of the present RF system.

Feasibility of such a total intensity increase requires further studies on topics such as the effect of electron cloud formation and an appropriate injection scheme.

A preliminary design for the eRHIC interaction region has been developed, providing early beam separation for the hadron and electron beams and including spin rotators in both the electron and the ion rings. The non-colliding RHIC ion beam avoids the IR region by a trajectory bypass. Preliminary issues related to the integration of a detector into the IR design have also been considered, anticipating regions of intense synchrotron radiation generated by the bends in the electron beam. An acceptable solution seems possible.

A possible alternative design for eRHIC is also presented as an appendix. This considers an electron accelerator based on an energy recovery superconducting linac (ERL), instead of a storage ring. Preliminary estimates suggest that this design option could produce higher luminosities, but requires significant R&D efforts for the polarized electron source and for the energy recovery technology. Consequently this has a longer time horizon and a larger uncertainty in the estimate of performance and costs involved. Work on both options for eRHIC will continue in the foreseeable future, until the final construction timescale demands freezing the design, and the technology.

1. PROJECT OVERVIEW

1.1 Scientific Frontiers Available for Exploration by eRHIC

The tremendous growth of knowledge about the fundamental structure of matter during the 20th century culminated in the 1970s with the emergence of the Standard Model. The Standard Model is an elegant theoretical framework based on experiment, which describes the structure of all matter in terms of point-like particles interacting by the exchange of gauge bosons. The point particles are termed leptons (electrons, neutrinos, etc.) or quarks (up, down, strange, etc.) and three types of gauge bosons; photons, weak bosons (W, Z), and gluons. Leptons can only exchange photons or weak bosons while the quarks may also exchange gluons. In addition, gluons, unlike photons, can interact with each other. The force governing the interaction of quarks and gluons is called the strong force. It is responsible for the structure of nucleons and their composite structures, atomic nuclei, as well as neutron stars.

Nucleons were born in the first minutes after the "Big Bang", and their subsequent synthesis into nuclei goes on in the ever-continuing process of nuclear synthesis in stars. Nuclear matter makes up most of the mass of the visible universe. It is the stuff that makes up our planet and its inhabitants. Nuclear matter was once remote and difficult for humans to access, but in the latter half of the 20th century, understanding nuclear matter and its interactions became central to research in nuclear physics and important to research in energy, astrophysics, and defense.

An essential goal of present day research is to investigate and understand the strong interactions between quarks and gluons that underpin the structure and interactions of nucleons and nuclei. The proposed electron-ion collider at BNL (eRHIC) is the essential next step needed to study the fundamental states of matter. We believe that it must be constructed by the end of the present decade to continue progress in this vital field of science.

1.1.1 Background and Scientific Questions

It is widely accepted that QCD is the exact theory of the strong interaction. QCD has a unique standing among all components of the Standard Model. It is the only theory that is not singular at short distances. The phenomenon of confinement ensures that QCD is well-behaved at large distances. Thus, QCD appears to be the only self-consistent nontrivial quantum field theory.

One of the greatest achievements of particle physics over the last 30 years was a quantitative verification of QCD in very hard collisions; those that occur over short distances at least 10 times smaller than the size of the proton. In hard collisions, the confined quarks and gluons act as if they are free particles exhibiting many properties that can be predicted by perturbative QCD (pQCD). However, when the interaction distance between partons (constituents of the nucleon) becomes comparable to or larger than the typical size of hadrons (pions and other heavier constituents that take part in the strong interaction), the partons are no longer free. They are confined by the strong force that does not allow observation of any free "colored" object. In this regime where most hadronic matter exists, many of the symmetries of the underlying quark-gluon theory are hidden and simple calculation methods are no longer valid. This is a fascinating many-body problem where very strong forces obscure the relationship with the simple underlying theory. Understanding the relationship

between the quark-gluon degrees of freedom and the hadrons that contain them is the most urgent challenge to any future experimental program in the domain of the strong interaction.

The most important difference between the theory of electromagnetic interactions, Quantum Electro-Dynamics (QED), and QCD is that gluons interact with each other while photons do not interact with other photons. This built-in non-linearity (non-Abelian structure) makes QCD calculations and theoretical predictions difficult, except in the high-energy (perturbative) or short space-time limit. The technical difficulties encountered in calculating QCD at the hadronic scale may be overcome by the use of lattice gauge calculations employing specifically designed powerful "tera-flop" computers. Over the next decade we expect that numerical computations of QCD will be extended into the non-perturbative regime. At that time, the properties of nucleons and nuclei will have a quantitative foundation in the fundamental theory. However, even at that time, the properties of hadrons at high energies will be well beyond the reach of the fastest computers. The thrust of this proposal is to provide physicists with an experimental tool that can explore all the partonic manifestations of QCD in nucleons and nuclei as well as explore the space-time structure of confinement.

Experimentally, the quark substructure of the nucleon was first revealed through electron-proton Deep Inelastic Scattering (DIS) experiments that took place at the Stanford Linear Accelerator Center (SLAC) in the early 1970s. These experiments earned a Nobel Prize for Friedman, Kendall, and Taylor. In a DIS collision, the electron transfers a large amount of energy and momentum. This energy and momentum is taken up by one of the quarks present in the proton. The struck quark carries a fraction of the proton's momentum, denoted by x, which is readily determined by the energy and momentum transferred in the collision. By varying the kinematics of the large momentum transfer scattering, on can measure the quark distribution as a function of that momentum.

A great deal has been learned since, at CERN, SLAC, Fermilab and DESY, about the quark and gluon structure of hadronic matter through measurements of quark and gluon distributions. In fact, the modifications of these distributions brought about by nucleons bound in nuclear medium were measured in groundbreaking experiments at SLAC, CERN and Fermilab. However, some of the crucial questions about the structure of hadronic matter remain open:

- What is the *structure* of hadrons in terms of their quark and gluon constituents?
- How do quarks and gluons *evolve* into hadrons through the dynamics of confinement?
- How do the quarks and gluons manifest themselves in the properties of atomic nuclei?

The term *"structure"* refers both to momentum distribution and to the spin carried by the various constituents. The answers to these questions are central to the ultimate characterization of the microscopic structure of strongly interacting matter.

However, a complete understanding of QCD and its full implications goes beyond these questions. The many-body aspects of QCD remain largely unexplored, and may contain a variety of surprises that can only be revealed by new measurements in domains that until now have been inaccessible. Finally, while today precision experiments test QED to its limits, similar explorations of QCD are incomplete because of the limitations in presently available experimental capabilities. Thus, there are a second group of questions:

- Does partonic matter saturate in a universal high-density state?
- Are there any long range correlations between produced partons?
- Can studies of the dependence of the parton densities on the nuclear density help constrain the properties of nuclear matter in the center of a neutron star?
- To what degree can QCD be demonstrated as an exact theory of the strong interaction?

1.1.2 The Electron Ion Collider at BNL: eRHIC

The electron-ion collider at BNL (eRHIC) is proposed as a means to obtain experimental answers to all of these questions. The design requirements are shaped by three decades of experimental work carried out with stationary or fixed targets at high-energy physics facilities such as SLAC, CERN, DESY, and Fermilab. In addition, a significant amount of effort was expended at DESY to investigate future polarized electron-proton (e-p) and unpolarized electron-ion (e-A) options. The inherent limitations of these facilities points to the need for a facility with the following characteristics:

- Collider geometry where electron beams collide with beams of protons or light and heavy nuclei,
- Wide range of collision energies (from E_{cm}/nucleon = 30 GeV to 100 GeV),
- High luminosity L = 10^{33} cm^{-2} s^{-1} per nucleon,
- Polarization of electron and proton spins, and
- Preferably, two interaction regions with dedicated, nearly hermetic, detectors.

Collider geometry offers two major advantages over fixed target electron-proton/ion (e - p/A) studies. First, the collider delivers vastly increased energy to the collision, providing a greater range for investigating partons with small momentum fractions (x) and their behavior over a wide range of momentum transfers (Q^2).
In DIS the accessible values of x are limited by the available collision center-of-mass energy. For example, collisions between a 10-GeV electron beam and nuclear beams of 100 GeV/nucleon provide access to values of x as small as $3x10^{-4}$. In a fixed target configuration a 2.1TeV electron beam would be required to produce the same collision energy. Figure 1.1 a-b shows the x-Q^2 range possible with the eRHIC and compares that range to the presently explored kinematic region. The beam energies assumed for the eRHIC are:

- 100 GeV/nucleon for nuclear beams,
- 50-250 GeV for polarized/unpolarized proton beams, and
- 5-10 GeV/c for polarized electron/positron beam.

The only electron-proton collider in existence is HERA, which is limited to unpolarized electron-proton collisions. Thus, in the case of electron-nucleus and polarized electron-polarized nucleon collisions the eRHIC is entering entirely new territory.

Secondly, the collider geometry is far superior to fixed-target experiments since it allows examination of final states of the target. If one wishes to examine the final state fragments from the struck nucleon or nucleus in fixed-target geometry, it is necessary to use a thin target so that the fragments can escape the target and be detected. The thin target makes acquisition of adequate statistics a serious problem. This is easily overcome in a high-luminosity collider, where high luminosity provides an adequate collision rate, and the boost acquired by target fragments in the collider mode makes them readily available for detection when separated from the beam.
High luminosities of the order of $L=10^{33}$ cm^{-2} s^{-1} for electron-nucleon scattering, are a necessary and crucial characteristic of the eRHIC. It corresponds to observing 86 pb^{-1} per day. Previous studies established that significant results are attained at 200 $(pb)^{-1}$, therefore the statistical precision required for significant physics is easily within the reach of the eRHIC. This luminosity can be achieved with either of two accelerator scenarios: a ring-ring configuration, and a ring-electron linac configuration. Each has advantages. Achieving the proposed luminosities requires electron cooling of the ion beams (except at the highest proton energies) and intense electron beams of about 500 mA. While challenging, the intense electron beams are already available at the presently operating B-factories (SLAC and KEK B). The electron linacs (one for cooling the ion beam and another providing high-

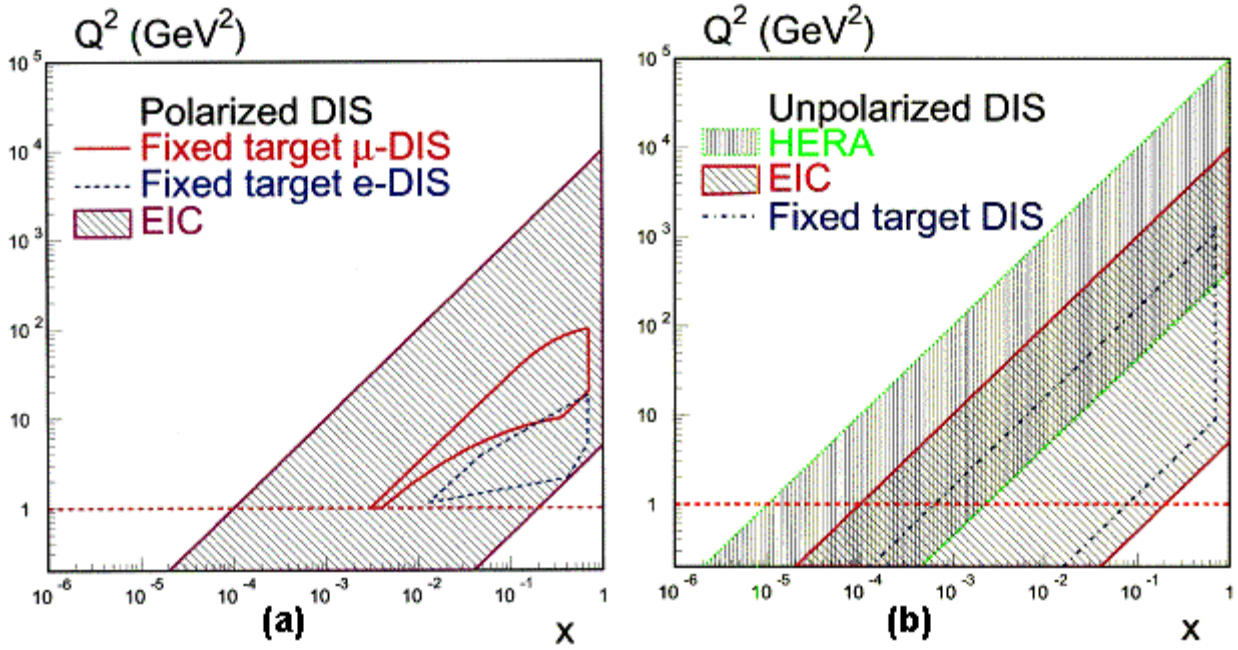

Figure 1.1: x-Q^2 Range of the Proposed Electron Ion Collider

The x-Q^2 coverage of the eRHIC is compared with previously measured ranges. Figure (a) is for polarized lepton - nucleon DIS while (b) is for unpolarized lepton-nucleon and lepton - nucleus DIS, where leptons can be electrons or muons. Note that the HERA coverage in (b) is for e – p scattering only while the fixed target and the eRHIC regions also include DIS off nuclear targets.

energy electrons in the collider) require full-energy recovery following the model of the full-energy recovery 50 MeV linac-based free electron laser at Thomas Jefferson Laboratory. Figure 1.2 shows the unique parameters of the eRHIC in the context of existing and planned lepton scattering facilities worldwide. The eRHIC will have higher energies than any existing fixed target machine and a higher luminosity than any existing collider.

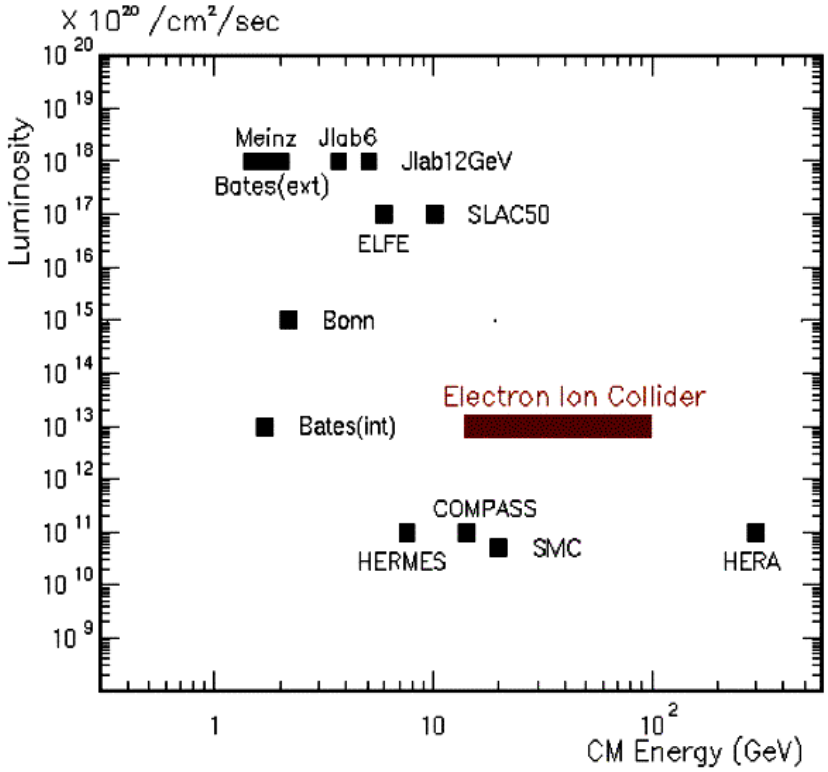

Figure 1.2 The Center-of-Mass Energy vs. Luminosity of eRHIC Relative to Other Facilities
The center-of-mass vs. energy of various existing facilities compared to that proposed for the eRHIC

1.1.3 Highlights of Scientific Frontiers Open to the eRHIC

Quark and Gluon Distributions in the Nucleon

The eRHIC offers a unique capability for measuring "flavor tagged" structure functions by providing access to a wide range of final states arising from the fragmentation of the virtual photon. The collider geometry makes measurement of semi-inclusive reactions very efficient so that quark and gluon distributions in nucleons, nuclei, and possibly even mesons can be mapped in a flavor-tagged mode. This will provide a decomposition of the parton densities, over a large kinematic range, into the contributions from different parton types: up, down and strange quarks as well as gluons. For example, with clean kaon identification both the momentum and spin distributions of strange quarks can be determined with high precision down to $x \sim 10^{-3}$. The ability to tag the hadronic final state will allow measurements of the neutron structure function at large x, so that a reliable and precise determination of the ratio of the quark distribution in neutrons and protons can be made in a regime where several competing theoretical predictions exist.

Spin Structure of the Nucleon

Fixed target polarized DIS experiments yielded the surprising information that the quark spins account for only ~30% of the total spin of the nucleon. Recent results, with large uncertainty, indicate that gluons may play a significant role in constituting the nucleon's spin. While experiments

with polarized protons at the Relativistic Heavy Ion Collider (RHIC) will provide significant information for unraveling the role of gluonic spin, energetic collisions using polarized electrons and protons will provide important complementary, and in some instances, essential new information using well established experimental methods and theoretical techniques presently used by the DIS community at HERA. The eRHIC, running at its highest energy, will provide crucial data at lower x than has been possible in any previous experiment. The use of tagging in polarized nuclei will allow measurement of the spin structure of the neutron at large x with better precision. At small x it will provide a separation between the polarization effects in the vacuum and nonvacuum channels. Determination of spin structure functions in this yet unmeasured low x region will bring a unique perspective to our understanding of pQCD. Direct measurement of the polarization of quarks in a broad range of x are needed to determine the polarization of quarks and antiquarks in the sea, currently a matter of controversy within sophisticated and successful models of the nucleon.

Correlations between Partons

A complete characterization of the partonic substructure of the nucleon must go beyond a picture of collinear non-interacting partons. It must include a description of the correlations between the partons densities over impact parameters, and a comparison of the parton wave functions of different baryons. Progress in this direction can be realized by measuring hard exclusive processes where, in the final state, a photon, a meson or several mesons are produced along the virtual photon direction, and a baryon is produced in the nucleon fragmentation region. These processes are expressed, as a result of the new QCD factorization theorems, through a new class of parton distributions termed *Generalized Parton Distributions* (GPD). The collider kinematics are optimal for detecting these processes. The presence of polarization provides additional exciting opportunities, for example, comparisons of the spin structure of hyperons and nucleons. If successful, such a program would greatly expand our knowledge about the role of non-perturbative QCD in hadronic structure.

The Role of Quarks and Gluons in Nuclei

Most hadronic matter exists in the form of nuclei. The ability of the eRHIC to collide electrons with light and heavy nuclei opens horizons fundamental to nuclear physics. For example, the role of quarks and gluons in nuclei may be investigated by comparing the changes in parton distributions per nucleon as a function of the number of nucleons. Seminal DIS experiments off nuclei showed that a) the distribution of quarks is altered by the nuclear medium from that observed in nucleons, b) led to the discovery of the lack of enhancement of sea quarks in the nuclei that was expected based on models of the meson picture of nuclear forces, and c) provided tantalizing indications of significant modifications of the gluon distributions at moderate x. Studies of parton modifications at $x \sim 0.1$ will be most sensitive to the underlying quark-gluon structure of the internucleon interactions that are usually described within effective low energy mesonic theories. It is particularly important to establish the quark distributions at small values of x where the presence of the other nucleons in the nucleus will alter ("shadow") the partonic distributions. A nuclear enhancement of valence quarks, sea quarks, or gluons would indicate the relative importance of meson, quark, and gluon exchange at various distance scales.

Hadronization in Nucleons and Nuclei

How do the colored quarks and gluons knocked out of nucleons in DIS evolve into the colorless hadrons that must eventually appear? This process is one of the clearest manifestations of confinement: the asymptotic physical states must be color-neutral. Hadronization is a complex process that involves both the structure of hadronic matter and the long range nonperturbative dynamics of confinement. A fundamental question related to hadronization is how and to what extent the spin of the quark is transferred to its hadronic daughters. The ability to "tag flavor" and a facility that creates readily detectable jets are crucial for these experiments. The eRHIC makes it possible to strike quarks and observe the complete array of decay products from the nucleon or nucleus. The fact that nuclei also may be used is essential to this study. The ability to place varying amounts of nuclear matter in proximity to the system produced forward along the photon direction and the recoiling quark system, allows one to perturb in a controlled way the early stages of its space-time evolution, and to measure the energy imparted to the nuclear matter by the emerging parton.

Partonic Matter Under Extreme Conditions

Very high energy DIS on nuclear targets with electromagnetic probes offers new opportunities for studying partonic matter under extreme conditions. Particularly intriguing is the regime of very low x ($x < 10^{-3}$) where gluons dominate. Measurements of the proton structure function showed that the gluon distribution grows rapidly at small x for Q^2 greater than a few GeV^2. When the density of gluons becomes large, they may saturate and give rise to a new form of partonic matter: a **color glass condensate**. It is a colored glass because the properties of the color-saturated gluons are analogous to that of a spin glass system in condensed matter physics. It is a condensate because the gluons have a large occupation number and are peaked in momentum about a typical scale of the saturation momentum Q_s.

This state of strongly interacting matter would be universal in that it is insensitive to the hadronic matter in which it resides. The gluonic density/cm^2 is enhanced in nuclei relative to that in individual nucleons by a factor $A^{1/3}$. Therefore, high parton density effects will appear at much lower energies in nuclei than in protons. The eRHIC, with its nuclear beams and e - A center-of-mass energies of at least 60 GeV, and ability to study inclusive and semi-inclusive observables, will probe this novel regime of Quantum Chromo Dynamics.

1.2 General accelerator concept and parameters

1.2.1 Project Goals

The physics program outlined in the previous section sets requirements and goals for the electron-ion collider to be successful and efficient tool for intended physics research . These goals include wanted luminosity level, range of beam collision energies and using polarized beams. On the other side, to be realistic, the goals should be based on the present understanding of the existing RHIC machine and limitations which arise from the machine itself. Possible realistic machine upgrades should be considered to overcome existing limitations and to achieve advanced machine parameters, but those upgrades should not be extensive and costly.

The intent to minimize required upgrades in the existing RHIC rings affects the choice of parameters and the set of goals. Another guideline, which was defined for the design described in this report and which affects the choice of the beam parameters and the value of achievable luminosity, is capability of the collider to operate in the same time with ion-ion and electron-ion collisions. In the main design line collisions in two ion-ion interaction regions, at the 6 and 8 o'clock, have to be allowed in parallel with electron-ion collisions.

Taking into account all mentioned above, following goals were defined for the accelerator design:

- The machine should be able to provide the beams in following energy ranges:
  - The electron accelerator:
    - 5-10 GeV polarized electrons;
    - 10 GeV polarized positrons;
  - The ion accelerator:
    - 50-250 GeV polarized protons;
    - 100 GeV/u Gold ions
- Luminosities:
  - in 10^{32}-10^{33} $cm^{-2}s^{-1}$ range for e-p collisions
  - in 10^{30}-10^{31} cm-2s-1 range for e-Au collisions
- 70% polarization degree for both lepton and proton beams
- Longitudinal polarization in the collision point for both lepton and proton beams

Additional goal for the design was to look at possibility of accelerating polarized ions, especially polarized ^{3}He ions.

1.2.2 General Layout

The present RHIC machine uses superconducting dipole and quadrupole magnets to keep ion beams circulating in two rings on 3834m circumference. The beam energy range covers 10.8-100 Gev/u for Au ions and 25-250 GeV for protons. There are in total 6 intersection points where two ion rings, Blue and Yellow, cross each other. Four of these intersection points are presently used by physics experiments and have experimental detectors installed.

General layout of a suggested eRHIC collider is shown in Figure 1.3. The main project line is to construct an electron storage ring which will intersect the RHIC Blue ion ring in one of existing interaction regions, not used by any of ion-ion collision experiments. The new detector, developed

and optimized for electron-ion collision physics studies, shall be constructed in that intersection point.

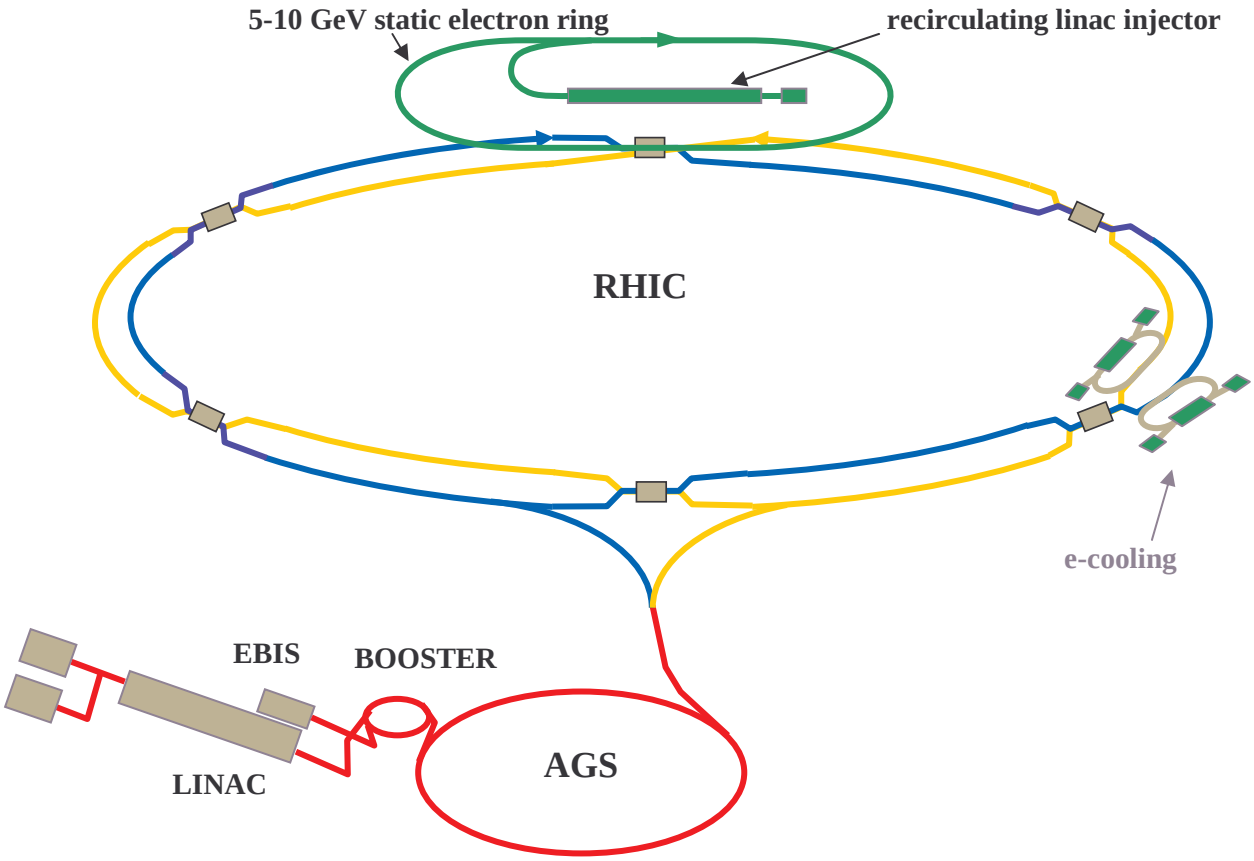

Figure 1.3: Design layout of the eRHIC collider.

Electron beam in this design is produced by polarized electron source and accelerated in a linac injector to the energies of 5 to 10 GeV. In order to reduce the injector size and , therefore, the injector cost, the injector design includes recirculation arcs, so that the electron beam passes same accelerating linac sections multiple times. Two possible linac designs, superconducting and normal conducting, have been considered. The beam is accelerated by the linac to the required collision energy and injected into the storage ring.

The electron storage ring should be capable of storage the electron beam at the energy range of 5 to 10 GeV with appropriate beam emittance values. It does not provide any additional acceleration for the beam. The electron ring should minimize depolarization effects in order to keep the electron beam polarization at the high level for the time of a store which is on the scale of several hours.

The injector system also includes the conversion system for positron production. After production the positrons are accelerated to 10 GeV energy and injected into the storage ring the same way as the electrons. Obviously the field polarities of all ring magnets should be switched to opposite at the positron operation mode. Unlike electrons the positrons are produced unpolarized and have to be polarized in the ring. Therefore the design of the ring should allow for sufficiently small polarization time. The current ring design provide polarization time about 20min at 10 GeV. But with polarization time increasing sharply as beam energy goes down the use of polarized positron beam in the present design are limited to 10 GeV energy.

The detailed description of the electron injector system, electron ring and all issues relevant for their design is presented in Chapter 2. It is important to note that the electron accelerator design described there is based on present day level of accelerator technology and does not require extensive R&D studies. This, in fact, has been one of requirements for the main design line for this ZDR.
In order to organize electron-ion collisions one of RHIC interaction regions has to be reconstructed. Figure 1.3 shows the design with electron accelerator located at 12 o'clock region . As discussed in section 2.2 of this report another possible location for the electron accelerator and for electron-ion collisions might be at 4 o'clock region. For collisions with electrons the ion beam in the RHIC Blue ring will be used, since the Blue ring can operate alone, even with another ion ring, Yellow, being down. The interaction region design which provides fast beam separation for electron and Blue ring ion bunches as well as strong focusing at the collision point is described in Chapter 4. In the design, another ion ring, Yellow, makes 3m vertical excursion around the collision region, avoiding collisions both with electrons and Blue ion beam. Interaction region includes spin rotators, in both electron and Blue ion rings, with a goal to produce longitudinally polarized beams of electrons and protons at the collision point.
Electron cooling system is one of upgrades required for ion rings. The cooling would be necessary to reach luminosity goals for electron collisions with gold ions and low (below 150 GeV) energy protons. The electron cooling is an essential part of RHIC upgrade for higher luminosity in ion-ion collisions, RHICII, which would be realized on a time scale before the eRHIC.
Also the present design considers using a total ion beam current higher than the current being used at the present RHIC operation. 360 bunch mode operation is evaluated in this report for the ion beam. The electron cooling, the beam intensity increase as well as proton and ion beam polarization issues, are described in Chapter 3 of the report.
Another proposed electron accelerator design is described in Appendix A. That design considers the use of high current polarized electron beam accelerated to collision energies by a superconducting energy recovery linac. In that case the electron beam is delivered to an interaction point directly from the linac. The design results in a higher luminosity value but requires intense R&D studies to develop and test technologies for high current polarized electron source and high beam power energy recovery.

1.2.3 Design Luminosities

The eRHIC design has been created and optimized to achieve luminosity goals listed in previous section The luminosity is limited mainly by maximum achievable beam-beam parameters and by interaction region magnet aperture limitations. Following those limitations it is most appropriate and convenient to use a luminosity expression through beam-beam parameters (ξ_e,ξ_i) and rms angular spread in the interaction point (σ'_{xi}, σ'_{ye}):

$$L = f_c \frac{\pi \gamma_i \gamma_e}{r_i r_e} \xi_{xi} \xi_{ye} \sigma'_{xi} \sigma'_{ye} \frac{(1+K)^2}{K} \qquad (1.1)$$

The f_c = 28.15 MHz is a collision frequency, assuming 360 bunches in the ion and 120 bunches in the electron ring. The parameter $K=\sigma_y/\sigma_x$ presents the ratio of beam sizes in the interaction point. One of basic conditions which defines the choice of beam parameters is a requirement on equal beam sizes of ion and electron beams at the interaction point: $\sigma_{xe}=\sigma_{xi}$ and $\sigma_{ye}=\sigma_{yi}$. The requirement is

based on operational experience of HERA collider and on the reasonable intention to minimize the amount of one beam passing through strongly nonlinear field in outside area of the counter rotating beam.

According to the expression (1.1) the luminosity reaches a limiting value at maximum values of beam-beam parameters, or at beam-beam parameter limits. For protons (an ions) the total beam-beam parameter limit was assumed at 0.02 value, following the experience and observation from other proton machines as well as initial experience from the RHIC operation. With three beam-beam interaction points, two for proton-proton and one for electron-proton collisions, the beam-beam parameter per interaction point should not exceed 0.007.

For the electron (or positron) beam a limiting value of beam-beam parameter has been put at 0.08 for 10GeV beam energy, following the results of beam-beam simulation (see Chapter 2), as well as the experience from electron machines of similar energy range. Since the beam-beam limit decreases proportionally with the beam energy, the limiting value for 5 GeV is reduced to 0.04.

The available magnet apertures in the interaction region also put a limit on the achievable luminosity. The work on the interaction region design revealed considerable difficulties to provide an acceptable design for collisions of round beams. The IR design, described in Chapter 4, has been worked out to provide low beta focusing and efficient separation of elliptical beams, with beam size ratio K=1/2. The main aperture limitation comes from the septum magnet, which leads to the limiting values of $\sigma'_{xp} = 93\mu\text{rad}$.

Another limitation, which should be taken into account is a minimum acceptable value of beta-function at the interaction point. With the proton rms bunch length of 20cm, decreasing β^* well below this number results in a luminosity degradation due to the hour-glass effect. The limiting value β^*=19cm has been used for the design, which results in hour-glass luminosity reduction only by about 12%. 20cm bunch length for Au ions would be achieved with electron cooling.

Table 1.1 and Table 1.2 below show design luminosities and beam parameters. A positron beam is supposed to be of similar to electron beam intensity (see Chapter 2), hence the luminosities for collisions involving positron beam are equivalent to electron-ion collision luminosities.

To achieve the high luminosity with low energy setup in Table 1.1 the electron cooling has to be used to shrink normalized transverse emittance of lower energy proton beam to 5π mm.mrad. Also, in that case the proton beam should have collisions only with electron beam. Proton-proton collisions in other two interaction points have to be avoided to allow for higher proton beam-beam parameter.

The maximum luminosity achieved at the present design is $4.4\text{x}10^{32}$ $\text{cm}^{-2}\text{s}^{-1}$ in high energy collision mode (10GeV electron on 250GeV protons). Section 2.4.2 discusses a possible path to luminosities (see Table 2.4.2-2) as high as 10^{33} , with studies planned to explore the feasibility of higher electron beam intensity operation.

To achieve and maintain Au normalized transverse beam emittances shown in Table 1.2 the electron cooling will be used. For the lower energy setup of electron-gold collisions, the intensity of the gold beam is considerably reduced because of reduced value of beam-beam parameter limit for the electron beam.

Table 1.3 shows parameters for possible electron-$^3\text{He}^{+2}$ operation mode with He beam intensity limited by electron beam-beam limit.

Table 1.1. Luminosities and main beam parameters for electron(positron)-proton collisions.

	High energy setup		Low energy setup	
	p	e	p	e
Energy, GeV	250	10	50	5
Bunch intensity, 10^{11}	1	1	1	1
Ion normalized emittance, π mm·mrad , x/y	15/15		5/5	
rms emittance, nm, x/y	9.5/9.5	53/9.5	16.1/16.1	85/38
β*, cm, x/y	108/27	19/27	186/46	35/20
Beam-beam parameters, x/y	0.0065/0.003	0.03/0.08	0.019/0.0095	0.036/0.04
$\kappa=\varepsilon_y/\varepsilon_x$	1	0.18	1	0.45
Luminosity, 1.e32 $cm^{-2}s^{-1}$	4.4		1.5	

Table 1.2. Luminosities and main beam parameters for electron(positron)-Au collisions.

	High energy setup		Low energy setup	
	Au	e	Au	e
Energy, GeV/u	100	10	100	5
Bunch intensity, 10^{11}	0.01	1	0.0045	1
Ion normalized emittance, π mm·mrad , x/y	6/6		6/6	
rms emittance, nm, x/y	9.5/9.5	54/7.5	9.5/9.5	54/13.5
β*, cm, x/y	108/27	19/34	108/27	19/19
Beam-beam parameters, x/y	0.0065/0.003	0.0224/0.08	0.0065/0.003	0.02/0.04
$\kappa=\varepsilon_y/\varepsilon_x$	1	0.14	1	0.25
Luminosity, 1.e30 $cm^{-2}s^{-1}$	4.4		2.0	

Table 1.3. . Luminosities and main beam parameters for electron(positron)-$^3He^{+2}$ collisions.

	High energy setup		Low energy setup	
	He	e	He	e
Energy, GeV/u	167	10	167	5
Bunch intensity, 10^{11}	0.7	1	0.18	1
Ion normalized emittance, π mm·mrad , x/y	10/10		10/10	
rms emittance, nm, x/y	9.4/9.4	48/13	9.4/9.4	48/13
β*, cm, x/y	108/27	21/19	108/27	21/19
Beam-beam parameters, x/y	0.0065/0.003	0.045/0.08	0.0065/0.003	0.02/0.04
$\kappa=\varepsilon_y/\varepsilon_x$	1	0.28	1	0.28
Luminosity, 1.e32 $cm^{-2}s^{-1}$	3.1		0.8	

2. ELECTRON BEAM

2.1 Design Concepts

Storage Ring

The current design of the electron beam envisages a race-track shaped storage ring for polarized electrons of 10 GeV with pro-visions to accommodate energies as low as 5 GeV, and for self-polarized positrons of 10 GeV. The main design goals are high beam polarization and maximum luminosity. The central concept arrives at a luminosity of $0.44 \times 10E^{33}/cm^2/s$ based on conservative beam stability and beam-beam interaction limits assuming a single interaction region for electron and hadron beams and two additional hadron-hadron interaction points. A more aggressive scheme is outlined producing a luminosity of $1 \times 10^{33}/cm^2/s$ requiring further R&D towards higher beam-beam tune shifts. The over-all dimensions of the proposed electron ring are governed by the following considerations: The length of the straight sections is given by the space needed for spin rotators (vertical spin in the arc, longitudinal spin at the intersection point), a polarimeter, and the interaction region including the detector. The minimal bending radius in the arcs is determined by the allowable synchrotron light power density deposited on the beam vacuum chambers and the maximal arc radius is governed by the acceptable self-polarization time for positrons, packing fraction of bending magnets and cost.

Optimization within these boundary conditions resulted in an electron (positron) ring of 1/3 of the RHIC circumference (L=1278m) with straight sections of 160m, an arc radius of 152m and a bending radius of ρ=81m (53% packing fraction). The expected synchrotron power density from a 0.5A, 10 GeV electron beam is p=11 kW/m, somewhat higher than values at existing B-factories but well within their upgrade goals and a positron polarization time of τ = 22 min at 10 GeV. In view of the relatively firm lower limits on the length of the straight sections and on the required space between bending magnets (packing fraction) which together make up over 50% of the ring circumference, and the strong dependence on ρ of the synchrotron light power density ($\propto \rho^{-2}$) and the polarization time ($\propto L\rho^2$), the choice of the ring circumference is quite restricted: e.g. a ring circumference of ¼ of RHIC would result in p≈17kW/m, $\tau \approx$10 min.; for ½ of RHIC circumference, p ≈ 4kW/m, $\tau \approx$ 81 min.

The current lattice design features an adjustable emittance to optimize luminosity at a range of energies. It features a “flat” beam with a vertical-to-horizontal emittance ratio of 0.18. Although this is not optimal for highest luminosity, the creation of "round" beams without loosing polarization is not trivial and needs to be explored further, possibly requiring R&D on the existing storage ring at Bates.

One of the most demanding problems is to design a lattice which preserves polarization (high equilibrium polarization) in the presence of magnet and alignment imperfections. One specific concern is the effect of solenoidal spin rotators proposed for the interaction straight section. Their use would provide near-longitudinal polarization at the interaction point for a range of energies without requiring mechanical reconfiguration of the spin rotators.

The requirement of varying the ion beam energy and thus ion beam velocities implies that either or both of the electron and ion beam ring circumferences have to be adjustable. Three schemes to accomplish this were considered. The first of splitting the 3m long lattice bending magnets into three units (super-bends) to vary the path length through the benders would only allow a path length

change of about 5.5 cm or $4.3.10^{-5}$ of the ring circumference to accommodate ions of 100 GeV/amu at the cost of reducing the electron energy to 7 GeV to keep synchrotron power density below 11 kW/m. A second scheme of moving one entire arc section uniformly to lengthen the straight sections would accommodate any ion energies without compromising the e-ring lattice or requiring any ion ring adjustment. The cost of the mechanical engineering for such a moveable arc is still being evaluated and may prove this scheme impractical. A third possibility is a number of fixed chicanes in the arcs which would allow discrete path length increases accompanied by a small continuous path variation in RHIC. A typical arrangement of four chicanes containing 6 displaced magnets and 6 displaced quadrupoles (3 FODO cells) and a continuous path length adjustment of .6m or $1.6.10^{-4}$ of the RHIC circumference would allow a continues ion energy range from 23 to 250 GeV. It would increase the cost of the e-ring arcs by about 20%. An optimized scheme is the subject of further studies.

Injection

Polarized electrons are to be injected into the ring at full energy (5 to 10 GeV) rather than relying on energy ramping and self-polarization of electrons injected at low energy. Although low-energy injection would be cheaper, full energy injection provides more stable, easier ring operations by avoiding ramping, and the possibility of "topping" up the stored electron beam to maximize average luminosity. There is no need for wigglers to self-polarize electrons below 10 GeV (self-polarization for ramped beams is indispensable since ramping most likely destroys any initial polarization. Full-energy polarized injection also would allow frequent injections should beam depolarization times prove too short.

An injection scheme is proposed using a 5 GeV linac with a Recirculator that would also naturally lend itself to include a positron source.

The variable pulse repetition frequencies required for the e-ring for different ion energies and the fixed linac frequency require special measures in the polarized electron source and injection to the linac to provide both relatively high pulse charge at variable pulse frequency.

Interaction Region

The design of the interaction region has to fulfill a number of conditions: maximum luminosity requires β-functions of the order of 10 to 20 cm for both electron and ion beams and both beams have to be separated less than 5m past the interaction point to avoid second collisions of the 28 MHz pulse trains. Both requirements limit the free space around the interaction point and restrict the available solid angle for detection of the reaction products from the electron-ion collisions. At the same time, background from intercepted synchrotron radiation produced in bending and focusing the electron beam must be minimized. Finally, the effects of the solenoidal magnetic field of the particle detector must be neutralized to maintain beam stability. In order to minimize depolarization of the electron beam, vertical bending of the electron beam should be avoided while vertically bending the ion beam requires large bending strengths. Keeping both beam in the horizontal plane then poses the problems of beam crossing in the arcs of the electron and ion rings.

An interaction region conceptual design addressing all those conditions has been arrived at using half-quadrupoles to separate and focus the interacting beams without unduly restricting solid angles for particle detection and minimizing synchrotron background. Further development of these ideas will require close cooperation with detector design.

2.2 Geometry and Location at the BNL Site

Existing RHIC collider has six interaction regions. Two of them, at 6 and 8 o'clock, are occupied by two large detectors, STAR and PHENIX. These regions are excluded from consideration for additional electron accelerator as they will continue their work for the physics studies with ion-ion collisions.
Although the two smaller experiments, PHOBOS and BRAHMS located at 10 and 2 o'clock interaction regions, correspondingly, will finish their experimental program before the eRHIC era, these regions also can not be used for eRHIC. The warm sections around 10 o'clock interaction region, where the PHOBOS detector is located, are used for the beam dump purposes. The electron ring cannot be put at 2 o'clock because of environmental restrictions due to a water flow of the Peconic River.

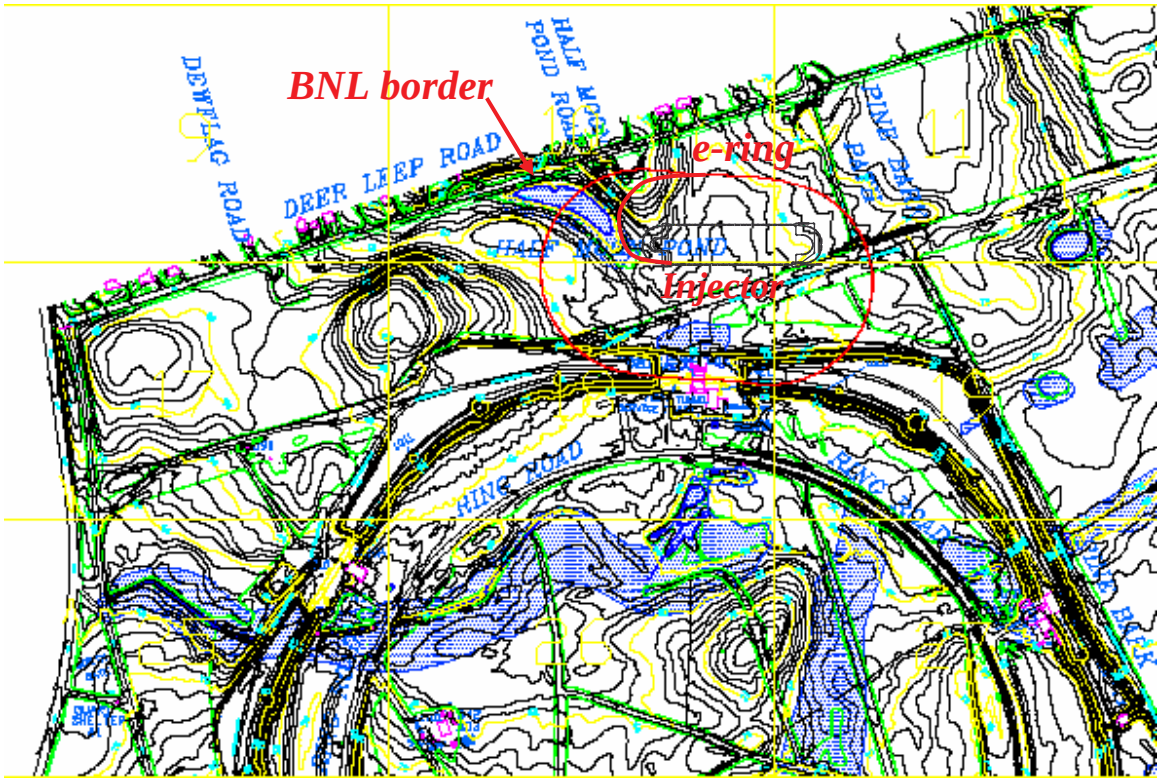

Figure 2.2-1**:** The scheme of the electron accelerator location at 12 o'clock RHIC region.

The remaining two interaction regions at 12 and 4 o'clock can be considered as possible locations of the electron accelerator. The first choice could beat the northern 12 o'clock interaction region as shown in Figure 2.2-1. The electron ring does fit within the BNL site but one section is relatively close to the laboratory border, about 50m at the closest point. There is a residential area outside of the laboratory border and this could be considered as definite disadvantage. The major advantage of that location is an already prepared excavation for a new detector. Because of limited space available in the 12 o'clock, the electron injector has to be placed inside the electron ring circumference, as presented in Figure 2.2-1 The injector design based on normal conducting linac could be easily placed inside the electron ring circumference.

The electron storage ring could be allocated more easily at the 4 o'clock region and it is far away from the BNL border, as shown in Figure 2.2-2. The injector with linac can be placed outside of the electron ring. The injector-to-ring transfer line does not contain bending arcs, as in the case of transfer line at 12 o'clock location. In the case of superconducting injector, the proximity of RHIC cryogenic plant may present an additional advantage for the choice of 4 o'clock region. The power supplies building in that area is far from the electron ring and does not need to be relocated. A disadvantage of this choice is an existing RHIC RF system located at the 4 o'clock area. It would have to be moved to another area, either to twelve or two clock interaction region.

The future electron cooling system can be built either at 12 or 4 o'clock depending on the choice for electron accelerator location.

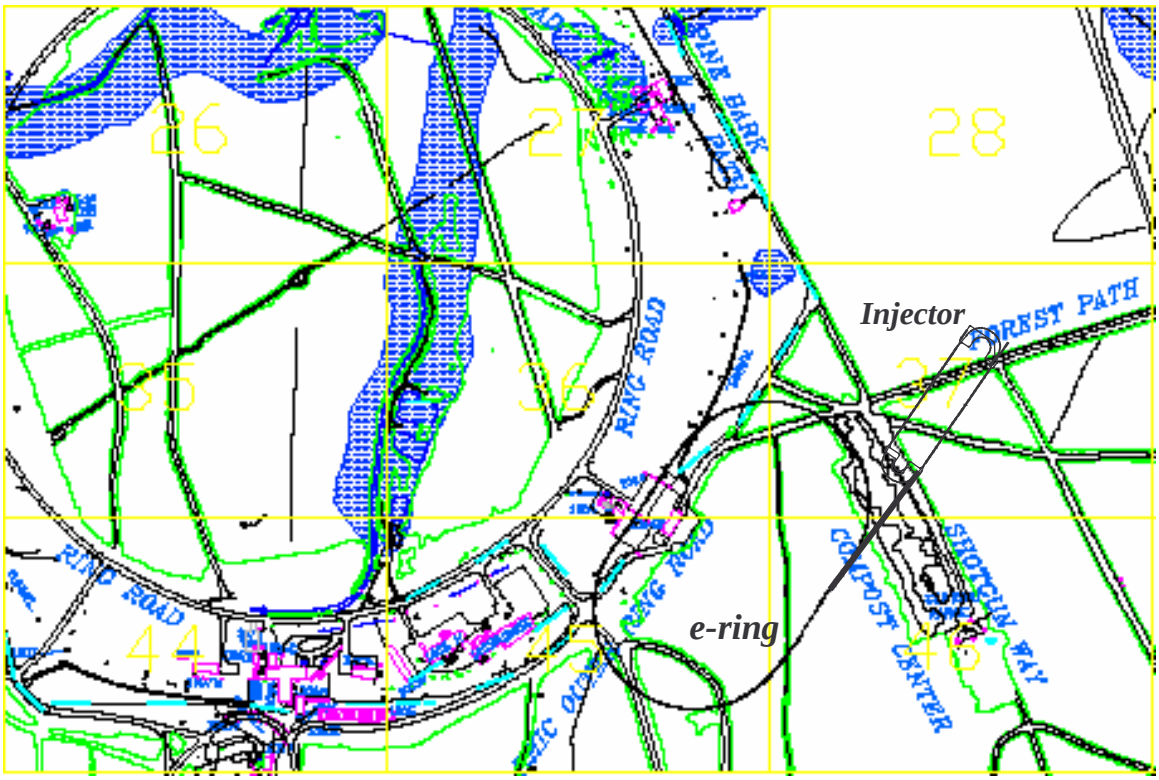

Figure 2.2-2**:** The scheme of the electron accelerator location at 4 o'clock RHIC region.

2.3 Injector Accelerator

2.3.1 Polarized Electron Photoinjector

Peak Current and Timing Requirements:

The advancement in the polarized electron source technology over the past decade at nuclear and particle physics accelerator centers have been substantial [1,2,3]. Highly polarized electron beams of diverse peak currents, time structures and duty cycles including CW beams are now routinely produced at Jefferson Lab, SLAC, HERA, MIT-Bates, Mainz and Bon [1,2,3,4,5]. These polarized injectors are based on photoemission process from strained GaAs based photocathodes illuminated by laser radiations at 800-850 nm followed by an extraction process with high gradient electric field. The stored current of order 0.5 A of highly polarized electron beam in a storage ring such as eRHIC normally would represent a modest technical requirement on present state of the art polarized source technology. The ability to stack multiple pulses in the storage ring presents a great advantage in achieving high stored average currents from repeated injection with relatively low linac peak currents. For instance, at MIT-Bates, highly polarized stored currents of few 100 mA are now routinely achieved by stacking of microsecond long pulses ~2 mA high. However, the collider nature of eRHIC with synchronized bunches precisely matching the proton bunches represents a great challenge to the injector setup and the polarized source architect. In this section we present two architects for the polarized injector and the front end of the accelerator that in principle can meet the injection requirements of the synchronized bunches for eRHIC. These options are presented assuming a room temperature copper accelerator at 2856 MHZ. Modification to the architect of these options may be required if a superconducting RF linac is used instead. The principles of the two options are still valid for SRF linac. The variations between these two options are in the time structure of the photoemission drive laser systems and in the electron beam line for bunching and chopping functions. In this section, the photoemission process from high polarization photocathodes are described followed by a description of the two options for the laser systems for the source.

High Polarization Photocathodes

Polarized electron beams for accelerators are generated by photoemission process using longitudinally polarized laser lights at 750-850 nm from the surface of GaAs based photocathodes under UHV conditions. The electrons are extracted from the surface using high gradient field present between the anode and cathode electrodes. The maximum theoretical limit for degree of polarization from a bulk GaAs surface is 50% and ~40% in practice due to depolarization effects in the bulk. The photoemission process in bulk GaAs is the simultaneous excitation of electrons in degenerate states in the valance band to the conduction band. To the degree that this degeneracy in the valance band is removed, higher degree of polarization can be achieved. A common technique to remove the existing degeneracy is to introduce strain in the lattice by growing GaAsP layers on substrate GaAs. The lattice mismatch between GaAs and GaAsP produces mechanical strain near the boundary surface [6]. The active layer must be very thin of the order few hundred nm to keep the strain present near the surface of the photocathode. The reduced depth in the active layer causes a substantial reduction in the Quantum Efficiency (QE) of the photocathode. QE is the fractional number of electrons generated by a single photon. QE for bulk GaAs photocathodes with pol~30-40% is of the order of 1-10 % and 0.01-0.1% for high polarization strained GaAsP, smaller by two decades. The high

polarization photocathodes therefore, have the inherent problem of low QE's. With a laser radiation of wavelength λ and power P, the maximum peak current generated from a photocathode of appropriate band gap structure is given by

$$I(\text{mA}) = \frac{QE \times P(\text{mW})\lambda(\text{nm})}{1239}$$

For instance, with P=1W, QE=0.1% at λ=800 nm, a peak current of ~0.64 mA can be generated. As shown in Figure 2.3.1-1, the QE and polarization are strong functions of λ.

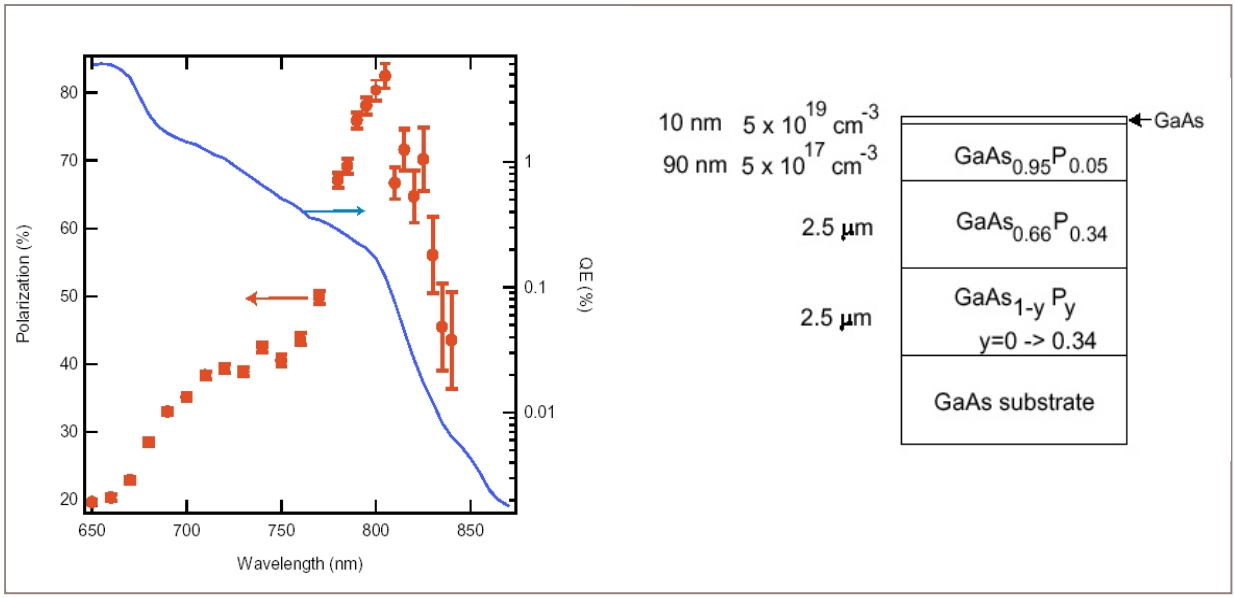

Figure 2.3.1-1. (Left) Photoemission data on a GaAsP from SLAC [7] showing Polarization and QE as a function of wavelength. (Right) A schematic diagram of the lattice structure of a high polarization high gradient doped strained GaAsP photocathode [8] now in use at SLAC and MIT-Bates. The peak polarization for this sample is near 800 nm where commercial high power lasers are more readily available The 10 nm thick layer is highly doped to reduce the surface charge limit effect.

Surface Charge Saturation Effect

In a perfectly atomically clean and freshly activated photocathode, the extracted charge is proportional to the incident laser power. However, as the QE of the photocathode decreases due to surface pollution, the relationship between the laser power and the extracted charge begins to deviate from linear. This is particularly pronounced at high laser power densities where due to an abundance of negative charges on the surface, the effective work function near the surface is increased causing a reduction in the extracted charge per bunch. This effect has been observed at SLAC and at MIT-Bates and studied in great detail at SLAC [8]. Figure 2.3.1-2 shows data from the MIT-Bates polarized injector that clearly indicates the deviation from linear as the photocathode is aged over the course of many months. As charge saturation effect increases more laser power is required for producing the current required. To reduce the surface charge limit in the high gradient doped sample currently used at SLAC and MIT-Bates, the top 10 nm GaAs layer is heavily doped. However, this thin layer is evaporated after several heat cleaning at near 600 C. Cares must be taken to reduce the number of heat cleaning for as long as possible. There are potentially several other methods to reduce the surface charge limit for high polarization photocathodes. These include cathode biasing, higher gun

voltage, higher QE and the use of superlattice structures [9]. These methods and have been tested in various photocathode and gun R&D programs mainly at SLAC and Nagoya but further R&D is required to make them practical.

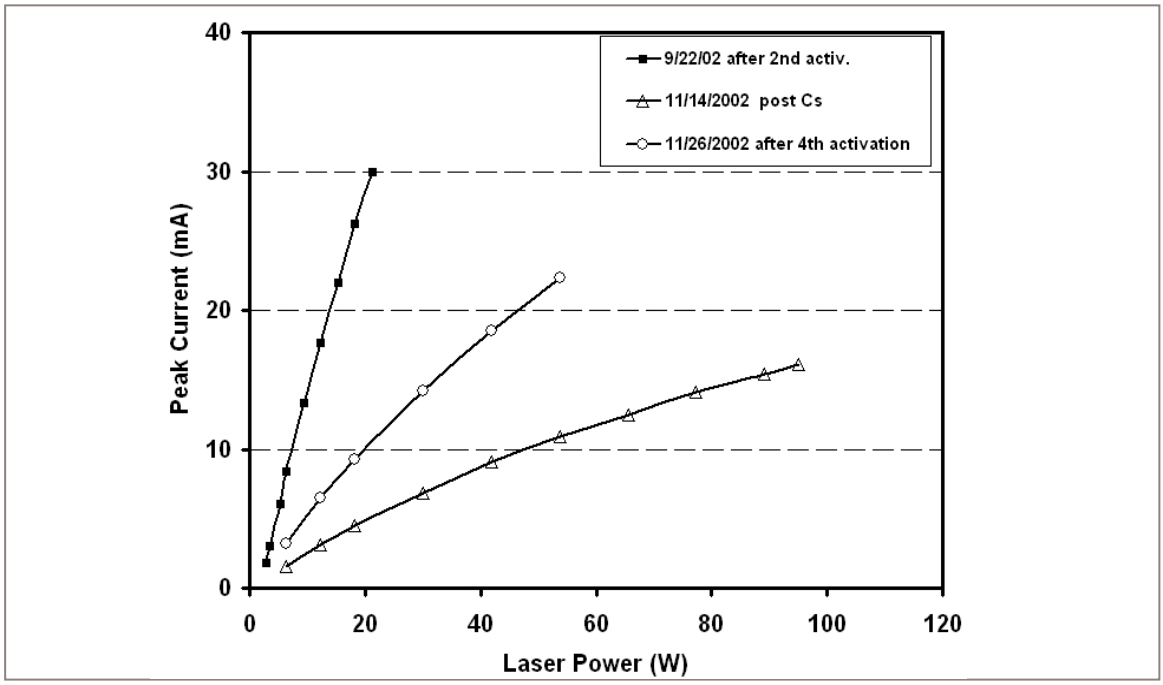

Figure 2.3.1-2. Peak current vs. laser power shown after several heat cleaning and activations for a two months period for the MIT-bates polarized injector. Due to surface charge limit effect the slope of the current vs. laser power decreased between 9/22 and 11/26 (squares and triangles). A heat cleaning and activation on 11/26 partially restored the slope (circles).

Charge per Bunch

Assuming 120 bunches distributed evenly in the eRHIC electron ring that is 4.3 μs long, a 480 mA stored current would correspond to 20 nC charge per collider bunch. With ~25 Hz injection repetition rate, and 10 minutes fill time a total of 15000 pulse trains (each 4.3 μs long , 35 MHz) with 1.3 pC in each bunch from the linac are required to stack the required 20 nC collider bunch. The charge per bunch from the polarized source to provide these bunches in the linac would be 1.3 pC divided by the capture efficiency of the injector to linac. The photoinjector to linac capture efficiencies will be discussed for the two photoinjector options discussed later in this section. Table 2.3.1-1 illustrates the important parameters of the collider ring, the linac and the polarized injector.

	Quantity	Value	Unit
Collider Ring	Stored current	480	mA
	Frequency	28.	MHz
	Ring circumference	4.3	μs
	Number of bunches in the ring	120	
	Charge per macroscopic bunch	20	nC
	stacking: pulse train rep. rate	25	Hz
	Duration	10	minutes
	Total pulse train from injector	15,000 (25x10x60)	
	Charge per bunch	1.3	pC
Photocathode	Bunch duration	~70	ps
	Bunch charge	1.3	pC
	Peak current	20	mA
Linac	Microscopic duty cycle (within 4.3 us)	$2x10^{-3}$	
	Macroscopic duty cycle during fill	$1x10^{-4}$	
	Macropulse average current	40	μA
	Average current during fill	4	nA

Table 2.3.1-1**. Important beam parameters for the collider ring, the electron linac and the polarized injector.**

Two Options for eRHIC Polarized Injector

There are two classes of options considered for the eRHIC polarized injector. In one option, the radiation from a mode locked laser system at the collider frequency of 28 MHz (102^{nd} sub-harmonic of 2856 MHz copper linac) is modulated and amplified with a shutter Pockels cell and an amplifier. The photoemitted electron beam has the synchronous bunch and time structures required for the collider ring. No further chopping or bunching is necessary. In the second option, a high power diode laser similar to one for the MIT-Bates polarized injector [11] produces DC radiation ~4.3 μs long directed to the photocathode. The 28 and 2856 MHz RF structures are introduced into the electron beam by a 102 MHz buncher and a 28 MHz chopper synchronous with the collider ring followed by a drift and a chopper-buncher system at 2856 MHz. These two options are described here. The microscopic and macroscopic pulse structures for the injector and the collider ring are shown schematically in Figure 2.3.1-3. The microscopic and macroscopic duty cycles for the current pulse structures are 2x10-3 and 1x10-4 respectively. The overall duty cycle of the injector and linac is 2x10-7.

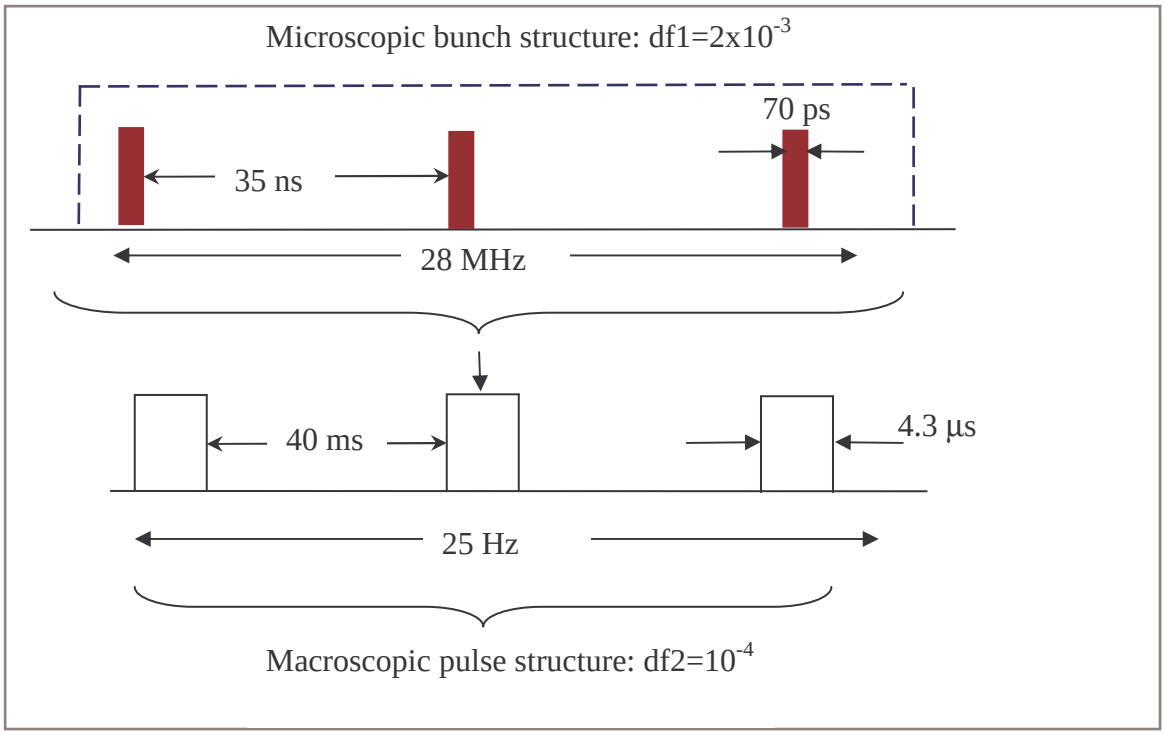

Figure 2.3.1-3. Schematic diagrams of microscopic bunch structure (top) and the macroscopic pulse structure (bottom). The duty factors are 2x10-3 and 1x10-4 respectively. The overall duty cycle of the injector and linac is 2x10-7.

Option 1: Mode locked laser with synchronous amplifier

This option would consist of a mode locked laser at 28 MHz, 102th-subharmonics of the 2856 MHz copper linac followed by a shutter Pockels cell (SPC) for generating the macroscopic pulse length of 4.3 μs and a possible laser amplifier operating synchronously at the collider frequency of 28 MHz. The λ/2 SPC combined with a polarizer would provide the necessary switching of the beam for long pulses. These ~100 ps wide pulses should arrive synchronously within the 2 ns wide storage ring bunches. A schematic view of this laser system is shown in Figure 2.3.1-4. The macroscopic pulse length and repetition rates are ~4.3 μs and ~25 Hz respectively.

Today, such mode locked lasers can produce 300 mW of average power. The peak power for 70 ps long pulses at 28 MHz would therefore be as high as 150 W as shown below

$$P_{peak} = \frac{\overline{P}}{f_{ring} * dt} \qquad \text{with } f_{ring}=28 \text{ MHz and } dt=70 \text{ ps}$$

As stated earlier in this section, to fill the ring to 480 mA with 120 bunches in the ring with 10 minutes fill time would require bunches from the linac with ~1.3 pC charge each. The peak current for these 70 ps wide pulses would be about 18 mA. With a QE of 5x10^{-4} and λ=800 nm, to produce 18 mA peak would require peak laser power of order ~50 W which is factor of 3 less than what a 28 MHz mode lock laser can produce. This is the safety factor required for degradation of QE over time. The capture efficiency of the injector with this laser system is 50-100% depending on the beam optics in the injector.

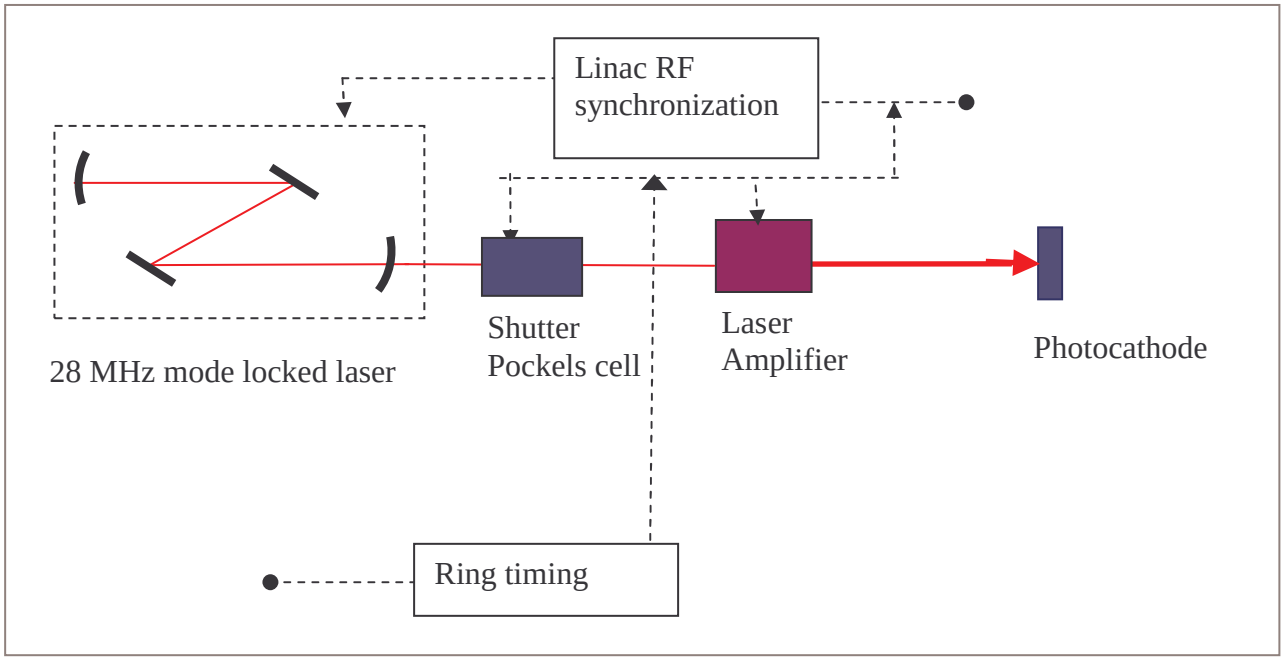

Figure 2.3.1.4. Schematic diagram of mode locked laser option for the eRHIC electron injector.

The drawback of this option is the timing stability requirement associated with mode locked lasers compared to DC or pulsed lasers. The advantage of this option is the built-in collider frequency into the photo-emitted electrons from the source. No chopping and bunching of the electron beam is necessary in this option.

Option 2: High power pulsed diode laser with e beam bunching

In this option, a high power fiber coupled DC diode laser produces 4.3 μs long laser pulses directed to the photocathode. After accelerating to several hundred keV, the photo-emitted polarized electron pulses pass through a structure consisting of a 102 MHz buncher and drift cavity, a 28 MHz chopper synchronous with the collider ring, and a 2856 MHz chopper and buncher system. The purpose of the 102 MHz buncher and the drift is to increase the peak current by a factor of 5-10 by compressing each 10 ns cycle down to about 1ns through velocity bunching at ~200 keV in a 5-10 m drift space. The corresponding drift space for a 28 MHz buncher is unrealistically long and the bunching gain for a 476 MHz buncher is not as much as the one from a 102 MHz buncher. Figure 2.3.1-5 shows this option schematically. As stated above, the charge per linac bunch required for the collider is ~1.3 pC. The requirement on the peak current from the source will be reduced by a factor of 5-10 if the 102 MHz buncher could efficiently capture a total of ~1ns of the DC beam near the zero crossing of the sinusoidal RF and compress it down to ~200-100 ps. The peak current in the linac for a 70 ps wide bunch and 1.3 pC charge is 18 mA. With a 102 MHz bunching fraction F_{bunch}, and a linac capture efficiency $\varepsilon_{capture}$ the required peak current in the polarized injector before bunching would then be

$$I_{peak} = \frac{I_{peak}^{linac} * \varepsilon_{capture}}{F_{bunch}}$$

Assuming a linac capture efficiency of $\varepsilon_{capture}$=0.5 and a bunching factor of F_{bunch}=5, the required peak current from the source to meet the linac charge per bunch of 1.3 pC is ~7 mA. This is quite possible with a high power diode laser system such as one used at MIT-Bates illuminating a high polarization photocathode that is not highly surface charge limited.

The advantage of this option is the simplicity and the stability of the DC high power diode laser array system that is commercially available and as the operational experience at MIT-bates indicates, they are trouble free and maintenance free operating for years. The drawback of this option is the complex chopping and bunching elements on the electron beam and the less than desired low capture fraction between the photocathode and accelerator.

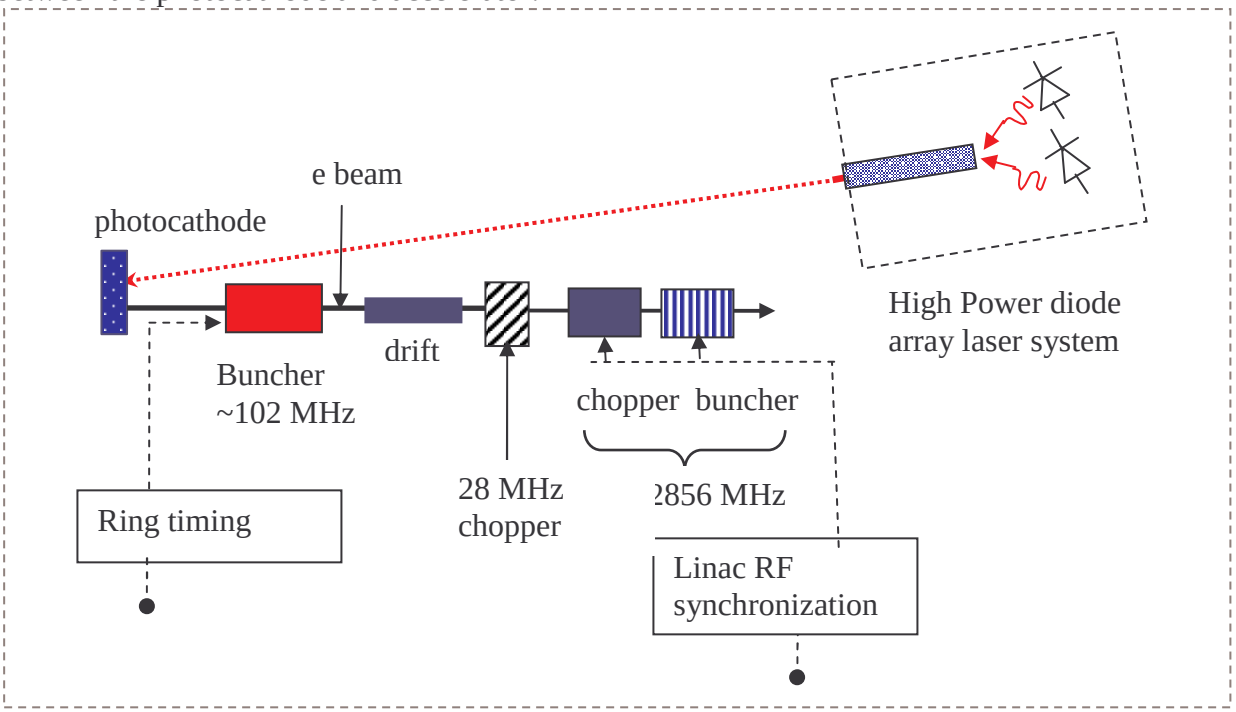

Figure 2.3.1-5. Schematic diagram of the eRHIC electron injector utilizing high power pulsed diode laser and electron beam bunching. The ~102 MHz buncher and the drift are intended to reduce the peak current requirements for the injector.

Multiple Injectors and Load Lock System:

For increase in the operation efficiency of the accelerator it is prudent to have a dual polarized injector each consisting of a polarized gun and the initial beam optics elements connected to the front end of the accelerator with isolation gate valves. This dual setup would permit the operation of one of the injectors at a time and the second as a stand by for backup. In addition, the gun chamber can be equipped with a load lock system that would provide the capability of loading of photocathodes into the gun assembly without a lengthy bakeout of the gun chamber often necessary to achieve UHV conditions. The SLAC polarized injector for instance, has a load lock system in use for many years. A load lock system is a more complex multiple chamber system with moving parts under UHV

conditions. However, a load lock system with proper design would provide up to half a dozen photocathode samples that can be moved into the photoemission position.

References:

1. "*Status of the Jefferson Lab Polarized beam*", J. Grames, AIP proceeding of SPIN2002 Vol. 675 p1047.
2. "*The SLAC Polarized Electron Source"*, J. E. Clendenin, AIP proceeding of SPIN2002 Vol. 675 p.1042
3. *"MIT-Bates Polarized Source*", M. Farkhondeh, PESP2002 workshop, Danvers, MA, AIP proceeding of SPIN2002 Vol. 675 p.1098.
4. "*Status of the polarized source at MAMI"*, K. Aulenbacher, AIP proceeding of SPIN2002 Vol. 675 p1088.
5. "*The polarized Electron Source at ELSA*", W. v. Drachenfels, AIP proceeding of SPIN2002 Vol. 675 p1053.
6. T. Maruyama, et. al., Phys. Rev. Lett. **66** (1991) 2376.
7. T. Maruyama etal., NIM A492, 199(2002)
8. Bandwidth Semiconductor Inc., Bedford, NH.
9. "Suppression *of the Surface Charge Limit in Strained GaAs Photocathodes*", T. Maruyama, AIP proceeding of SPIN2002 Vol. 675 p1083.
10. Jpn J. Appl. Physics Vol. 34 (1995) pp. 355, and SLAC-PUB-6350, July 1994
11. Spectra-Physics Opto Power diode laser model OPC-DO60-mmm-FC. Also" *High power Diode Laser System for SHR*", E. Tsentalovich, AIP proceeding of SPIN2002 Vol. 675 p1019.

2.3.2 eRHIC Injector

Preliminary Design Considerations for a 10 GeV Electron/Positron Accelerator

The baseline injector for the proposed eRHIC collider is a 10 GeV machine capable of accelerating either electrons (polarized) or positrons (unpolarized). The successful realization of the eRHIC physics program requires the highest possible luminosity, ~10^{33} cm^{-2} s^{-1}, and highest possible polarization of the colliding beams. To maintain the optimum currents, ~0.5 Amps, in the eRHIC electron/positron (e-/e+) ring and preserve the high electron polarization available from today's photoinjectors, P>70%, the most straightforward technique is to inject into the e-/e+ ring at its operating energy of up to 10 GeV.

Injecting on energy into the eRHIC e-/e+ ring has the three important benefits listed below.

1) **Stability:** Injecting at the full energy allows the e-/e+ ring to run under CW conditions. The stability and control will be superior for a ring with static conditions, compared to one where the beam energy is ramped. This stability will be important for the fine tuning of the e-/e+ ring that will be required to maximize the luminosity of the colliding beams.

2) **Rapid Filling:** Injecting on energy allows for rapid filling of the e-/e+ ring. This will reduce the filling time that is required for the e-/e+ ring. If the filling time is too long it will reduce the integrated luminosity. In practice, the eRHIC collider fill time is likely to be limited by the fill time required for the hadron side. However, it is still desirable to keep the e-/e+ fill time short enough so it has a negligible impact on the integrated luminosity. Further, on energy injection allows a "top-off" mode of operation where the current in the electron ring is periodically topped-off at intervals which are much more frequent than the hadron storage time. This will increase the maximum achievable peak luminosity by allowing the eRHIC ring to operate at a higher beam-beam tune shift. The shorter e-/e+ lifetime is compensated by more frequent filling. This also increases the integrated luminosity by running the electron current at nearly constant value at all times.

3) **Highest Electron Polarization at all Energies/High Positron Polarization at 10 GeV:** For low energies, 5 GeV, the electron polarization will be determined by the source. This avoids the high radiation load and complexity in the main ring that would be required to radiatively polarize electrons at the low energies. On energy injection also avoids depolarization that is likely to occur if the main ring is ramped. This depolarization occurs principally as spin resonances are crossed during the ramping cycle. This effect has been observed at many existing synchrotrons [1, 2] and would severely impact the physics program requiring polarization observables.

The performance requirements of an on energy injector are listed below:

- Accelerate polarized electrons to the e-/e+ ring operating energy, a maximum of 10 GeV.
- Preserve the electron polarization during the acceleration process.

- Create and accelerate unpolarized positrons to the e-/e+ ring operating energy, a maximum of 10 GeV
- Fill the e-/+ ring to its operating current of 0.5 A in 10 minutes for either positrons or electrons
- Maintain the capability to "top off" the current in the e-/e+ ring by delivering a pulse of a few mA every few minutes.
- Fill the e-/e+ ring with the bunch structure required by the collider. The present design calls for 35 ns bunch spacing. The ideal injector will deliver good bunch to bunch charge uniformity, <1%. The injector should allow flexible filling patterns including other bunch spacings and unpopulated bunches to limit ion trapping and accommodate finite rise time of the e-/e+ ring injector elements.

Since the eRHIC program uses stored colliding beams with lifetimes well in excess of one hour the average current requirements of the injector accelerator complex are quite modest. However, details of the collider timing requirements place some additional demands on the injector accelerator complex. Table 2.3.2-1 lists the necessary properties of the beam delivered to the eRHIC electron/positron ring. Ideally the positron beam would meet the same performance specifications (excepting polarization) as the electron beam.

Beam Energy	10 GeV
Macro Pulse Repetition Rate (during fill)	30 Hz
Electron Bunch Spacing	35 ns
Bunch Train Length	4.3 us (single turn in the e-/e+ ring)
Charge/Bunch	3 pC
Fill time (Machine on time)	<10 minutes
Time between fills (Machine idle time)	>2 Hrs
Injection Efficiency (Qring/Qsource)	>50%

Table 2.3.2-1. eRHIC electron/positron injector accelerator parameters.

The small macro current of 100 μA in table 2.3.2-1 results in very small beam loading for all of the injector variants considered below. The parameters here reflect a mode of operation where the eRHIC e-/e+ ring is not "topped-off." If a "top-off" mode is adopted the accelerator would be required to periodically wake up and deliver a pulse to the eRHIC e-/e+ ring at approximately 10 minute intervals.

While several multi-GeV injectors are operational at existing facilities [3-5], there is considerable performance risk for the eRHIC physics program depending on the particulars of the injector design. As a principle design tenet we assert that the maximum luminosity of the collider and maximum polarization of the electron/positron ring should not be limited by the performance of the injector.

Several distinct accelerator topologies appear to have the potential to meet these requirements. At this early stage of design we consider three variants:

1) Recirculating copper S-band linac,
2) Recirculating superconducting linac
3) Figure-eight booster synchrotron.

Considerations that will affect the choice of injector include performance, performance risk, reliability, and cost. Another important factor will be the possible use of the eRHIC injector for multiple purposes on the Brookhaven site. At this point all three topologies are viable options. Each is presented in more detail below.

Recirculating Copper Linac

Figure 2.3.2-1 shows a possible layout of an injector based on a copper linac and recirculator. Here the linac structures are 3 m SLAC 2856 MHz traveling wave sections. The 2856 MHz frequency is well established and the accelerator and high power RF sources are commercially available. The performance characteristics of this technology are known and therefore this design presents little risk for an eRHIC injector.

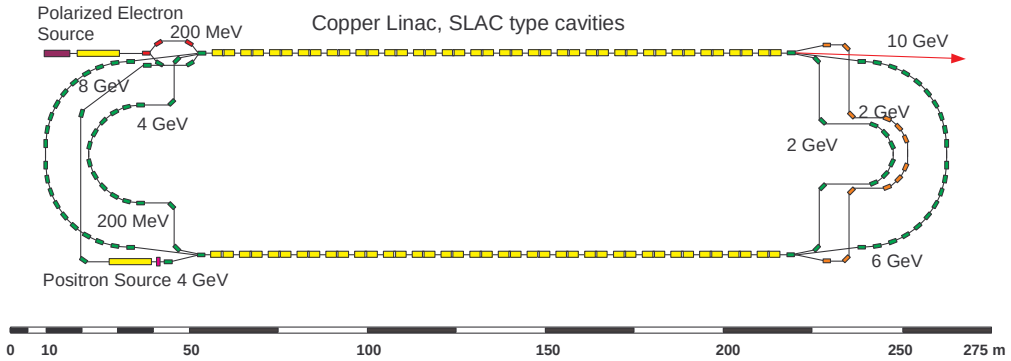

Figure 2.3.2-1. eRHIC injector accelerator. A polarized electron beam is accelerated to 200 MeV and injected into a 2 GeV copper linac. At the end of the linac the beam is transported through a 180 deg isochronous recirculation arc into a 2nd 2 GeV linac where the beam is accelerated to 4 GeV. One and a half subsequent recirculations increase the beam energy to a total of 10 GeV. Positron production is supported.

The parameters of a copper linac that would satisfy the eRHIC requirements are listed in Table 2.3.2-2 Below we consider a pre-conceptual design of a copper accelerating “module,” where a module consists of a 350 kV power supply, a capacitor bank, a HV modulator switch, a 50 MW klystron, RF waveguide distribution, 2 three meter accelerating sections and their associated RF loads.

Linac Frequency	2856 MHz
Linac Gradient	16 MV/m
Number of Linacs	2
Active Linac Length	120 m
Linac Length	170 m
Linac Section Length	3 m
Shunt Impedance	53 MOhm/m
RF Input Power/Section	25 MW
RF Macropulse Length	10 μs
Beam Pulse Length	2 μs (one recirculation period)
Macropulse Current	0.1 mA
Pulse Repetion Rate	30 Hz
Section Fill time	0.820 μs
Klystron Power	50 MW
Klystron Current	350 A
Klystron Voltage	350 kV
Klystrons/Modulator	1
Accelerating Sections/Klystron	2
Number of Sections	80 (40/Linac)
Number of Klystrons	40 (20/Linac)

Table 2.3.2-2. RF parameters – Copper S-band eRHIC injector linac.

The pulse repetition rate of 30 Hz is a reasonable requirement for a linac of this type. An average power of 30 kW per klystron is expected. These pulses would be line locked for increased stability. The rate is also well matched with the main eRHIC damping time of 7 (58) ms at 10 (5) GeV. Optimal filling of the main ring is achieved at repetition rates equal to approximately three inverse damping times.

The copper linac is limited to a smaller number of recirculations (2-3) due to constraints on the pulse widths available from the high power klystrons, i.e. pulses <10 us in duration. The circulation time in the linac is 2 μs. So the required RF pulse width for two turns of beam acceleration is 6 μs where two microseconds have been allocated for the RF turn on. This is a good match with the pulse widths that are available from these high power 50 MW klystrons. For 6 μs of RF 8 μs of video current from the klystron would be required.

A beam pulse length of 2 μs is matched to the injector circulation time so that a “head-to-tail” mode of operation may be used. This keeps the current in the linac constant after the initial turn and limits the impact of beam loading. The linac would be required to pulse twice to fill the full 4.3 us circumference of the e^-/e^+ ring.

In principle RF compression (SLED) technology could be used to increase the peak power from the klystron from 50 to ~100 MW. Higher gradients of 24 MV/m would be possible. However typical pulse widths from these compression schemes are 1-3 μs long and therefore not readily compatible with a recirculating linac. Therefore we have not adopted RF compression for this variant.

More detailed considerations of the RF sources and modulators for a copper linac are presented in the following sections.

Pulse-Modulated RF Power Amplifier

The existing technology baseline is the Toshiba 50 MW peak-power 2.856 GHz klystron MVED capable of 10 us pulse duration, at 40% efficiency, requiring 125 MW peak beam power input (350 kV beam voltage and 350 A beam current). An emerging technology option (development required) is the Multiple-Beam Klystron (MBK) with higher efficiency (50-65%), due to lower perveance of individual beams (typically 0.5 micropervs per beam, compared with 2.0 micropervs for single-beam gun), and operating at lower beam voltage, typically half that of single-beam klystron of same peak power, due to higher conversion efficiency and, more importantly, higher *total* beam perveance (typically 4 micropervs for 8-beam gun). A block diagram of a pulsed S-band transmitter is shown in figure 2.3.2-2

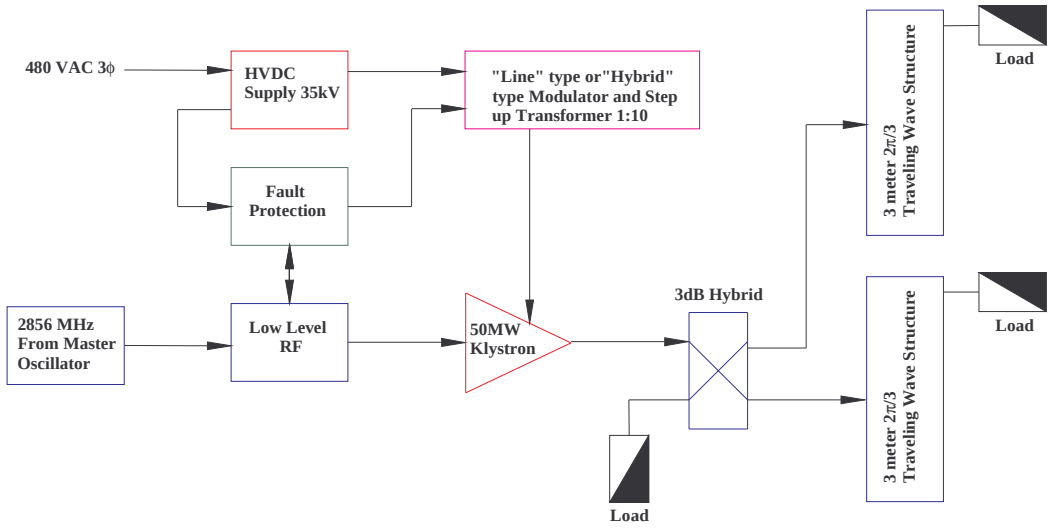

Fig 2.3.2-2 Block diagram of a Pulsed S- band Transmitter

Pulse Modulator

The traditional technology baseline is the “Line-type” modulator, as shown in Figure 2.3.2-3, using an artificial transmission-line pulse-forming network with characteristic impedance matched to transformed load (klystron beam) impedance, switched by half-control (closing switch only) such as Hydrogen Thyratron or high-current Thyristor stack. The pulse duration is determined by time delay

of network. The Klystron load is coupled by step-up pulse transformer, typically 10:1 turns ratio. All of the stored network energy is transferred to the klystron load each pulse. Referenced to pulse-transformer primary, the modulator switch must be rated at twice the output voltage, for normal operation, and twice the normal load current, for a short-circuit load fault condition, a non-simultaneous rating that is 4 times the load power under normal conditions. The switch peak power rating, therefore, must be 500 MW, for 125 MW peak load power.

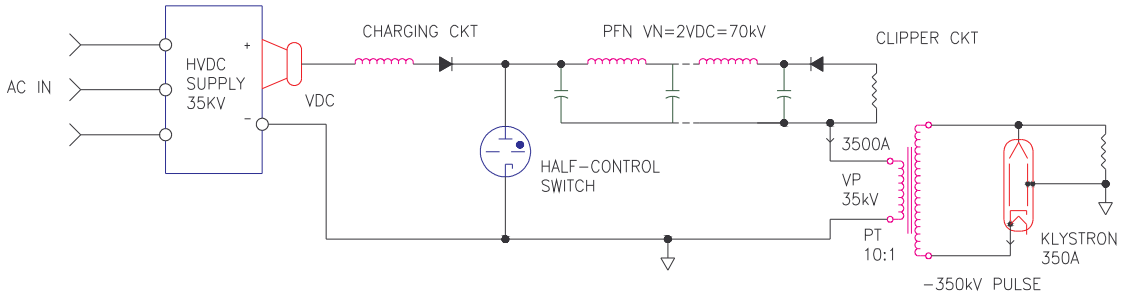

Fig. 2.3.2-3 Simplified schematic of basic "line" type modulator

An option is the so-called "Hybrid" modulator, as shown in Figure 2.3.2-4, using a step-up pulse transformer but with the PFN replaced by a capacitor bank and the half-control switch replaced with a solid-state full-control switch (turn-on and turn-off), comprising series-connected Insulated-Gate Bipolar Transistors (IGBTs). The duration of the output pulse is the same as that of the IGBT gate-drive. The voltage droop of the output pulse is determined by the ratio of capacitor-bank charge storage to the charge delivered to the load each pulse. Referenced to the pulse-transformer primary winding, the switch voltage rating is the same as the output voltage. Short-circuit fault current is interrupted by opening the IGBT switch (less than 1 u-sec opening time). The switch peak-power rating is the same as the load power, or 125 MW, assuming a large capacitor bank, and negligible voltage droop. A variant replaces the capacitor bank with an under-matched PFN, having a characteristic impedance small compared to that of the transformed klystron beam impedance. PFN delay-time must be more than half of the longest output pulse duration. The output pulse has zero droop, but has a voltage step at the leading edge, (depending on degree of under-match), continuing throughout the pulse, and pulse-top voltage ripple, determined by number of network stages. The pulse duration is the same as the IGBT gate-drive. The switch voltage and power rating must be greater than output voltage and power, depending on degree of under-match (for instance, 10% greater, for 10% undermatch).

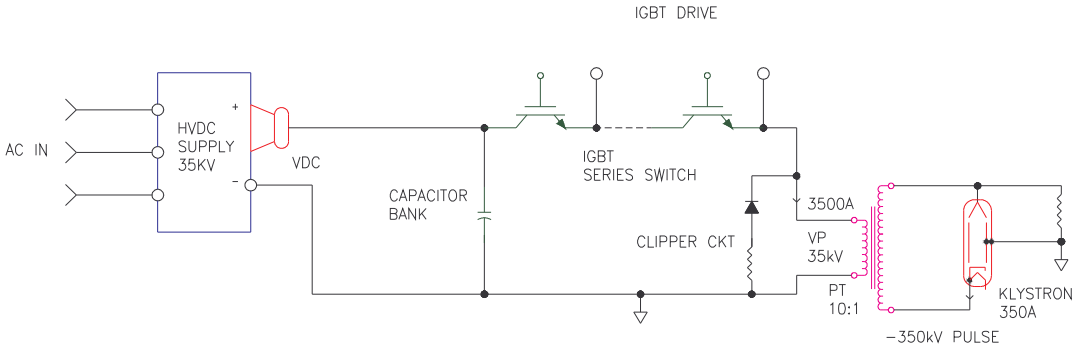

Fig 2.3.2-4 Simplified schematic of "hybrid" type modulator

Other options, in the category of emerging technology (development required) are the direct-drive, series-connected IGBT switch, with no step-up pulse-transformer, and an adaptation of the so-called "Marx" generator topology. Energy storage capacitors are charged from a relatively low-voltage DC source, in parallel, and discharged, in series, by means of IGBT switch modules distributed throughout the generator.

High-Voltage DC Power Supply

Except for the emerging-technology options, the required DC power supply output voltages is less than the peak pulse output voltage by a factor equal to the pulse-transformer turns-ratio. Notwithstanding the continuing improvement in power output capability of high-frequency switch-mode DC power supplies, the optimum power-supply topology is the poly-phase (typically 12-pulse) line-frequency transformer-rectifier. It is the simplest (no active components), most reliable (fewer components)) and most efficient (lowest total losses) source of high-quality DC output. It is also the largest and heaviest, but these are factors of only secondary importance. Voltage regulation, soft-start, and high-speed fault disconnect can be provided by SCR primary conduction-angle control.

Recirculating Superconducting Linac

Figure 2.3.2-5 shows a possible layout of an injector based on a superconducting accelerator and recirculator. Here the TESLA frequency of 1300 MHz is chosen due to their established performance [6], but the use of other frequencies between 500 – 1500 MHz is also possible.

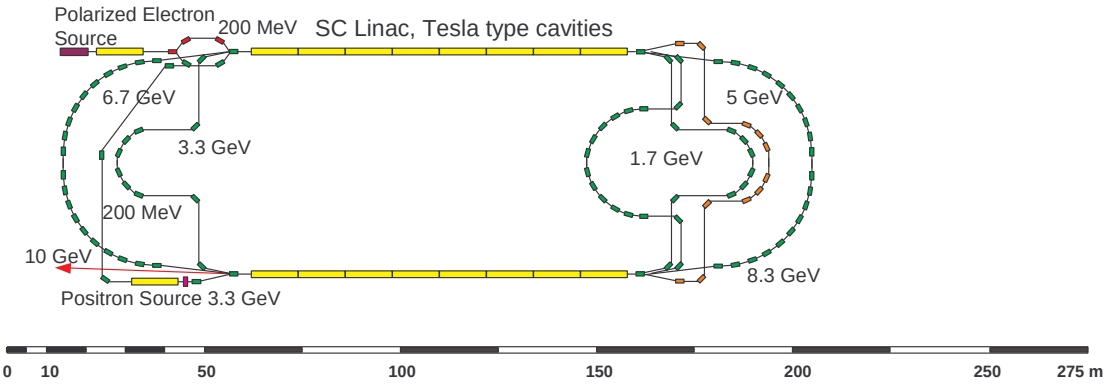

Figure 2.3.2-5. **Same as Figure 2.3.2-1 except that here the linac is two 1.7 GeV superconducting TESLA style structures. The electron beam is accelerated through 3 revolutions before reaching the maximum eRHIC energy of 10 GeV. Not shown here, a positron damping ring may be necessary to limit beam losses in the superconducting structure. Notice that the scale of the superconducting complex is ~200 m x 50 m while the normal conducting is ~300 m x 50 m.**

The parameters of a possible superconducting linac for eRHIC are listed below in Table 2.3.2-3 are baseline consideration of the superconducting version we use the
parameters of a TESLA type 1.3 GHz accelerator.

Linac Frequency	1300 MHz
Linac Gradient	26 MV/m
Number of Linacs	2
Active Linac Length	64 m
Linac Length	92 m
Linac Cavity Length	1 m
Shunt Impedance (R/Q)	1038 Ohm
Cavities/Cryomodule	8
RF Macropulse Length	40 ms – CW
Average Macropulse Current	0.01 μA
RF Pulse Repetion Rate	CW – 10 Hz
External Coupling (Q_ext)	$2\text{-}10^{+7}$
Cavity Fill time	1-4 ms
Klystron Power/Cavity	<10 kW
Cavities/Klystron	1
Maximum Heat Load at 2K	5 kW (for CW operation)
Average Heat Load at 2K	100 W (10 minute fill every 8 hrs) + 80 W (10 sec top up every 10 minutes)

Table 2.3.2-3. Parameters for a possible superconducting linac for eRHIC.

Unlike the copper linac, the number of circulations for the superconducting linac will not be limited by the maximum RF pulse width but by the complexity and cost of the recirculation. The cost differential for one incremental recirculation scales with the required length of the linac. The incremental linac cost for one additional recirculation is proportional to [1/N – 1/ (N+1)] where N is the number of recirculations. Further, each incremental recirculation arc is more expensive than the previous as it is transporting beam at a higher energy and must not interfere with the prior recirculation arcs. Figure 2.3.2-6 shows capital cost as a function of the number of recirculations, where a very simple cost model is adopted. The superconducting linac is costed at $0.5M per active meter and the recirculator is costed at $0.1M/m multiplied by a weakly increasing function which reflects the additional cost of transporting a higher energy beam. These considerations show that the largest cost benefit is in the first recirculation and that an optimum exists near two recirculations (three passes). Not included are the substantial offset costs of other accelerator systems including injector accelerator, cryogenic refrigerator, polarized electron source, positron damping ring and other infrastructure. This optimization can be compared with the existing Jefferson Lab Accelerator which has four recirculations (5 passes). Here the optimum (lowest capital cost) is at a lower number of turns than Jlab due to the high gradient, 25 MV/m available from the TESLA accelerating cavities.

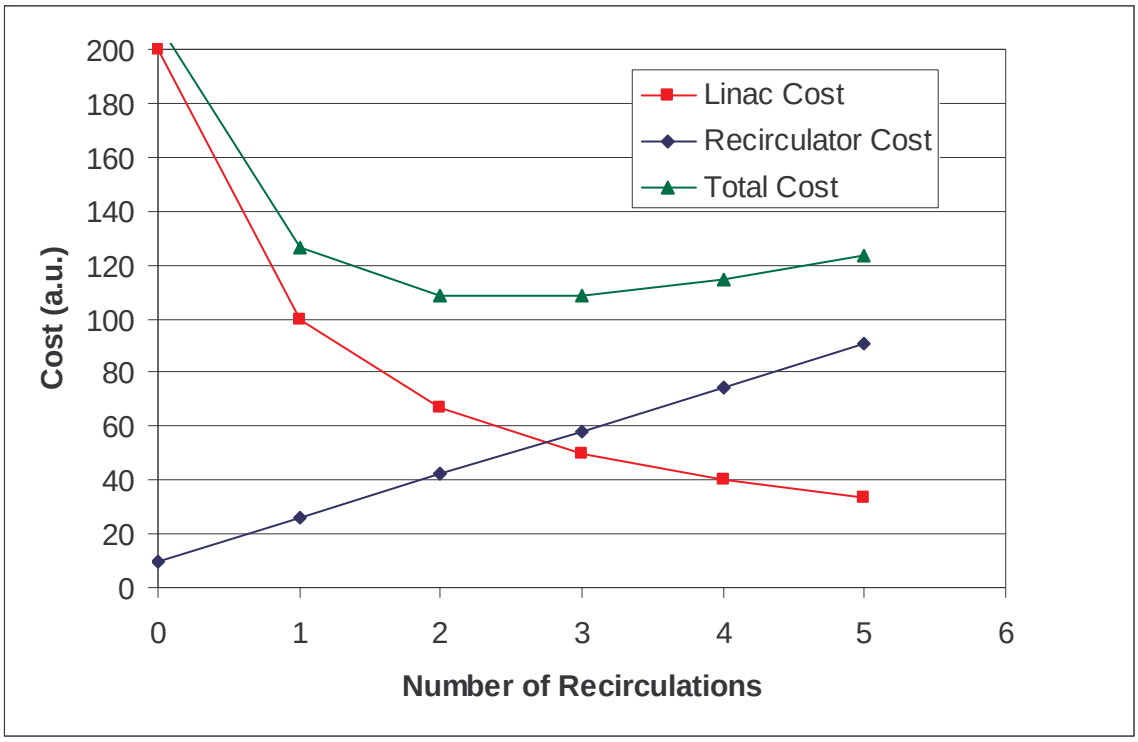

Figure 2.3.2-6. Capital cost scaling of a superconducting eRHIC accelerator injector as a function of the number of recirculations. The falling cost for the linac is balanced against a rising cost of the recirculator leading to an optimum near two recirculations (three passes).

The time structure of the beam required to fill eRHIC, (4 μs, 0.1mA pulses at 30 Hz with a micro structure of 3 pC every 35 ns) gives a very modest requirement on the beam power that the RF sources need to deliver. The average beam current is less than 20 nA and therefore the beam power per cavity is less than one Watt. This is to be contrasted with the TESLA collider requirement where the macropulse beam current is 10 mA and the required RF power for the beam is 200 kW per cavity. Clearly a very different RF source is required. For negligible beam power as above and very low wall losses in the superconducting cavity (P~30W at 25 MV/m), the limitations on the minimum required RF power come from control and stability requirements of the superconducting cavities. Several institutions are pursuing active piezo-restrictive tuners that would control the cavity center frequency [7]. These devices show great promise, but require operation inside the cryomass and themselves have resonant behavior which places limits on their performance. Bates is developing an RF recycling concept that would make use of an external tuner and phase shifter, which would allow the RF sources to be much more closely matched to the intrinsic power requirements of ~100 W. This topology may allow the use of solid state amplifiers rather than klystrons. If successful, this effort would substantially reduce both the capital and the operating cost associated with the eRHIC a superconducting recirculating linac injector.

Another RF source, a 30 kW, 1.3 GHz Inductive Output Tube (IOT) is also under development by industry. This is a gridded vacuum tube which does not require the use of a High Voltage modulator. The removal of low level RF from the grid stops the current emission from the cathode, eliminating all power demand. Further, these devices have very high AC to RF efficiency (~65%) due to the bunched nature of the current emission from the cathode. The sinusoidal potential on the RF grid

limits the emission angle of the cathode to less than 180 degrees thus increasing the bunching (and RF source) efficiency. Since the IOT is capable of delivering 30 kW it has the ability to overdrive a superconducting cavity system during the long fill time (up to 4 ms) which requires only a few kW in equilibrium. This would make higher pulse rates possible for a pulsed superconducting eRHIC injector accelerator.

The 2K dynamic heat load of this accelerator is substantial, 30W per cavity at 25 MV/m and $Q_0 = 10^{10}$. For 128 cavities this will correspond to a refrigerator power demand in excess of 5 MW for CW operation of the linac. However the periodic nature of eRHIC filling, 10 minutes every eight hours, or 10 seconds every 10 minutes every half for top-up operation, allow operation of the linac with a macroscopic duty factor substantially less than 10%.

Positron losses must be kept to a minimum in the superconducting structures. Average positron currents of 20 nA, an average energy of 5 GeV and 50% current losses distributed over the length of the linac would add an additional heat load of 100 W at 2K. This should be contrasted with the dynamic heat load of ~ 5 kW for CW operation. More serious would be localized losses that could cause a cavity quench or even permanent damage to the superconducting structure.

The success of the JLAB superconducting recirculating accelerator demonstrates that such a machine could accommodate the requirements for electron injection into the

eRHIC e-/e+ ring. Further work is necessary to optimize this type of injector with consideration of recent progress in superconducting RF systems. The integration of positron acceleration will also require significant effort. A normal conducting positron pre-accelerator and damping ring may be required.

Figure Eight Booster Synchrotron

Another variant of the eRHIC injector that merits consideration is the figure eight synchrotron. This injector topology (Figure 2.3.2-7) is similar to that proposed for the electron Light Ion Collider (ELIC) presently under consideration by a machine design group at JLAB [8]. Due to the two opposing 270 degree arcs, this geometry has the attractive feature that the forward spin precession in one half is cancelled by that in the other half, i.e. the net spin precession is zero and independent of energy. Therefore this synchrotron should be able to ramp at moderate rates, ~60 Hz, with little loss of polarization. No spin resonances will be crossed during the ramping process.

The parameters of this type of synchrotron are listed in Table 2.3.2-4. For this geometry the synchrotron losses per turn at 10 GeV are substantial, 47 MV, so 75 MV of RF voltage must be installed in the ring. However, the average energy during the ramp is only 5 GeV, the supported current is also quite modest, I~1 mA and the synchrotron has a duty factor of less than 50%. Therefore the average beam power is much less than 10 kW. This combination of high voltage and low beam power might be well matched to a superconducting RF system. These RF parameters are quite distinct from the main eRHIC electron ring where currents of 0.5 A and synchrotron losses of 10 MV require in excess of 5 MW. A critical task for the “figure eight” geometry will be a detailed

simulation of the polarization behavior during the ramp to assess the level of polarization that would be achievable for the electron and positron beams delivered to the eRHIC main ring.

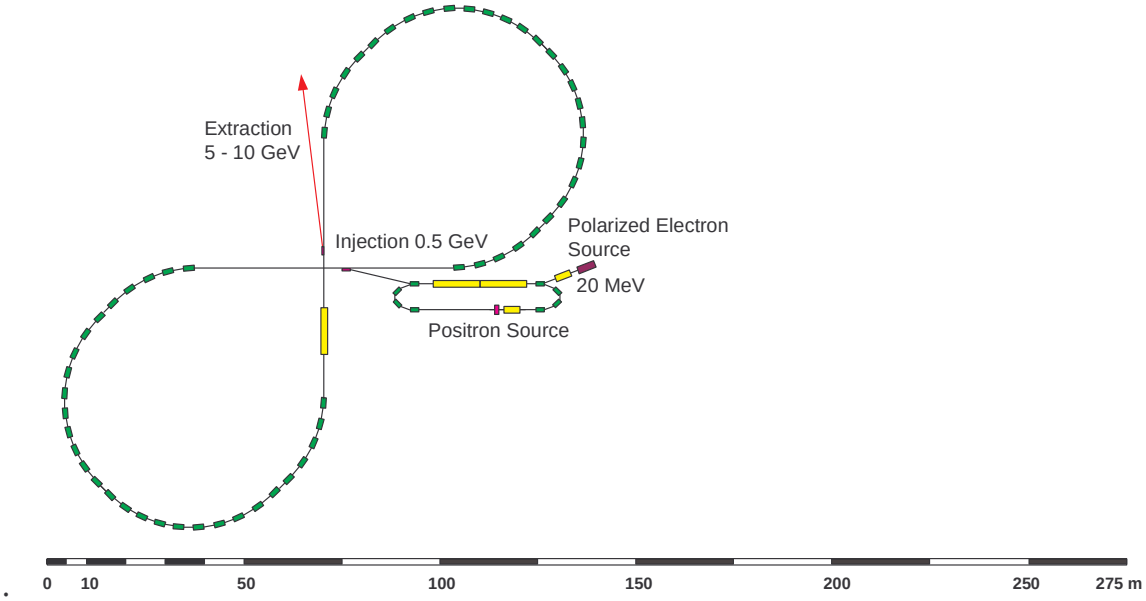

Figure 2.3.2-7. eRHIC injector synchrotron with "figure eight" geometry. A 20 MeV injector and 500 MeV linac fill the synchrotron ring to 0.1-1 mA after which it is ramped in energy from 0.5 à 10 GeV in 10-100 ms.

Due to the small dipole curvature, ~30 m, the ring will have a polarization damping time of 40 s at 10 GeV. This should not cause significant depolarization as the beam circulates in the booster for less than 100 ms.

Maximum Energy	10 GeV
Injection Energy	500 MeV
Circumference	500 m
Dipole Curvature	30 m
Synchrotron Radiation Losses/Turn	47 MV @ 10 GeV
Accelerated Current	1 mA
Peak Beam Power @ 10 GeV	50 kW
Installed RF Voltage	75 MV
Installed RF Power	100 kW
Synchrotron Cycling Frequency	<60 Hz
Polarization Damping Time	40 s
Equilibrium Polarization	0

Table 2.3.2-4. Parameters for a possible figure eight synchrotron injector for eRHIC.

If the polarization properties (small depolarization) of the accelerated beam permit a slower ramp it would be desirable to fill the synchrotron with several pulses (~10) at its injection energy to a peak current of ~1 mA and operate the synchrotron at a lower frequency of 5-10 Hz. The multiple pulse filling could be achieved with either momentum stacking from a 60 Hz 500 MeV copper linac (160 ms) or phase space painting with a superconducting 500 MeV injector linac (20 μs).

Positrons

The requirement to deliver 10 GeV positrons to the eRHIC ring adds considerable complexity to the eRHIC injector. As illustrated in Figures 2.3.2-1 and 2.3.2-5 our preliminary concept for positron production with either a normal or superconducting linac is accomplished by accelerating electrons through one turn before striking the production target. In the positron acceleration mode the electron transport is indicated in the figures by the red magnets. The subsequent positron transport is then indicated by the green magnets.

The specifications for the positron production target are comparable are less demanding than performance already demonstrated by the Stanford Linear Collider (SLC) positron source. [9] Table 2.3.2-5 lists the parameters for the SLC positron target and for the target for all three of the above injector topologies

	SLC 94	Copper Linac	SC Linac	Figure Eight Synchrotron
Electron Drive Beam				
Energy (GeV)	30	4	3.3	0.5
Pulse Charge (nC)	5.6	2	4	20
Pulse Width (us)	Single Bunch	2	4	2
Repetion Rate (Hz)	120	30	30	60 (Linac freq)
Beam Energy/Pulse (J)	160	8	13	10
Avg. Beam Power (kW)	20	0.24	0.4	1.2
Positron Yield/e-	2.4	~0.1	~0.1	~0.01

Table 2.3.2-5. Positron Production Specification for eRHIC accelerator injector and SLC94 .

For the two recirculating linacs (copper and superconducting) the peak electron current can be increased from 100 uA to ~1 mA to compensate for the lower electron energy striking the production target. This still results in much lower pulse energy and average power than was achieved at the SLC. A positron yield of 0.1 per incident electron could then deliver the same average currents as when the eRHIC injector operates in the electron mode. The 500 MeV linac injector of the figure eight synchrotron could compensate for the lower energy of the electron drive beam by running at macro pulse currents of 10 mA and a slightly higher repetition rate of 60 Hz.

Summary

The design of a 5-10 GeV eRHIC injector accelerator for electrons and positrons is a tractable problem. The three distinct architectures described above may all meet the needs of the eRHIC

physics program. Five important questions that must be addressed to clarify the choice of injector are listed below:

1) How will the reliability and operability of each injector affect the performance of the eRHIC program?
2) To what degree will the figure eight synchrotron maintain the electron polarization during the synchrotron's acceleration?
3) How best can positron production and acceleration be integrated into a superconducting recirculating linac?
4) Will this injector serve other functions on the Brookhaven site in addition to e-/e+ injection into eRHIC?
5) What are the costs of each injector system?

Future work that will help address these questions includes:

1) Development of an operational model for the eRHIC collider complex
2) Computer simulation of the polarization behavior in the figure eight synchrotron
3) Development of a consistent cost model for each of the considered injectors.
4) Detailed integration of positron production and acceleration for each of the considered injectors.

The guiding principle for the eRHIC injector should be to develop an injector which will not limit the physics performance of the eRHIC program and will deliver this performance with the least cost and most reliability.

References:

1. C. Steier et. al., "Acceleration of Polarized Electrons in ELSA" European Particle Accelerator Conference EPAC 98 p.433 1998.
2. H. Huang et. al., Preserving Polarization through an Intrinsic Depolarizing Resonance with a Partial Snake at the AGS" in AIP proceedings of SPIN 2002 Vol.675, p. 794, 2003.
3. S. Milton, "The APS Booster Synchrotron: Commissioning and Operational Experience" in 16th IEEE Particle Accelerator Conference (PAC 95) Vol. 1 p 594, 1995.
4. http://www.slac.stanford.edu/accel/pepii/pep2aerial.gif
5. R. Schmitz, "**A** CONTROL SYSTEM FOR THE DESY ACCELERATOR CHAINS" in 2nd International Workshop on Personal Computers and Particle Accelerator Controls (PCaPAC 99) Tsukuba, Japan 1999.
6. http://tesla.desy.de/new_pages/TDR_CD/start.html p II-32
7. S. Simrock et. al., "First Demonstration of Microphonic Control of a Superconducting Cavity with a fast Piezoelectric Tuner" in PAC 03, Portland Oregon 2003.
8. Nucl.Phys.A721:1067-1070,2003.
9. Tang et. al., "The NLC Positron Source" http://ccdb3fs.kek.jp/cgi-bin/img/allpdf?199611228

2.4 Electron Storage Ring

In this chapter we describe the physics design of the electron ring of the eRHIC collider. The performance goals of the ring are summarized based on the physics requirements outlined in chapter 1.1 and the expected performance of the existing RHIC collider in chapter 1.2. We first discuss the choices of main ring parameters and major technical approaches. Then a preliminary ring lattice design is presented as a baseline design. Following the design section, beam dynamics topics are discussed, including beam collective effects, beam-beam physics, and polarization issues. The RF system is discussed in the final section. The choice of RF parameters and technology has a strong impact on ring performance, technical risk, and cost.

The scope of the eRHIC physics experiments is very broad. First, the extent of center of mass energies that the experiments intend to cover, and then the wide variety of hadron species that will collide with the electron or positron beams require a collider with an unusually wide range of operating parameters. The electron ring is required to have a large energy operation range: 5-10 GeV, and the electron beam emittance is required to change by more than one order of magnitude to maximize luminosities in collisions with various hadron species of different energies. Another major feature of this design is that the electron (or positron) beam must be highly polarized. Section 2.4.6 is devoted to polarization issues. These ring design features are quite different from both the existing e^+e^- colliders PEP II [1] and KEKB [2], and from the existent lepton-hadron collider HERA [3].

The electron ring design as part of the eRHIC project must be site-specific to the existing RHIC facility. RHIC is a well-established ion collider and has a well defined upgrade path. The electron ring will be built in a separate tunnel from the RHIC tunnel, with a different circumference. This gives the electron ring designer the freedom to choose appropriate lattice structure and parameters that are best matched to RHIC, enabling much higher luminosity under all of the many collision scenarios than the existing collider and fixed target facilities can provide. The nominal design luminosity for collisions of 10 GeV electron on 250 GeV protons is 10^{32}-10^{33} $cm^{-2}s^{-1}$.

It is clear that to accommodate all of the physics requirements, tuning flexibility must be embedded in the design from the outset, rather than as a future upgrade. The second design criterion is operational reliability, which has proven to be extremely important in the successful e+e- B-factory projects. Reliability means uninterrupted operation and high integrated luminosity. Each of the important technical approaches and choices must be decided within the context of its impact on reliability. A number of straightforward but essential measures are adopted to ensure reliable operation. Two important features are full energy injection of a polarized electron beam, allowing top-off or continuous injection with instant polarization and quick recovery from catastrophic beam loss, and sophisticated closed orbit correction schemes with adequate beam position monitors and correction capacities to insure high equilibrium polarization.

2.4.1 Design Overview

The primary goals for the electron ring design are shown in table 2.4.1-1. These goals must be achieved with adequate beam lifetime and acceptable detector backgrounds. In addition, to maximize

luminosity over the wide range of collision scenarios with different ion species, the normalized emittance must be adjustable by an order of magnitude over the range of design energies.

Peak luminosity for 10 GeV e on 250 GeV p	$10^{32} – 10^{33}$ $cm^{-2}s^{-1}$
Longitudinal polarization	> 70% at IP
Average current	0.45 Amp
Electrons per bunch	10^{11}
Number of electron bunches	120
Energy range	5 – 10 GeV
Polarized positron energy	10 GeV

Table 2.4.1- 1 **Primary goals for electron ring design.**

The key features of the baseline ring design are:

- Flat beam, head on collisions.
- High emittance ratio of the elliptical electron beam at the IP.
- Anti-symmetry solenoidal spin rotators in the IR straight, pure longitudinal spin at 8.5 GeV. 4% reduction at 10 GeV and 20% reduction at 5GeV.
- Flexible FODO arc structure for electron beam emittance adjustment. Wigglers or super-bends to increase synchrotron radiation damping for higher beam-beam tune shift limits at low energy.
- Electron path length adjustments up to 0.2 m.
- Adequate vertical closed orbit correction capacities for high beam equilibrium polarization.
- Full energy, polarized electron beam injector with flexible bunch to bunch filling capacity. Feasible for top-off and continuous injection.
- Reliable high power RF system.
- Low field solenoids around the ring to suppress electron-cloud effect for positron beam.
- Low-photodesorption, low impedance, high radiation power resist vacuum chamber.
- Feed back system for suppressing multi-bunch instability.
- Provisions for longitudinal polarimeter operation in the IR straight.

The electron ring will be located either at the RHIC IP12 or IP4 location, as described in section 2.2. The ring circumference is chosen to be one third of the RHIC ring. This length is an optimum based on balancing the requirements from the length of the interaction region, the arc length and mechanical structures considering the range of electron beam emittance, the synchrotron radiation wall power density, and the beam self polarization time at 10 GeV. The self polarization time at 10 GeV is important because, although the electron beam is generated by a polarized full energy injector, the positron beam still depends on self polarization. Cost optimization is always a major factor in the ring circumference consideration as well. There are still concerns about the possibility that coherent beam-beam effects could compromise the performance of any collider with unequal-circumference rings [4]. This is under active investigation and more discussions on this topic are presented in section 2.4.5.

The e-ring RF frequency must be a harmonic of the colliding frequency which is varied from ~28.15 MHz to ~28.13 MHz depending on the ion beam energies (ion velocity variation). The RHIC RF

frequency (~197 MHz) is the 7th harmonic of the colliding frequency. It is not necessary to make the e-ring RF frequency a harmonic of the RHIC RF frequency. Higher RF frequencies are preferred for technical reasons as described in section 2.4.7. It is also not possible to make the ring RF frequency a precise sub-harmonic of the linac frequency (either S-band at 2856 MHz or L-band at 1300 MHz) and the harmonic of the colliding frequency at same time. This adds complication to the timing synchronization of the injector, which must provide a flexible bunch filling pattern to the ring. The timing system synchronizing the beam source to the ring is discussed in the injector section 2.3.

A major technology choice is whether to use room temperature copper RF structures or to adopt superconducting structures, which have made rapid advances in recent years. Both technologies are now mature [5] [6] and proven in user facilities. The cavities in use at SLAC at 476 MHz or the KEKB 508 MHz cavities with modifications are both suitable candidates. Further investigation of the reliability and cost of each system is required before a choice is made.

Figure 2.4.1-1 shows the quasi race-track e-ring layout in a detailed scale. The general layout of eRHIC is presented in chapter 1.

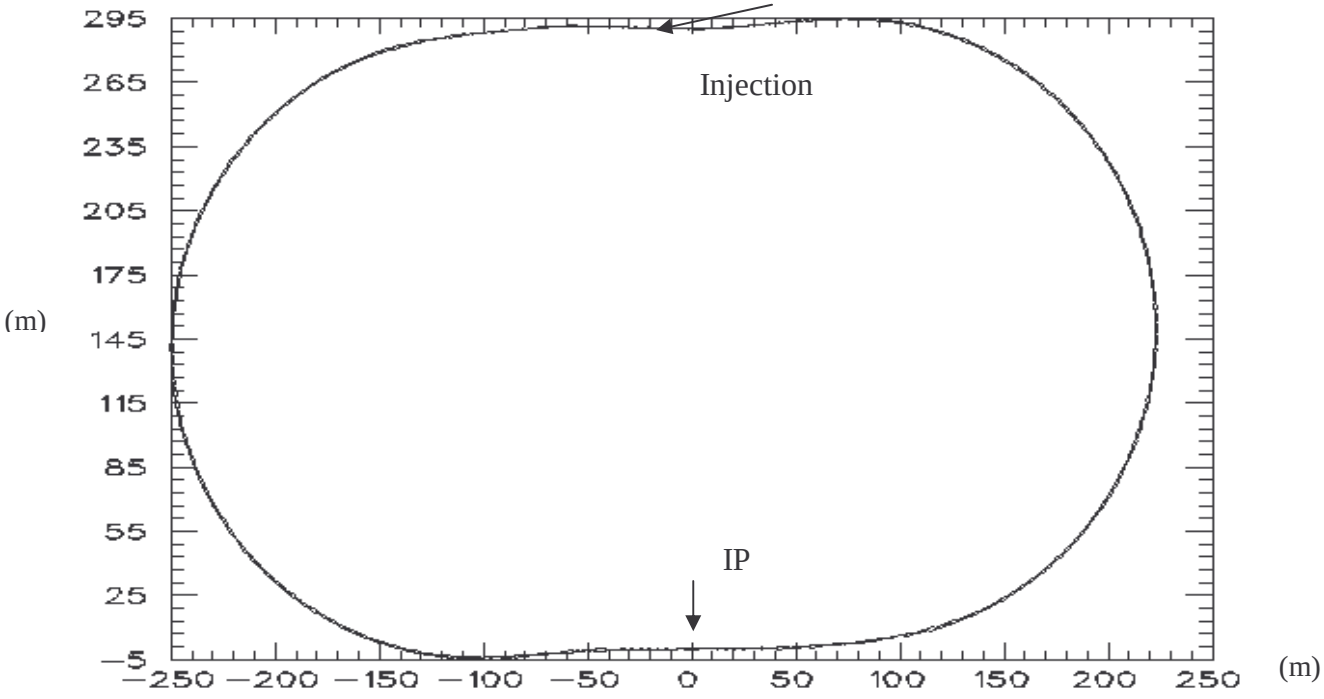

Figure 2.4.1- 1 **Electron ring layout**

The main ring parameters are listed in Table 2.4.1-2. The nominal parameters are specified for collisions of 10 GeV electrons on 250 GeV protons with the provision of parallel operation of two other hadron beam interaction regions. The goal luminosity is 10^{32}-10^{33} $cm^{-2}s^{-1}$. The proton ring parameters are also listed to give a set of self consistent parameters and appropriate luminosity value. The 10^{33} $cm^{-2}s^{-1}$ luminosity is not yet been reached (~50% less) with the present IP region design and electron beam parameters in the table. Further design considerations for higher luminosity are detailed in section 2.4.2.

		Electron	Proton
Energy E	[GeV]	10	250
Circumference, C	[m]	1277.948	3833.845
Arc dipole radius	[m]	81.02	
k=εy/εx		0.18	1
Kσ=σy/σx		0.50	0.50
Nominal emittance(ion) ε_n	[π mm mrad]		15.0
Emittancs εx	[nm.rad]	53.0	9.4
Emittancs εy	[nm.rad]	9.5	9.4
Beta function at IP x, βx*	[m]	0.19	1.08
Beta function at IP y, βy*	[m]	0.27	0.27
Beam-beam parameter x, ξx		0.029	0.0065
Beam-beam parameter y, ξy		0.08	0.0033
RF frequency (Warm/SC)	[MHz]	478.6/506.7	
RF voltage	[MV]	25	
Bunch length σ_z	[cm]	1.17	
Number of bunches		120	360
Bunch separation	[ns]	35.52	35.52
Particles/bunch		1.00E+11	1.00E+11
Total current	[A]	0.45	0.45
Synch. rad, Loss/turn	[MeV]	10.92	
Linear radiation power density	[kW/m]	9.68	
Damping time (x/s)	[ms]	7.2/3.6	
Luminosity £	[cm-2s-1]		4.4E+32

Table 2.4.1- 2 **Nominal Machine Parameters**

References:

1. "PEP II Conceptual Design Report",LBL-PUB-5379, SLAC-418,…, June 1993
2. "KEKB B-Factory Design report", KEK Report 95-7, 1995
3. U. Schneekloth, (ed) "The Luminosity Upgrade" DESY HERA -98-05, 1998

4. F. Zimmermann, “Summary of Working Group on Interaction Region, Beam-Beam Interaction & Optics” , Workshop e+e- factories 2003, Stanford, CA October 13-16, 2003.
5. T. Furuya, “Update on the performance of Superconducting Cavities in KEKB”, Workshop e+e- Factories 2003, Stanford, CA USA, October 13-16, 2003.
6. P. Corredoura et al. “Experience with the PEP II RF System at High Beam Currents”, p.1891, Proceedings of EPAC 2000, Vienna, Austria.

2.4.2 Luminosity Considerations

The general luminosity expression for a lepton-hadron collider, if the colliding beams are totally overlapped at the interaction point, is:

$$L = \frac{F_c N_i N_e}{4\pi\sigma_x\sigma_y} \qquad (2.4.2\text{- }1)$$

Where F_c is the colliding frequency, N_i is the number of ions per bunch, N_e is the number of electrons per bunch, and σ_x and σ_y are the rms transverse beam sizes.

If we assume equal beam-beam tune shift limits for both transverse planes for each of the hadron and lepton beams, then the luminosity expression in terms of linear beam-beam tune shifts can be written as [1]:

$$\begin{aligned} L &= \frac{\pi}{r_e r_i} F_c \gamma_e \gamma_i \xi_i \xi_e \sqrt{\frac{\varepsilon_i}{\beta_{i,x}}} \sqrt{\frac{\varepsilon_{e,x}}{\beta_{e,x}}} k_e \frac{(1+k)^2}{k^2} \\ &= \frac{\pi}{r_e r_i} F_c \gamma_e \gamma_i \xi_i \xi_e \sigma'_{i,x} \sigma'_{e,x} k_e \frac{(1+k)^2}{k^2} \end{aligned} \qquad (2.4.2\text{- }2)$$

Where

$\xi_{i \text{ or } e}$ is the beam-beam tune shift limit for ion beam or electron beam
β represents the betatron function at the interaction point
ε is the ion or electron beam geometric emittance
$k_e = \varepsilon_{e,y}/\varepsilon_{e,x}$ is the electron beam emittance ratio
$k=\sigma_y/\sigma_x$ is the beam aspect ratio at IP.
σ' is the beam angular amplitude.

In the above expression, we also assumed that the smaller beam size is in the vertical (y) direction and ke/k≤1, then the dominant linear beam-beam tune shift limits are:

$$\begin{aligned} \xi_{i,x} &= \frac{r_i}{2\pi Z} \frac{N_e}{\gamma_i \varepsilon_i} \frac{1}{(1+k)} \\ \xi_{e,y} &= \frac{r_e Z}{2\pi} \frac{N_i}{\gamma_e \varepsilon_{e,x}} \frac{1}{k_e (1+1/k)} \end{aligned} \qquad (2.4.2\text{- }3)$$

The classical radius r_i of the ion is:

$$r_i = \frac{Z^2}{A}\frac{e^2}{4\pi\varepsilon_0}\frac{1}{M_0 c^2} \qquad (2.4.2\text{- }4)$$

where Z is the atomic number, A is the atomic mass number, and M_0 is the mass per nucleon. The r_i value for proton is $r_p = 1.53\text{x}10^{-18}$ m, for gold $r_{Au}=49.0\text{x}10^{-18}$ m, and $r_e=2.82\text{x}10^{-15}$ m for electrons.

Equation (2.4.2-2) is equivalent to equation (1.1) in section 1.2.3 except writing parameters relevant to luminosity limitations more explicitly, i.e. including the electron beam emittance ratio and electron beam emittance instead of electron beam vertical angular amplitude which does not reach the actual aperture limit in our cases. Our luminosity discussion here will be focused on collisions of 10 GeV electrons on 250 GeV protons, as this is the primary design feature. Other collision scenarios will be discussed accordingly.

Colliding frequency

The colliding frequency is limited by the achievable RHIC bunch number. It comes as a RHIC machine operation and upgrade limit (section 3.2), and it is also raised as a minimum bunch separation requirement from the detector design. The nominal colliding frequency is 28.15 MHz.

Applied to collisions of 10 GeV electrons on 250 Gev protons we have:

$$L = 4.29\times10^{43}\,\xi_i\xi_e\sigma'_{i,x}\sqrt{\frac{\varepsilon_{e,x}}{\beta_{e,x}}}\frac{k_e}{4}\frac{(1+k)^2}{k^2} \qquad [cm^{-2}s^{-1}]$$

$$\xi_{i,x} = 9.14\times10^{-19}\frac{N_e}{\varepsilon_i}\frac{1}{(1+k)} \qquad (2.4.2\text{- }5)$$

$$\xi_{e,y} = 2.29\times10^{-23}\frac{N_i}{\varepsilon_{e,x}}\frac{1}{k_e(1+1/k)}$$

Round beam or flat beam collisions and IP magnet aperture limits

Round beam means equal beam sizes in both transverse directions for both lepton and hadron beams, and equal beam emittances in both transverse directions for lepton beam (the ion beams are always supposed to have equal emittances in transverse plans) as well. The luminosity of a round beam compared to a flat beam with the *same beam angular sizes at the IP* is higher due to equal beam-beam tune shift in both transverse plans. From equation 2.4.2-5, compare to flat beam collisions with reasonable beam cross section ratio and lepton beam emittance ratio, say $k_e=0.1$, $k=0.5$, the luminosity can be four times higher for round beam collisions. A realistic interaction design in chapter 4 has described a small horizontal angular limit of 93 μrad for the hadron beam. This means a relatively larger horizontal cross section. To bring the luminosity up, the vertical cross section has to be small. However, the minimum vertical beta function amplitude at IP of the ion beam determined by the ion bunch length sets the lower limit of the beam cross section ratio which is about 0.5 in this design.

The second fundamental problem for round beam collisions comes from electron beam polarization. The electron beam is flat in nature in a storage ring. A round beam can be created by strong coupling between transverse planes or introduction of a vertical synchrotron radiation mechanism to generate vertical beam emittance. As the bending plane is horizontal and the beam spin closed orbit direction is vertical, both methods can end up depolarizing the beam resulting in lower equilibrium polarization [2]. We will concentrate on flat beam collisions in this report.

Electron beam emittance ratio

The lepton beam emittance ratio shown in equations 2.4.2-2 and 2.4.2-3 is an important design parameter that requires further exploration. For flat beam collisions, when beam-beam tune shift limits can be reached for both beams, the luminosity increases linearly with the emittance ratio of the lepton beam. This statement is valid as long as the proton bunch intensity is not a limit (equation 2.4.2-3).

For an accurate evaluation of how luminosity is related to the emittance ratio, we must impose limits from the IR design and minimum β* values (see following bunch length discussion). We take the e/p, 10 GeV/250 GeV collision as an example. In table 2.4.2-1, the minimum β* is set to be 0.19m, and the resulting electron beam-beam tune shift limit is 0.08. The IR magnet aperture limits are set from the IR design: $\beta_{i,x}$*=1.08m, $\beta_{i,y}$*=0.27m, ε_i=15 nm. No proton beam intensity limit is imposed. The electron bunch density is set at 1×10^{11} electrons per bunch.

A significant luminosity gain from very low emittance ratio to the balance point of k_e=0.25, where $\beta_{e,x}$*= $\beta_{e,y}$*=0.19m. Further increase of k_e will requires very low electron beam emittance to match the low proton beam emittance and does not help luminosity. The proton beam intensity has to follow up in the sensitive luminosity improvement region (k_e=0 to 0.25).

The parameters in table 2.4.2-1 are generated for a special IR design and β* limit. But we can conclude that luminosity performance is sensitive to lepton beam emittance ratio in a k_e range from very low up to some value (here 0.25) depending on specific IR design (magnet aperture limits) and β* limits. However to manipulate (increase) electron beam emittance ratio and to maintain high polarization level at the same time can be difficult.

Ke= εe,y/εe,x	$\varepsilon_{e,x}$ (nm.rad)	$\beta_{e,x}$* (m)	$\beta_{e,y}$* (m)	Protons ($1e^{11}$) per bunch	ξx	ξy	L 1e32 ($cm^{-2}s^{-1}$)
0.1	54	0.19	0.47	0.57	0.016	0.08	2.5
0.15	54	0.19	0.31	0.85	0.024	0.08	3.8
0.18	54	0.19	0.26	1.0	0.029	0.08	4.5
0.20	54	0.19	0.23	1.13	0.032	0.08	5.0
0.25	54	0.19	0.19	1.41	0.04	0.08	6.3
0.30	45	0.23	0.19	1.41	0.048	0.08	6.3
0.5	27	0.38	0.19	1.41	0.08	0.08	6.3

Table 2.4.2- 1 Lepton beam emittance ratio vs. luminosity

As an example, HERA operation has reached a beam emittance ratio (coupling) of 10% with a beam cross section aspect ratio of 1:4 and electron beam polarization of 60%. They are currently undergoing a luminosity upgrade that aims at achieving 17% coupling with similar beam aspect ratio and ~40% smaller beam cross section. The upgrade is expected to increase luminosity by a factor of 3.5 while maintaining high electron beam polarization. Final results of HERA upgrade are yet to come. Comparing the present design to HERA, the main difference is that the electron beam energy

is ~1/3 of HERA. The spin resonant strengths are strongly dependent on beam energy, so the challenges at eRHIC should be manageable compared to HERA.

There are ideas [5] and an experimental demonstration [6] of transformation between a round beam and a flat beam using a beam "emittance adaptor". It is of great interest to have an experimental investigation to see whether this could be applied for a circulating machine. It is especially interesting to establish whether it could work near the IP region where the spin is nearly longitudinal. The goal in this study is to increase the electron beam emittance ratio without depolarizing the beam instead of making a round beam.

Zero crossing angle

Introducing crossing angle can ease beam separation and synchrotron radiation fan problems [3]. A crab cavity would be needed for the hadron beam to avoid luminosity loss [4]. However, the RF voltage of such a crab cavity for the proton beam in this application would be too high, and is technically unrealistic. Therefore, this option is excluded.

Beam-beam tune shift limits

Beam-beam tune shift limits can be reached for both lepton and hadron beams in the eRHIC collider. The lepton beam intensity in particular can be much higher than HERA due to the lower operation energy, and this will drive a higher beam-beam tune shift for the hadron beam.

The beam-beam tune shift limit assumed in this report is 0.0065 for ion beams (per interaction point of three interaction points) and is 0.08 for the lepton beam. They are based on RHIC upgrade parameters [7] and achieved parameters at PEP-II [8]. Even higher lepton beam-beam tune shift limit could be reached if beam loss can be compensated by continuous injection [9]. However, the beam-beam limit for this machine may be different from both the e^+e^- colliding B factories [10] and the ion collisions in RHIC. More discussions are presented in section 2.4.5.

Beam intensity

The nominal design beam current in the electron ring is 0.45 A. The major concern generated by this average current is the linear power density of the synchrotron radiation at 10 GeV. However, this design average current is rather moderate compared to existing B-factories. The number of electrons per bunch, $1*10^{11}$, is high compared to other rings. For example, e^+ and e^- per bunch achieved in the PEP II Low (3.1 GeV) and High (9 GeV) Energy Rings are 0.5×10^{11} and 0.8×10^{11} respectively (peak performance, 2.43A and 1.38A, 1317 bunches [8]). The long bunch length and large bunch spacing in the eRHIC e-ring will permit higher limits for bunch charge. The single-bunch charge instability threshold is discussed in section 2.4.4.

The ion beam intensity limits have been defined through RHIC operation. The nominal limit of the number of protons per bunch is ~ $1*10^{11}$, and is $1*10^9$ for Au. Both beam intensities are key adjustable parameters in optimization studies for higher luminosity.

Beam emittance

Electron emittance should be adjusted to match the ion beam for maximum luminosity. However, the electron beam emittance is a parameter of the ring lattice, and is proportional to γ^2. For example, if the electron beam is run at 5 GeV instead of 10 GeV, then to match the same ion beam the lattice should be adjusted to provide an emittance four times larger than that for 10 GeV. In the present design, the emittance can be varied from ~40 nm to ~360 nm (at 10 GeV). At low energy (5 GeV), an "emittance wiggler" may be needed to further increase the emittance.

The ion beam emittances are well understood through RHIC operation. The normalized proton beam emittance is ε_{in}=15 μm-rad. By RHIC convention, the geometrical emittance is $\varepsilon_i = \varepsilon_{in} /(6\pi(\beta\gamma)_i)$ which is 9.4 nm at 250 GeV. And the normalized Au beam emittance is 6 μm-rad with electron cooling, corresponding to 9.4 nm geometrical emittance at 100GeV/μ.

Beta function at IP and bunch length

Low β* means small cross section at IP and higher luminosities. However, the relatively long ion bunch lengths have set limits to minimum β* values. The constraint is $\beta^* \leq \sigma_z$ in order to avoid reduction of luminosity by the hourglass effect [11]. The minimum proton bunch length in RHIC is ~13 cm, according to the limit of cryogenic power load of 0.5 W/m for 10^{11} protons per bunch. However for 250 GeV proton beam, the bunch length without cooling is about 25 cm. The electron bunch length is only ~2cm, much less than β_e^* at IP, and is not an issue itself. But β_e^* is subjected to the hourglass effect while traveling through the long proton bunch. A low limit of 19 cm for β_e^* is set, corresponding to luminosity reduction of less than 10%. More simulations will be done to evaluate possible lower β_e^* values.

Further Improvement of Luminosity Performance

The luminosity value listed in Table 2.4-1 is $0.44*10^{33}$ $cm^{-2}s^{-2}$ for the collisions of 10 GeV electrons on 250 GeV proton. To reach this goal requires upgrades to the existing RHIC collider, and the design of the electron machine may require further development. These are the major topics of this report. Here we discuss further ideas for achieving higher luminosity of $1*10^{33}$ $cm^{-2}s^{-2}$ or above with the ring-ring collider option.

From equation (2.4.2-2) and (2.4.2-3), there are several parameters that the luminosity is very sensitive to, including β*, the emittance ratio, and beam-beam parameters. β* is limited by ion bunch length. The emittance ratio effect is sensitive within a certain range as discussed above. The actually achievable value of emittance ratio with high beam polarization is not yet clear. The electron beam-beam parameter could be higher if continuous electron beam injection can compensate for higher electron losses due to higher beam-beam tune shift. And the proton beam-beam parameter can be higher if there is only one collision point. However all these sensitive improvements require higher beam intensity.

To make the case for the above arguments, we present two tables similar to our nominal design luminosity and basic parameter tables in section 1.2.3. Table 2.4.2-2 lists two sets of higher luminosity operation parameters for e-p and e-Au collisions at 10 GeV electron beam energy. The main difference between these sets of parameters and the nominal design values are the beam-beam

parameters, and the bunch densities. In table 2.4.2-2, the hadron beam beam-beam parameter is set 1.5 times higher in light of electron-ion collisions only operation scenario. This change requires 1.4 times higher electron beam intensity. Also, the optimization of other parameters and a possible increase of lepton beam beam-beam parameter by 20%, require a similar increase of hadron beam intensity. At this point, from discussions in section 2.4.4 and 3.3, it should be possible to run higher bunch intensities for both electron and ion beams.

A significant challenge to meeting the higher intensity requirements is that they are required in the high electron energy range. The linear radiation power density will be increased to 14 kW/m at 10 GeV for beam current of ~0.65 A. While challenging, the vacuum chamber under such radiation power levels is still technically feasible based on results from R&D for B-factory upgrades.

Energy E	[GeV]	10	250	10	100
k=εy/εx		0.18	1	0.18	1
Kσ=σy/σx		0.43	0.43	0.43	0.43
ε_n (ion)	[π mm mrad]		15.0		6.0
Emittancs εx	[nm.rad]	54.0	9.4	54.0	9.4
Emittancs εy	[nm.rad]	9.7	9.4	9.7	9.4
βx*	[m]	0.19	1.08	0.19	1.08
βy*	[m]	0.19	0.2	0.19	0.2
ξx		0.042	0.0095	0.033	0.0095
ξy		0.1	0.0041	0.08	0.0041
Particles/Bunch		1.40E+11	1.41E+11	1.38E+11	1.43E+09
Luminosity £	[$cm^{-2}s^{-1}$]		1.0E+33		1.0E+31

Table 2.4.2- 2 Parameters for higher luminosity--high electron beam energy.

Table 2.4.2-3 is for low electron energy (5 GeV). The table uses the same higher beam-beam parameters and shorter ion bunch length as applicable. The electron emittance ratio used is slightly higher (0.25) in light of the weaker spin resonance strengths at lower electron beam energy.

The beam intensity requirement for the ion beams are relaxed due to lower electron beam beam-beam parameters in lower electron beam energy operation where less synchrotron radiation and less damping are expected. However, the demand for a higher intensity electron beam remains when the ion beam energy is high. At very low ion beam energy, a much larger electron beam emittance is required to match the proton beam with large geometrical emittance. The very large electron beam emittance will be difficult to produce with normal FODO arc lattice without the help of wigglers or super-bends. The low energy operation will be discussed in the lattice design section.

		Electron	Proton	Electron	Au
Energy E	[GeV]	5	50	5	100
k=εy/εx		0.25	1	0.25	1
Kσ=σy/σx		0.50	0.50	0.43	0.43
ε_n (ion)	[π mm mrad]		5.0		6.0
Emittancs εx	[nm.rad]	130.0	15.6	56.0	9.4
Emittancs εy	[nm.rad]	32.5	15.6	14.0	9.4
βx*	[m]	0.22	1.86	0.18	1.08
βy*	[m]	0.22	0.46	0.13	0.2
ξx		0.025	0.019	0.029	0.0095
ξy		0.050	0.0094	0.050	0.0041
Particles/Bunch		9.74E+10	1.07E+11	1.38E+11	6.42E+08
Luminosity £	[$cm^{-2}s^{-1}$]		1.6E+32		4.5E+30

Table 2.4.2- 3 Parameters for higher luminosity -- low electron beam energy

To summarize, we note that critical steps forward are improvements in IP region design, RHIC upgrades to permit higher ion beam intensity, and shorter bunch lengths to generate higher luminosity. From the electron ring side, higher beam intensity and higher emittance ratio for polarized beams are essential. The immediate task for the electron ring design team is to explore the feasibility of higher beam intensity operation. The goal is 1.4×10^{11} particles/bunch and ~0.65A of average current at 10 GeV. Many of the technical system specifications need to be verified to achieve higher beam intensity operation. An R&D plan to understand and realize higher emittance ratio for highly polarized electron beam is under development.

References:

1. F.Wang “e-ring ZDR progress”, talk at eRHIC collaboration meeting, BNL, August 19-20, 2003.
2. D.P Barber, “Increased vertical $e^{\pm}$ beam size and polarization ?”, Workshop on the Performance of HERA after Upgrade, Salzau, Germany, May 2003.
3. B. Parker, “IP design with warm proton magnets”, talk at eRHIC collaboration meeting, BNL, August 19-20, 2003.
4. K.Oide and K.Yokoya, “The Crab-Crossing Scheme for Storage-ring Colliders”, Phys.Rev.A40:315,1989.
5. Ya. Derbenev, University of Michigan Report No. UM-HE-98-04, 1998
6. D. Edwards et al. “Status of Flat electron Beam Production” p.73, Proceddings of PAC 2001, Chicago, USA. June, 2001.

7. T. Roser, "RHIC STATUS AND PLANS" PAC 2003, Portland , Oregon May 12-16, 2003.
8. J. T. Seeman, "Accelerator Plans at SLAC" e+e- Super-B-Factory Workshop, Hawaii, USA, January 19-22, 2004.
9. U. Wienands et al. "Continuous Injection ("Trickle Charge") at PEP II", Workshop e+e- Factories 2003, Stanford, CA USA, October 13-16, 2003.
10. K. Ohmi, "Beam-beam limit estimated by a quasi-strong-strong simulation", Workshop e+e- Factories 2003, Stanford, CA USA, October 13-16, 2003.
11. G.H. Hoffstaetter el al. "Beam-Beam Limit with Hourglass Effect in HERA", p.401, Proceedings of EPAC 2002, Paris, France.

2.4.3 Lattice Design

The electron ring has a quasi racetrack layout. The anti-symmetrical spin rotator arrangement in the IR straight makes the "straight" section a zigzag line, as is the utility straight on the opposite side of the ring. See Figures 2.4.1-1 and 2.4.3-5.

The lattice design must meet the following criteria:

- Energy range: 5-10 GeV.
- Beam emittance range: ~40-60 nm.rad at 10 GeV, ~50-90 nm.rad at 5GeV.
- Adequate damping rate regarding beam-beam blow up.
- Good dynamic aperture for all lattice configurations.
- High equilibrium polarization (≥70%) and longitudinal spin at IP.
- Reasonable self-polarization time at 10 GeV.

Arc Lattice

The two 180^0 arc sections consist of regular FODO periods with dispersion suppressors at each end. The rationale of choices for each of the basic parameters is discussed below. Figure 2.4.3-1 shows the lattice functions for one arc section.

The dipole bending radius

The design dipole bending radius ρ is ~81m. Synchrotron radiation wall power, electron energy loss per turn and self polarization time at 10 GeV are concerned in choosing the appropriate bending radius.

For constant bend radius, the synchrotron radiation linear power density is

$$P_{linear}(kW/m) \approx 14.085 \frac{E^4(GeV) I(A)}{\rho^2(m)} = 9.7 \text{ kW/m} \qquad (2.4.3\text{- }1)$$

For nominal stored current of 0.45A, the maximum power density is ~10 kW/m. At this synchrotron radiation (SR) power density level, the technologies for the vacuum chamber are mature [1]. Vacuum chamber technology developed for higher SR power density (~20kW/m) is of interest as we may go for higher stored current. Increasing the bending radius to reduce SR power density is also an option in future lattice design.

The energy loss per turn and total synchrotron radiation power at 10 GeV is

$$P(MW) = U_0(MeV) * I(A) \approx 0.0885 \frac{E^4(GeV)}{\rho(m)} \text{ (isomag.) } = 10.9(\text{MeV}) * \text{I(A)} \quad (2.4.3\text{- }2)$$

Need enough RF gap voltage for beam life time and concern of RF system cost.

A reasonable self polarization time at 10 GeV without use of wigglers is

$$\tau_{POL}(\text{Sokolov}-\text{Ternov}) \approx \frac{99R(m)\rho^2(m)}{E^5(GeV)}(\text{sec.}) = 22 \text{ minutes.} \qquad (2.4.3\text{- }3)$$

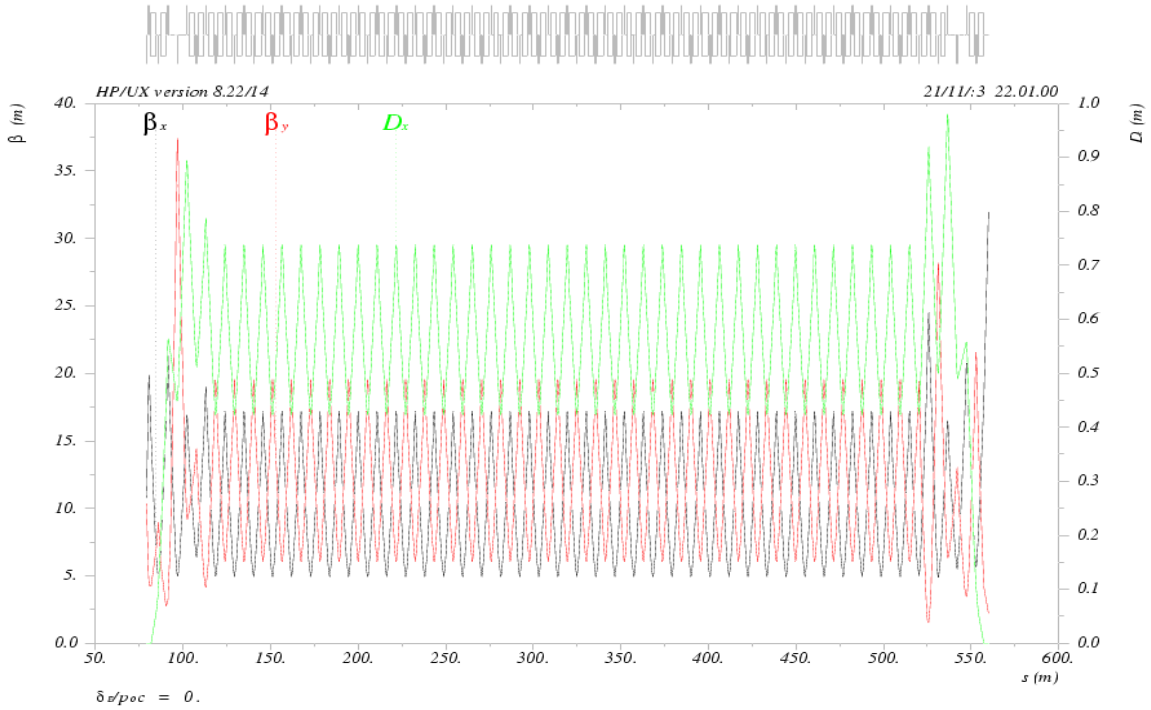

Figure 2.4.3- 1 Layout and optics functions of the arc

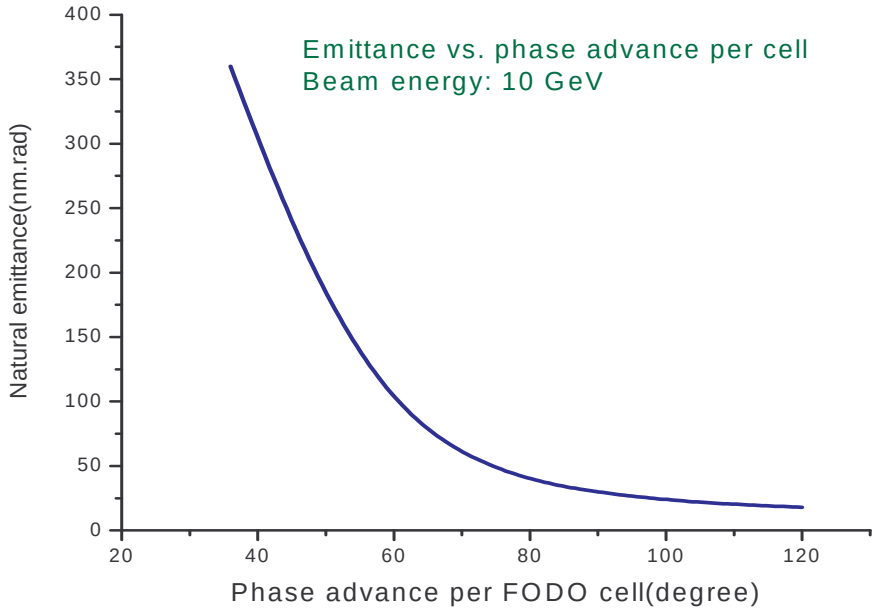

Figure 2.4.3- 2 The natural beam emittance vs. phase advance per FODO cell.

Number of FODO cells and cell length

The number of cells is 84, and cell length is 10.86m. The emittance can be written as [2]:

$$\varepsilon = F(\nu_x, lattice)\frac{E^2[GeV]}{J_x N_c^3} m.rad \qquad (2.4.3\text{- }4)$$

We choose N_c to put the beam's natural emittance in the proper range. The natural emittance vs. phase advance per cell of this design lattice [3] is shown in Figure 2.4.3-2. There should be enough space in a cell for magnets, instrumentation, and vacuum components, and the arc length must fit the ring circumference.

FODO cell betatron phase advance

The horizontal phase shift per cell is used as an emittance adjustment knob. It can be varied from 30 to 80 degrees. The vertical phase shift per cell is somewhat fixed: 60^0 at low and moderate emittances, and ~30^0 for very large emittance. The fixed phase shift per cell facilitates vertical chromaticity correction sextupole grouping for partial cancellation of second order aberrations from these sextupoles.

Low energy operation with damping wigglers or with super-bends

At 5 GeV the synchrotron damping time is 8 times longer (~ 60 msec.) compared with 10 GeV operation. This has significant impacts on the machine performance, (e.g. the peak and integrated luminosities) since the beam-beam tune shift is limited by intensity dependent beam-beam blow-up. The beam-beam parameter is a function of the damping time [4]:

$$\xi_y^{\infty} = f[\lambda_d] = f[\frac{1}{f_{rev}\cdot\tau\cdot n_{IP}}] \qquad (2.4.3\text{- }5)$$

where ξ_y^{∞} is the beam-beam parameter before beam-beam blow up, τ is the transverse damping time, and n_{IP} is the number of interaction points. From experimental data, it is suggested that

$$\xi_y^{\infty} \propto \lambda_d^{\sim 0.3-0.4}. \qquad (2.4.3\text{- }6)$$

The damping decrement λ_d is proportional to γ^3 in an isomagnetic field ring. For the eRHIC electron ring, the expected beam-beam tune shift limit will be reduced by a factor of 2 as the energy drops from 10GeV to 5 GeV.

The injection rate at 10 GeV can be 50 Hz, but this reduces to ~5Hz at 5 GeV limited by synchrotron radiation damping.
There are two options to increase the synchrotron damping to deal with these problems. One of the options is to install damping wigglers. When wiggler radiation is dominant, the vertical synchrotron damping time is:

$$\tau_y(ms) \approx 10.52\frac{C[m]}{E[GeV]B_0^2[T]L_w[m]} \qquad (2.4.3\text{- }7)$$

where B_0 is the maximum magnet field in the wiggler, L_w is the wiggler length C is the ring circumference, and E the electron beam energy. For example: asking for τ of ~25ms at 5 GeV will give a beam-beam parameter reduction of 30% instead of 50% from the value at 10 GeV. From equation 2.4.3-7, the damping wiggler will be 25 m in length with peak field of 2 Tesla. With the

wiggler the injection rate should reach 13 Hz. Another benefit of using the wiggler is that it increases the beam emittance at low energy, reducing the required range of phase advance in the FODO cell. This will be important for very large emittance (>100 nm at 5 GeV) when FODO phase adjustment is not enough to increase the emittance. The challenges posed by installation of the wiggler include high synchrotron radiation power, about 700kW in a narrow fan of ~100mrad angle, and other unwanted effects on beam optics such as increased momentum spread. The merits and disadvantages of using damping wigglers for the low energy operation need to be further evaluated. The CESR collider lower energy upgrade is based on using damping wigglers [5]. There are comparable machine and operation scenarios between CESR and eRHIC e-ring low energy operations. Therefore the CESR operation can provide useful design and operation experiences to the decision making of the e-ring damping wiggler option. The damping wigglers can be located in the short straight section in the dispersion suppressor sections that have missing dipoles. Local dispersion there is not zero, leading to a desirable increase in emittance growth from the wigglers. The local Twiss parameters are shown in Figure 2.3.4-3.

Another option is to redesign the ring bending magnet to be like a “super-bend”. The super-bend magnets in the original self-polarizing electron ring design [6] are used to provide short polarization time at low energies. Here the 'radiation' super-bend will be made of three separately powered short bends. The total effective length of these three dipoles is equivalent to the 3m long arc dipole in the nominal machine design. The magnetic field of the center dipole can be 50% higher than the outer ones. At low energy, this allows the outer ones to be turned off and leave the center one on. The bending radius of the short center bend will be 27m. For such a “super-bend” configuration, the total radiation at 5 GeV for 0.5A is 1 MW, three times higher than the 0.34 MW for the nominal design. This radiation power is comparable to the 1.04 MW radiation power of the above described ring with damping wigglers (1.04 MW). The transverse damping time will be 21 ms. The “super-bend “ design avoids the complicated wiggler insertions, but has more complicated designs for the arc magnets and vacuum chambers all around the ring. Further comparison of the two options will be based on their effects on optics and beam parameters, technical feasibility, operational flexibility and cost.

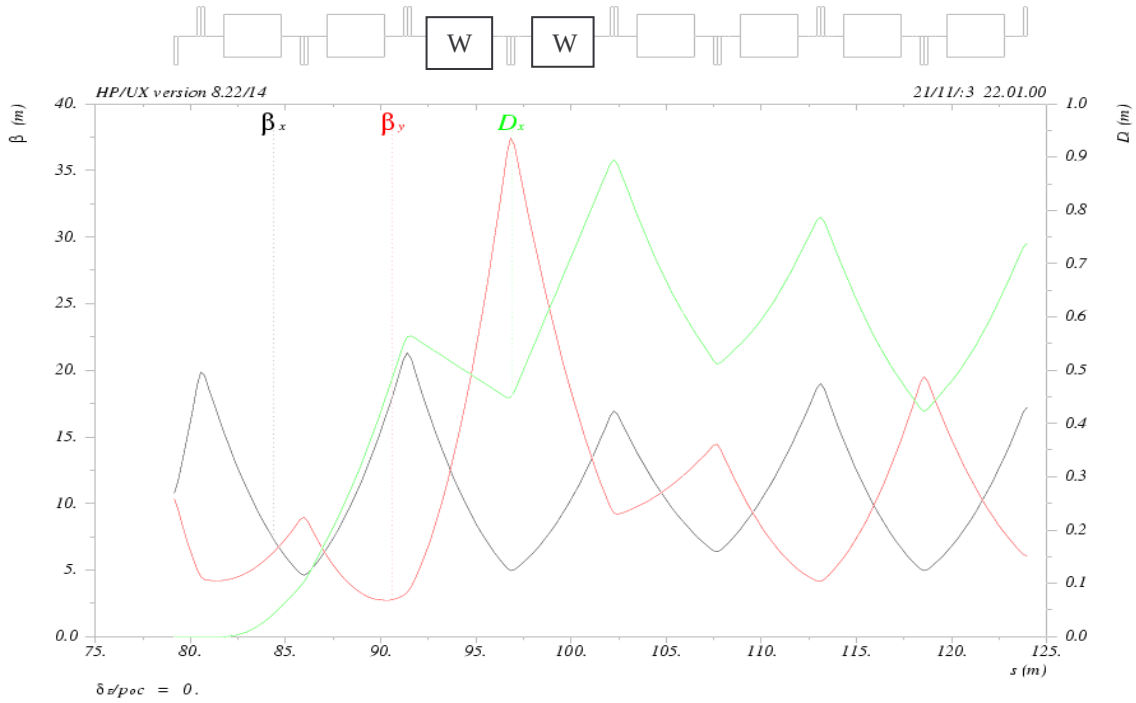

Figure 2.4.3- 3 The dispersion suppressor: arc to IR.

The Interaction Straight

The interaction straight has the most complex optics. The major subsections are the interaction region detailed in Chapter 4, and the antisymmetric solenoid spin rotators described in sections 2.4.6 and 4.4. Figure 2.4.3-4 show the layout of this straight.

The spin is designed to be pure longitudinal at 8.5 GeV. At that energy, the horizontal spin rotation angle is 90 degrees from the end of the solenoid to the IP. The corresponding horizontal orbit bending angle is ~4.7 degree. There will be 4% reduction of longitudinal polarization at 10 GeV and 20% reduction at 5GeV. The anti-symmetric horizontal spin rotation bends at either side of the IP consist of six dipoles. Three of them are combined function magnets near the detector which also serve as IP beam separators. A small reverse bend dipole (BRp in figure 2.4.3-6) is arranged to facilitate longitudinal polarimeter installation (actually, only the one downstream of IP exactly serves that purpose). Then two identical dipoles (BR) complete the required rotation.

The lattice optics near the IP has to be adjusted to accommodate various beam sizes (different combination of β^* and beam emittance) required for different collision scenarios. It is important to keep the peak betas at the IR region quadrupoles low to reduce chromaticity to begin with. Another import issue is spin transparency. We leave that discussion to section 2.4-6. Figure 2.4.3-4 shows the IR optics for $\beta^*_{x,y}$=0.19/0.27m. The maximum β function amplitude is only ~55m.

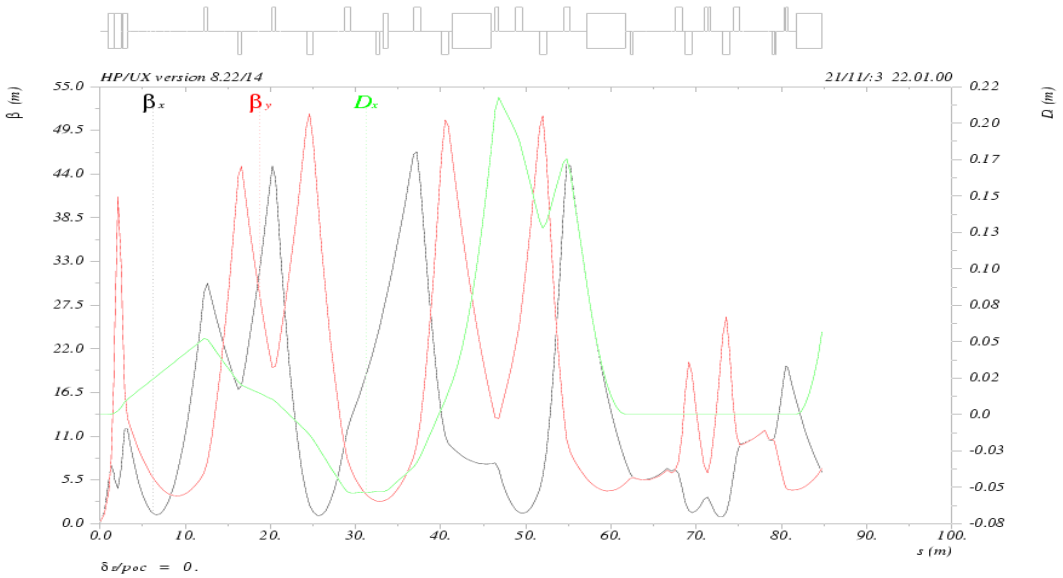

Figure 2.4.3- 4 IR optics with $\beta^*_{x,y}$= 0.19, 0.27m

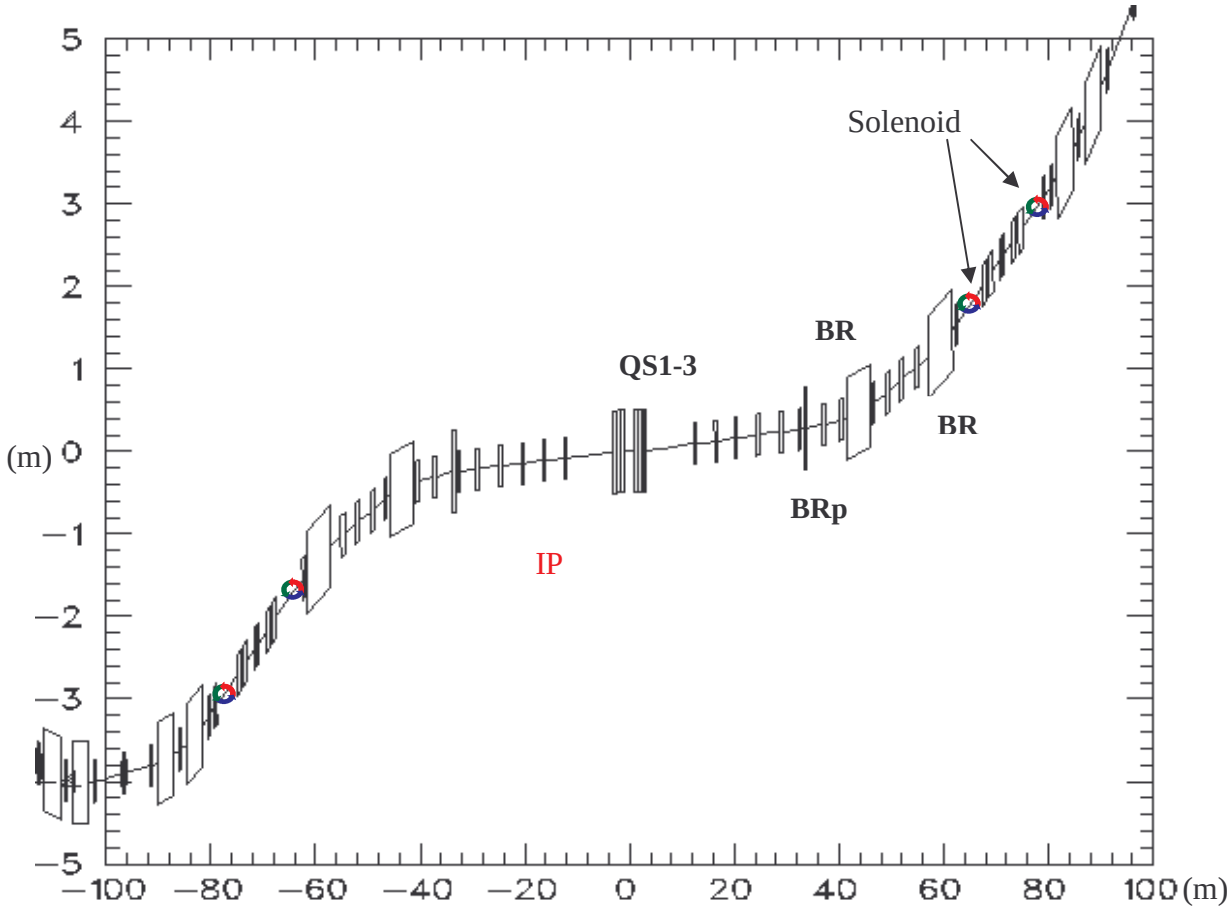

Figure 2.4.3- 5 Interaction straight layout

In Figure 2.4.3-5, the IP coordinate is (0,0). Colored circles indicate solenoid locations of the spin rotators. There are six horizontal spin rotation dipoles on either sides of the IP. They are labeled as

BR, BR, BRp, and QS1-3. QS1-3 are combined function beam separation bends. BRp reverses the deflecting direction. The BRs are normal spin rotation bends.

Compensation of the x-y coupling effects generated by the detector solenoid field is one of the important issues in designing the optics around the IP. The detector is expected to have a maximum solenoid field of 2 Tesla. The plan is to use bucking solenoids to cancel the integrated field around the IP. The merit of using bucking solenoids instead of skew quadrupoles is that this works for particles of any energy, and the bucking solenoids could be placed around the beam pipe insider the detector. Detailed design is still under way.

The Utility Straight

This "straight" has similar zigzag geometry as the IR straight. The injection section is in the middle of the straight. On both sides of the injection section are the two achromats that somewhat resemble the asymmetry layout of the IR region and facilitate ring closure.
The two straight sections connecting the center part of the utility straight to the arcs are used for fractional tune adjustments for ring operation. The optical structure of the two fractional tune adjustment sections are basically FODO cells. The tune adjustment range with the two sections is about 0.1, good for small adjustments in operation.

The RF cavities will be located in these two fractional tune adjustment sections. For example, in the copper RF cavity design option, there will be 28 cavities powered by 14 klystrons. Each two cavity structure has a physical length of ~3.0m. Figure 2.4.3-6 shows half of the utility straight and the RF cavity locations.

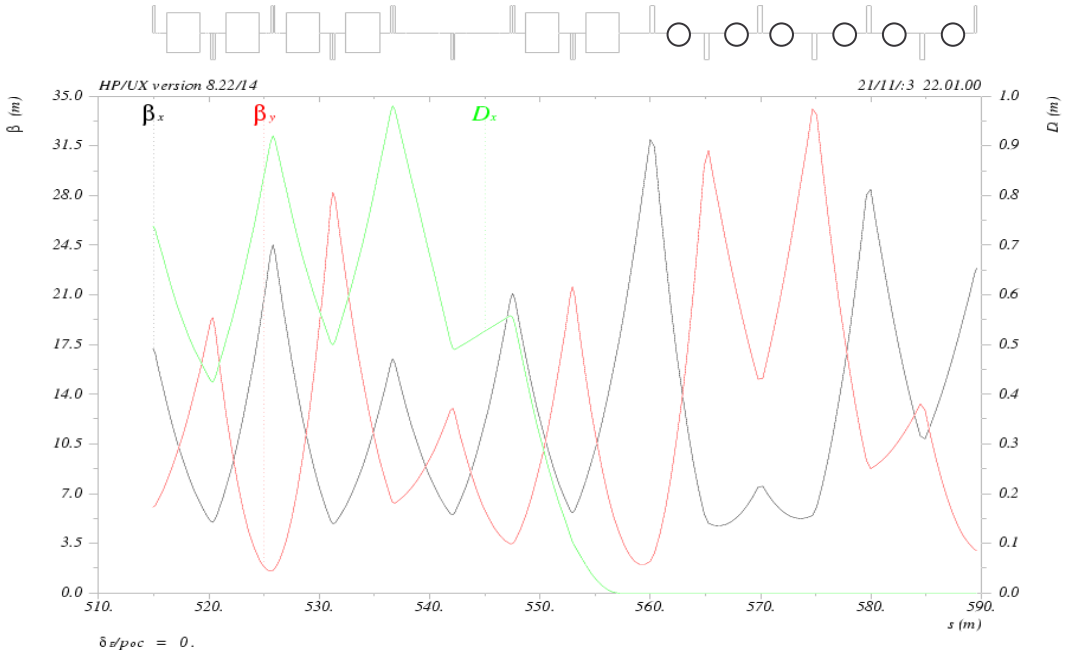

Figure 2.4.3- 6 Optics of the Dispersion suppressor from arc-UT straight and the fractional tune adjustment and RF section. Circles: RF cavity locations.

Electron Beam Path Length Adjustment

Table 2.4.3-1 lists the path length adjustment of the electron ring for matching to different proton beam energies. The required path length change is up to ~0.9 m if the lower end of the proton beam energy is 25 GeV. This length adjustment is large and is difficult to achieve in a conventional way. However if the low end of the proton beam energy is 50 GeV, then the path length adjustment is 0.2m, a much relaxed requirement.

Proton Energy	Proton bunch spacing in time (ns)	Colliding frequency (MHz)	Electron ring RF frequency (MHz)	Electron bunch spacing (m)	Electron beam path length (m)	Electron beam path length changes (m)
25	35.5471	28.1317	478.238	10.6568	1278.812	0.8919
50	35.5283	28.1465	478.491	10.6511	1278.136	0.2161
100	35.5237	28.1503	478.554	10.6497	1277.967	0.0473
250	35.5223	28.1513	478.572	10.6493	1277.920	0.0

Table 2.4.3- 1 Electron beam path length vs. proton beam energy

The conventional means to change path length is with magnetic chicanes in the straights or in the arcs. The most likely scheme is to make chicanes in the arc [7], which saves precious straight sections for other usages. There are technical constraints when making magnet chicanes. The first constraint is the limiting synchrotron radiation power density from a strong bend. The linear radiation power density from a normal dipole is ~10kW/m at 10 GeV with 0.45 A stored current. We require that the power density from a chicane dipole not exceed 20 kW/m, so that the special vacuum chamber technology needed could be obtained from existing B factories. This gives a limit of maximum bending field about 1.4 times of the normal dipole. Other concerns with the chicane are the cost and technical feasibility of a particular design.

Figure 2.4.3-7 shows an eight bend chicane in the arc. It is converted from a normal section of 4 FODO cells. To make the largest path length change with the chicane, the first and the last dipoles are turned off; the lost bending angles will be picked up by the six dipoles in the middle. So the maximum bending field is 4/3 times higher than the normal dipole. Linear radiation power density is about 17kW/m. The first and last dipole can be turned to bend beam in reverse direction to get even larger path length adjustment, but then the middle dipoles will have to bend more strongly and the radiation power density will exceed the limit we have imposed.

Each such chicane can produce a path length difference of 8.25 cm. The path length change can be continuous if precise and reliable mechanical motion control is feasible. Alternatively one can make a fixed change by building another beam line which will be very close to the normal FODO section, in which case the path length change will be discrete. The cost impact and operation reliability issues for the chicane choices have to be further evaluated. The local optics distortion from such a chicane is shown in Figure 2.4.3-8. The overall effect on the ring lattice remains to be examined.

One can activate a number of such chicanes to obtain required path length difference. It seems reasonable to activate four chicanes to get ~20cm path length changes for the 50 GeV proton

collisions. The total length of the moving sections is then about 160 m! And the mechanical motion is complicated. The cost impact will be significant.
However it will be too costly and very destructive to the normal lattice if ten such chicanes (total 80 dipoles, about half of total arc section) have to be activated to make the 0.9 m difference.

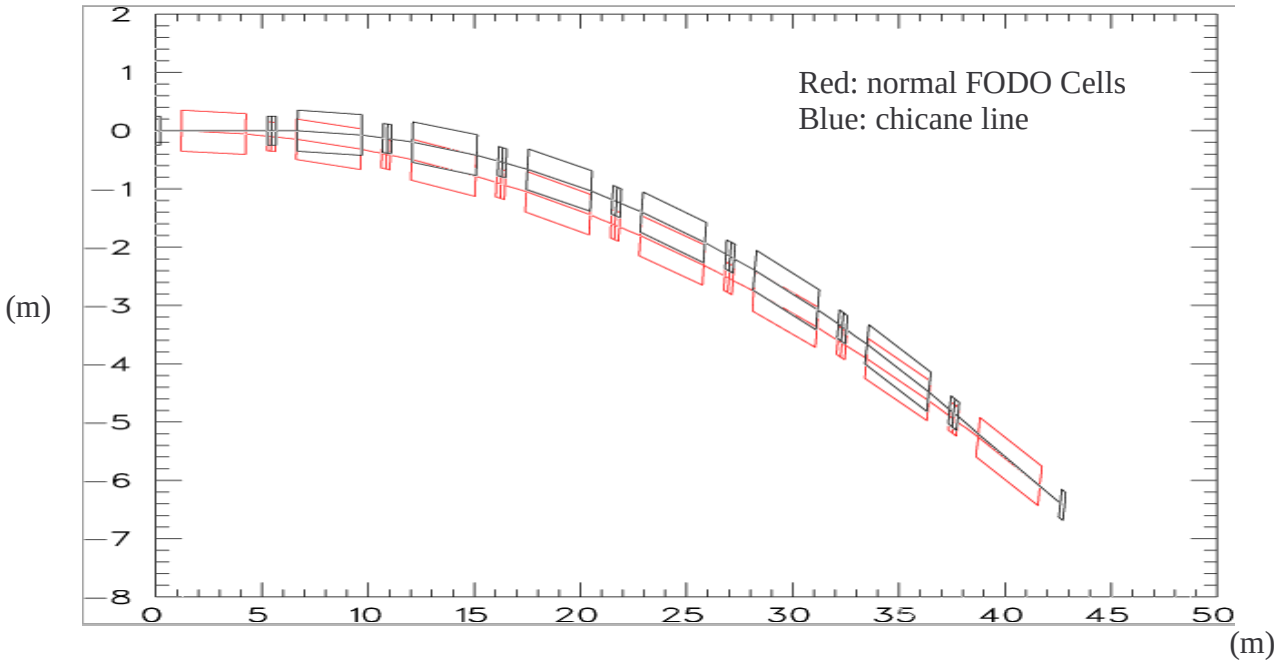

Figure 2.4.3- 7 Layout of an eight bend chicane for path length adjustment.

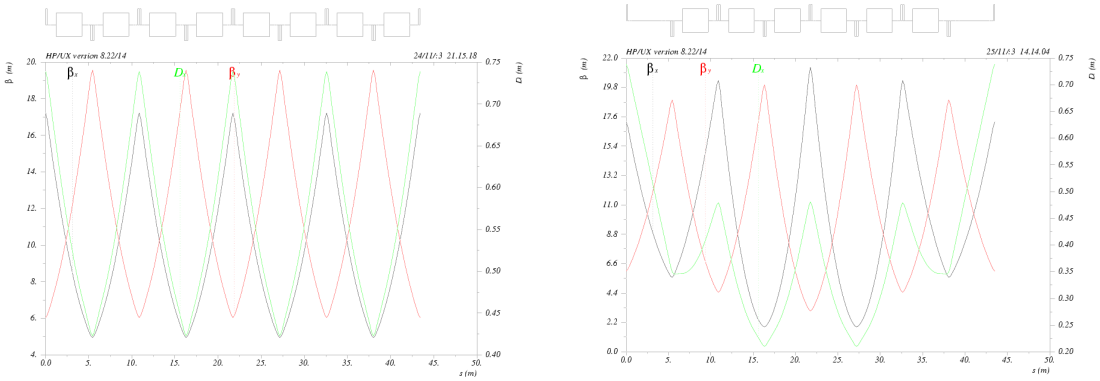

Figure 2.4.3- 8 Optical distortion of the eight bend chicane. Left: the original 4 FODO periods. Right: the chicane optics.

One way to relieve the electron ring path length issue is to adjust the proton ring path length as well [8]. One of the proton rings (YELLOW ring) has to adjust its path length anyway when the BLUE ring is in colliding with electrons while the two proton beams keep colliding at other locations at same time. A comprehensive solution of the path length changes for all the three rings has to be further developed.
For a large path length adjustment scheme, there is not yet an easy solution. One attractive option is to move one of the electron ring arc sections as a whole by 0-0.45m. This option has the advantages of no impact on lattice, no concerns of extra magnets, simple one direction mechanical movement and meets all path length change requirements by one “knob”. The technical details and cost of such a “big move” will be carefully evaluated.

Dynamic Aperture

The criteria of the ring dynamic aperture are set by two requirements: it must be sufficiently large for efficient injection and a long beam lifetime is required under colliding conditions.

Injection takes place in the horizontal plane, so the injection point is horizontally displaced from the closed orbit. For injection, the transverse aperture should include the injection point and several rms beam sizes around it, and the momentum aperture should be at least ± 0.5% of the nominal injection energy. For colliding beam, the dynamic aperture should be larger than 10 σ for both transverse plans, and the momentum aperture must be at least ~±7 σ_E to guarantee long quantum beam lifetime. An even larger momentum aperture is desirable to tolerate effects other than synchrotron radiation excitation. A larger dynamic aperture is always strongly favored. In this report we will take as the design goal a momentum aperture of ± 10 σ_E and transverse aperture >± 10 σ with all machines errors and under colliding conditions. The damped beam momentum spread σ_E of the ring is about 1×10^{-3} at 10 GeV and ~0.5×10^{-3} at 5 GeV.

The emittance of the full energy injected electron beam is usually smaller than the ring natural emittance. So the ±10σ transverse aperture requirements are good for injection. However, for the positron beam, the expected emittance at 10 GeV could be as high as 100 nm-rad if no damping ring is included in the positron injector system. More simulation will be performed to see if any significant beam loss could happen and also to investigate the effects on colliding beams in such an operation scenario.

The major cause of reduction of dynamic aperture is the nonlinearity of the sextupole magnets which are introduced to correct chromaticity in the ring. One can expect that a ring with lower chromaticity will need less sextupole strengths and therefore possibly obtain a larger dynamic aperture.

Modern light source rings implement low emittance lattices with strong focusing, and consequently have to deal with strong correction sextupoles that generate high negative chromaticity. Achieving a good dynamic aperture is a major challenge [9]. For collider rings, the arc lattice usually consists of FODO cells with moderate quadrupole focusing and phase shift per cell. Correction of the chromaticity caused by the FODO cell quadrupoles alone will not jeopardize the dynamic aperture. The challenges are to correct the large chromaticity generated by the strong focusing quadrupoles at large β locations near the interaction region.

The ideal way to reduce the nonlinearity by the chromaticity correction sextupole magnets is to use equal strength sextupole pairs that are connected with –I transformers in both transverse plans [10]. This applies to both local corrections around the IP and in the arcs. The noninterleaved 2.5π cell design for the KEKB rings is a good example. The noninterleaved sextupole chromaticity correction scheme is difficult to realize here due to limited space. Also, as mentioned in arc lattice design, the horizontal phase advance has to be widely adjusted to achieve the required beam emittance. At 10 GeV, it varies from ~60-80 degrees, and can be as low as ~30 degrees at 5 GeV. This makes even a conventional interleaved scheme (same phase advance for both transverse planes) not possible. The vertical phase advance per FODO cell has little to do with beam emittance. Smaller vertical phase advance means lower β_y at quadrupoles, and less chromaticity. Therefore, for low and moderate emittance lattices, vertical phase advances are fixed at 60 degrees. Then the sextupoles that are

separated by π phase difference can be paired to partially cancel the second order geometric aberrations.

Repetitive geometric correction is also practiced to cancel second-order geometric aberrations. It requires a lattice made of n identical cells (n>3) having a total phase shift of $2m\pi$[10]. We have 36 normal FODO cells in each of the 180^0 arc section. In the vertical plane, three sextupole families are arranged. Then there is a –I transformation for every three FODO cells, and this structure repeats 12 times in an arc section. Horizontal sextupoles will be grouped depending on the phase advance per cell of the specific lattice configuration. Tracking shows that carefully grouping sextupoles according to lattice configurations give much better dynamical apertures then using only two fixed families of sextupoles.

The chromaticity correction scheme in the arc is limited by the large emittance adjustment requirements. However, since we choose the best scheme for the low emittance lattice, the less optimal arrangement for the larger emittance lattice is not necessarily bad for the dynamic aperture because the strengths of the cell quadrupoles are weak for this case, requiring also smaller correction sextupole strengths. For each of the different emittance lattices, the dynamic aperture situation has to be optimized with possible chromaticity correction schemes.

Local chromaticity correction schemes for the IR straight are under development to solve the problem at its source. Due to the different colliding scenarios, the β^* values of the electron beam at IP are required to be varied from 0.19 m to 0.35 m. The local correction scheme has to survive over different IR optics configurations. The space limit in that region also could drive one to consider a scheme like the PEP II High Energy Ring beta-beat scheme for semi-local chromaticity correction [11] which involved a dispersion suppressor and a few arc FODO cells adjacent to the IR straight.

The dynamic aperture is sensitive to working point locations in the betatron tune map to avoid strong resonance lines. The electron ring betatron tunes in e+e- colliders are chosen slightly above half-integer for high luminosity based on beam-beam effects [12]. However, in the eRHIC electron ring, the tunes have to be chosen slightly above integer for high polarization. This is because of the absence of parametric resonances k+1/2 for the linear spin resonances [13]. The best spin tune is a half-integer spin tune. Therefore the fractional parts of the orbital tunes should be as far away from 1/2 as is practical to “leave space” around the half integer spin tune. More details are described in section 2.4.6.

The linear lattice is designed using MAD [14]. Chromaticity correction is first optimized with the HARMON module in MAD. High order chromaticities and momentum dependent beta function variations at IP are minimized. Notice that HARMON does not count coupling, so small residual chromaticity exist, and will be further corrected later.

The vertical sextupoles are further divided into six families to facilitate the above process. The horizontal sextupole family number is also doubled. Chromaticity correction results for tune and β^* are plotted in Figure 2.4.3-9.

The initial dynamic apertures are estimated using MAD in the six-dimensional phase space as well. However thick lens tracking in MAD uses maps that are not symplectic by nature, and therefore have to be “symplectified” in order to guarantee energy conservation. This procedure makes them

somewhat unphysical, and makes long-term tracking questionable [15]. We do have concerns about tracking at the edge of apertures with large synchrotron momentum oscillations. The automatic dynamic aperture search DYNAP in MAD could give very sharp drop of apertures at edge for large off-momentum particles. Therefore the dynamic apertures are further evaluated using the two fully symplectic tracking codes LEGO[16] and SAD[17] which show very consistent results when tracking with large synchrotron motions.

Figure 2.4.3-10 and Figure 2.4.3-11 give the dynamic aperture tracking results from both LEGO and SAD. The resulting dynamic apertures are consistent: large momentum aperture of dp/p= ± 0.01.

In all the tracking processes, the horizontal emittance is assumed to be the natural beam emittance and the vertical emittance is half of the natural emittance corresponding to full coupling. We track for 1024 turns, including synchrotron motion and damping. The 1024 turn circulation time corresponds to ~0.6 transverse damping time at beam energy of 10 GeV. Longer period tracking of 8096 turns shows very little aperture difference (Figure 2.4.3-10). Therefore, we consider the 1024 turn tracking sufficient to estimate the appropriate dynamic aperture. Dynamic aperture tracking including all magnet errors with proper closed orbit corrections and beam-beam effects are still in progress.

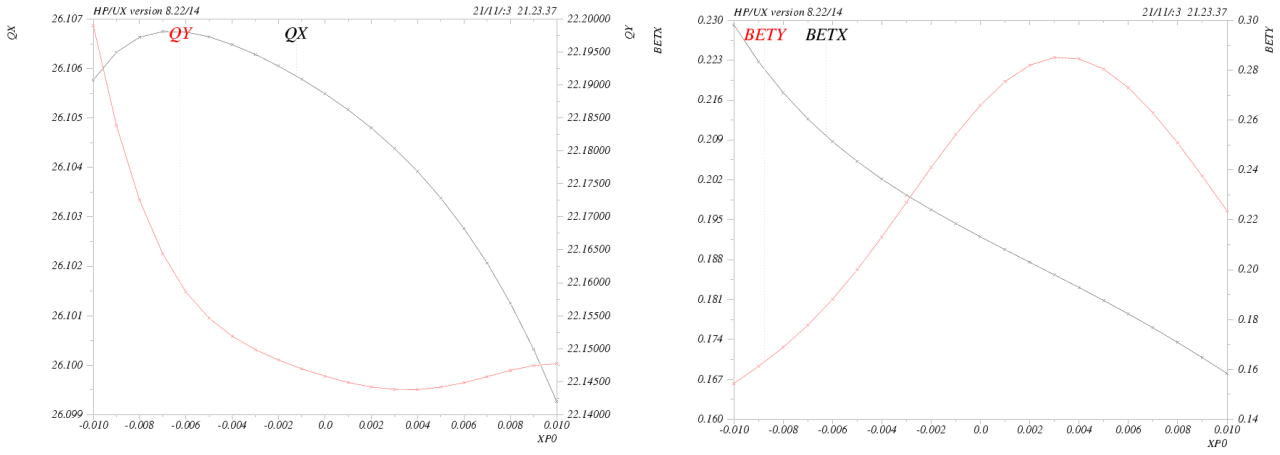

Figure 2.4.3- 9 Chromatic properties of betatron tune and betatron amplitude functions at IP

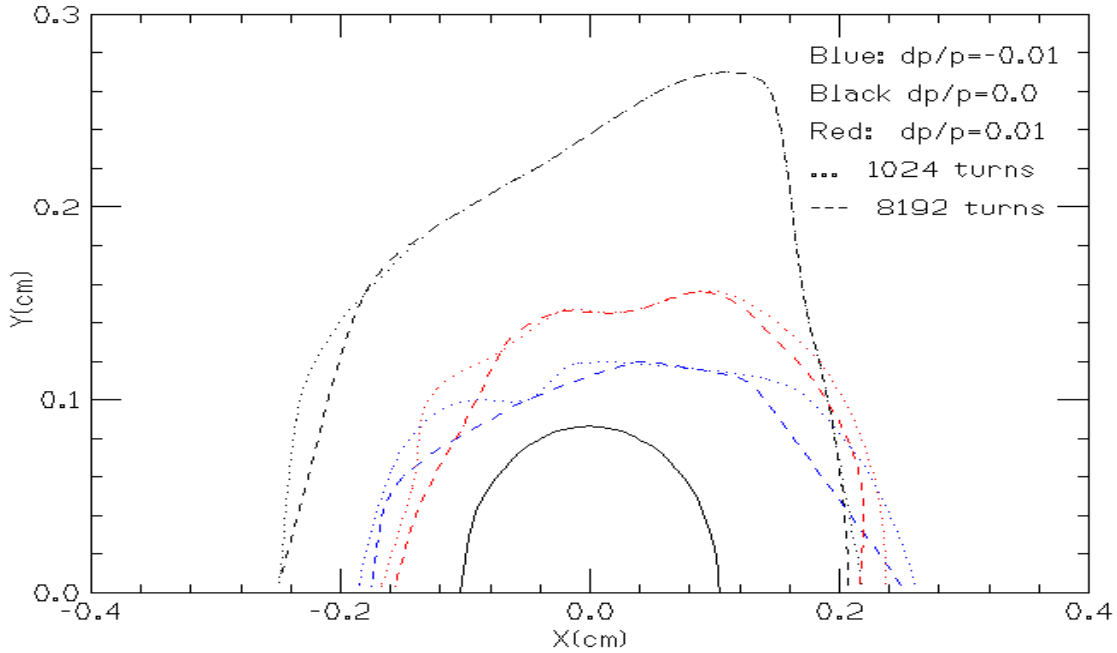

Figure 2.4.3- 10 Dynamic aperture from LEGO tracking. The centered half circle is the 10 σ transverse aperture boundary.

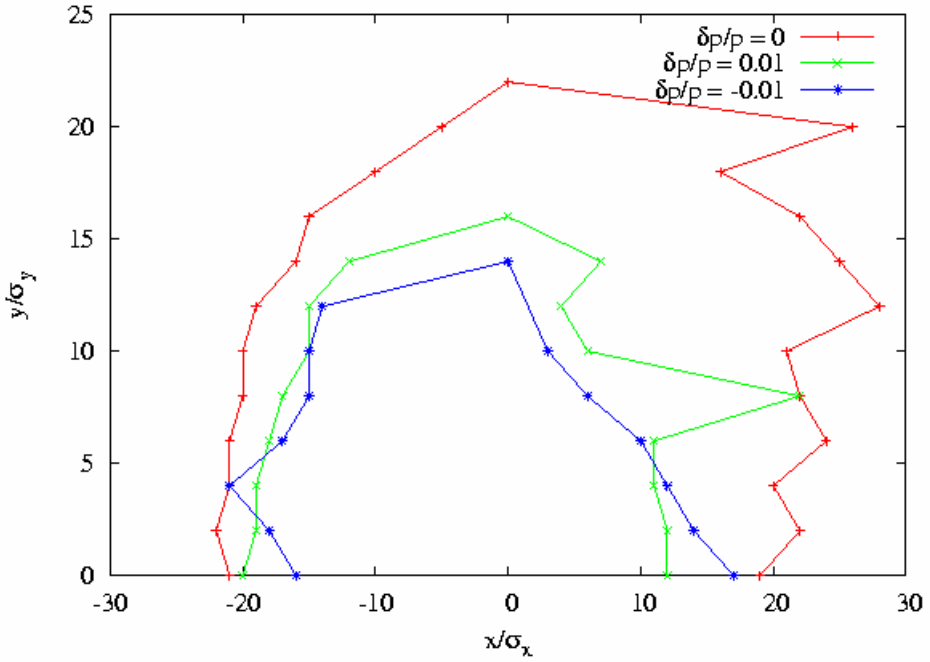

Figure 2.4.3- 11 Dynamic Aperture tracking from SAD

Magnet Errors

Magnet errors include both magnetic field errors and alignment errors. They reduce dynamic apertures, change optics, effect beam polarization and beam lifetime. Table 2.4.3-1 lists typical magnet errors and their effects.

Error	Effect
Dipole Field	Orbit
Dipole Roll	Vertical orbit
Quadrupole Misalignment	Orbit, polarization
Quadrupole Field	Tune, beta and dispersion beat
Quadrupole Roll	Transverse coupling, polarization
Multipole Fields	Nonlinearity

Table 2.4.3- 2 Magnet Errors

The closed orbit errors change particle trajectories through nonlinear elements and will cause detuning. They can reduce dynamic aperture significantly. To obtain small vertical closed orbit distortion is also essential for sustaining high beam polarization (see section 2.4.6). Therefore enough orbit correction magnets and beam monitors with adequate precision should be planned at the design stage. The rms deviation of the closed orbit from the design machine orbit should be 0.1 mm or less. This will greatly reduce the effect of orbit distortion on dynamic aperture. Dynamic aperture will be evaluated under all magnet errors with appropriate orbit correction schemes in place.

While detailed magnet error tolerance study is not the subject of this report. We do track with typical magnet error statistics. In general, tracking with errors to examine their effect on dynamic aperture, luminosity and polarization level will provide the necessary basis for developing various beam-based tuning procedures. Figure 2.4.3-12 shows the dynamic aperture with typical quadrupole and sextupole field errors: 0.1% for quadrupoles and 0.2% for sextupoles.

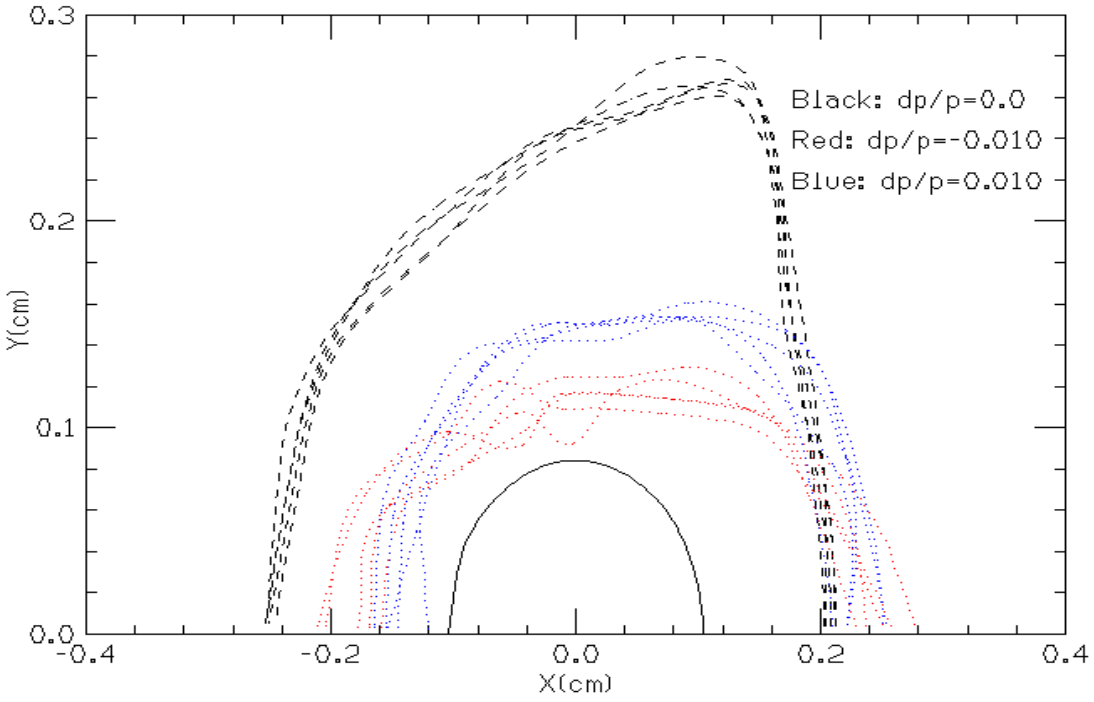

Figure 2.4.3- 12 Dynamic Aperture of lattice ZDR2.0 with multipole field errors**.**

Machine Parameters

Table 2.4.3- 3 Summary of Machine Design Parameters*,**

* Beam current at 10 GeV in the table is twice the nominal design value in table 2.4.1-2.

** Path length adjustments are not shown in the table.

ZDR 2.0 2003				
Electron beam energy	10GeV	10GeV	5GeV	5GeV
Ion beam energy	p 250 GeV	Au 100GeV/u	p 50 GeV	Au 100 GeV/u
Circumference(m)	1277.95	1277.95	1277.95	1277.95
Energy (GeV)	10	10	5	5
Bending radius(m)	81.0162	81.0162	81.0162	81.0162
Bunch spacing (ns)	35.52	35.52	35.52	35.52
Bunch spacing(m)	10.65	10.65	10.65	10.65
Number of bunches	120	120	120	120
Bunch population	2.00E+11	2.00E+11	1.00E+11	1.00E+11
Beam current(A)	0.90	0.90	0.45	0.45
Arc cell	FODO	FODO	FODO	FODO
RF frequency MHz	478.572	478.572	478.572	478.572
Harmonic number	2040	2040	2040	2040
Energy loss/turn (MeV)	11.74	11.74	0.72	0.72
Accelarting voltage(MV)	25	25	5	5
Synchrotron tune	0.04	0.04	0.05	0.05
Total rad. power(MW)	10.53	10.53	0.32	0.32
Syn. rad. power/m (KW) in arc	19.25	19.25	0.60	0.60
(from normal bends)				
Self-pola. time at 10GeV(minutes)	22.03	22.03	704.87	704.87
Emittance-x, no coupling (n m.rad)	56.6	56.6	85	54
Beta function at IP (cm) β_y^*/β_x^*	19.2/26.6	19/34	35/20	19/19
Emittance ratio ($\varepsilon_y/\varepsilon_x$)	0.18	0.18	0.45	0.25
Beam size at IP(um) σ_x	104.25	103.70	172.48	101.29
Beam size at IP(um) σ_y	52.06	58.86	87.46	50.65
Momentum compaction α	2.62E-03		9.10E-03	
Momentum spread σ_ε	9.61E-04		4.80E-04	
Bunch length (cm) σ_z	1.20	1.20	1.6	1.6
S.R. damping time(x) (mS)	7.3	7.3	58.6	58.6
Beta tune μ_x	26.105			
Beta tune μ_y	22.145			
Natural chromaticity $\xi x/\xi y$	-35.6/-33.8		-28.5/-29.0	

References:

1. Y. Suetsugu et al., “Conceptual Design of Vacuum System for Super KEKB”, PAC 2003, Portland, Oregon. May 12-26, 2003.
2. J.B. Murphy “Synchrotron Light Source Data Book”, ©1992 American Institute of Physics.
3. D.Wang “Lattice Design of a 10 GeV electron ring for eRHIC”, Workshop e+e- Factories 2003, Stanford, CA USA, October 13-16, 2003.
4. R. Assmann and K. Cornelis, "The Beam-Beam Interaction in the Presence of Strong radiation Damping” , P.1187, EPAC 2000, Vienna, Austria. June 2000.
5. D. Rice, “CESR-c Status and Accelerator Physics”, Workshop e+e- Factories 2003, Stanford, CA USA, October 13-16, 2003.
6. V.Ptitsyn et. al., "Electron-ion collisions at RHIC using a high intensity self-polarizing electron ring", Proceedings of the 2003 Particle Accelerator Conference, p.373, 2003.
7. C. Tschalaer, “Ring path length adjustment”, talk at eRHIC collaboration meeting, BNL, August 19-20, 2003
8. B. Weng, S. Peggs, F. Wang, private communications, September-October, 2003.
9. H. Owen et al. “Optimization of the DIAMOND Storage Ring Lattice”, p.751, Proceedings of EPAC 2002, Paris, France.
10. K.L. Brown and R.V. Servranckx, “First- and Second-order Charged Particle Optics”, SLAC-PUB-3381, July 1984.
11. M.H.R. Donald et al. “Lattice Design for the High Energy Ring of the SLAC B-Factory (PEP-II), p.576 proceedings of PAC 95, Dallas, TX 1995.
12. Y. Cai and Y. Nosochkov “Tracking Simulations Near Half-Integer Resonance at PEP-II”, SLAC-PUB-9812, May 2003.
13. J. Buon, “Polarization of Electron and Proton Beams”, CERN 95-06 , 1995.
14. H. Grote, F. C.Iselin, “The MAD Program (Methodical Accelerator Design)” CERN/SL/90-13.
15. Hans Grote and J. Cardona, Private Communication, Aug. 7, 2003.
16. Y. Cai, “LEGO -- A Class Library for Accelerator Design and Simulation” , SLAC-PUB-8011, November 1998.
17. K. Hirata, “An introduction to SAD”, Second Advanced ICFA Beam Dynamics Workshop, CERN 88-04 (1988). See http://acc-physics.kek.jp/SAD/sad.html.

2.4.4 Beam Instabilities

In previous chapters we discussed the parameter choices of eRHIC. The lattice design of the electron ring presented in 2.4.3 is based on these choices. In this chapter the influence of the various intensity-dependent effects on the machine performance is investigated.

The main parameters of electron ring of the eRHIC are

- Beam energy: 5 -10 GeV
- Particle species: electron and positron
- Beam currents: ~450 mA
- Bunch length: ~ a few cm
- Beam emittance: ~ 50 to 100 nm.rad
- Beam energy spread: 6~10 E-4
- Bunch spacing: ~10.6 m
- Particles/bunch: $\sim 1\times 10^{11}$

In the current eRHIC design, the bunch spacing is primarily determined by the existing hadron machine complex. There is little flexibility for generating different bunch patterns. One has to deal with a high bunch current and a relatively high total beam current. Since the bunch length of the hadron beams is longer than 10 cm, the bunch length of lepton beams (1-2cm is expected) is not an issue. The main concern for single bunch effect is the transverse mode-coupling instability. We also discuss the power deposition generated by a beam in the form of the higher order mode (HOM) losses by interacting with its surroundings. The narrow-band impedance and related instabilities need to be evaluated carefully due to the relatively large number of RF cavities. The eRHIC machine is planned to operate over a wide range of beam energies. Many collective effects exhibit their strongest behavior at low energy where the beam is less rigid and damping time is much longer than at higher energies. Since electron and positron beams are required by the physics programs, the lepton machine has to account for both electron cloud effects (ECE) for positron operation, and fast beam-ion instability (FBII) for electron operation in the ring design.

Compared to the achieved beam performance in several new machines at the same energy ranges, especially two B-factories, the requirements for eRHIC electron ring appear reasonable and achievable.

In terms of collective effects, several issues are of particular concern including:

- Single bunch instabilities
- Higher-order-mode (HOM) heating
- Coupled bunch instabilities
- Ion related effects
- Electron cloud effects, etc.

The major parameters of eRHIC and other existing machines in the same energy range are summarized in the Table 2.4.4-1.

	eRHIC	PEP-II LER/HER	KEKB LER/HER	CESR-III
Energy(GeV)	**5 - 10**	3.1/9.0	3.5/8.0	5.3
Circumference(m)	**1278**	2200	3016	776
RF freq.(MHz)	**478.6 or 506.6**	476	508	500
RF voltage(MV)	**5 - 25**	6/15	10/18	3
Total current(A)	**0.45**	2.4/1.4	1.9/1.2	0.72
Particle/bunch(10^{11})	**1.0**	1.0/0.6	1.1/0.7	1.3
Bunch spacing(m)	**10.6**	1.9	2.4	2.4(in train)
Momentum comp.	**0.009/0.0026**	0.0018	0.0012	0.0025
Energy loss/turn(MeV)	**0.72/11.7**	1.2/3.6	1.6/3.5	1.0
Average beta(m)	**~15**	~17	~10	~20
Bunch length(cm)	**1~2**	1.0	0.4	1.5

Table 2.4.4- 1 Comparison of beam parameters of eRHIC and major existing lepton rings in the same energy **range**

Impedance Budget

We start with the estimate of impedance contributions from various components in the eRHIC lepton ring. Among the impedance-generating elements in the ring, the largest contributors are RF cavities, the resistive vacuum chamber walls, the IR chambers, bellows and masks.

RF cavities

The main contribution to the narrow-band impedance comes from the RF cavities. To substantially reduce the narrow-band impedance a small number of deeply-damped RF cavities will be adopted. At the current design stage, the PEP-II 476 MHz normal conducting RF cavities and KEKB superconducting cavities are both highly successful for operation of high current B-factory storage rings. These two cavity designs are the major candidates for the eRHIC electron ring. The superconducting cavities are especially attractive because their higher accelerating voltage reduces the total number of cavities needed, thus reducing their impedance contribution. Brookhaven also has a long history in superconducting technology, and has recently been developing a facility to test superconducting RF cavities. To compensate energy loss due to synchrotron radiation and keep a reasonable quantum lifetime, a total RF voltage of about 18 MV is needed at 10 GeV. It is assumed that the RF system should be able to provide up to 25 MV total RF voltage. Figure 2.4.4- 1 and Figure 2.4.4- 2 show the bunch length with different beam energies. Over major operating ranges the bunch length would be 1-1.5 cm.

Resistive-wall

Detailed designs of vacuum chamber and components are not yet available, but we can discuss design principles and outline an impedance budget. A vacuum chamber with about 3.5 cm radius, which is comparable to similar machines, is assumed in our current calculations. Copper is the material of choice for its excellent conducting properties. For comparison, aluminum and stainless steel are also simulated.

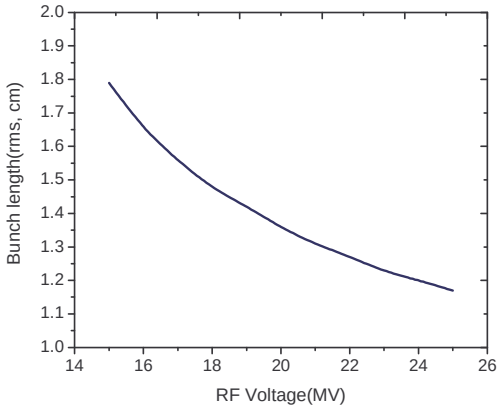

Figure 2.4.4- 1 Bunch length at 10 GeV

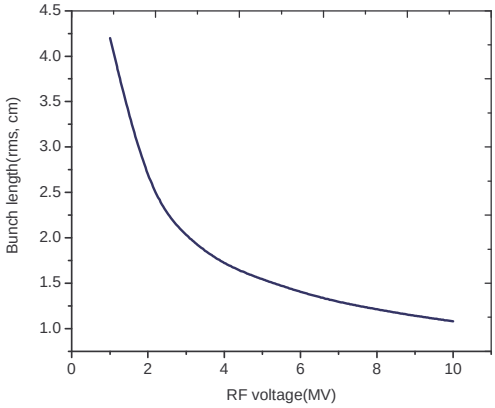

Figure 2.4.4- 2 Bunch length at 5 GeV

Other components

- Pumping slots
- BPMs
- Masks
- IR chambers(including two Y-shape recombination chambers)
- Bellows
- Tapers, etc.

Preliminary estimates of the quantities of each component and the budget of their contribution to the inductive impedance and loss factor (assuming 1 cm bunch length) are shown in Table 2.4.4-2.

component	No. of items (estimated)	Inductive impedance(ohm)	Loss factor budget(V/pC)
Cavities	28(n.c.)/13(s.c.)		~14/10
Resistive wall	1278 m	2e-3	2.0
Masks	TBD	3e-2	2.0
Valves	TBD	6e-3	0.3
BPMs	~300	1e-4	0.6
IR chambers	1+2	2e-3	2.0
Tapers	TBD	2e-2	2.0
Bellows	TBD	1e-2	2.0
Total		~0.06	~25/21

Table 2.4.4- 2 Impedance and loss factor budgets

Based upon above budget the total loss factor with some contingency is ~25 V/pC, which is comparable to that for KEKB [1] and PEP-II [3]. A very conservative estimate for total impedance, 1 ohm, is used for the instability simulations. These should be considered a very preliminary study because number of items is a rough estimate and some of the components, such as feedback pickups, injection kickers, some chamber tapers connecting various components and so on, are not among the listed items. Inclusion of all the detailed beamline components may change these calculations in some extent. For these reasons, a wide range of loss factor and impedance values are considered in calculating the impedance-related collective effects.

Higher Order Mode (HOM) Heating

The estimated total higher-order-mode power of the electron ring is up to about 240 kW with 450 mA current. Compare to that of B-factories the HOM power in eRHIC e-ring is moderate. In case of high intensity operation with 1 A beam current the HOM energy loss would approach to the level of B-factories.

Loss factor(V/pC)	15	25	35
I = 450 mA	120 kW	200 kW	280 kW
I = 1000 mA	590 kW	980 kW	1370 kW

Table 2.4.4- 3 HOM power with different loss factor and beam current

Transverse Mode Coupling Instability (TMCI)

This instability occurs when two head-tail modes (m=0 and m=-1 in most cases) share the same coherent frequencies. The instability is a severe limitation on the single bunch current in large storage rings with a low beam energy and a low synchrotron tune. Using the estimated transverse wake potential and average beta function of 15 m, it is found that coherent tune shift of the m=0 dipole mode is very small at the design bunch current. The transverse mode-coupling instability threshold is expected to scale as

$$I_b = \frac{4(E/e)\nu_s}{\langle \mathrm{Im}(Z_\perp)\beta_\perp \rangle R} \frac{4\sqrt{\pi}}{3}\sigma_l \qquad \textbf{(2.4.4-1)}$$

where ν_s is the synchrotron tune, β is the beta function at the location of the impedance, and R is the average ring radius. Compared to the B-factory low energy rings, the eRHIC collider has higher energy, higher synchrotron tune, longer bunch length, shorter circumference, and comparable impedance and beta function. The calculated threshold currents are about 46 mA at 10 GeV and 16 mA, respectively, which are higher than the nominal value (3.8 mA) with comfortable margins. For all of these reasons the transverse mode-coupling instability threshold will not impose a threat to the performance of the lepton ring.

Longitudinal Microwave Instability Threshold

Although not a source of beam loss or intensity limitation, the longitudinal microwave instability together with the potential well effect is considered to be the major source of bunch lengthening. The design beta-functions at IP of the lepton beam are about 15 to 30 cm. Since the bunch length of hadron beams is very long (above, say, 10 cm or longer) the much shorter bunch length of lepton beams (1~2cm is expected) is not considered to be a problem (hourglass effect is negligible). Figure 2.4.4-3 shows the threshold of the longitudinal microwave instability [6].

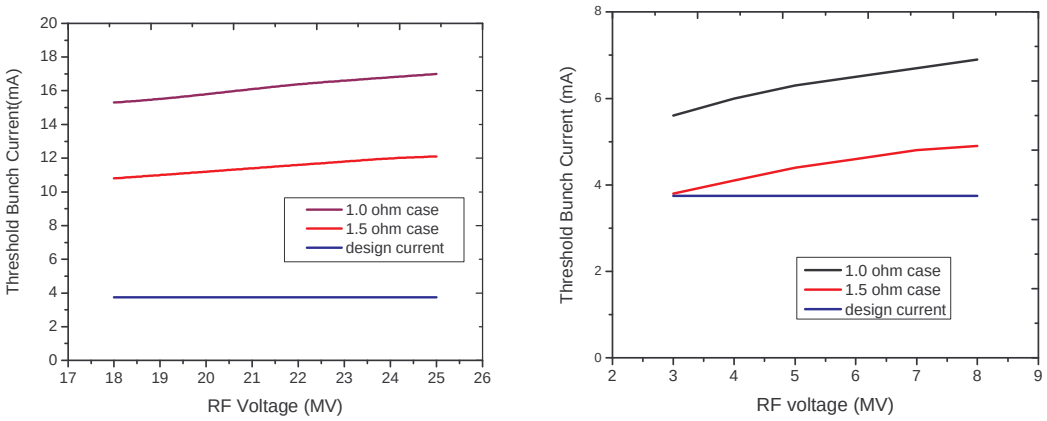

Figure 2.4.4- 3, 4: Single bunch threshold at 10 GeV (left) and 5 GeV (right) with different broadband impedance scaling.

Longitudinal Coupled Bunch Instability

The wake fields in high-Q structures in a storage ring, such as RF cavities and resistive-wall beam pipes, cause different beam bunches to interact. For certain values of relative phase between bunches, the coupled-bunch motion can grow and become unstable, leading to beam loss. The instabilities are characterized by their motion in longitudinal phase space. Longitudinally, the a=0 mode can not become unstable, so the lowest longitudinal instabilities are characterized by a=1 synchrotron motion. Table 2.4.4-3 and 2.4.4-4 summarize the major monopole modes for these two kinds of RF cavities.[2][4]

f(MHz)	R/Q(ohms)	Q
758	44.6	28
1009	0.006	246
1283	7.68	66
1295	6.57	907
1595	5.06	178
1710	0.44	54
1820	0.13	0.0
2109	3.52	233
2253	1.21	500

Table 2.4.4- 4 Major monopole modes of PEP-II RF cavity

f(MHz)	R/Q(ohm)	Q
783.0	0.12	132
834.0	0.34	72
1018.0	6.6	106
1027.0	6.4	95
1064.9	1.6	76
1076.0	3.2	65
1134.0	1.7	54

Table 2.4.4- 5 Major monopole modes in KEKB sc RF cavity

Mode	Growth time (ms)
a=1	τ_1 = 228 τ_2 = 229 τ_3 = 230
a=2	τ_1 = 2139 τ_2 = 2148 τ_3 = 2153

Table 2.4.4- 6 Growth rates: longitudinal, at 5 GeV

Calculations are performed using the ZAP code [6] with the cavity characteristics given above. Table 2.4.4-5 shows the modes with the fastest growth rates in 5 GeV operations. The growth times are longer in 10 GeV case.

Transverse Coupled Bunch Instability

Tables 2.4.4-6 and 2.4.4-7 summarize the major dipole modes for these two kinds of RF cavities [2][4]. In the transverse plane, the a=0 motion is the lowest mode of instability. Table 2.4.4-7 gives the a=0 and a=1 modes with the fast growth rates for eRHIC electron ring. Again they occur when beam energy is low (5GeV). The situation at higher energy is better.

f(MHz)	R_{tran} (k ohm/m)	Q
792	9.7	96
1063	50.4	34
1133	1.3	0
1202	0.6	642
1327	5.6	510
1420	5.3	554

Table 2.4.4- 7 Transverse modes in PEP-II 476 MHz cavity

(MHz)	R/Q' (ohm/m)	Q
609.0	1.9	92
648.0	40.2	120
688.0	170.4	145
705.0	227.3	94
825.0	6.2	60
888.0	3.5	97

Table 2.4.4- 8 Transverse modes in KEKB sc RF cavity

Note: different units/conventions in transverse modes of two cavities.

Mode	Growth time (ms)
a=0	τ_1 = 38 τ_2 = 55 τ_3 = 67
a=1	τ_1 = 164 τ_2 = 165 τ_3 = 166

Table 2.4.4- 9 Growth rate of transverse modes

The damping times in the electron ring are about 7.4 ms (transverse) and 3.7 ms (longitudinal) at 10 GeV and 58 ms (transverse) and 29 ms (longitudinal) at 5 GeV. The worst situation occurs in the low energy operation, where the coupled-bunch instabilities have the fastest growth rates and damping time is long. The preliminary simulations suggest that a feedback system is needed and sufficient.

Fast Beam-Ion Instabilities (FBII)

The relatively large bunch spacing in the eRHIC electron ring causes a small ion trapping effect. However, the ions accumulated during a single passage of the bunch can cause a transient instability. This so-called 'fast beam-ion instability' (FBII) is similar to the multi-bunch beam break-up in a linac. Usually the FBII is more severe in the vertical plane as the vertical emittance is smaller in the lepton machine. According to the linear model [5], the rise time can be described as

$$\frac{1}{\tau} = \frac{4 d_{gas} \sigma_{ion} \beta_y N_b^{3/2} n_b^2 r_e r_p^{1/2} L_{sep}^{1/2} c}{3\sqrt{3}\sigma_y^{3/2} \gamma (\sigma_x + \sigma_y)^{3/2} A^{1/2}} \qquad \textbf{(2.4.4-2)}$$

where $d_{gas} = p/k_bT$ = 5.1E13 m^{-3} is the density of residual gas, σ_{ion} is the ionization cross section, N_b is the particle number per bunch, r_e *and* r_p are the classical radius of the electron and proton respectively, L_{sep} is the bunch spacing, σ_x and σ_y are the horizontal and vertical beam sizes, and A is the ion mass in unit of proton mass.

	B-factory parameters	eRHIC scaling factor over B-F parameters
N_b	~ 1E11	~ 1
L_{sep}	~ 2.5 m	~ 4
σ_x	~ 0.8 mm	~ 1
σ_y	~ 0.12 mm	~ 3
E	~9 GeV	~ 0.5~1.2

Table 2.4.4- 10 Scaling FBII effects in electron ring of eRHIC

Above table shows that the eRHIC lepton ring has some advantages over today's B-factories on FBII. Below is a more detailed analysis.

Taking into account of the coherent frequency spread, the linear theory gives the couple bunch motion in the bunch train like y ~ exp(t/τ_e), the growth time is given by

$$\frac{1}{\tau_e} = \frac{1}{\tau}\frac{c}{2\sqrt{2}l_{train}(\Delta\tilde{\omega}_i)_{rms}} \qquad \textbf{(2.4.4-3)}$$

where $(\Delta\tilde{\omega}_i)_{rms}$ is rms spread of ion coherent angular frequency, l_{train} is bunch train length.

$$\omega_i = \left(\frac{4N_b r_p c^2}{3AL_{sep}\sigma_y(\sigma_x+\sigma_y)}\right)^{1/2} \qquad \textbf{(2.4.4-4)}$$

The growth rates of FBII at 10 GeV and 5 GeV are shown in Figure 2.4.4-5 and 6.

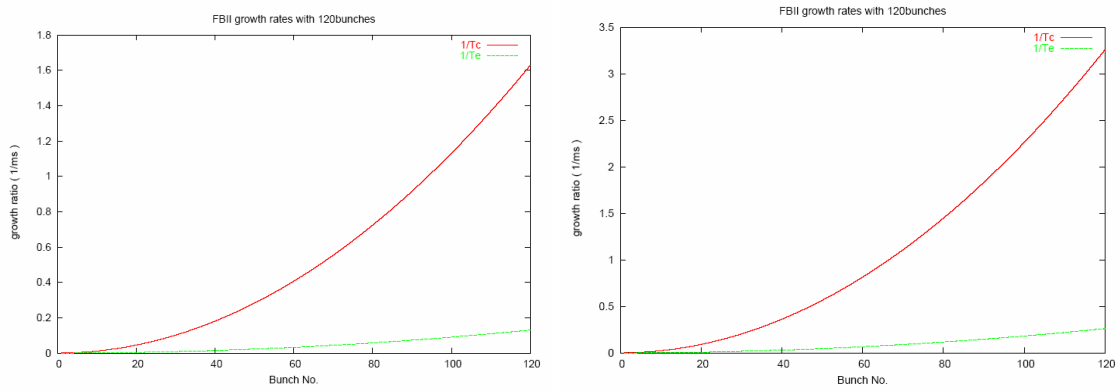

Figure 2.4.4- 2, 6: Growth rates of FBII at 10 GeV (left) and 5 GeV (right), 450 mA

If a total beam current of 1000 mA is assumed, compared to the achieved parameters of the two high energy rings at the B-factories the bunch population of the electron ring of eRHIC would be higher by a factor 2. However, its vertical beam size is larger (for matching the hadron beam size), which improves the situation. We expect the FBII effect with 1000 mA current in the electron ring of the eRHIC collider to be comparable with that in two B-factories. See Figure 2.4.4-7 and Figure 2.4.4-8. A feedback system like those used at PEP-II and KEKB should be able to handle the required beam intensity.

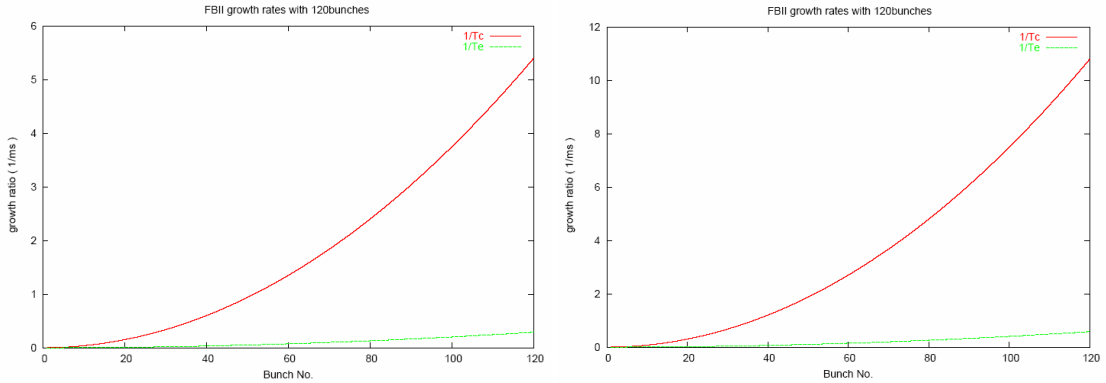

Figure 2.4.4- 7, 8: Growth rates of FBII at 10 GeV (left) and 5 GeV (right), 1000 mA

Electron Cloud Effects (ECE)

In the positron-hadron collision operation of eRHIC, the photo electrons generated by synchrotron radiation hitting the vacuum chamber walls, and secondary emission due to multipacting in the presence of the electric field of the positron beam, can accumulate in the beam pipe during the multi-bunch operation with short bunch spacing. This gives rise to a so-called 'electron cloud' (EC). Several effects have been observed in different machines, including

- Pressure rise
- Beam-size blow-up
- Coupled-bunch instability, etc.

Multi-bunch effect
For coupled-bunch instability due to EC, if we assume that the density of the electron cloud is saturated, then the growth time can be estimated as [10]

$$\tau_{CB} = \frac{\gamma \omega_\beta h_x h_y L_{sep}}{2 r_e N_b c^2} \qquad \textbf{(2.4.4-5)}$$

γ is relative energy factor, ω_β is betatron frequency, h_x, h_y are transverse dimensions of the vacuum chamber, L_{sep} is bunch spacing, N_b is number of particles per bunch. Assuming similar vacuum chamber dimensions to that of the existing lepton machines, the growth time is at the level of 1.0 ms in e+ operation.

Single bunch effect
The electron cloud can also drive single bunch instability. Here we use treat it as a transverse mode-coupling instability. With a two-particle model, the threshold electron density of TMCI is [11]

$$\rho_{e,threshold} \approx \frac{2\gamma \nu_s}{\pi \beta_y r_e C} \qquad \textbf{(2.4.4-6)}$$

C is ring circumference, ν_s is synchrotron tune. The threshold is about 1.2×10^{13} at 10 GeV and 0.6×10^{13} at 5 GeV, respectively. The preliminary simulation shows that the electron cloud density in eRHIC lepton ring could reach this level if no precautionary measure is taken.

To better examine the EC effect for the eRHIC electron operation a comparison is also made among eRHIC and the two Low Energy Rings of B-factories. See Table 2.4.4-11.

The major cures include:

- a vacuum ante-chamber
- coating of the chamber with TiN or NEG
- installation of solenoid coils

The first two measures may reduce the electron cloud density by a factor 3~10. The solenoids field (20~30 Gauss) also prove to be a very effective method to suppress the electron cloud effects in low energy rings of B-Factories [7][8]. The eRHIC lepton ring will adopt the ante-chamber concept with proper coatings in vacuum system designs and the solenoid coils can be the backup solution.

	B-factory parameters	eRHIC scaling factor over B-F parameters
N_b	~ 1E11	1~2
L_{sep}	~ 2.5 m	~ 4
σ_x	~ 0.8 mm	~ 1
σ_y	~ 0.12 mm	~ 3
E	3.1~3.5 GeV	~ 1.5~3
C	2200~3100 m	1.7 ~ 2.4

Table 2.4.4- 11 Scaling ECE effects in positron operation of eRHIC

It appears that the electron cloud effects in positron mode will not be stronger than those in today's B-factories, mainly due to the longer bunch spacing and higher beam energy in eRHIC. By taking the necessary measures mentioned above, the electron could effects in positron operation will be under control. The more detailed numerical simulations are underway.

In conclusion, we have made preliminary investigations of the major expected instabilities through analytical calculations, simulations, and scaled performance from the other lepton machines, mainly B-factories. These estimates indicate that good engineering design and feedback can limit the instabilities to a similar or lower level than the B-factories at similar energy.

References:

1. T. Ieiri, et al., Impedance Measurements in the KEKB, EPAC 2000, Vienna, Austria (2000)
2. R. Rimmer, J. Bird, D. Li, Comparison of calculated, measured, and beam sampled impedances of a higher-order-mode-damped rf cavity, Physical Review Special Topics, Volume 3, 102001(2000)
3. PEP-II, an Asymmetric B Factory: A Conceptual Design Report, SLAC-R-418(1993)
4. KEKB B-factory Design Report, KEK Report 95-7(1995)
5. T. Raubenheimer and F. Zimmermann, Physical Review E 52, no.5, p.5487(1995)
6. M. Zisman, S. Chattopadhyay, J. Bisognano, ZAP User's Manual, LBL-21270(1986)
7. J. T. Seeman, Invited Talk in Super B-Factory Workshop in Hawaii, Honolulu, Jan. 19~22, 2004(2004)
8. J. Flanagan, Invited talk in Super B-Factory Workshop in Hawaii, Honolulu, Jan. 19 ~22, 2004(2004)
9. A. Chao, M. Tigner, Handbook of Accelerator Physics and Engineering, World Scientific(1999)
10. F. Zimmermann, G, Rumolo, APAC 2001, 352(2001)
11. K. Ohmi, F. Zimmermann, Physical Review Letters 85, 3821(2000)
12. D. H. Rubin, et al., CESR Status and Performance, PAC 2001, Chicago, 3520(2001)

2.4.5 Beam-Beam Issues

Overview

The beam-beam interaction is one of the most fundamental limitations of colliding beam storage rings. In the eRHIC collider, the beam-beam interaction varies depending on beam energy, colliding particle species, beam current, emittance, and other parameters, and can be quite different under different experimental scenarios. We work from the basic premise that: when the beam-beam interaction is weak, the luminosity performance is mainly dependent on single beam parameters of the e-ring or the RHIC ring; when beam-beam interactions are strong, beam-beam interaction can cause beam blowup, and coherent beam-beam oscillations are likely to be the major obstacle to reaching high luminosity. The following issues are discussed below in addition to the preliminary simulation worked presented in the next section.

Beam-beam interaction, interpretation

The eRHIC collider is similar in nature to HERA except for operating in a different range of center of mass energy and with much higher luminosity. In HERA the proton bunch intensity is ~10^{11}, which is comparable to RHIC proton beam intensity. But the electron beam current is limited by available RF power to about 58 mA. Therefore a weak-strong model can be applied to simulations. In the eRHIC electron ring, beam energy is only one third that of HERA, so that RF power does not limit beam current. The design beam intensity is 0.45A, about 10 times higher than HERA. And even higher beam intensities are under consideration to generate higher luminosity. Therefore, in many of the eRHIC collision scenarios both the lepton and the hadron beam-beam tune shift limits can be reached. In this case quasi strong-strong or strong-strong models of collision for simulation will be the more accurate tools.

Coherent beam-beam limit (asymmetric collider)

A distinguishing difference of the eRHIC from the existing colliders is the asymmetric circumference of the two colliding rings. The different and smaller circumference of the e–ring permits freedom of design optimization and substantial cost saving. However, coherent beam-beam interactions for the asymmetrical system may limit its performance and must be carefully accounted for. According to reference [1], the instability region of a 1:3 asymmetric e+e- ring collider compared to a symmetric one is about 30% larger with a beam-beam parameter of 0.03. In the present case we have a more complicated collision pattern and our beam-beam tune shift limit is much higher.

Weak radiation damping at low electron beam energy

Operating the electron ring at low energy (5GeV) significantly reduces synchrotron radiation damping, which will reduce the electron beam-beam tune shift limit to half. Measures to increase the damping at low electron energy are discussed in section 2.4.3.

Luminosity reduction from hourglass effect

The minimum proton beam bunch length is limited by the heat load on the cryogenic system for RHIC [2], and is considered to be ~20 cm at present. This sets a limit on minimum β^* for both hadron and lepton beams due to the luminosity reduction caused by hourglass effects.

Beam-beam effect on polarization

There were observations in HERA operation [3]. And will be an important issue here. Initial simulations have been done with a weak-strong mode and with linear lattice. That allows us to make a quick evaluation of possible maximum tune shift limits to select the appropriate working point.

Beam-Beam Simulations with Linear Lattice

RHIC is currently operating with beams colliding in four of its six interaction points, where beam-beam tune shift parameters exceeding $\xi x = 0.005$ per IP have been achieved. It is therefore expected to be safe to assume the same beam-beam parameter for the eRHIC IP, especially since it is most likely that by the time eRHIC is operational the number of actual RHIC IPs will be reduced.

To investigate the feasibility of beam-beam interactions with nominal beam-beam tune shift parameters as high as $\xi x = 0.025, \xi y = 0.08$ in the eRHIC electron ring, simulation studies have been performed [4]. In these simulations, the accelerator is represented by a linear one-turn matrix. The tunes of this one-turn matrix are scanned in the range below the quarter resonance to determine the best working point. Synchrotron radiation damping and quantum excitation is included, currently based on an older lattice version that did not produce the emittances required for the interaction region parameters presented here. However, these simulations can nevertheless be considered useful at the present design stage. As a first step, the hadron bunch intensity was lowered suh that a vertical beam-beam tune shift of $,\xi y = 0.05$ was achieved, which is the design value of the KEK B-Factory. With a radiation damping time corresponding to 1740 revolutions in the eRHIC electron ring, no beam blow-up and resulting luminosity degradation is observed over a wide tune range around Qx = .10, Qy = .15, as shown in Figure 2.4.5-1. It should however be emphasized here that due to the lack of a consistent lattice solution, the dynamic emittance effect caused by the modification of the H function,

$$H(s) = \gamma(s)\eta^{2}(s) + 2\alpha(s)\eta(s)\eta(s) + \beta(s)\eta^{,2}(s), \qquad \textbf{(2.4.5-1)}$$

by the presence of a strong beam-beam lens could not be taken into account. Since these effects are mainly observed for tunes very close to the integer or half-integer, this is not expected to significantly alter the results.

Since the nominal hadron bunch intensity had to be lowered by about 40 percent compare to what is routinely accelerated in RHIC to limit the electron beam-beam tune shift to $\xi y = 0.05$, we studied the effect of the eRHIC design beam-beam parameter, $\xi x = 0.025$, $\xi y = 0.08$, as it results from the regular RHIC bunch intensity of $1.0 \cdot 10^{11}$ protons per bunch. As Figure 2.4.5-2 indicates, there are still large areas in the working diagram where the resulting luminosity is 95% of the nominal geometric value.

These results still have to be checked by full 6D tracking, including lattice nonlinearities and realistic machine imperfections. This work is currently in progress.

Electrons:	
ring circumference [m]	1278
geometric emittance hor./vert. [nm]	53/9.5
β functions hor./vert. [m]	0.19/0.27
particles/bunch	$6.7 \cdot 10^{10}$
beam-beam tune shift hor./vert.	0.025/0.08
damping times hor./vert./long. [turns]	1740/1740/870
Hadrons:	
ring circumference [m]	3834
geometric emittance hor./vert. [nm]	9.5/9.5
β functions hor./vert. [m]	1.04/0.27
particles/bunch	$8.2 \cdot 10^{10}$ (p),
	$1.0 \cdot 10^{9}$ (Au)
beam-beam tune shift hor./vert.	0.005/0.005
luminosity [$cm^{-2}sec^{-1}$]	$2.7 \cdot 10^{32}$

Table 2.4.5- 1: Parameter table.

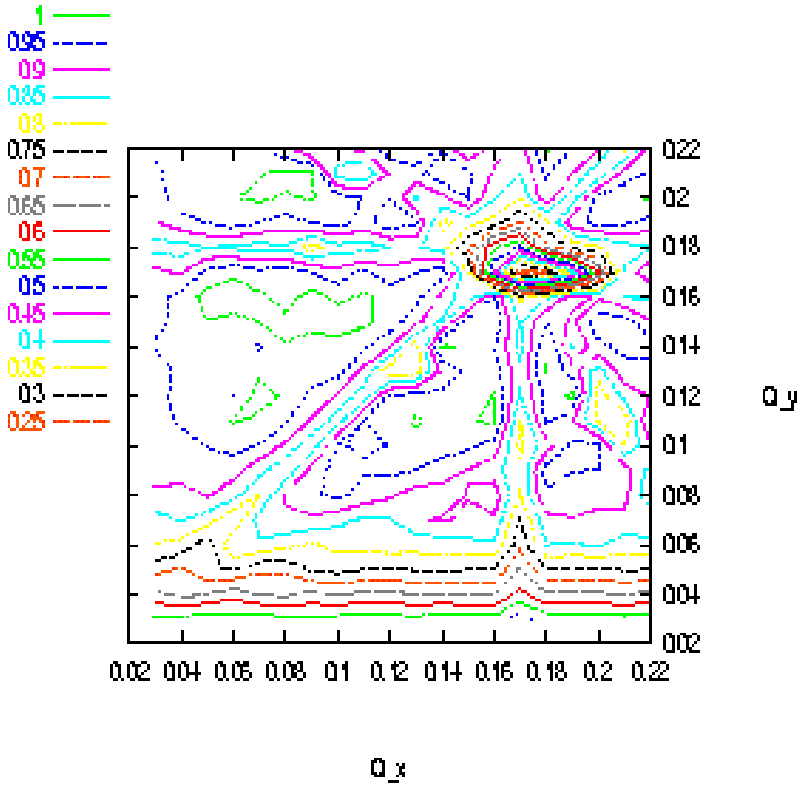

Figure 2.4.5- 1: Beam-beam contour plot for nominal beam-beam tune shift parameters of $\xi x = 0.015$, $\xi y = 0.05$..

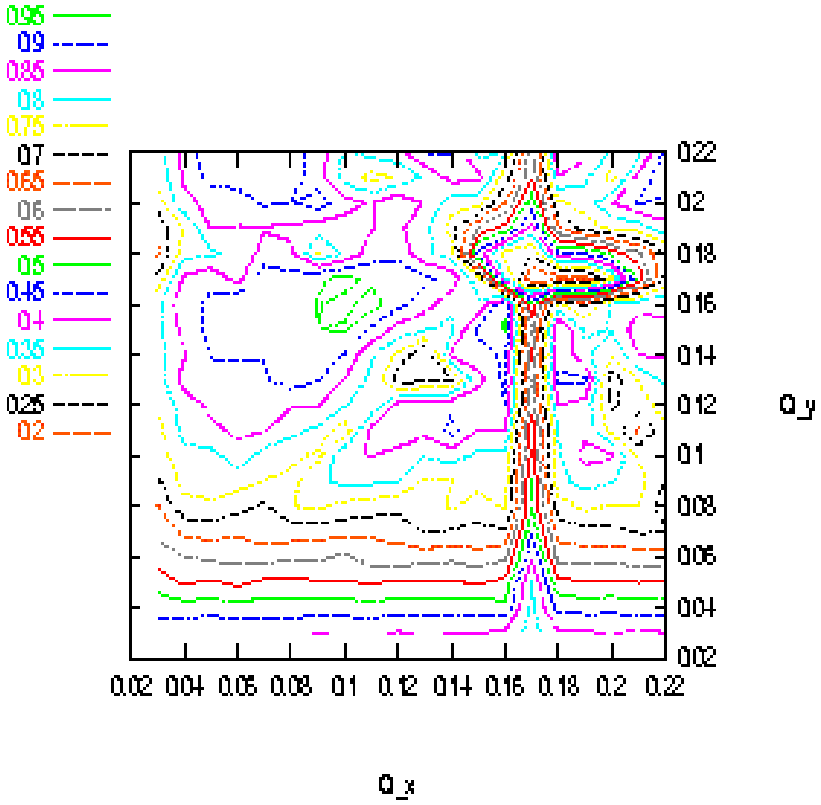

Figure 2.4.5- 2: Beam-beam contour plot for $\xi x = 0.025, \xi y = 0.08$, which corresponds to a proton bunch population of $1.0 \cdot 10^{11}$/bunch.

References:

1. K. Hirata and E. Keil "Coherent beam-beam interaction limit in asymmetric ring colliders", CERN/LEP-TH/89-54.
2. I. Ben-Zvi at al. "Accelerator physics issues in eRHIC", NIM A 463(2001) 94-117.
3. M. Bieler at al., "Recent and past experiences with beam-beam effects at HERA", LHC99 beam-beam workshop.
4. C. Montag, Proceedings of the 30th Advanced ICFA Beam Dynamics Workshop on high Luminosity e+e- Collisions, Stanford, 2003

2.4.6 Beam Polarization

Spin Polarization – an Overview

Before describing concepts for attaining electron and positron spin polarization for eRHIC we present a brief overview of the theory and phenomenology. We can then draw on this later as required. This overview is necessarily brief but more details can be found in [1, 2].

Self polarization

The spin polarization of an ensemble of spin-$\frac{1}{2}$ fermions with the same energies traveling in the same direction is defined as

$$\vec{P} = \left\langle \frac{2}{\hbar}\vec{\sigma} \right\rangle \qquad \textbf{(2.4.6- 1)}$$

where $\vec{\sigma}$ is the spin operator in the center of mass and $\langle\rangle$ denotes the expectation value for the mixed spin state. We denote the single particle center–of–mass expectation value of $\frac{2}{\hbar}\vec{\sigma}$ by $\vec{S}$ and we call this the "spin". The polarization is then the average of $\vec{S}$ over an ensemble of particles such as that of a bunch of particles.

Relativistic $e^{\pm}$ circulating in the (vertical) guide field of a storage ring emit synchrotron radiation and a tiny fraction of the photons can cause spin flip from up to down and vice versa. However, the up–to–down and down–to–up rates differ, with the result that in ideal circumstances the electron (positron) beam can become spin polarized anti–parallel (parallel) to the field, reaching a maximum polarization, $P_{\rm st}$, of $\frac{8}{5\sqrt{3}}$ = 92.4%. This, the Sokolov–Ternov (S–T) polarizing process, is very slow on the time scale of other dynamical phenomena occurring in storage rings, and the inverse time constant for the exponential build up is [3]:

$$\tau_{\rm st}^{-1} = \frac{5\sqrt{3}}{8}\frac{r_{\rm e}\gamma^5\hbar}{m_{\rm e}\left|\rho\right|^3} \qquad \textbf{(2.4.6- 2)}$$

where $r_{\rm e}$ is the classical electron radius, γ is the Lorentz factor, ρ is the radius of curvature in the magnets and the other symbols have their usual meanings. The time constant is usually in the range of a few minutes to a few hours.

However, even without radiative spin flip, the spins are not stationary but precess in the external fields. In particular, the motion of $\vec{S}$ for a relativistic charged particle traveling in electric and magnetic fields is governed by the Thomas–BMT equation $d\vec{S}/ds = \vec{\Omega}\times\vec{S}$ where s is the distance around the ring [2, 4]. The vector $\vec{\Omega}$ depends on the electric $(\vec{E})$ and magnetic $(\vec{B})$ fields, the energy and the velocity $\vec{v}$ which evolves according to the Lorentz equation:

$$\vec{\Omega} = \frac{e}{m_{\rm e}c}\left[-\left(\frac{1}{\gamma}+a\right)\vec{B} + \frac{a\gamma}{1+\gamma}\frac{1}{c^2}\left(\vec{v}\cdot\vec{B}\right)\vec{v} + \frac{1}{c^2}\left(a+\frac{1}{1+\gamma}\right)\left(\vec{v}\times\vec{E}\right)\right] \qquad \textbf{(2.4.6- 3)}$$

$$= \frac{e}{m_{\rm e}c}\left[-\left(\frac{1}{\gamma}+a\right)\vec{B}_{\perp} - \frac{g}{2\gamma}\vec{B}_{\parallel} + \frac{1}{c^2}\left(a+\frac{1}{1+\gamma}\right)\left(\vec{v}\times\vec{E}\right)\right]. \qquad \textbf{(2.4.6- 4)}$$

Thus $\vec{\Omega}$ depends on s and on the position of the particle $u \equiv (x, p_x, y, p_y, l, \delta)$ in the 6–D phase space of the motion. The coordinate δ is the fractional deviation of the energy from the energy of a synchronous particle ("the beam energy") and l is the distance from the center of the bunch. The

coordinates x and y are the horizontal and vertical positions of the particle relative to the reference trajectory and (except in solenoids) $p_x = x'$ and $p_y = y'$ are their conjugate momenta. The quantity g is the appropriate gyromagnetic factor and $a = (g-2)/2$ is the gyromagnetic anomaly. For $e^{\pm}$, $a \approx 0.0011596$. $\vec{B}_{\parallel}$ and $\vec{B}_{\perp}$ are the magnetic fields parallel and perpendicular to the velocity.

In a simplified picture the majority of the photons in the synchrotron radiation do not cause spin flip but tend instead to randomize the $e^{\pm}$ orbital motion in the (inhomogeneous) magnetic fields. Then, if the ring is insufficiently well geometrically aligned and/or if it contains special magnet systems like the "spin rotators" needed to produce longitudinal polarization at a detector (see below), the spin–orbit coupling embodied in the Thomas–BMT equation can cause spin diffusion, i.e. depolarization. Compared to the S–T polarizing effect the depolarization tends to rise very strongly with beam energy. The equilibrium polarization is then less than 92.4% and will depend on the relative strengths of the polarization and depolarization processes. As we shall see later, even without depolarization certain dipole layouts can reduce the equilibrium polarization to below 92.4 %.

Analytical estimates of the attainable equilibrium polarization are best based on the Derbenev–Kondratenko (D–K) formalism [5, 6]. This implicitly asserts that the value of the equilibrium polarization in an $e^{\pm}$ storage ring is the same at all points in phase space and is given by

$$P_{\mathrm{dk}} = \mp \frac{8}{5\sqrt{3}} \frac{\oint ds \left\langle \frac{1}{|\rho(s)|^3} \hat{b} \cdot \left(\hat{n} - \frac{\partial \hat{n}}{\partial \delta} \right) \right\rangle_s}{\oint ds \left\langle \frac{1}{|\rho(s)|^3} \left(1 - \frac{2}{9} (\hat{n} \cdot \hat{s})^2 + \frac{11}{18} \left(\frac{\partial \hat{n}}{\partial \delta} \right)^2 \right) \right\rangle_s} \qquad \textbf{(2.4.6- 5)}$$

where $\langle\ \rangle_s$ denotes an average over phase space at azimuth s, $\hat{s}$ is the direction of motion and $\hat{b} = (\hat{s} \times \dot{\hat{s}}) / |\dot{\hat{s}}|$. $\hat{b}$ is the magnetic field direction if the electric field vanishes and the motion is perpendicular to the magnetic field. $\hat{n}$ is a unit 3–vector field over the phase space satisfying the Thomas–BMT equation along particle trajectories $u(s)$ (which are assumed to be integrable) and it is 1–turn periodic: $\hat{n}(u; s + C) = \hat{n}(u; s)$ where C is the circumference of the ring.

The field $\hat{n}(u; s)$ is a key object for systematizing spin dynamics in storage rings. It provides a reference direction for spin at each point in phase space and it is now called the *"invariant spin field"* [2, 7, 8]. At zero orbital amplitude, i.e. on the periodic ("closed") orbit, the $\hat{n}(0; s)$ is written as $\hat{n}_0(s)$. For $e^{\pm}$ rings and away from spin–orbit resonances (see below), $\hat{n}$ is normally at most a few milliradians away from $\hat{n}_0$.

A central ingredient of the D–K formalism is the implicit assumption that the $e^{\pm}$ polarization at each point in phase space is parallel to $\hat{n}$ at that point. In the approximation that the particles have the same energies and are traveling in the same direction, the polarization of a bunch measured in a polarimeter at s is then the ensemble average

$$\vec{P}_{\mathrm{ens,dk}}(s) = P_{\mathrm{dk}} \left\langle \vec{n} \right\rangle_s . \qquad \textbf{(2.4.6- 6)}$$

In conventional situations in $e^{\pm}$ rings, $\langle \hat{n} \rangle_s$ is very nearly aligned along $\hat{n}_0(s)$. The *value* of the ensemble average, $P_{\mathrm{ens,dk}}(s)$, is essentially independent of s.

Equation 2.4.6-5 can be viewed as having three components. The piece

$$P_{\text{bk}} = \mp\frac{8}{5\sqrt{3}}\frac{\oint ds\left\langle \frac{1}{\left|\rho(s)\right|^3}\hat{b}\cdot\hat{n}\right\rangle_s}{\oint ds\left\langle \frac{1}{\left|\rho(s)\right|^3}\left(1-\frac{2}{9}(\hat{n}\cdot\hat{s})^2\right)\right\rangle_s} \approx \mp\frac{8}{5\sqrt{3}}\frac{\oint ds\frac{1}{\left|\rho(s)\right|^3}\hat{b}\cdot\hat{n}_0}{\oint ds\frac{1}{\left|\rho(s)\right|^3}\left(1-\frac{2}{9}n_{0s}^2\right)} \qquad \textbf{(2.4.6- 7)}$$

gives the equilibrium polarization due to radiative spin flip. The quantity n_{0s} is the component of $\hat{n}_0$ along the closed orbit. The subscript "bk" is used here instead of "st" to reflect the fact that this is the generalization by Baier and Katkov [9, 10] of the original S–T expression to cover the case of piecewise homogeneous fields. Depolarization is then accounted for by including the term with $\frac{11}{18}\left(\frac{\partial\hat{n}}{\partial\delta}\right)^2$ in the denominator. Finally, the term with $\frac{\partial\hat{n}}{\partial\delta}$ in the numerator is the so-called kinetic polarization term. This results from the dependence of the radiation power on the initial spin direction and is not associated with spin flip. It can normally be neglected but is still of interest in rings with special layouts.

In the presence of radiative depolarization the rate in Eq. 2.4.6- 2 must be replaced by

$$\tau_{\text{dk}}^{-1} = \frac{5\sqrt{3}}{8}\frac{r_{\text{e}}\gamma^5\hbar}{m_{\text{e}}}\frac{1}{C}\oint ds\left\langle \frac{1}{\left|\rho(s)\right|^3}\left(1-\frac{2}{9}(\hat{n}\cdot\hat{s})^2+\frac{11}{18}\left(\frac{\partial\hat{n}}{\partial\delta}\right)^2\right)\right\rangle_s \qquad \textbf{(2.4.6- 8)}$$

This can be written in terms of the spin-flip polarization rate, τ_{bk}^{-1}, and the depolarization rate, τ_{dep}^{-1}, as:

$$\frac{1}{\tau_{\text{dk}}} = \frac{1}{\tau_{\text{bk}}} + \frac{1}{\tau_{\text{dep}}}\ , \qquad \textbf{(2.4.6- 9)}$$

where

$$\tau_{\text{dep}}^{-1} = \frac{5\sqrt{3}}{8}\frac{r_{\text{e}}\gamma^5\hbar}{m_{\text{e}}}\frac{1}{C}\oint ds\left\langle \frac{1}{\left|\rho(s)\right|^3}\frac{11}{18}\left(\frac{\partial\hat{n}}{\partial\delta}\right)^2\right\rangle_s \qquad \textbf{(2.4.6- 10)}$$

and

$$\tau_{\text{bk}}^{-1} = \frac{5\sqrt{3}}{8}\frac{r_{\text{e}}\gamma^5\hbar}{m_{\text{e}}}\frac{1}{C}\oint ds\left\langle \frac{1}{\left|\rho(s)\right|^3}\left(1-\frac{2}{9}(\hat{n}\cdot\hat{s})^2\right)\right\rangle_s \qquad \textbf{(2.4.6- 11)}$$

The time dependence for build–up from an initial polarization P_0 to equilibrium is

$$P(t) = P_{\text{ens,dk}}\left[1-e^{-t/\tau_{\text{dk}}}\right] + P_0 e^{-t/\tau_{\text{dk}}}. \qquad \textbf{(2.4.6- 12)}$$

In perfectly aligned $e^{\pm}$ storage rings containing just horizontal bends, quadrupoles and accelerating cavities, there is no vertical betatron motion and $\hat{n}_0(s)$ is vertical. Since the spins do not "see" radial quadrupole fields and since the electric fields in the cavities are essentially parallel to the particle motion, $\hat{n}$ is vertical, parallel to the guide fields and to $\hat{n}_0(s)$ at all u and s. Then the derivative $\frac{\partial\hat{n}}{\partial\delta}$ vanishes and there is no depolarization. However, real rings have misalignments. Then there is

vertical betatron motion so that the spins also see radial fields which tilt them from the vertical. Moreover, $\hat{n}_0(s)$ is also tilted and the spins can couple to vertical quadrupole fields too. As a result $\hat{n}$ becomes dependent on u and "fans out" away from $\hat{n}_0(s)$ by an amount which usually increases with the orbit amplitudes. Then in general $\frac{\partial \hat{n}}{\partial \delta}$ no longer vanishes in the dipoles (where $1/|\rho|^3$ is large) and depolarization occurs. In the presence of skew quadrupoles and solenoids and in particular in the presence of spin rotators, $\frac{\partial \hat{n}}{\partial \delta}$ can be non–zero in dipoles even with perfect alignment. The deviation of $\hat{n}$ from $\hat{n}_0(s)$ and the depolarization tend to be particularly large near to the spin–orbit resonance condition

$$\nu_{\text{spin}} = k_0 + k_I \nu_I + k_{II} \nu_{II} + k_{III} \nu_{III}. \qquad \textbf{(2.4.6- 13)}$$

Here $k_0, k_I, k_{II}, k_{III}$ are integers, $\nu_I, \nu_{II}, \nu_{III}$ are the three tunes of the synchrobetatron motion and ν_{spin} is the spin tune on the closed orbit, i.e. the number of precessions around $\hat{n}_0(s)$ per turn, made by a spin on the closed orbit[1]. In the special case, or in the approximation, of no synchrobetatron coupling one can make the associations: $I \to x$, $II \to y$ and $III \to s$, where, here, the subscript s labels the synchrotron mode. In a simple flat ring with no closed orbit distortion, $\nu_{\text{spin}} = a\gamma_0$ where γ_0 is the Lorentz factor for the nominal beam energy. For $e^{\pm}$, $a\gamma_0$ increments by 1 for every 441 MeV increase in beam energy. In the presence of misalignments and special elements like rotators, ν_{spin} is usually still approximately proportional to the beam energy. Thus an energy scan will show peaks in τ_{dep}^{-1} and dips in $P_{\text{ens,dk}}(s)$, namely at the resonances. Examples can be seen in figure 2.4.6-3 below. The resonance condition expresses the fact that the disturbance to spins is greatest when the $|\vec{\Omega}(u;s) - \vec{\Omega}(0;s)|$ along an orbit is coherent ("in step") with the natural spin precession. The quantity $(|k_I| + |k_{II}| + |k_{III}|)$ is called the order of the resonance. Usually, the strongest resonances are those for which $|k_I| + |k_{II}| + |k_{III}| = 1$, i.e. the first order resonances. The next strongest are usually the so-called *"synchrotron sideband resonances"* of parent first order resonances, i.e. resonances for which $\nu_{\text{spin}} = k_0 \pm \nu_{I,II,III} + \tilde{k}_{III} \nu_{III}$ where $\tilde{k}_{III}$ is an integer and mode III is associated with synchrotron motion. All resonances are due to the non–commutation of successive spin rotations in 3–D and they therefore occur even with purely linear orbital motion.

We now list some keys points.

- The approximation in the second row of Eq. 2.4.6- 7 makes it clear that if there are dipole magnets with fields not parallel to $\hat{n}_0$, as is the case, for example, when spin rotators are used, then P_{bk} can be lower than the 92.4% achievable in the case of a simple ring with no solenoids and where all dipole fields and $\hat{n}_0(s)$ are vertical.

- If, as is usual, the kinetic polarization term makes just a small contribution, the above formulae can be combined to give

$$P_{\text{ens,dk}} \approx P_{\text{bk}} \frac{\tau_{\text{dk}}}{\tau_{\text{bk}}}. \qquad \textbf{(2.4.6- 14)}$$

  From Eq. 2.4.6- 9 it is clear that $\tau_{\text{dk}} \leq \tau_{\text{bk}}$.

- The underlying rate of polarization due to the S–T effect, τ_{bk}^{-1}, increases with the fifth power

[1] In fact the resonance condition should be more precisely expressed in terms of the so-called amplitude dependent spin tune [2, 7, 8]. But for typical $e^{\pm}$ rings, the amplitude dependent spin tune differs only insignificantly from ν_{spin}.

of the energy and decreases with the third power of the bending radii.

- It can be shown that as a general rule the "normalized" strength of the depolarization, $\tau_{\mathrm{dep}}^{-1} / \tau_{\mathrm{bk}}^{-1}$, increases with beam energy according to a tune dependent polynomial in even powers of the beam energy.

Pre–polarization

Instead of relying on self polarization, for e^- one can inject a pre–polarized beam. The polarized e^- are supplied by a gallium arsenide source and then accelerated to full energy in a linear accelerator. Gallium arsenide sources can provide polarizations of 80%. Acceleration in a recirculating device is also possible provided measures are taken to avoid depolarization when accelerating through resonances. The CEBAF machine at the Thomas Jefferson National Accelerator Facility is an example of such a device. These matters are discussed in other sections. It would be necessary to inject the pre-polarized e^- at full energy since it is unlikely that the polarization would survive resonance crossing during acceleration in the ring itself.

Since no simple polarized sources exist for e^+, a pre–polarized e^+ beam would have to be polarized by the S–T effect in a dedicated preceding ring.

To avoid an immediate loss of polarization in the recipient ring, the polarization vector should lie along the $\hat{n}_0$ vector at the injection point. In that case the subsequent time dependence is given by Eq. 2.4.6- 12. Note that if the injected polarization is higher than the $P_{\mathrm{ens,dk}}$, the polarization will *fall* to this value with the characteristic time τ_{dk}. Furthermore, if the injected polarization has the "wrong" sign, the S–T effect will drive the polarization through zero and into the natural direction. Again, the characteristic time will be τ_{dk} and the final value will be $P_{\mathrm{ens,dk}}$. Injecting a pre–polarized beam is the only solution if the required energy of the stored beam is so low that τ_{bk} is impractically large. It is also useful if the lifetime of the stored beam is small: full polarization is immediately available while the luminosity is still high.

Software

There are two classes of computer algorithm for estimating the equilibrium polarization in real $e^{\pm}$ rings:

(i) Methods based on evaluating $\hat{n}$ and $\left(\frac{\partial \hat{n}}{\partial \delta}\right)^2$ in the D–K formula given the ring layout and magnet strengths; and

(ii) A more pragmatic approach in which particles and their spins are tracked while photon emission is simulated approximately within a Monte–Carlo framework and τ_{dep} is "measured". Eqs. 2.4.6- 9 and 2.4.6- 14 then provide an estimate of τ_{dk} and the equilibrium polarization. The programs SITROS [11] and SLICKTRACK [12] exemplify this approach.

The class (i) algorithms are further divided according to the degree of linearization of the spin and orbital motion:

(ia) The SLIM family (SLIM [13, 14], SLICK [15], SITF [11]) and SOM [16] and ASPIRRIN [17]. The last two utilize approximate versions of the "*betatron–dispersion*" formalism [1]

and all are based on a linearization of the orbital and spin motion. For spin, the linearization involves assuming that the angle between $\hat{n}$ and $\hat{n}_0$ is small at all positions in phase space so that $\hat{n}$ can be approximated by the form $\hat{n}(u;s) \approx \hat{n}_0(s) + \alpha(u;s)\hat{m}(s) + \beta(u;s)\hat{l}(s)$. The unit vectors $\hat{m}$ and $\hat{l}$ are 1–turn periodic and chosen so that the set $\{\hat{n}_0, \hat{m}, \hat{l}\}$ is orthonormal. It is assumed that $\sqrt{\alpha^2 + \beta^2} \ll 1$. This approximation reveals just the first order spin–orbit resonances and it breaks down when $\sqrt{\alpha^2 + \beta^2}$ becomes large very close to these resonances.

(ib) SMILE [6]: Linearized orbital motion but "full" spin motion using a high order perturbation theory.

(ic) SODOM [18]: Linearized orbital motion but full spin motion expressed by a Fourier expansion.

Note that the precise evaluation of $\hat{n}$ and $\left(\frac{\partial \hat{n}}{\partial \delta}\right)^2$ requires calculating beyond the linear approximation. Then large amounts of computer power are needed, especially if a large number of resonances must be taken into account. Thus the calculations presented here are based on a class (ia) algorithm, in particular that in SLICK. This executes very quickly and it furnishes valuable first impressions, even though it can only exhibit the first order resonances. At a later stage results from SLICKTRACK based on a class (ii) algorithm and full spin motion will be available. Then the influence of higher order resonances will be seen. This kind of algorithm also allows the effect of non–linear orbital motion and the beam–beam interaction to be studied. The class (ii) algorithm is mathematically much simpler than the class (i) algorithm but it still requires a large amount of computing power for the simulation for long enough of the motion of enough particles and their spins.

Spin rotators

The eRHIC project, like all analogous projects involving spin, needs longitudinal polarization at the interaction point. However, if the S–T effect is to be the means of making or maintaining the polarization, then as is clear from Eq. 2.4.6- 7, $\hat{n}_0$ must be close to vertical in most of the dipoles. We have seen at Eq. 2.4.6- 6 that the polarization is essentially parallel to $\hat{n}_0$. So to get longitudinal polarization at a detector, it must be arranged that $\hat{n}_0$ is longitudinal at the detector but vertical in the rest of the ring. This can be achieved with magnet systems called spin rotators which rotate $\hat{n}_0$ from vertical to longitudinal on one side of the detector and back to vertical again on the other side. Eq. 2.4.6- 7 shows that $P_{\rm bk}$ essentially scales with the cosine of the angle of tilt of $\hat{n}_0$ from the vertical in the arc dipoles. Thus a rotation error resulting in a tilt of $\hat{n}_0$ of even a few degrees would not reduce $P_{\rm bk}$ by too much. However, as was mentioned above, a tilt of $\hat{n}_0$ in the arcs can lead to depolarization and calculations show that tilts of more than about a degree produce significant depolarization. Thus well tuned rotators are essential for maintaining polarization even if the beam is pre–polarized before injection.

Suppression of depolarization – spin matching

Although the S–T effect offers a convenient way to obtain stored high energy $e^{\pm}$ beams, it is only useful in practice if there is not too much depolarization. Depolarization can also limit the usefulness of beams pre–polarized before injection: $\tau_{\rm dk}$ must be large enough to ensure that the large injected polarization survives until it is safe to switch on the sensitive parts of the detector after injection and survives long enough for collecting enough data in the detector. Depolarization can be significant if

the ring is misaligned, if it contains spin rotators or if it contains uncompensated solenoids or skew quadrupoles. Then if $P_{\mathrm{ens,dk}}$ and/or τ_{dk} are too small, the layout and the optic must be adjusted so that $\left(\frac{\partial \hat{n}}{\partial \delta}\right)^2$ is small where $1/|\rho|^3$ is large. So far it is only possible to do this within the linear approximation for spin motion. This technique is called "*linear spin matching*" and when successful, as for example at HERA [19], it immediately reduces the strengths of the first order spin–orbit resonances. Spin matching requires two steps: "*strong synchrobeta spin matching*" is applied to the optics and layout of the perfectly aligned ring and then "*harmonic closed orbit spin matching*" is applied to soften the effects of misalignments. This latter technique aims to adjust the closed orbit so as to reduce the tilt of $\hat{n}_0$ from the vertical in the arcs. Since the misalignments can vary in time and are usually not sufficiently well known, the adjustments are applied empirically while the polarization is being measured.

Spin matching must be approached on a case by case basis. An overview can be found in [1]. Spin matching for eRHIC will discussed later.

Higher order resonances

Even if the beam energy is chosen so that first order resonances are avoided and in linear approximation $P_{\mathrm{ens,dk}}$ and/or τ_{dk} are expected to be large, it can happen that that beam energy corresponds to a higher order resonance. In practice the most intrusive higher order resonances are those for which $\nu_{\mathrm{spin}} = k_0 \pm \nu_k + \tilde{k}_s \nu_s \, (k \equiv I, II \text{ or } III)$. These synchrotron sideband resonances of the first order parent resonances are due to modulation by energy oscillations of the instantaneous rate of spin precession around $\hat{n}_0$. The depolarization rates associated with sidebands of isolated parent resonances $\left(\nu_{\mathrm{spin}} = k_0 \pm \nu_k\right)$ are related to the depolarization rates for the parent resonances. For example, if the beam energy is such that the system is near to a dominant ν_y resonance we can approximate τ_{dep}^{-1} in the form

$$\tau_{\mathrm{dep}}^{-1} \propto \frac{A_y}{\left(\nu_{\mathrm{spin}} - k_0 \pm \nu_y\right)^2} \,. \qquad \textbf{(2.4.6- 15)}$$

This becomes

$$\tau_{\mathrm{dep}}^{-1} \propto \sum_{\tilde{k}_s=-\infty}^{\infty} \frac{A_y B_y\left(\zeta; \tilde{k}_s\right)}{\left(\nu_{\mathrm{spin}} - k_0 \pm \nu_y + \tilde{k}_s \nu_s\right)^2}$$

if the synchrotron sidebands are included. The quantity A_y depends on the beam energy and the optics and is reduced by spin matching. The proportionality constants $B_y\left(\zeta; \tilde{k}_s\right)$ are called *enhancement factors*, and they contain modified Bessel functions $I_{|\tilde{k}_s|}(\zeta)$ and $I_{|\tilde{k}_s|+1}(\zeta)$ which depend on the *modulation index* $\zeta = (a\gamma_0\sigma_\delta/\nu_s)^2$. More formulae can be found in [20].

Thus the effects of synchrotron sideband resonances can be reduced by doing the spin matches described above. Note that these formulae are just meant as a guide since they are approximate and explicitly neglect interference between the first order parent resonances. To get a complete impression, the Monte–Carlo simulation mentioned earlier must be used. The sideband strengths generally increase with the energy spread and the beam energy.

Spin Polarization in eRHIC

Choice of rotators

For rings like eRHIC two kinds of rotator can be considered: "*solenoid rotators*" and "*dipole rotators*". The current design employs solenoid rotators. Dipole rotators will be mentioned later.

Various layouts of rotators involving solenoids can be conceived [21, 22, 23]. The layout considered for eRHIC is sketched in figure 2.4.6-1. The vertical $\hat{n}_0$ in the arc is rotated by 45 degrees towards the horizontal by the longitudinal field of the first solenoid. A second solenoid completes the rotation into the horizontal plane. The vector $\hat{n}_0$ is then rotated from the radial direction towards the longitudinal direction by a string of horizontally bending dipoles. The orbital deflection required is $90/a\gamma_0$ degrees.

After the interaction point a string of dipoles of reverse polarity rotates $\hat{n}_0$ back to the radial direction and two solenoids with polarity opposite to that of the first two rotate $\hat{n}_0$ back to the vertical. Then $\hat{n}_0$ is vertical in the arcs at all energies. If a solenoid rotates $\hat{n}_0$ by 45 degrees, then for $e^{\pm}$ the plane of the transverse particle distribution is rotated by about 22.5 degrees so that the rotator can generate strong transverse orbital coupling.

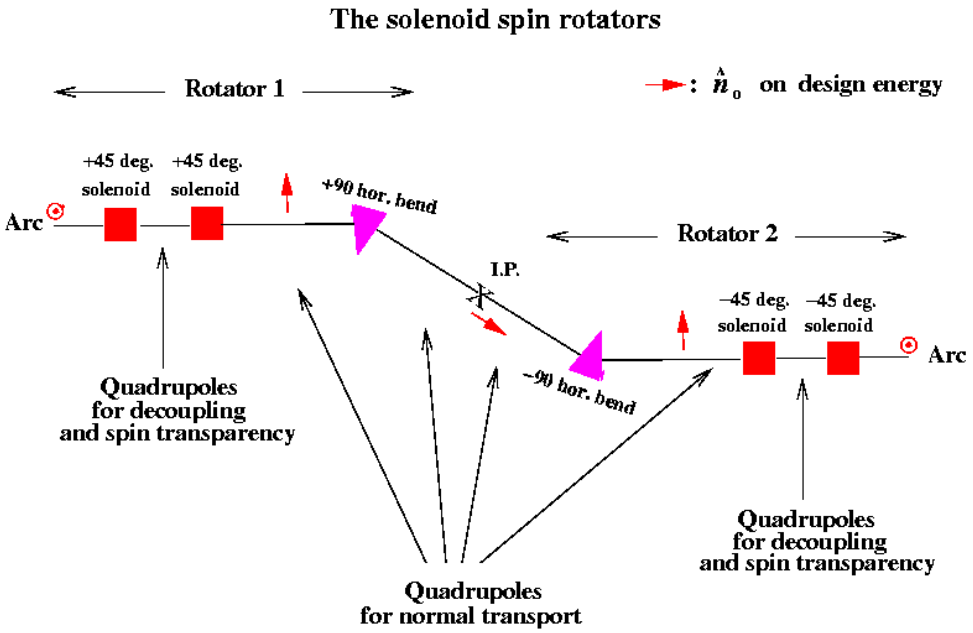

Figure 2.4.6- 1: The schematic layout of the solenoid rotators. Only the positions and functions of the key elements are shown. Each rotator consists of two solenoids and horizontal bend magnets, to rotate $\hat{n}_0$ into (or out of) the longitudinal direction. Quadrupoles tuned to ensure transverse decoupling and spin transparency w.r.t. x and x' are placed between each solenoid in each rotator. Antisymmetric horizontal bends very near the interaction point are not shown.

However, this coupling can be eliminated by correctly choosing the strengths and positions of quadrupoles placed within the first pair of solenoids and within the last pair (Figure 2.4.6- 1). The orbital motion between the first and second pair of solenoids is uncoupled and the quadrupole strengths in that region can be chosen as required.

Some advantages and disadvantages of solenoid rotators are:

Advantages:

- The arrangement is compact.
- In contrast to the dipole rotators discussed later, no vertical orbit excursion is needed.
- The sign of the longitudinal component of the equilibrium polarization at the interaction point can be reversed by simply changing the polarities of all the solenoids.

Disadvantages:

- The polarization is longitudinal at just one beam energy and that energy is defined by the field integrals of the horizontally bending dipoles on each side of the interaction point. Any remedy for this restriction would require elaborate engineering involving moving the solenoids. However, if it is planned to run eRHIC just around 10 GeV, say in the range 9.69 to 10.13 GeV $\left(\Rightarrow 22 \leq a\gamma_0 \leq 23\right)$, $\hat{n}_0$ will always be within about 2 degrees of the beam direction.
- By the Thomas–BMT equation the rate of spin precession in a solenoid is inversely proportional to the beam energy. So solenoid spin rotators are only practical at low energy. At 10 GeV each solenoid needs a field integral of about 26.7 Tm and must therefore be superconducting.
- The solenoids cause transverse coupling which must be eliminated by introducing special quadrupole arrangements. Solenoid spin rotators are also not automatically spin transparent (see below).

A corresponding list of advantages and disadvantages for dipole rotators is given later.

The horizontal dispersion should be zero on entry to the first solenoid and at the exit from the last and the horizontal dispersion is set to zero at the interaction point.

Spin matching with the solenoid rotators

To explain the spin matching conditions needed when the solenoid rotators are used we begin by considering a flat, perfectly aligned ring without the rotators, the detector and the oncoming proton beam. In this case there is no vertical closed orbit distortion and the radiation damping together with the absence of vertical dispersion ensure that the beam has essentially zero thickness. Then as explained earlier, $\hat{n}_0$ is vertical and $\hat{n}(u;s)$ is vertical at all u and all s. The derivative $\frac{\partial \hat{n}}{\partial \delta}$ is then zero and there is no depolarization.

However, the solenoids have radial end fields which can tilt spins from the vertical and the longitudinal fields tilt spins step–wise into and out of the horizontal plane so that they then precess in the vertical fields of the quadrupoles inside and between the rotators. Inside a rotator, they also precess in the radial quadrupole fields at the non-zero y induced by the first solenoid of a pair.

Moreover, the total angle of rotation in the two solenoids of a rotator is ± 90 degrees only at $\delta = 0$. Since $\hat{n}(u;s)$ is a functional of the geometry and optics of the ring we see that unless special measures are taken, the solenoid rotators will cause $\hat{n}$ to depend on u and s. Then $\frac{\partial \hat{n}}{\partial \delta}$ will not vanish in the dipoles in the arcs and there will be depolarization.

The remedy is to make the section from the entrance of the first rotator to the exit of the second rotator "*spin transparent*", i.e. to choose the strengths and positions of quadrupoles and dipoles in this section so that in the approximation of linearized spin motion, the total rotation of a spin around and w.r.t. $\hat{n}_0$ vanishes for a spin beginning with arbitrary u and traversing this section. We have already mentioned that we eliminate the generation of transverse coupling by the solenoids with the aid of quadrupoles placed within the solenoid pairs. It then turns out that spin transparency w.r.t. x and x' can be arranged in addition, and in a straightforward way, by setting these quadrupoles such that the 4×4 transfer matrix for the transverse motion through a pair has the form [21]

$$\begin{pmatrix} 0 & -2r & 0 & 0 \\ 1/2r & 0 & 0 & 0 \\ 0 & 0 & 0 & 2r \\ 0 & 0 & -1/2r & 0 \end{pmatrix} \qquad \textbf{(2.4.6- 16)}$$

where r is the radius of orbit curvature in the longitudinal field of a solenoid and where the elimination of coupling is explicit. The optic between the rotators should be uncoupled. Since the integral of the solenoid fields vanishes for the whole region, at first order there is no net spin perturbation resulting from non–zero δ in the solenoids. Moreover, the constraints on the horizontal dispersion and the layout of the dipoles around the interaction point ensure that the change in direction of the horizontal dispersion, due to quadrupole fields, vanishes for the stretch between the second and third solenoids. Thus there is transparency w.r.t. longitudinal motion too [1]. Providing that the constraints on the dispersion are satisfied, the optic between the second and third solenoids can be chosen at will independently of the need to ensure spin transparency, once the matrices for the rotators have the form just given. So far it has not been necessary to consider spin transparency w.r.t. y and y' since in the perfectly aligned ring and with transverse coupling restricted to the rotators themselves, synchrotron radiation in the arcs does not excite vertical motion. Then $y = 0$ and $y' = 0$ on entering a rotator from the arc. With these conditions it is easy to show that with linearized spin motion and perfect alignment, $\frac{\partial \hat{n}}{\partial \delta}$ indeed vanishes at all dipoles in the arcs [1]. We say that the ring is spin matched at each dipole in the arcs.

Thus although an isolated solenoid is not spin transparent, we have a very elegant way to ensure sufficient overall spin transparency of the whole rotator insertion. Moreover, from the above discussion about the requirements for the optic in the stretch between the second and third solenoids, it is clear that the depolarizing effects from beam-beam forces should be suppressed. The same probably applies to the detector field if it can be prevented from generating coupling. These count among the advantages of such solenoid spin rotators.

Note that our spin matching conditions do not ensure that $\frac{\partial \hat{n}}{\partial \delta}$ vanishes in the dipoles between the rotators. Moreover, since $\hat{n}_0$ is horizontal in the vertical fields of those dipoles, Eq. 2.4.6- 7 implies that P_{bk} can be lower than 92.4%. However, this lowering of P_{bk} can be limited by making the

dipoles long enough to ensure that their $\int ds\,/\,|\rho(s)|^3$ is small compared to that in the arcs. We return to these two points below.

Calculations of the $e^{\pm}$ polarization in eRHIC

Following this lengthy introduction we now present first calculations of the polarization. The calculations are carried out with the thick lens code SLICK. This accounts for just the first order spin–orbit resonances. No account is taken of the magnetic field of the detector and there is no beam–beam force from oncoming protons. The horizontal and vertical betatron phase advances in the arc cells are 72 and 60 degrees respectively and the fractional parts of the betatron tunes are $[\nu_x] = 0.105$ and $[\nu_y] = 0.146$. The synchrotron tune, ν_s, is 0.044. SLICK automatically produces the correct transverse and longitudinal emittances.

Figure 2.4.6- 2 shows the equilibrium polarization for the perfectly aligned ring in the range 9.25 to 10.58 GeV. With these rotators the spin tune, $\nu_{\rm spin}$, on the design orbit is $a\gamma_0$. Thus this energy range corresponds to $21 \le \nu_{\rm spin} \le 24$, i.e. it spans three full integers. It is seen that $P_{\rm bk}$ (labeled as S–T Polarization) is almost independent of energy at about 84.3%. It is below 92.4% because $\hat{n}_0$ is perpendicular to the fields in the dipoles around the interaction point. Recall Eq. 2.4.6- 7. The actual polarization, $P_{\rm dk}$ (labeled as Total Polarization), is about 81.7%. The additional decrease of about 2.6% is due to the depolarization caused by the non–zero $\left(\frac{\partial \hat{n}}{\partial \delta}\right)^2$ in those dipoles. It is interesting that although there is some depolarization, this depolarization shows no resonant structure. This can be understood in terms of some 1–turn integrals appearing in the calculation of $\frac{\partial \hat{n}}{\partial \delta}$ [1]. When these integrals are evaluated starting somewhere in the arc, they are zero because of the spin matching. At resonance these integrals are independent of the starting point. Then they are zero starting at the dipoles around the interaction point and the factors A_x and A_s analogous to the A_y of Eq. 2.4.6- 15, vanish at resonance.

As stated earlier, misalignments can lead to depolarization. In fact experience shows that misalignments can be very dangerous and that care should be invested in the alignment of the ring and measurement of the orbit. Care is also needed for realistic simulations. Figure 2.4.6- 3 shows results of calculations of equilibrium polarizations with SLICK for typical realistic misalignments and after orbit correction. Figure 2.4.6- 4 shows the corresponding $\tau_{\rm bk}$ and $\tau_{\rm dk}$. The $\tau_{\rm bk}$ exhibits the characteristic γ_0^{-5} dependence. At 9.91 GeV ($a\gamma_0$ = 22.5) $\tau_{\rm bk}$ and $\tau_{\rm dk}$ are about 21 and 20 minutes respectively. At 5 GeV $\tau_{\rm bk}$ would be about 11 hours. In that case self polarization would not be practical and a pre-polarised beam would be needed. Otherwise the average $1/|\rho|^3$ would have to be greatly increased [24].

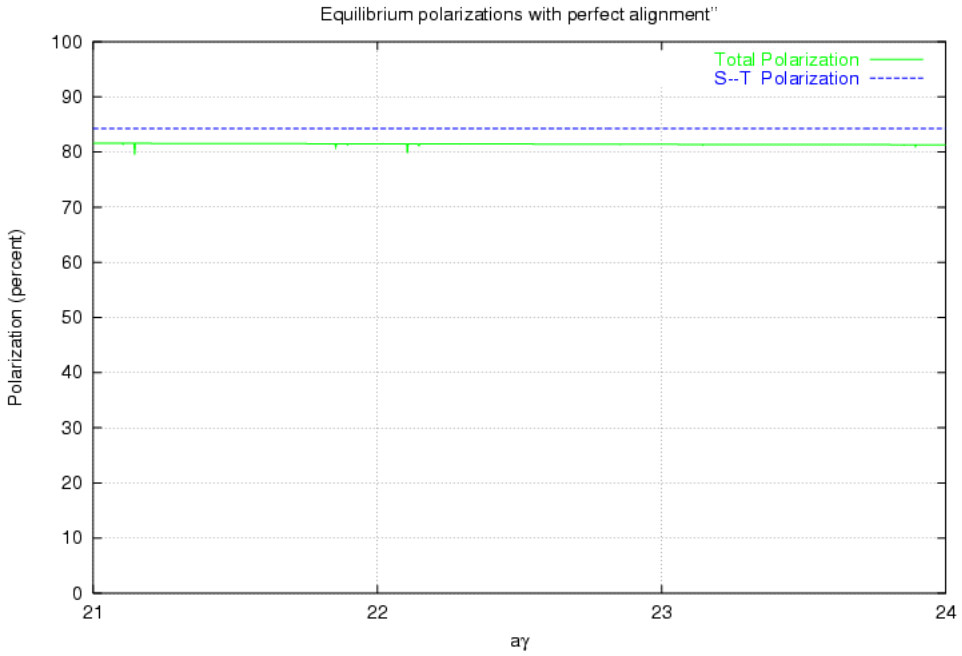

Figure 2.4.6- 2: The polarizations $P_{\rm bk}$ and $P_{\rm dk}$ for a perfectly aligned ring containing a spin transparent pair of solenoid spin rotators.

The misalignments include vertical shifts and roll on the quadrupoles, roll on the dipoles and errors on the beam position monitors. Scale errors on the quadruple strengths are also included. A monitor and horizontal and vertical correction coils are assigned to each quadrupole. Figure 2.4.6- 3 shows five curves: $P_{\rm bk}$ (labeled as S–T Polarization), $P_{\rm dk}$ (bold and labeled as Total Polarization), and each of the polarizations that would be reached if just one orbital mode were excited. The first order resonances are clearly visible and can easily be identified using the known values of $[\nu_x]$, $[\nu_y]$ and ν_s. Note that the ν_s resonances are so strong that they overlap around integer values of $\nu_{\rm spin}$ [2]. In this simulation the peak values of $P_{\rm dk}$ are about 81.5% and occur near half integer values of $\nu_{\rm spin}$. This is characteristic behavior and shows that the beam energy should be set for such values. It is also clear, as usual, that the fractional parts of the orbital tunes should be as far away from 1/2 as is practical to "leave space" around half integer spin tune. It might then be the case that the synchrotron sideband resonances are weak at the recommended energies. This conjecture will be checked at a later stage using a class (ii) simulation. Different choices of the random numbers specifying the imperfections lead to curves which differ in detail from those in figures 2.4.6- 3 and 2.4.6- 4. However, the curves remain qualitatively similar. Before orbit correction the polarization is very small.

In this simulation the tilt of $\hat{n}_0$ in the arcs is about 2.5 milliradians at the maxima of $P_{\rm dk}$. The r.m.s. vertical deviation of the closed orbit from the design machine plane is 0.034 mm after the orbit correction mentioned above. The maximum deviation is 0.18 mm. Such small residual closed orbit deviations might look optimistic but realistic misalignments have been assumed and these small residuals arise naturally with the orbit correction algorithm used here. Moreover, the problem of

[2] But for this first order calculation $\tau_{\rm dk}$ does *not* vanish at integer values of $\nu_{\rm spin}$: there are no 'integer resonances' in $\tau_{\rm dk}^{-1}$. However, the S–T effect becomes very weak at integer values of $\nu_{\rm spin}$ as $\hat{n}_0$ tilts strongly from the vertical in the arcs.

obtaining very small residual closed orbit deviations has been conquered for modern synchrotron radiation sources. Note that the closed orbit deviations remain small and the peak polarizations remain high even if a random sample of 20% of the monitors is taken out of service. In any case the sensitivity of the polarization to such small deviations shows that *it would be a false economy to skimp on good alignment of the ring, on the provision of correction magnets and on the precision of the beam position monitors.* One should also avoid stray fields from the proton ring and magnetic material in the beam pipe. Experience at HERA [19] supports this view.

Since the tilt of $\hat{n}_0$ is already small, harmonic closed orbit spin matching has not yet been applied. Perhaps with good enough alignment and corrections it would not be needed.

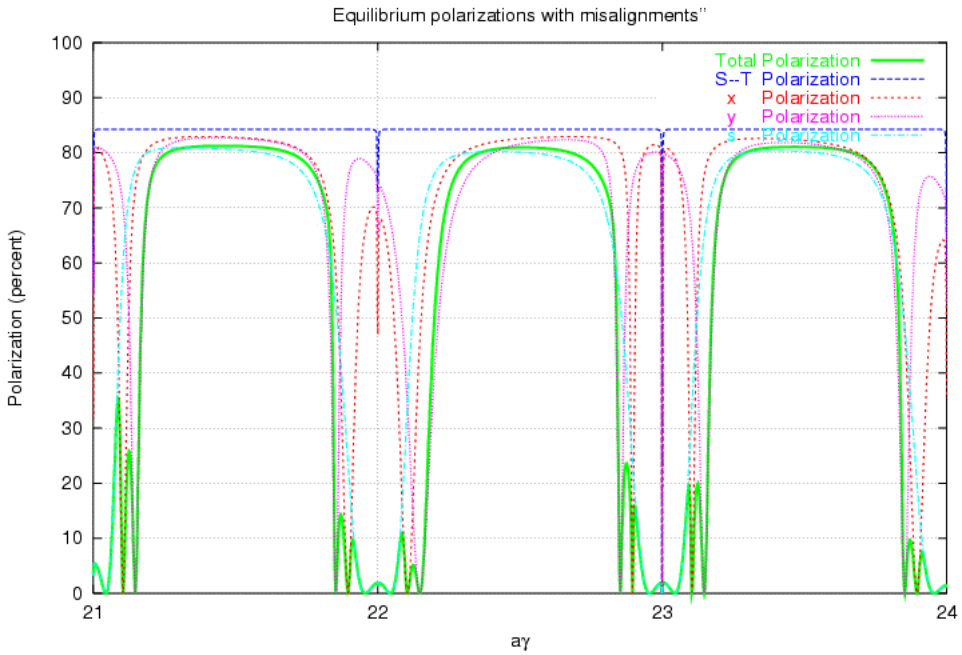

Figure 2.4.6- 3: The polarizations P_{bk} and P_{dk} and the polarizations associated with each of the three orbital modes when realistic imperfections are applied and the orbit is subsequently corrected.

The calculations carried out so far show that with linearized spin motion and in the absence of detector fields and beam-beam forces, both high equilibrium polarizations and reasonable τ_{dk} can be achieved around 10 GeV. Then operation with either self polarized $e^{\pm}$ or with pre-polarized e^{-} would be comfortable. For the latter it would be necessary to avoid loss of polarization during injection. Note that in contrast to the injection of polarized protons into a ring, e^{-} are subject to stochastic depolarization as the beam reaches equilibrium.

Although the results from linearized calculations give strong grounds for optimism, a complete picture will only emerge once full spin motion has been included as well as other effects which have been neglected so far. Some next steps in this direction are discussed below. In the meantime it is important to note that 51% longitudinal e^{+} polarization has already been achieved simultaneously at three interaction points at HERA at the almost three times higher energy of 27.5 GeV [25, 26].

To achieve high luminosity it will be necessary to mount quadrupoles inside the detector solenoid. These magnets will then be subject to large inter–magnet forces. Thus, special efforts should be invested in the stability of their mounts and the monitoring of their positions so that they do not cause excessive closed orbit distortion and resultant depolarization. Use should be made of experience with HERA [25].

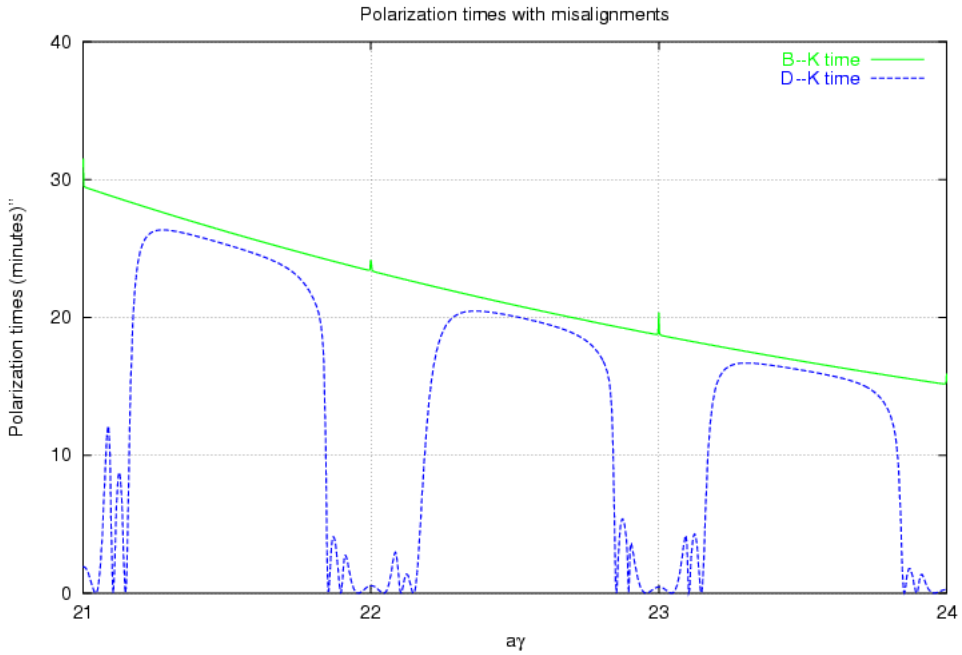

Figure 2.4.6- 4: The characteristic times τ_{bk} and τ_{dk} (minutes) for the simulation in figure 2.4.6- 3.

Some next steps

So far, it appears that with good orbit correction, harmonic closed orbit spin matching will not be needed. Nevertheless, this topic still needs to be thoroughly studied.

Since there is no simple way in standard optics software to represent the effects on the trajectories and the spins of the complicated overlapping fields of solenoids and quadrupoles, special spin–orbit maps for the interaction regions should be established. The calculations with SLICK should then be repeated using the linear parts of these maps to establish whether in linear approximation these combined fields have a significant influence on the spin transparency of the rotator section and on the polarization. The methods used for HERA could be adopted here [27, 26].

The calculations with linearized spin motion do not include the effects of higher order spin–orbit resonances. Thus, a next step will be to carry out class (ii) simulations with SLICKTRACK. This will, for example, give a picture of the strengths of the synchrotron sideband resonances and of whether there are advantages in choosing a special ν_s.

Even with misalignments the natural beam height will be very small. But as has been mentioned elsewhere, to reach high luminosity it will be necessary to increase the beam height. This might be achieved by, for example, running close to a transverse coupling resonance. Perhaps other methods

can be found. In any case experience shows that a proper picture of the polarization for such situations will require using a class (ii) simulation.

Class (ii) simulations are also essential for understanding the full effects of beam–beam forces on the polarization and the effects of non–linear orbital motion including the motion in the complicated fields in the detector.

Class (ii) simulations will also be necessary for evaluating the behavior of the polarization of a pre–polarized beam during injection.

Spin flip

As stated earlier, with the solenoid rotators the sign of the equilibrium longitudinal polarization can be changed by reversing the polarity of the solenoids. But this cannot be done while the beam is stored. However, it might still be possible to reverse the polarization on short time scales and without dumping the beam, by using resonant spin flip driven by an external radio frequency magnetic field. Note that after a reversal the polarization would return through zero to its original orientation with the characteristic time τ_{dk}. Resonant flipping of electron spins has been demonstrated at low energy [28] but it remains to be seen whether it is practical at the much higher energy of 10 GeV where spin diffusion might limit the efficiency [29, 30]. Class (ii) simulations will also provide insights here.

Further aspects of spin rotation

Although solenoid rotators have been chosen for eRHIC, dipole rotators can be kept in reserve.

The simplest kind of dipole rotator system involves just vertical bends which generate a Z shaped modification of the design orbit in the vertical plane [31, 32]. But the design orbit is then sloped at the interaction point and the detector which are just at the midpoint of the system. To reverse the sign of the equilibrium longitudinal polarization, the polarities of the vertical bends and the vertical positions of all the magnets w.r.t. the plane of the ring must be reversed. This in turn requires very flexible bellows between magnets and a mechanical jacking system for the whole interaction region including the quadrupoles very close to the detector.

A much more practical and economical solution is to use spin rotators consisting of strings of interleaved vertical and horizontal bends arranged so that they produce interleaved horizontal and vertical closed beam bumps. Such rotators stand apart from the detector and its nearby quadrupoles. According to the Thomas–BMT equation an orbit deflection of $\delta\theta_{\mathrm{orb}}$ in a transverse magnetic field produces a spin rotation of $\delta\theta_{\mathrm{spin}} = (a\gamma + 1)\,\delta\theta_{\mathrm{orb}}$. Then at high energy small orbit deflections lead to large spin rotations and although the combined orbit bumps close, $\hat{n}_0$ can be rotated from vertical to longitudinal before the interaction point. A second rotator returns $\hat{n}_0$ to the vertical before the next arc. This is the scheme successfully used at HERA [19].
Some advantages and disadvantages of this second kind of dipole scheme are:

Advantages:

- The design orbit is horizontal in the detector and the nearby surrounding quadrupoles.

- By varying the fields and the geometry of the rotators the required rotation can be achieved for a range of energies. Then the polarization can be made essentially longitudinal at any energy in the design range.

- If the rotator is sufficiently short, it need not contain quadrupoles. It is then automatically essentially spin transparent.

Disadvantages:

- As in the case of the Z bend rotator, reversal of the sign of the longitudinal polarization requires the reversal of dipole polarities, very flexible bellows and a jacking system. But in this case only the rotators themselves need jacks, not the whole interaction region. Note that such a jacking system has been in service in HERA since 1994 [19].

- At low energy the relation $\delta\theta_{\mathrm{spin}} = (a\gamma + 1)\,\delta\theta_{\mathrm{orb}}$ implies that sufficient spin rotation can only be achieved with vertical orbit bumps that might be impractically large.

- Dipole rotators can decrease P_{bk} since $\hat{n}_0$ is not parallel to the field in most of the magnets. The decrease is most marked if the magnets are short ($\Rightarrow 1/|\,\rho\,|^3$ large) in order to save space.

- The generation of vertical emittance in the vertical bends can require strong vertical betatron spin matching [1].

Dipole rotators are best suited for high energy. But it is likely that for energies around 10 GeV or above, a dipole rotator with a tolerable vertical design orbit excursion could be designed for eRHIC.

If these dipole rotators contain no quadrupoles, spin matching involves making the straight sections between the rotators spin transparent for all three modes of motion and involves making the arcs between the rotators spin transparent for vertical motion [1, 19, 27].

References:

1. D.P. Barber, G. Ripken, Handbook of Accelerator Physics and Engineering, Eds.A.W. Chao and M. Tigner, World Scientific, 2nd edition (2001).
2. Articles by D.P. Barber (some with co–authors), in proceedings of ICFA workshop “Quantum Aspects of Beam Physics”, Monterey, U.S.A., 1998, World Scientific (1999). Also as DESY Report 98–96 and at the e-print archive: physics/9901038 – physics/9901044.
3. A.A. Sokolov, I.M. Ternov, Sov. Phys. Dokl. 8(12) (1964) 1203.
4. J.D. Jackson, “Classical Electrodynamics”, 3rd edition, Wiley (1998).
5. Ya.S. Derbenev, A.M. Kondratenko, Sov. Phys. JETP. 37 (1973) 968.
6. S.R. Mane, Phys. Rev. A36 (1987) 105–130.
7. G.H. Hoffstaetter, M. Vogt, D.P. Barber, Phys. Rev. ST Accel. Beams 11 (2) 114001

(1999).
8. D.P. Barber, G.H. Hoffstaetter, M. Vogt, Proc. 14th Int. Spin Physics Symp., AIP Proc. 570 (2001).
9. V.N. Baier, V.M. Katkov, Sov. Phys. JETP. 25 (1967) 944.
10. V.N. Baier, V.M. Katkov, V.M. Strakhovenko, Sov. Phys. JETP. 31 (1970) 908.
11. J. Kewisch et al., Phys.Rev.Lett. 62(4) (1989) 419. The program SITF is part of the SITROS package.
12. D.P. Barber. SLICKTRACK is the version of SLICK [15] which includes Monte–Carlo spin–orbit tracking.
13. A.W. Chao, Nucl. Inst. Meth. 180 (1981) 29.
14. A.W. Chao, AIP Proc. 87 (1981) 395.
15. SLICK is a thick lens version of SLIM by D.P. Barber. Private notes (1982).
16. K. Yokoya, User's manual of SOM: Spin–Orbit Matching (1996).
17. C.W. de Jager, V. Ptitsin, Yu.M. Shatunov, Proc. 12th Int. Symp. High Energy Spin Physics, World Scientific (1997).
18. K. Yokoya, KEK Report 92-6 (1992).
K. Yokoya, DESY Report 99–006 (1999)
and at the e-print archive: physics/9902068.
19. D.P. Barber et al., Phys. Lett. 343B (1995) 436.
20. S.R. Mane, Nucl. Inst. Meth. A292 (1990) 52.
S.R. Mane, Nucl. Inst. Meth. A321 (1992) 21.
21. A.A. Zholents, V.N. Litvinenko, BINP (Novosibirsk) Preprint 81–80 (1981). English translation: DESY Report L–Trans 289 (1984).
22. D.P. Barber et al., DESY Report 82–76 (1982). Note that in that paper, the symbol $\vec{n}$ should be replaced with $\vec{n}_0$ to correspond with modern notation.
23. D.P. Barber et al., Particle Accelerators 17 (1985) 243. Note that in that paper, the symbol $\vec{n}$ should be replaced with $\vec{n}_0$ to correspond with modern notation.
24. V. Ptitsyn et al., Proc. 2003 IEEE Particle Accelerator Conference (PAC2003), Portland, U.S.A., (2003).
25. F. Willeke et al., Proc. 2003 IEEE Particle Accelerator Conference (PAC2003), Portland, U.S.A., (2003).
26. D.P. Barber, E. Gianfelice-Wendt, M. Berglund, Physics World, July 2003.
27. G.Z.M. Berglund, Ph.D. thesis, DESY-THESIS-2001-044 (2001).
28. V.S. Morozov et al., Phys. Rev. ST Accel. Beams (4) 104002 (2001).
29. D.P. Barber et al., Proc. 11th Int. Symp. High Energy Spin Physics, AIP Proc. 343 (1995).
30. K. Heinemann, DESY Report 97–166 (1997) and at the e-print archive: physics/9709025.
31. R. Schwitters, B.Richter, SLAC PEP Note 87 (1974).
32. J. Buon, Nucl. Inst. Meth. A275 (1989) 226.

2.4.7 RF System for the Storage Ring

Choice of Operating Radio Frequency

The choice of RF operating frequency is strongly influenced by practical considerations. First, the requirement for a storage-ring RF cavity having a large aperture, as discussed in the following, limits the choice to a small band of frequencies, between 300 and 500 MHz, for which high-power klystron RF amplifiers are commercially available. Second, the electron-ring operating frequency must be harmonically-related to the eRHIC colliding-frequency.

The highest practicable frequency is preferred in B-factory application, where high bunch-numbers and short bunch-lengths are desired for maximum luminosity. In this application, however, the bunch-number in the ring is determined by the collision frequency, and the electron bunch-length is much shorter than the ion-beam bunch length, by which the minimum β^* at the interaction point is set.

Nevertheless, higher operating frequency is still favorable for reasons such as longer Touschek life-time, and cost-effectiveness of longitudinal focusing. The frequency, therefore, is chosen to be at the upper-end of available klystron technology. For the room-temperature, copper-cavity option, it is 478.57 MHz, the 17^{th} harmonic of the collision frequency. For the super-conducting cavity option, it is 506.723 MHz, the 18^{th} harmonic of the collision frequency.

Choice of RF Cavity Type

The choice, for the type of RF cavity to use in the electron-ring system, is between cryogenic superconducting and room-temperature copper. A superconducting system has the capability of producing the requisite accelerating RF gap voltage with fewer cavities. This is important in terms of the coupled-bunch instability impedance, which is driven by the higher-order-mode (HOM) RF fields in the cavities. The HOM is proportional to the number of cavities. The number of cavities is determined by the power-handling capability of the RF input coupler. The RF power required is determined by beam loading, or the amount of input power delivered to the accelerated beam. With superconducting cavities virtually all of the input power is delivered to the beam, whereas with room-temperature cavities about one-third of the input power will be dissipated in the cavity walls. Therefore, the number of superconducting cavities can be one-third fewer than the number of room-temperature cavities. The use of superconducting cavities introduces a technological challenge: how to remove the hundreds of kilowatts of HOM power induced in the cavities by the high-current beam. The solution to this problem, for room-temperature cavities, has been demonstrated by the SLAC B-factory. The choice of cavity type is based on the high performance of the high-luminosity, high-current SLAC B-factory, using a conventional room-temperature RF system.

Room Temperature RF Cavity Design

The RF cavity design challenge is to determine the optimum cavity geometry, which simultaneously maximizes the cavity shunt impedance, at 478.57 MHz, which is important for efficient beam acceleration, while minimizing the longitudinal and transverse shunt impedances at the higher-order modes (HOM), which is important for beam stability. The high average beam current of the electron

ring, with beam in a large number of RF buckets, makes the minimization of HOM shunt impedances crucial to successful operation.
The cavity geometry for the eRHIC must provide for a large aperture, through which HOMs are coupled from the cavity into the beam pipe. The cavity profile must be consistent with maximizing the separation between the TM010 fundamental mode, at 478.57 MHz, and the next lowest azimuthally-symmetric (monopole) transverse magnetic (TM) modes. All of these TM modes, other than the TM 010, and all cavity dipole modes are above the corresponding mode cut-off frequencies in the beam pipe.

To minimize HOM impedance, the number of cavities must be minimized, and they must be single-cell, rather than multiple-cell, the type used in PETRA/DESY. As a consequence, the single-cell cavities must operate with higher voltage gradient to produce the required gap voltage and power delivered to the beam.

Optimization of cavity geometry will require a series of computations which analyze cavity modes as a function of cavity shape, making use of the RF computer codes URMEL-Tcode (triangle-mesh version) and Superfish, and analysis of cavity temperature-profiles and thermal-mechanical stress, at nominal dissipated RF power, using MAFIA, in a thermal model, with ANSYS code.

A cavity shape similar to that of the SLAC B-factory, can be used, as shown in Figure 2.4.7-1. The RF system can meet all requirements using 10 klystrons, driving 20 cavities, in the electron ring for eRHIC. The RF system parameters are summarized in Table 2.4.7-1.

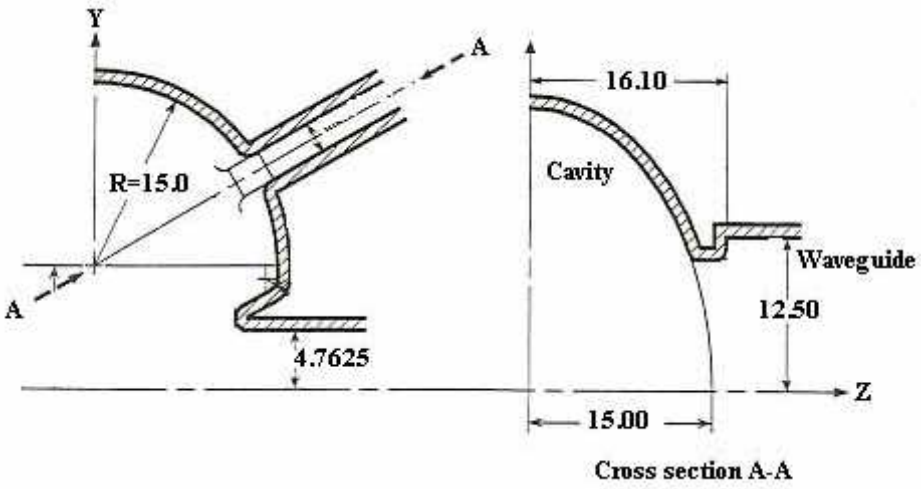

Figure 2.4.7-1 Schematic of a quadrant of the SLAC B-Factory (dim are cm).

RF Operating Frequency	478.57 MHz
Harmonic Number	2040
Gap Voltage, V	25 MV
Beam Current, I	450 mA
Energy Loss/Turn	11.7 MeV
Shunt Impedance/Cavity, R_s	3.5 MΩ
Number of Klystrons	14
Number of Cavities	28
Accelerating Voltage Gradient	4.15 MV/m
HOM Power (est)	100 kW
Wall Loss/Cavity	122 kW
Coupling Factor, β	1-9
Unloaded Q	30,000

Table 2.4.7-1: Electron-Ring RF System Parameters

Higher-Order Mode (HOM) Damping

In the design of accelerating cavities it is customary to maximize the shunt impedance in the fundamental mode, which maximizes the RF accelerating voltage gradient as a function of RF input power. However, in many storage rings, parasitic effects, such as the decelerating and deflecting fields arising from higher-order modes, and the transient-wake forces inside an electron bunch, can have serious cumulative effects that limit the achievable charge-per-bunch to a value well below the fundamental beam limit. In order to evaluate the overall performance of an accelerating system, including the parasitic effects, high-level computational means are required, which include the computer codes MAFIA, URMEL and ARGUS.

Two major cumulative effects are to be considered early in the design of the HOM coupler. These are the multi-bunch instabilities caused by resonant higher-order modes in the cavities, excited by the beam, and single-passage effects due to the wake-fields excited by the beam during its transit of a cavity (e.g. head-tail turbulence, bunch lengthening, and synchro-betatron resonances).

The most important performance goals in the design of a HOM damping system are broad bandwidth and the suppression of coupling to the fundamental cavity mode. Coaxial dampers are used in both normal and super-conducting particle-accelerator cavities. Aperture-coupled hollow waveguide dampers are used in multiple, usually three, to damp the degenerate mode. Suppression of coupling to the fundamental mode is provided by the cutoff characteristic of the waveguide.

The feasibility of obtaining high charge-per-bunch has been demonstrated by the SLAC B-factory RF system. An important feature of the B-factory RF system is an extremely unique waveguide HOM-damper system. It is likely that a design similar or identical to this will be chosen, due to its state-of-the-art status and present availability.

Tuner and Adjustable RF Coupler

To accommodate the high average power dissipation and wide range of beam-loading conditions, associated with the storage mode of operation, cavity tuning and coupling systems with considerable adjustability are required. The design requirements for the tuner and RF coupling systems are given in Tables 2.4.7-2,3, respectively.

Cavity Frequency	478.57 MHz
Frequency Range	3.0 MHz
Travel Range	12 cm
Tuning-Angle Precision	+/- 0.5 Deg.

Table 2.4.7-2: Cavity Tuner Specifications

Design RF Power	500 kW
Input Line	WR-2100 Waveguide
Input VSWR	≤ 1.5:1
Coupling Factor	Adjustable up to 10

Table 2.4.7-3: RF Coupling System Characteristics

Tuner Design

A cavity tuning range of 2 MHz is adequate to accommodate the expected detuning caused by beam loading effect and for frequency shift caused by thermal expansion of the cavity body, a function of RF power dissipation. Additional tuning range is required, however, to compensate for frequency shifts, as much as 200 kHz, resulting from changes in RF coupling to the cavity, and as much as 340 kHz resulting from collision frequencies for different proton (ion) energies. Consequently, the tuner is designed for greater than 2.5 MHz, centered about 478.57 MHz. A cross-sectional view of the cavity, in the plane of the tuner, is shown in Figure 2.4.7-2.

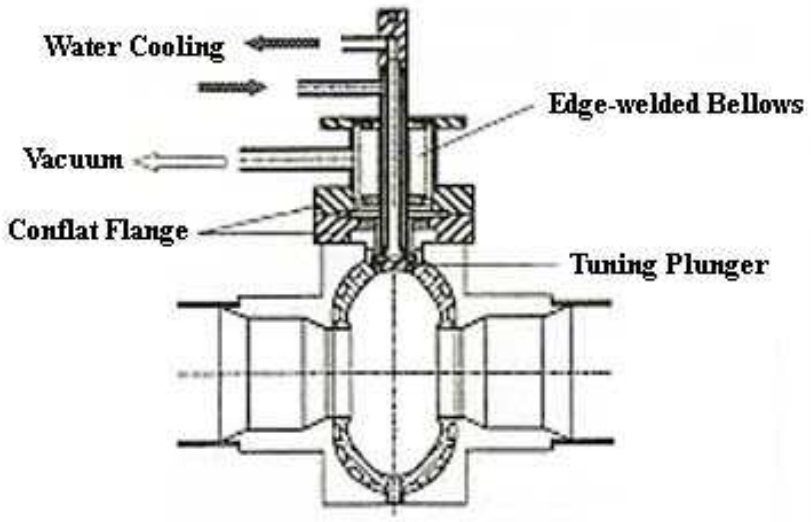

Figure 2.4.7-2: Cross section of cavity and tuner

Input RF Coupler Design

There are two types of input coupling that are appropriate for use at the 500 kW power level. The first is a rotatable loop, terminating a coaxial drive line, introduced at the cavity wall, having a coupling factor, β, adjustable between 1 and 10. The ceramic coupling window must be shielded

from the direct path of ions produced by the beam traversing the cavity. The other type of coupling is by means of an aperture. The design procedure begins with an aperture with a coupling factor of 10, and then the means of reducing the coupling factor without producing significant change in the frequency of the fundamental cavity mode (TM010). Such a means is a capacitive post, of adjustable depth of penetration, located at the first electric-field minimum of the standing-wave present in the drive-line waveguide. Such a coupler has been successfully designed, fabricated, and operated in the storage ring of the MIT Bates linear accelerator, as shown in Figures 2.4.7-3,4.

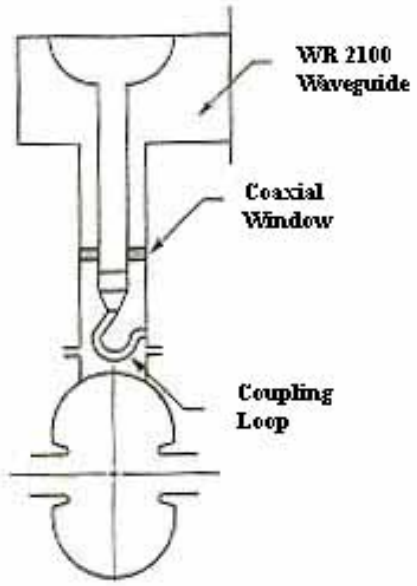

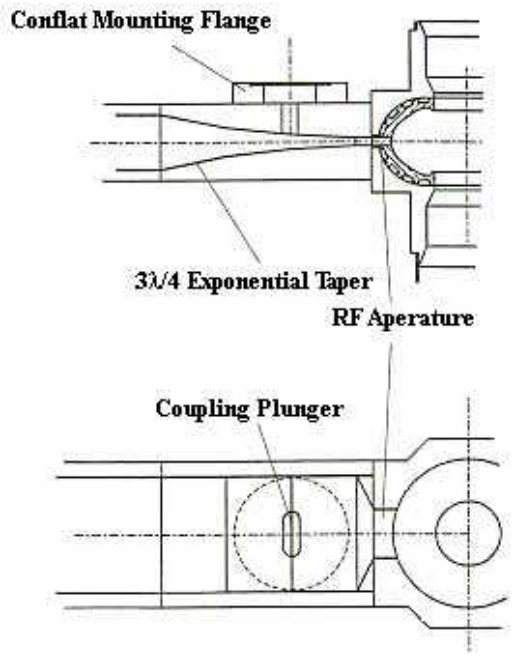

Figure 2.4.7-3 Coaxial Coupling Network **Figure 2.4.7-4** RF input waveguide and Aperture Control

Cavity Window

The cavity window must be capable of the transmission of 500 kW incident power and the RF voltage associated with the standing wave produced by significant reflected power. A coaxial ceramic-disc window, similar to the type used in the SLAC B-factory, is being designed to handle the thermal stress associated with the transmission of up to 2 MW of RF power.

High-Power RF Distribution

The high-power RF distribution system is implemented in WR-2100 rectangular waveguide, consistent with low-loss transmission of 1.2 MW CW, at 478.57 MHz. The output of each klystron is split, by means of a 3-dB, quadrature, high-power hybrid, chosen for superior power-handling capability, and directed to the inputs of two accelerating cavities. The path length from one of the two hybrid outputs is corrected by one-quarter wavelength, to compensate for the 90-degree phase-shift between hybrid outputs, producing in-phase signals at the two cavity inputs. The path between klystron output and hybrid input includes a load-isolator in the form of a four-port, differential-phase-shift, ferrite circulator. This produces a nominally matched-load condition for the klystron, enhancing

its operational stability, regardless of reflections from the cavities. To the extent that the cavity voltage (or current) reflections are matched in amplitude and phase, all of the reflected power will be dissipated in the waster load of the circulator. To the extent that the reflections are mismatched, in amplitude and phase, the reflected power will be shared by the waster load of the hybrid junction (the limiting case is equi-amplitude, quadrature-phase reflections, where all reflected power is directed to the hybrid load).

Both high-power klystrons and high-power circulators (both forward and reverse power), at 1.2 MW CW and 478.57 MHz, are within the range of commercial availability.

Low-Level RF Control System For Room-Temperature Cavities

The low-level RF control system comprises four feedback loops, as listed in Table 4, consistent with the general system performance specifications.
The overall configuration of the control loops is shown in figure 5. The gain of the klystron power amplifier is regulated by the innermost loop, which compares the input and output power levels of the klystron. The variable-attenuation capability of a PIN-diode RF modulator, inserted in the klystron input line, is used to compensate for gain changes in the klystron. A digital phase-shifter is the transducer, connected in the klystron drive line, which responds to error-signals from the phase-comparator to maintain constant transmission-phase across the klystron. Together, these two loops regulate complex klystron gain, so that the stability and performance of the cavity-voltage loop are not perturbed by parameter variations such as klystron cathode voltage and RF drive power.

The cavity resonant frequency is maintained constant by positioning a cavity tuning plunger in response to an error signal generated by comparing the phase of the RF input to the cavity with the phase of the cavity gap voltage. Cavity voltage is also down-converted in a quadrature mixer (vector demodulator and modulator), using a 478.57 MHz reference signal. The resulting in-phase (I) and quadrature (Q) signals are processed in video-bandwidth electronics, up-converted using the same 478.57 MHz reference signal, and applied to the RF drive line. The sensitivity of the down/up conversion process to variations in the amplitude of the reference signal are minimized by the use of automatic level control (ALC) prior to the mixers. The signal processing is accomplished by means of Bitmus-equipped computers, as shown in the block-diagram of the low-level RF system, Figure 2.4.7-5.

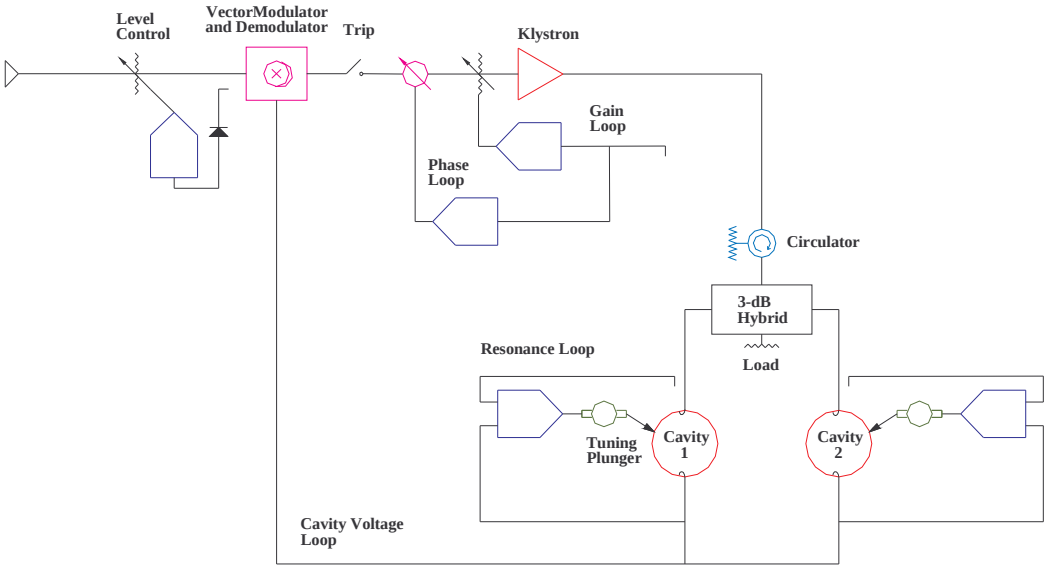

Figure 2.4.7-5: Block diagram of the low level RF system

Loop	Regulated Variable
Voltage	Cavity Voltage (Amplitude and Phase)
Resonance	Cavity Resonant Frequency
Gain	Klystron Transmission Gain
Phase	Klystron Transmission Phase

Table 2.4.7-4: Feedback Loop Function

Superconducting (SC) RF Cavity Design

The design objectives for SC cavities are no different than for room-temperature cavities: maximize the impedance and voltage gradient of the accelerating mode while minimizing the impedances for higher-order modes (HOMs). SC cavities have the advantage of high voltage-gradient (on the order of 10 MV/m, which is significantly greater than that of room-temperature cavities) and much higher values of unloaded Q, due to the greatly diminished surface losses. The high accelerating gradient allows the design of an accelerator with fewer cavities and gaps, which ameliorates the HOM problem and diminishes the sensitivity to coupled-bunch instability, just as in a room-temperature design.

The high unloaded Q permits cavity geometry with large- aperture beam holes, since R/Q is not critical, allowing HOMs to be coupled out into the beam pipes, where absorptive material can be deployed. Single-cell, spherical designs are attractive, minimizing the

number of HOMs and the required RF input-coupler power-handling capability. Each cavity is powered by its own RF source, through a load-isolating ferrite circulator, also obviating an RF distribution system. The same computer programs which aid in the design of room-temperature cavities are appropriate for the optimization of SC cavities, as the same cavity parameters are important in both cases. A Cryomodule for a superconducting cavity with HOM-ferrite absorber is shown in Figure 2.4.7-6.

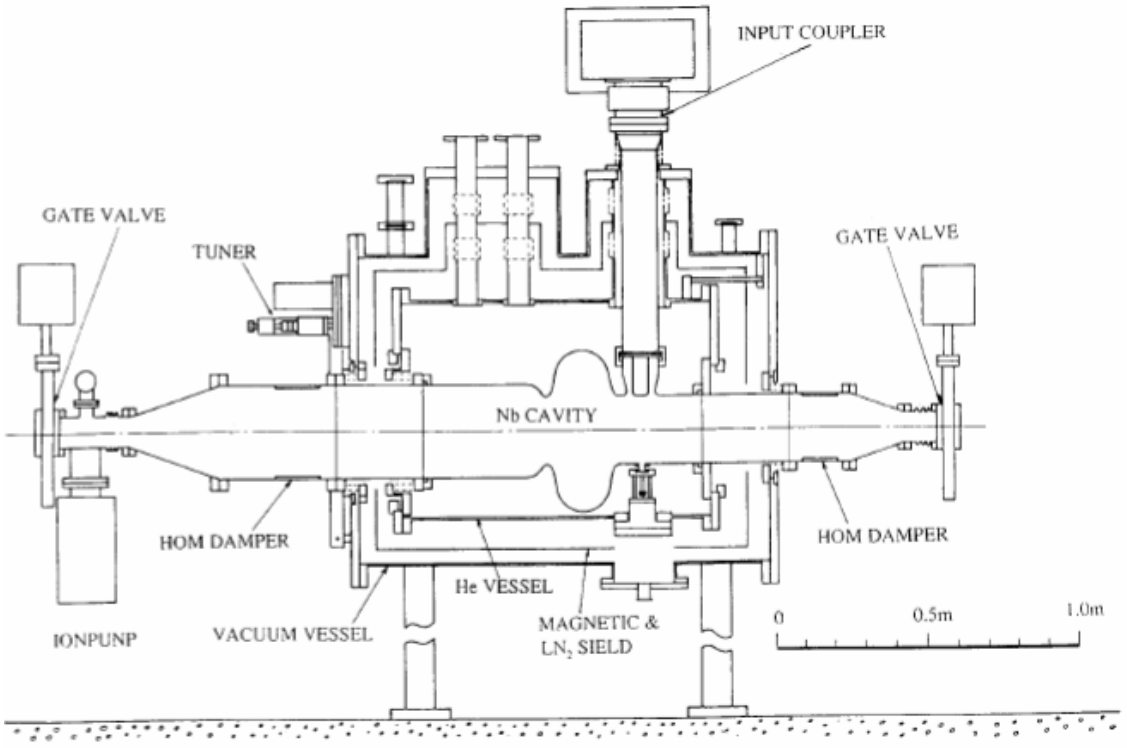

Figure 2.4.7-6: Superconducting Cavity Module KKB Factory

The RF system parameters, for an electron ring using KEKB SC cavities, are given in Table 2.4.7-5.

RF Operating Frequency	506.723 MHz
Harmonic Number	2160
Gap Voltage, V	25 MV
Beam Current, I	450 mA
Energy-Loss/Turn	11.7 MeV
R/Q	93 Ω
HOM Power (est.)	20 kW
Accelerating Voltage Gradient	~ 10 MV/m
Unloaded Q	$\geq 1 \times 10^9$
Number of Cavities	13
Number of MVEDs (Klystron or IOT)	13
Cryostat LHe Volume at 4.2 K	290 Liters
Static loss per Cryomodule at 4.2K	31 W

Table2.4.7- 5. Electron Ring (Superconducting Cavities) RF System Parameters

Higher-Order Mode (HOM) Damping

Major design issues, for a high-current accelerator, are the nature of the HOM dampers, how to remove the heat produced by the absorbed power (cryostat load) and out-gassing by the absorptive material (ion-pump load). Success has been achieved using ferrite damping material, in the shape of thin cylinders, brazed or sintered to the inside walls of the beam pipes, adjacent to the accelerating cavities. In addition, the location and geometry of the HOM dampers, which affect HOM RF field distribution in the absorptive material, power-density and temperature-rise profiles, and other characteristics, must be optimized.

Low Level RF Control System for SC Cavities

The extremely high Q and narrow bandwidth of SC cavities, compared with ambient-temperature copper cavities, causes phase and amplitude characteristics to be affected to a much higher degree by dimensional perturbations. The design of the low-level RF control system is particularly challenging, therefore, for the following reasons. First, mechanical deformation of the cavities, due to Lorentz Force, will cause cavity detuning by an amount greater than one bandwidth. Second, regardless of the required pre-detuning, in the absence of beam, the cavity resonant frequency will be modulated by unavoidable microphonically-induced mechanical forces. Third, higher stability, in the control of phase and amplitude will be required, with amplitude stability on the order of 10^{-4} and phase stability of 0.5 degrees.

The cavity resonant frequency is maintained constant by driving a Piezo-electric actuator, within each cavity, in response to an error signal generated by comparing the phase of the cavity rf input with the phase of the cavity gap voltage. Cavity voltage is also down-converted, in a quadrature mixer (vector demodulator and modulator), using a 506.723 MHz reference signal. The resulting in-phase (I) and quadrature (Q) signals are processed in video-bandwidth electronics, up-converted using the same 506.723 MHz reference signal, and applied to the RF drive line, to maintain klystron transmission gain and phase. The sensitivity of the down/up conversion process to variations in the amplitude of the reference signal is minimized by the use of automatic level control (ALC) prior to the mixers. The RF control block diagram for superconducting cavity is shown in Figure 2.4.7-7.

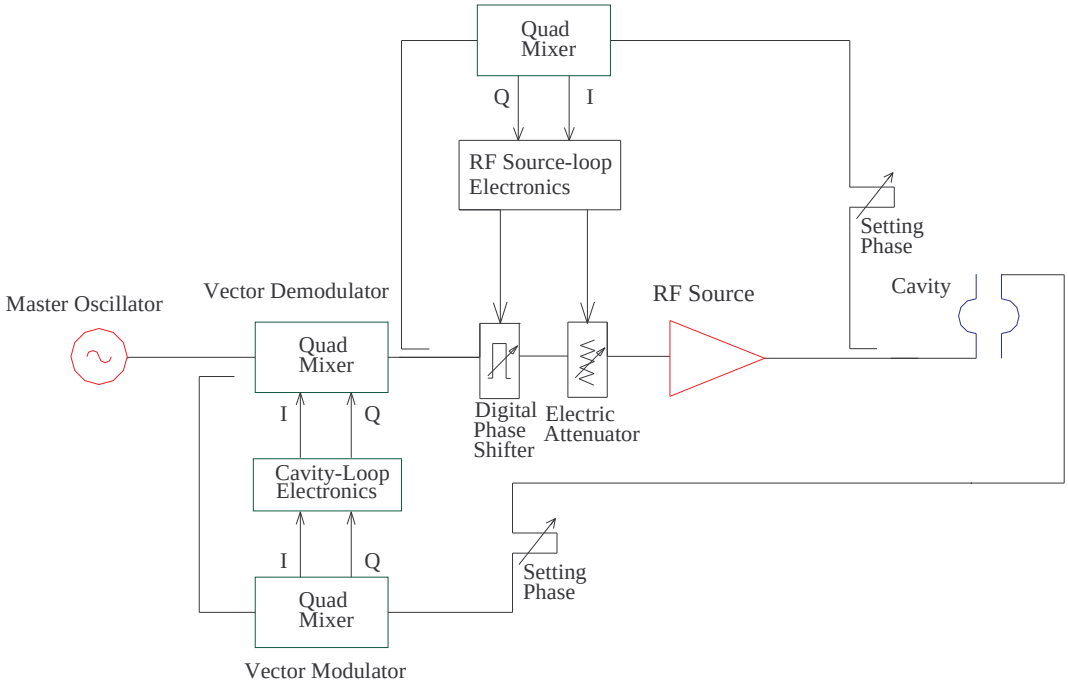

Figure 2.4.7-7: The RF control block diagram for superconducting cavity

CW RF Power Amplifier

Microwave Vacuum Electron Device (MVED) Considerations

High-power multi-cavity klystrons, capable of 1.2 MW, CW, are available from EEV, Thales, Phillips and Toshiba, but must be modified for operation at either 478.57 MHz, or 506.723 MHz, and for extended bandwidth, consistent with group-delay on the order of 100 ns. A klystron, of SLAC/CPI collaborative-design, produces 1.2 MW at 478.57 MHz, with DC beam input of 2 MW (beam voltage of 84 kVDC and beam current of 24 A), for a conversion efficiency of 60%.

DC Power Supply System

In its simplest form, the electrical part of a CW RF source is an MVED and a DC power supply. Again, the optimum (least complicated, most reliable, highest efficiency) form of such a power supply is the line-frequency, poly-phase, full-wave (typically 12-pulse) transformer-rectifier. The DC energy-storage requirements are determined by the required ripple-reduction factor, and can be either in the form of inductive or capacitive storage, or a combination of both.

Protection of the high-power MVED from internal damage resulting from the discharge of energy and electrical charge stored in shunt filter capacitance, by an electron-gun arc, is always an issue. Many RF systems, especially at MW power levels, use a triggered shunt charge-diverter, called an “electronic crowbar” for protection. The low-impedance “crowbar” diverter cannot dissipate stored energy itself, and is therefore used in conjunction with resistance, in series with the MVED cathode,

which can. This resistance also limits peak fault current, but also must dissipate continuous power during normal operation. With short-circuit current limited by resistance, the energy dissipated in the electron-gun arc is directly proportional to the total charge transport, since the voltage drop of the arc (on the order of 20 V.) is nearly constant, regardless of current amplitude (up to several thousand amperes). If stored charge is less than one Coulomb, series resistance alone can provide adequate protection, since it will dissipate all but a tiny fraction of the stored energy. Often the short-circuit "follow-on" current from the transformer-rectifier, limited by total leakage reactance to approximately 10 times normal current, will produce a greater amount of charge transport, unless it is interrupted at the first zero-crossing (1/2 cycle) by high-speed, solid-state (SCR) switchgear. In many cases, an SCR primary phase-shift voltage controller also provides the high-speed interrupt. The latest of protection means is the high-voltage, solid-state, IGBT DC-interrupting switch, in series with the MVED cathode, supplanting all other forms of protection, with insignificant charge let-through and the capability of short-duration automatic reset. Presently it is also the most expensive means of protection.

References:

1. KEKB B Factory Conceptual Design Report
2. SLACB PEP-II "An Asymmetric B-factory", Conceptual Design Report 1993
3. Shin-Ichi Kurokowa" Status of KEKB Project"
4. A. Zolfaghari et al. "Bates South Hall Ring RF Control System" 1993
5. A. Zolfaghari et al. "Design of a tuner and adjustable RF Coupler for CW 2856 MHz RF Cavity" 1991

2.5 Electron Polarimetry

The First Electron Beam Polarimeter Workshop at BNL was held on November 8, 2002 [1]. Representatives from five laboratories participated in discussions of polarimetry for an electron-ion collider. This section is based on discussions held during and following the workshop on important questions related to eRHIC polarimetry. Since a detailed design for a beam polarimeter has yet to be formulated, this section emphasizes items which require significant development or careful consideration in the design of the electron accelerator and ring.

2.5.1 Introduction

Accurate measurements of the electron polarization are essential for the experimental program at eRHIC. Measurements will be provided by polarimeters which can be separated into two categories: those which determine the beam polarization prior to injection into the electron storage ring, and those which monitor the beam polarization during storage. These two types of polarimeters provide complementary information valuable for optimizing the electron polarization and minimizing systematic errors.

The initial polarization will be established by measurements performed in the polarized source and accelerator through a combination of methods. Because the ring will be filled only infrequently, the use of methods which are destructive to the beam is acceptable in the linac. One possible scenario would include a low energy polarimeter monitor the polarization from the polarized source on a continuous basis. This can be accomplished through the well-known technique of Mott polarimetry [2] or other promising methods[3,4]. The polarization should also be periodically measured following acceleration. This can be accomplished efficiently by a Moller polarimeter which stops the beam or samples some fraction of it. Such devices are in use for highly energetic external beams at several other labs including SLAC [5] and Jefferson Lab. Overall, it should be possible to determine the electron polarization prior to injection very accurately. Details of linac polarimetry are not discussed in this report.

Because the polarization in the ring changes dynamically, it is essential to have accurate polarization measurements for the stored electron beam as a function of time. The polarization build-up time and equilibrium polarization due to synchrotron radiation has been calculated for the eRHIC design and it is essential to be able to compare to measurements to ensure that optimal performance is being achieved. It will also provide the only determination of polarization for positron beams, which will be initially unpolarized. An efficient polarimeter will provide important feedback for beam tuning in minimizing the effects of depolarizing resonances. A fast polarimeter also allows consideration of an adiabatic spin flipper for the eRHIC ring [6].

Polarimeters for the storage ring must employ a mechanism which is nondestructive to the beam. A proven method meeting this criterion is that of laser back-scattering, which entails Compton scattering of laser photons from the stored beam. This method is based on the coupling between electron (or positron) polarization and circularly polarized photons in the Compton scattering cross section. Compton polarimetry can be used to determine both longitudinal and transverse components of the beam polarization. Longitudinal polarimetry relies on the measurement of an asymmetry as a

function of the backscattered photon energy. Transverse polarimetry relies on the measurement of an azimuthal asymmetry with respect to the electron momentum in the backscattered photon flux.

At eRHIC, a longitudinal polarimeter will be located between the spin rotators in the electron-ion Interaction Region, thereby directly measuring the quantity needed for experiments. A second polarimeter in the eRHIC electron ring, located outside the spin rotators where the polarization is predominantly perpendicular to the circulation plane will measure the transverse polarization, thereby providing a consistency check which is independent of the spin rotators. This technique has been successfully employed at the HERA electron-proton collider [7,8,9], where complementary information provided by two independent polarimeters has provided important consistency checks and improved the accuracy of both measurements. A proposed layout for eRHIC polarimeters is shown in Fig. 2.5-1.

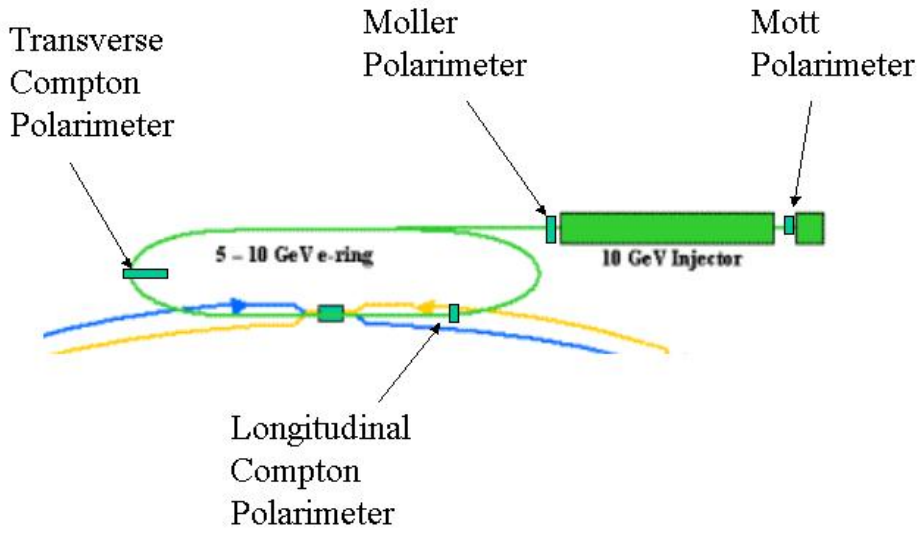

Figure 2.5 -1: Proposed locations for electron polarimeters at eRHIC.

Compton polarimetry is very effective in high energy electron storage rings for several reasons. The electromagnetic interaction can be modeled well, allowing an accurate determination of the absolute analyzing power of the polarimeter. The analyzing power for Compton scattering rises with electron energy, thereby improving the attainable statistical and systematic accuracy. In addition, increasing the energy of the electron beam also boosts the energy of backscattered photons and focuses them into a narrower kinematics cone. Both improve the ratio of signal to background, an essential consideration due to the very high intensity of eRHIC beams. Narrowing the cone of scattered photons reduces the size of detector needed. Higher energy photons can be more readily separated from the bremsstrahlung background, which is also focused in the beam direction. The electron energy at eRHIC, assuming a range of 5-10 GeV, will be sufficient to allow for accurate polarization measurements. Compton polarimeters in the Amsterdam Pulse Stretcher Ring at NIKHEF [10] and the South Hall Ring at MIT-Bates [11] have been successfully built and operated for high precision polarization experiments. Jefferson Lab [12] has also successfully operated Compton polarimeters for external beams at lower energies than eRHIC will operate.

As shown schematically in Fig 2.5-2, each Compton polarimeter at eRHIC will feature a laser system, an interaction region for the laser and electron beam, and a detector for products of Compton scattering, either backscattered photons or Compton scattered electrons.

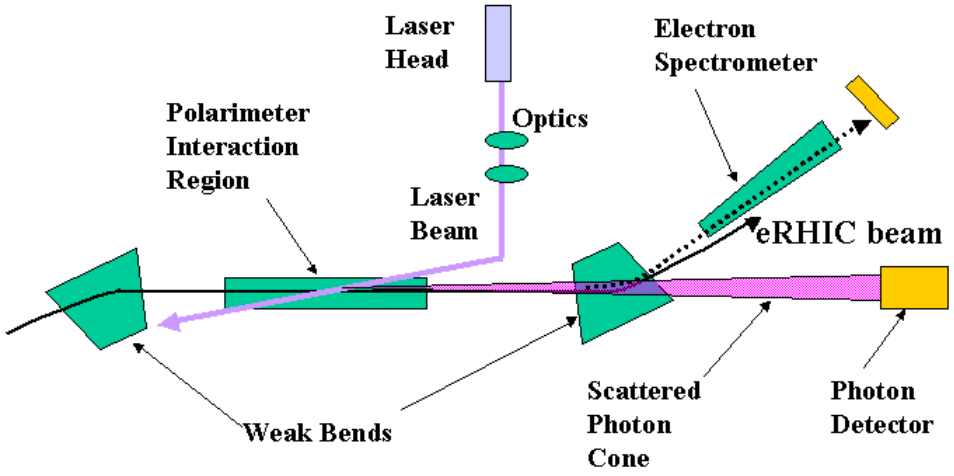

Figure 2.5-2: Schematic view (not to scale) of Compton polarimeter for eRHIC.

While details will differ, many issues are common to longitudinal and transverse polarimetry. An overview of questions related to each of these systems is presented in the remainder of this section, with primary consideration given to the identification of issues potentially affecting design of the ring. The section concludes with a discussion of the statistical and systematic accuracy which could be expected for these types of polarimeters.

2.5.2 Electron beam

The design of the polarimeter will be governed by properties of the electron beam. To accurately sample the beam polarization, the interactions between laser and electron beams for the Compton polarimeters must be placed in straight sections of the eRHIC ring. In these regions, accurate diagnostics and controls for the electron beam trajectory are essential. To a high degree, the electron trajectory defines the momentum direction of backscattered photons. This places a premium on electron beam, particularly in the transverse polarimeter. The location of this device is planned for a 3-m long straight section in the east arc of the ring. The longitudinal polarimeter must be placed in the south straight section downstream of the electron-ion interaction point.

A complicating factor for the longitudinal polarimeter placement is the rapid spin precession of the electron beam when it is polarized in the plane of the ring, as is the case between the spin rotators. The spin precession angle is directly proportional to the bending angle and for a 10 GeV beam, a bend of 1 degree will rotate the spin by nearly 25 degrees. Because the detector includes a magnetic field, the longitudinal projection of the beam polarization will precess as the electron beam is extracted from the electron-ion IP. To compensate for this effect, a weak bend will be introduced upstream of the polarimeter to rotate the spin back to its orientation at the collision point. Once again, very good local diagnostics are necessary to constrain the beam trajectory and minimize systematic uncertainties in the polarization measurement due to spin precession.

The use of short straight sections should aid in the minimization of background. This is a particularly important consideration in eRHIC where the intense beam will generate copious quantities of bremsstrahlung photons. Bremsstrahlung is likely to be the dominant source of background, as its angular distribution is peaked in the same direction as that of backscattered photons. In addition to reducing the efficiency of the measurement, excessive fluxes of bremsstrahlung photons can cause additional problems such as damage to ring vacuum windows. Minimization of bremsstrahlung can be achieved through a combination of vacuum optimization and reduction of the length of the polarimeter's interaction region. The interaction regions should be limited to a few meters in length.

Other considerations related to the electron beam concern focusing. Focusing the electron beam at the interaction point improves the statistical accuracy of the polarization measurement. The beam size should be considered carefully though, as very strong focusing of the electron beam introduces divergence into the backscattered flux, thereby diminishing the correlation between position and energy needed for transverse polarimetry. Typical beam sizes in existing Compton polarimeters are of the order of a few tenths of a millimeter with divergence of the order of tens of microradians.

2.5.3 Laser system

The design of the laser system is another important element in the design of the Compton polarimeters. Multiple criteria merit consideration in the selection of the laser including wavelength, power, emittance, stability, and pulse structure. The laser optics, particularly in the interaction with the electron beam must also be considered carefully in the interaction region design.

The spectrum of gamma rays produced by Compton scattering will have an endpoint energy directly proportional to the energy of incident photons. Maximizing the endpoint energy in the backscatter spectrum is desirable to increase the asymmetry and improve the signal-to-background ratio. In this respect, the relationship between laser wavelength and scattered photon energy strongly favors the use of a short wavelength laser in or near the ultraviolet region. Fig 2.5-3 shows the longitudinal analyzing power as a function of scattered photon energy for lasers at 266 nm and 532 nm.

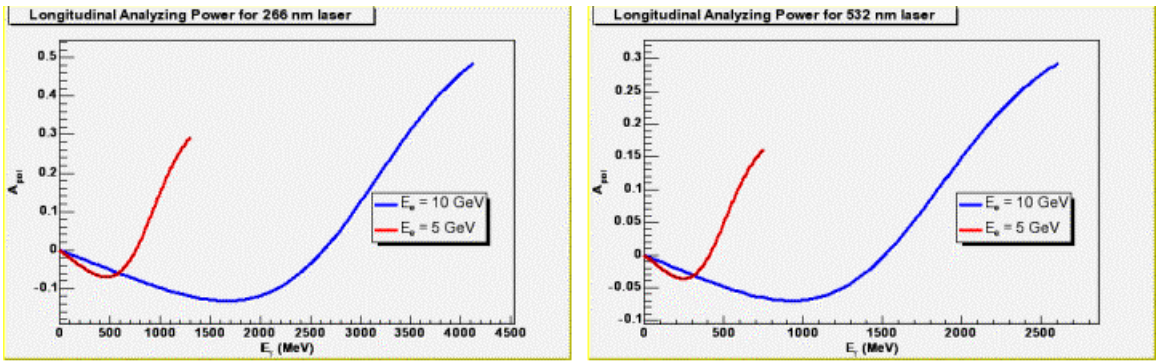

Figure 2.5-3: Analyzing powers as a function of scattered photon energy for longitudinal Compton polarimeters with 266 nm (left plot) and 532 nm (right plot) lasers at electron energies of 5 GeV (red) and 10 GeV (blue).

The selection of a laser system will also be influenced by intensity requirements. It has been observed in other colliders that significant variation in polarization between bunches can occur. The laser should be sufficiently powerful to provide a statistically precise measurement of the polarization for

each fill. With commercially available UV lasers of order 10 Watts, it is estimated that statistical precision of better than 1% in the polarization can be attained within an hour. However, there is substantial uncertainty in the background that will be generated by bremsstrahlung from residual gas, which will be dependent upon vacuum conditions. It is also desirable to have sufficient laser intensity to accurately sample the electron polarization on a pulse-by-pulse basis. One possible option for increasing the laser intensity is the use of a Fabry-Perot amplification cavity. Such a device is in operation in the Hall A Compton Polarimeter at Jefferson Lab [13] and is being instrumented in the HERA Longitudinal Polarimeter. Such a device could substantially increase the statistical accuracy of polarization measurements at eRHIC. If such a system is planned, it should be included early in the design of the polarimeter interaction region. The use of an amplification cavity would require enclosure in the vacuum system. It may restrict the crossing angle between the laser and electron beam and would influence both the laser and electron optics. In addition, the use of a build-up cavity may limit the frequency at which the laser helicity can be changed. Such an arrangement is acceptable for external beams for which the current remains constant and its polarization can be reversed pulse-by-pulse. In the eRHIC ring where the electron beam polarization cannot be frequently reversed, it is desirable to be able to change the laser circular polarization frequently. The performance of the cavity in the HERA Longitudinal Polarimeter should provide a good basis for evaluating the utility of such devices in storage rings.

Besides raising the laser power, the statistical accuracy of the polarization measurement can be improved by either lengthening the interaction region or tightly focusing the laser and introducing a small crossing angle between the beams. The desired crossing angle between the laser and the electron beam will dictate the design of the laser optics. For very small angles of incidence, long focal length lenses are required. Provision must also be made for introducing the laser into the ring's vacuum system. The transverse polarimeter at HERA features a crossing angle of 3 mrad between the laser and electron beam [14]. A comparable crossing angle for eRHIC appears desirable as a means of defining the Compton scattering vertex accurately. The laser systems in most polarimeters suffer at some level from helicity-dependent translations of the laser position. The use of a larger crossing angle decreases the sensitivity of the scattering vertex position to such translations, thereby reducing systematic false asymmetries resulting from helicity-dependent luminosity and helicity-dependent laser trajectories. The use of a well-focused laser can also allow measurements of the beam's intensity and polarization profile if highly stable optical mounts and feedback are used to stabilize the laser and electron trajectories. The use of a crossing angle has the additional benefit that optics can be removed and from the vacuum system from the line of sight of backscattered photons. This allows for easier access, increases versatility and minimizes damage to the optics. It also allows circular polarization to be generated close to the interaction region substantially reducing polarization transport asymmetries.

2.5.4 Detection options

The eRHIC Compton polarimeters will require detectors capable of analyzing backscattered photons, scattered electrons, or both. There are precedents for both options. Most Compton polarimeters have relied on gamma ray calorimeters. The use of a calorimeter for scattered photons is a scheme offering many attractive features. It is proven technology, having been used in a number of laboratories. Calorimeters consisting of dense materials such as lead glass or cesium iodide can be constructed in a compact manner for relatively low cost. The photon kinematics also features a

correlation between angle and energy. A segmented calorimeter can use this information for beam alignment and reduction of instantaneous rate. This correlation is essential to preserve in the transverse polarimeter as it forms the basis for the polarization measurement.

The primary concern related to photon calorimetry is the intensity of the eRHIC electron beam. The electron beams of eRHIC will be the most intense beams to use Compton polarimetry. While the beam intensity will increase the rate of backscattered photons, thereby improving the statistical accuracy of measurements, it will also produce substantial background from bremsstrahlung. Because this radiation is emitted in the same direction and cannot be distinguished from backscattered photons, a creative solution will be required to eliminate background contributions to the measurement. At the very least, highly segmented detectors and fast data acquisition systems will be required with proper gain matching and summing of detectors. Even very fast scintillators will suffer serious problems with piled up pulses. Operation in a single-photon counting mode is likely to prove impossible. Operation in multi-photon mode works well from a statistical point of view, but relies heavily on very accurate modeling of the polarimeter's analyzing power and stable performance of the calorimeter.

A possible alternative or complementary approach involves detection of the scattered electron. This approach has not been used often in polarimetry, but has been used to produce tagged photon beams at facilities including such as LEGS [15] at Brookhaven's NSLS. Detection of the electron would require some sort of magnetic field for momentum analysis. A magnetic analyzer could range from a bending magnet to a separate magnetic channel, possibly including a septum magnet to separate scattered electrons from the beam. Any such device would have to include a robust position-sensitive detector.

The use of a magnetic spectrometer would have a few significant advantages over a calorimeter. Foremost among these is that the energy analysis would allow an energy spectrum to be constructed for any segmented detector. It would not be necessary to run in an integration mode. Each cell of the detector could produce its own asymmetry which could be compared to the projected shape from Monte Carlo simulations.
Another important advantage is that the spectrometer would serve as a filter for the rejection of bremsstrahlung. This is particularly significant because the electrons producing very high energy bremsstrahlung photons, would not traverse the spectrometer.

There are many open questions and issues related to detection of the electron. This detection scheme clearly requires additional space in the polarimeter interaction region. The use of a septum magnet could lead to problems with radiation and beam storage. The introduction of a new magnetic field would affect the beam trajectory and may complicate efforts to account for spin precession correctly. It would significantly complicate the interpretation of positional information for the transverse polarimeter. Also, unless the scattering vertex between the laser and electron beam is very well defined, the acceptance of the spectrometer could be helicity-dependent and variable. The nonlinear relationship between the energy of the Compton edge and the beam energy would increase the demands for the necessary momentum bite and resolution. Momentum resolution of at least 1% would be desirable at both 5 and 10 GeV.

One possible compromise would involve combining the two approaches. The benefits of coincident detection of scattered electrons and backscattered photons have been demonstrated in the Jefferson

Lab Hall-A Compton Polarimeter. The photon counters are fast plastic scintillators with low energy resolution. Energy analysis is provided by a bending magnet and a silicon detector internal to the vacuum system. A similar approach could be considered for eRHIC polarimetry, in which the asymmetry is based on a photon counter, but complementary information on the energy resolution is obtained by detecting the electron for a limited fraction of events.

2.5.5 Summary

Overall, the outlook for electron polarimetry at eRHIC appears promising. No insurmountable hurdles are foreseen in the construction of laser-backscattering polarimeter. Realistic estimates for statistical precision can be obtained by looking at the performance of existing Compton polarimeters. For the Hall-A Polarimeter at Jefferson Lab, statistical uncertainties of 1% are obtained within an hour for a 4 GeV electron beam. Raising the beam energy reduces the time needed to reach this level of precision. The HERA Longitudinal Polarimeter at 27 GeV reaches this level of precision in about one minute.

The accuracy of beam polarization measurements will ultimately be limited by systematic errors. SLAC has reduced systematic uncertainties to the level of 0.5% for an external 46 GeV beam. Systematics of 1-2% are more commonly attained, although reaching this level is not trivial. All depend on specifics of the instrument, but are often dominated by modeling of the analyzing power, detector stability, and beam alignment issues. Careful consideration of these issues from the outset will increase the chance of success.

References:

1. http://www.phenix.bnl.gov/WWW/publish/abhay/Home_of_EIC/e_polarimetry/epol_8nov2002_ws.html
2. T.J. Gay and F.B. Dunning, Rev. Sci. Instrum 63 (1992) 1635.
3. T.J. Gay et al, Phys Rev A, 53 (1996) 1623.
4. C. Cacho et al, Phys Rev Lett, **88** (2002) 066601.
5. H.R. Band et al, Nuclear Instruments and Methods **A400** (1997) 24.
6. V.S. Morozov et al, Phys Rev ST Accel. Beams **4** (2001) 104002 .
7. D.P. Barber et al, Nuclear Instruments and Methods **A329** (1993) 79-111.
8. D.P. Barber et al, Physics Letters B **343** (1995) 436-443.
9. M. Beckmann et al, Nuclear Instruments and Methods **A479** (2002) 334-348.
10. I. Passchier et al, Nuclear Instruments and Methods **A414** (1998) 446-458.
11. W.A. Franklin et al, AIP Conf Proc **675** (2002) 1058-1062.
12. N. Falletto et al, Nuclear Instruments and Methods **A459** (2001) 412-425.
13. N. Falletto et al, Nuclear Instruments and Methods **A459** (2001) 412-425.
14. D.P. Barber et al, Nuclear Instruments and Methods **A329** (1993) 79-111
15. C.E. Thorn et al, Nuclear Instruments and Methods **A285**(1989) 447.

3. ION BEAM

In order to reach luminosity goals for the eRHIC, several improvements and upgrades have to be made in ion rings. These upgrades are discussed in this chapter.
The required beam emittance values for eRHIC operation with Au or low energy proton beam are below the typical values used presently at the RHIC operation. The electron cooling technique has to be applied to bring transverse emittances down and maintain them at the required level. The cooling can be used also to reach 20cm rms bunch length required for ion bunches in the eRHIC, or even go to shorter bunches. The electron cooling is described in details in section 3.1.
While ion bunch intensity in the eRHIC is at the level of bunch intensities used at the present RHIC operation, the total beam current should be increased considerably, by about factor 6. All this current increase is provided by increasing number of ion bunches circulating in the RHIC rings. Since the present RHIC RF accelerating system is at 360th harmonic of revolution frequency, the maximum number of bunches which can be put into the ion rings is 360. In reality the necessity for an abort gap will decrease the maximum number of bunches, that can be used, to about 335. Still we will talk about 360 bunch mode, assuming 360 bunch pattern by these words.
In order to maximize the eRHIC luminosity this report evaluated consequences and considered required upgrades to reach 360 bunch mode. The number of issues which rise up with increasing the number of bunches are discussed in section 3.2. They include injection upgrade, the evaluation of pressure rise and electron cloud problems, abort system upgrade and an evaluation of heat load in the cold pipe of ion rings.
Beam instabilities are revised in section 3.3.
The proton polarization issues to provide a proton beam with longitudinal polarization direction at the eRHIC interaction point is discussed in section 3.4. The same section considers using polarized beams of other ion species, with $^{3}He^{+2}$ as best possible candidate.

3.1 Electron Cooling for eRHIC

3.1.1 Luminosity and Electron Cooling

The purpose of the luminosity upgrade for eRHIC is to decrease the emittance of the stored ion beams and maintain it at a required level. This will be achieved with a suitable cooling techniques. Present baseline parameters require the following:

1. Decrease of the transverse emittance of Au ions at 100 GeV energy from the 95% normalized emittance of 15 π μm to 6 π μm. Presently, emittance is increased during storage time from 15 π μm to 40 π μm due to the IBS.
2. Decrease of the transverse normalized emittance of protons to 5 π μm at lower energies 25-50 GeV.
3. Decrease of the longitudinal emittance which provides bunch shortening. The beta-star function at IP requires shortening of the rms bunch length below 25 cm for both protons and Au ions.

An initial study indicates that all three major tasks described above can be achieved with the electron cooler presently under design for the RHIC upgrade project, designated RHIC II [1]-[2].

3.1.2 Electron Cooler

The layout of the cooler is shown in Figure 3.1.

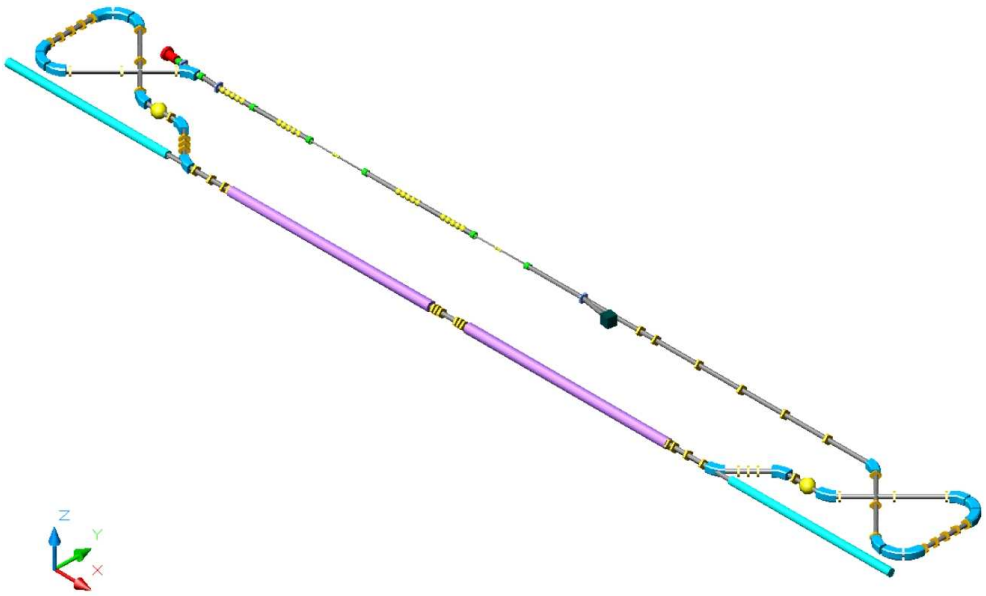

Figure 3.1: Schematic layout of the RHIC electron cooler (system shown for one ring). The photoinjector is shown in red, the superconducting energy-recovery linac is shown in yellow, the solenoid in purple and a section of the RHIC ring is shown in green.

The electron beam will be produced with a cw photoinjector (laser photocathode RF gun), with the cathode of the gun being immersed in a magnetic field to produce a 'magnetized' electron beam (an angular momentum dominated beam). Following the initial acceleration in the gun to about 2.5 MeV the beam will be injected into a superconducting energy recovery linac. The beam transport has to preserve the magnetization of the beam in the transport with discontinuous magnetic field. The magnetized electron beam (with its velocity matched to the ion beam) is then introduced into a 1 T cooling solenoid. Since the ion beam is much longer than the electron beam, the phase of the electron beam will be modulated in order to cool the required longitudinal extent of the ion beam. Other modulations (in energy and radial coordinates) may be introduced to shape the ion beam in phase-space. Emerging from the 30 m long cooling solenoid, the electron beam will be separated from the ion beam, rebunched (to match the linac acceptance) and decelerated to recover its energy. The beam will be dumped at about 2.5 MeV.
An R&D on a number of system elements is presently underway [2]: the photoinjector (including its laser and photocathode deposition system), a high-current superconducting cavity for the ERL of the cooler, beam dynamics of the complete system, electron cooling simulation codes and the high-precision superconducting solenoid.

Electron gun

An electron beam will be produced with a CW photoinjector (laser photocathode RF gun). It is planned to use CsK2Sb (cesium potassium antimonite) cathodes. These cathodes exhibit a very high

quantum efficiency of over 5% for green light. The diode-pumped solid-state laser at a wavelength of 1064nm is planned. The design of the Los-Alamos / Advanced Energy Systems of a 2.5 cell, 700 MHz normal-conducting photoinjector is adopted. The device will be powered by a 1 MW CW klystron and produce about 2.5 MeV beam at over 100 mA. A computer-generated drawing of the photoinjector is shown in Figure 3.2.

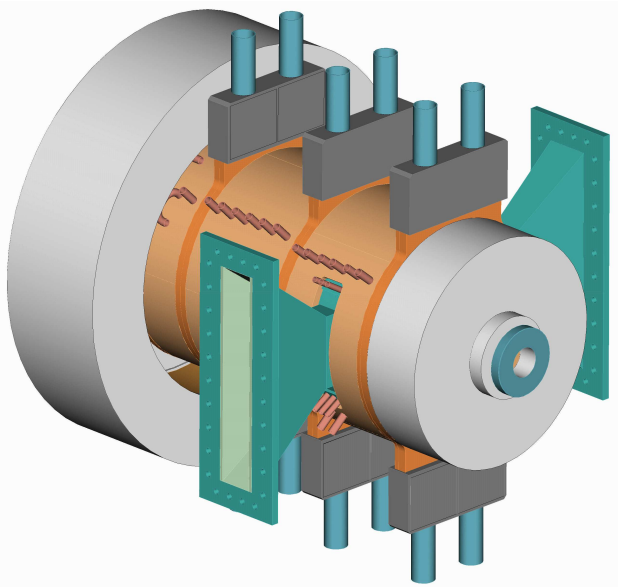

Figure 3.2: The LANL / AES photoinjector which will be used for the electron cooler.

Energy recovery linac

Following the initial acceleration to about 2.5 MeV the beam will be injected into a 703.75 MHz superconducting Energy Recovery Linac (ERL). Each linac cavity has 5 cells with aperture of 17 cm diameter (see Figure 3.3). The plan is to intercept the Higher-Order Mode (HOM) power by ferrite absorbers located in the beam pipe at room temperature [3]. The cavity opens into a 24 cm beam pipe. This large diameter is chosen in order to conduct the HOM power away from the cavity. For the TE11 mode, the enlarged pipe (24cm) has a cutoff frequency of 732 MHz, which is below all HOMs. This structure has been simulated by MAFIA computer code [2]. The HOMs with higher frequencies are less important. The simulations show that all the higher order modes couple extremely well to the ferrite, resulting in a beam breakup threshold current of 1.8 ampere.

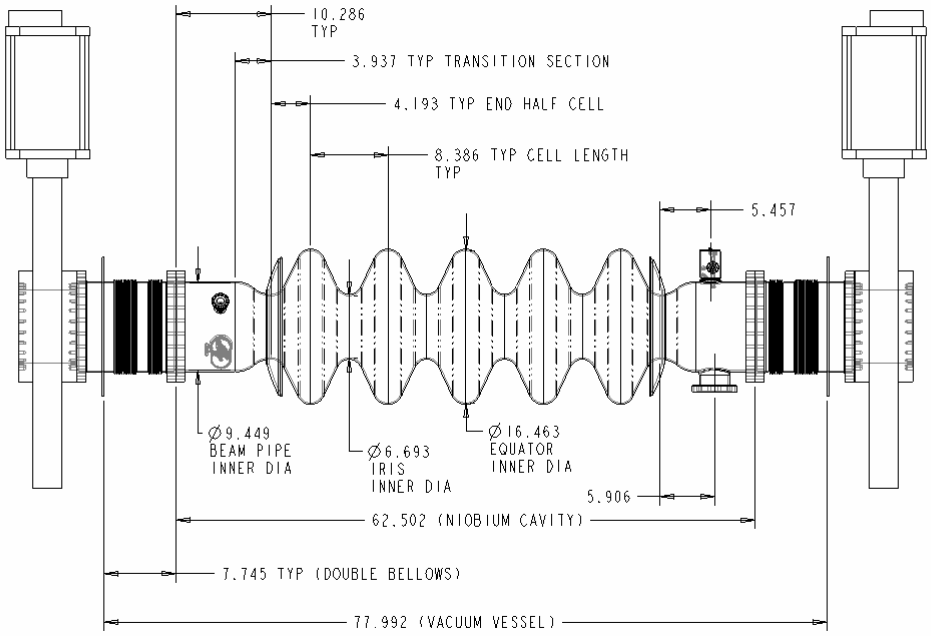

Figure 3.3: A cross section of the superconducting cavity assembly.

Magnetized beam transport

There are a few straight sections in RHIC where the electron cooler may be introduced. Presently, its placement is considered next to IP4 of RHIC, in the straight section between Q3 and Q4, which can accept about 30 m long solenoids. The electron accelerators will reside outside the RHIC tunnel. The lattice can debunch the beam in order to reduce the space-charge interaction of the electron and ion beams or to reduce the energy spread of the electron beam. The beam transport has to obey certain rules in order to preserve the magnetization of the beam in the transport with a discontinuous magnetic field. Emerging from a long cooling solenoid, an electron beam will be separated from the ion beam, rebunched (to match the linac acceptance) and decelerated to recover its energy. The beam is then dumped at about 2.5 MeV. Merging the low energy and high-energy beams at the entrance of the linac is done using two weak dipoles with a Stabenov solenoid. The linac design assumes the use of 3rd harmonic cavities for additional control of the longitudinal phase space. The two solenoids with opposing fields in the cooling section are proposed to eliminate the coupling in the ion beam. A quadrupole matching section between the solenoids maintains magnetization [4].

Superconducting solenoid

The superconducting solenoid for electron cooling in RHIC is designed for a 1 T field, with an ample quench margin. The total available space for solenoids is approximately 26 meters. This long solenoid will be manufactured as two shorter sections, 13 m each. The two solenoids will have opposite magnetic field in order to not to introduce horizontal-vertical coupling to the RHIC lattice. A dedicated matching section of 6 quadrupole lenses will flip the direction of the magnetization of the beam between the two solenoids. The solenoid must meet very stringent field quality requirement with a solenoid field-error below 1x10-5. It will also have concentric arrays of ~150mm long vertical and horizontal dipole correctors to compensate for any transverse components. These dipole

correctors will be built using printed circuit coils [5] and will provide corrections of up to 10–3 T with a maximum operating current of 2 A.

3.1.3 Cooling Times

Electron cooling times grow with beam energy. As a result, an accurate estimate of cooling times at high-energy becomes extremely important. An order of magnitude estimate, typically sufficient for conventional low-energy coolers, is no longer acceptable. A systematic R&D is presently under way to simulate high-energy electron cooling for RHIC. Presently available analytic formulas for the friction force are different from one another by a significant factor. In addition, the accuracy of their applicability requires detailed examination for the electron cooling parameters relevant for RHIC. A dedicated computer code Vorpal [6] is being developed by Tech-X Company to produce a direct numerical simulation of the friction force and to benchmark available analytic friction-force formulas for RHIC regime of parameters. After detailed benchmarking, reliable friction-force formulas or friction coefficients (directly obtained from simulations) will be used in simulations of the cooling dynamics. Presently, the cooling dynamics is being simulated with the two codes: SimCool [7] and BetaCool [8].

An initial study indicates that cooling in RHIC at full energy for gold ions and some intermediate energy for protons is feasible. The RHIC gold beam evolution is dominated by Intra-Beam Scattering (IBS), which leads to emittance growth and beam loss. Electron cooling is planned during the storage phase of the machine to control IBS and reduce emittances to required values (limited by beam-beam parameters).

Some examples obtained with the BetaCool code (with the parameters of electron cooler given in Refs.[1]-[2]), which show control of the IBS and reduction of beam emittances and bunch length for Au ions at 100 GeV energy, are shown in Figure 3.4 and Figure 3.5 , respectively.

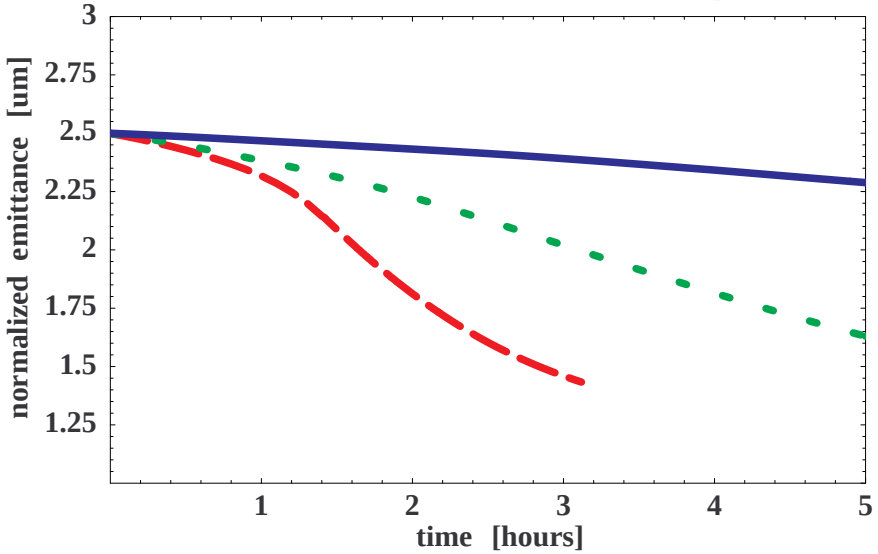

Figure 3.4: BetaCool simulation code: emittance evolution for Au ions (number of ions in a bunch Ni=1x10^{9}) at 100 GeV, with three different electron-cooler currents: 1) number of electrons (Ne) in a bunch Ne=6x10^{10} – blue (solid line), 2) Ne=8x10^{10} – green (short-dash), 3) Ne=12x10^{10} – red (long-dash).

Faster cooling times and reduction of beam emittances can be achieved by adjusting beam current in the electron cooler or by employing additional manipulations with the electron beam, which is presently the subject of R&D studies.

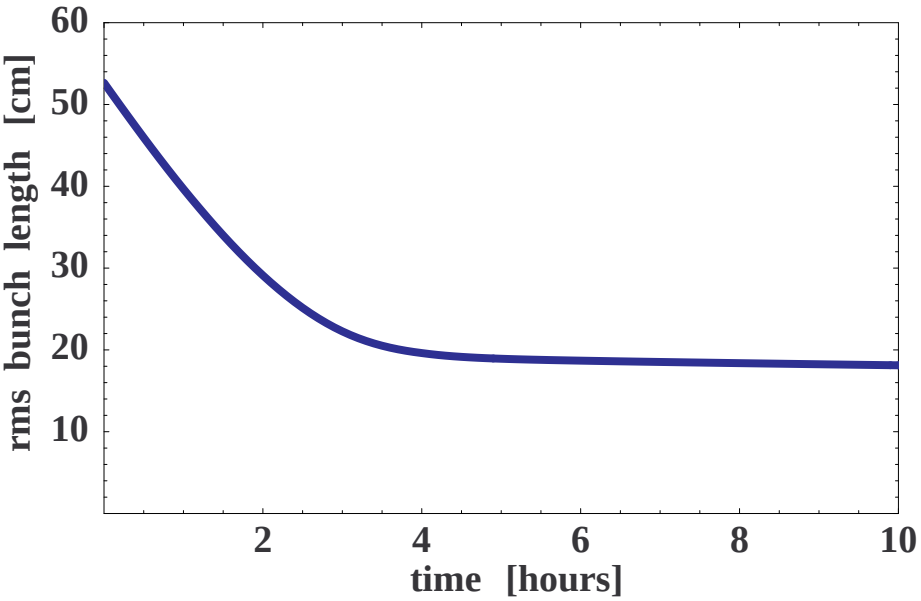

Figure 3.5: BetaCool simulation code: shortening of bunch length for 100GeV Au ions (Ni=1x10^{9}) with the electron cooler current corresponding to Ne=6x10^{10} electrons in a bunch.

For protons at high energy in the range of 100-250 GeV, direct electron cooling is not effective. This suggest a staged cooling [9] for high-energy protons, were an initial cooling is first done at low energy close to the injection. In addition, the electron beam area can be varied with time to control reduction of beam emittances to a desired level. At low proton energies in the range 25-50 GeV, cooling becomes more effective and can be used to control transverse beam emittances and an rms bunch length to required values, imposed by an achievable beta-star at the interaction point. Figure 3.6 shows an example for protons at a full energy of 50 GeV, which indicates that beam emittances can be maintained at a required level even when cooling is applied directly at 50 GeV energy.

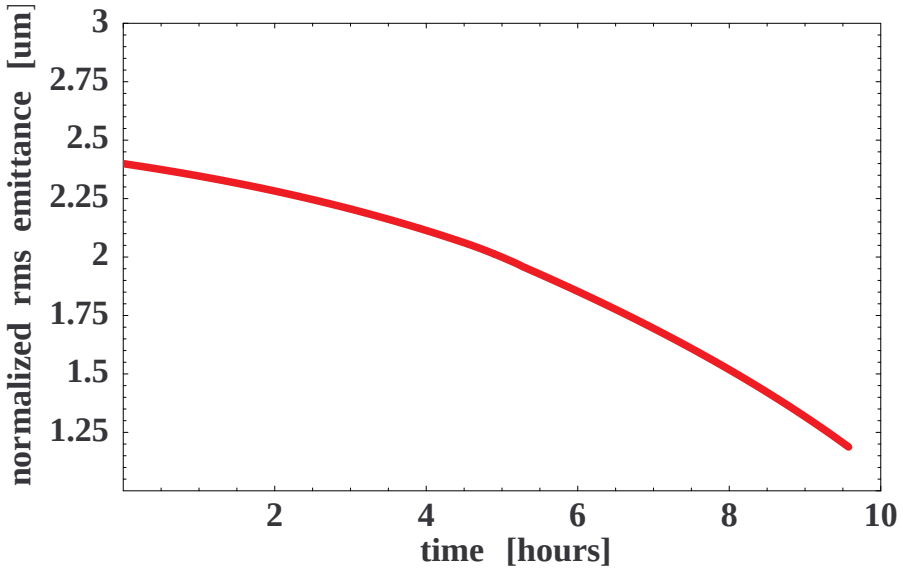

Figure 3.6: BetaCool: rms emittance reduction for 50 GeV protons (number of protons in a bunch Np=1x10^{11}) with the electron cooler current corresponding to Ne=6x10^{10} electrons in a bunch.

Since electron cooling is effective only at low energy, protons may be first cooled at low energy and then accelerated to a required energy. Figure 3.7 shows emittance reduction for the 27 GeV protons with the number of particles in the electron bunch Ne=5x10^{10} and Ne=1x10^{11}, shown with red and green color, respectively. Some reduction of beam emittance with higher electron cooler current maybe found desirable if the beam-beam limit in electron beam is relaxed, as in the case of the linac-ring approach for a collider. Corresponding bunch length compression for low and high current of electron cooler is shown in Figure 3.8 and Figure 3.9, respectively.

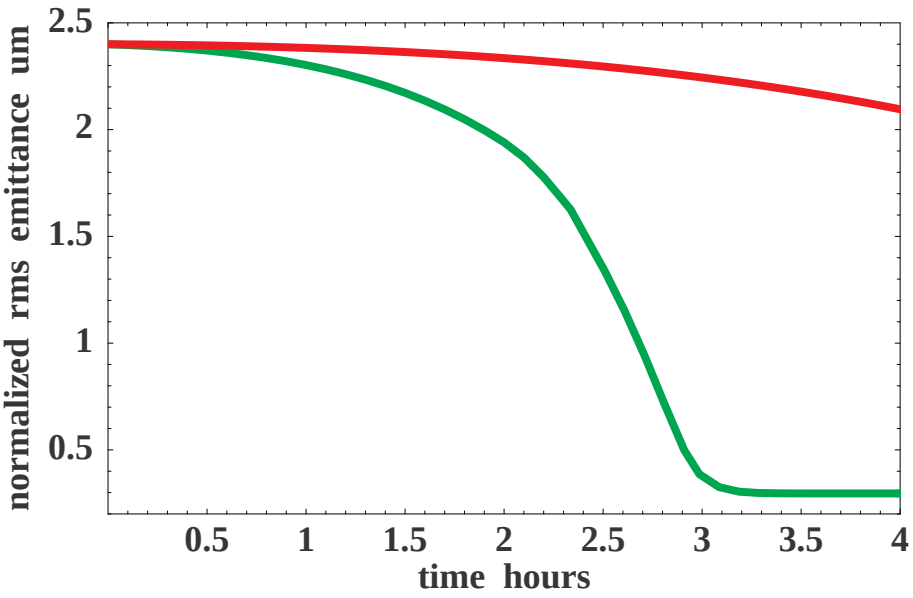

Figure 3.7: BetaCool: rms emittance reduction for 27GeV protons (Np=1x10^{11}) with two currents of electron cooler 1) Ne=5x10^{10} – red curve, 2) Ne=1x10^{11} – green curve

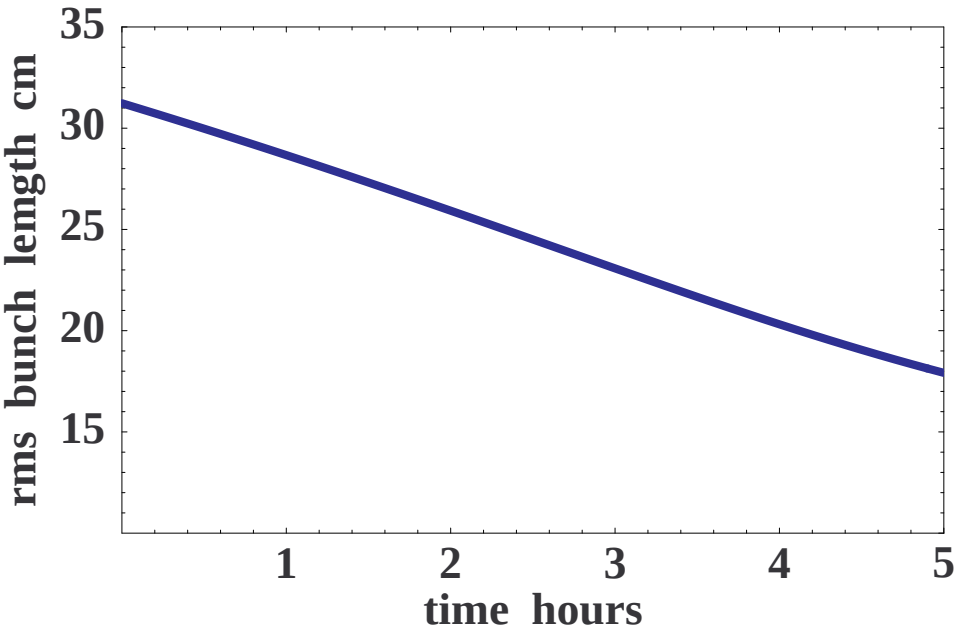

Figure 3.8: BetaCool: rms bunch length compression for 27GeV protons (Np=1x10^{11}) with Ne=5x10^{10} electrons in a bunch.

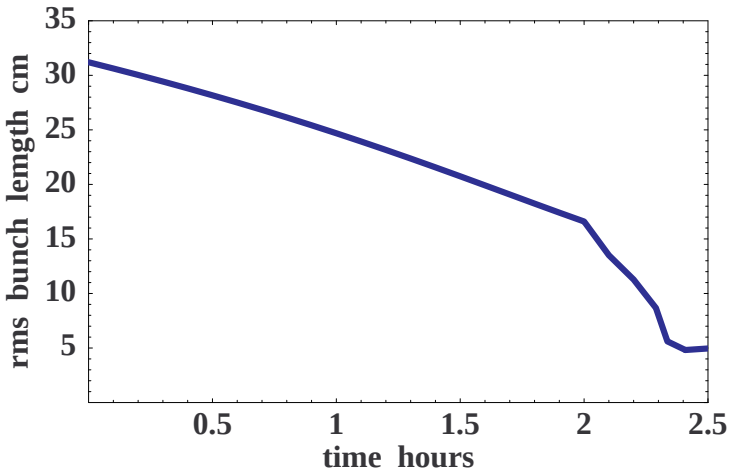

Figure 3.9: BetaCool: rms bunch compression for protons (Np=1x10^{11}) at 27 GeV, with electron cooler current corresponding to Ne=1x10^{11} in a bunch.

The protons, initially cooled at low energy are accelerated to a full energy of 250 GeV, where only a very weak diffusion due to the IBS occurs. For example, storage at 250 GeV is shown in Figure 3.10 and Figure 3.11 for protons initially cooled to a normalized rms emittance of 0.8 μm (4.8 μm 95% emittance) and 1.2 μm (7.2 μm 95% emittance), respectively. Cooling of protons and Au ion bunches of even higher intensity is discussed in Appendix A.

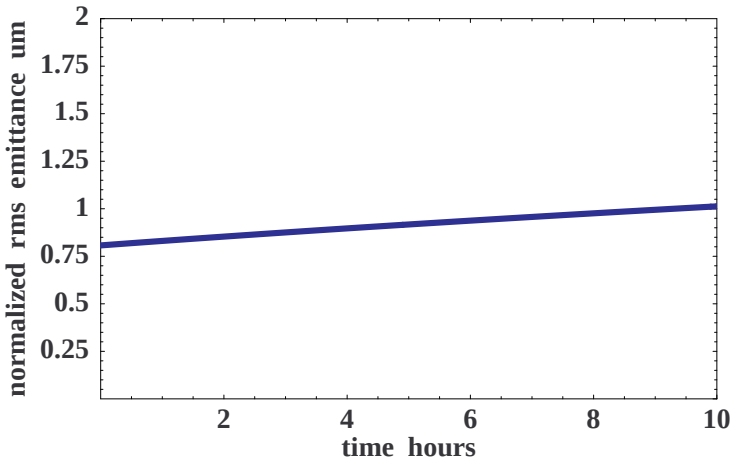

Figure 3.10: BetaCool: Emittance growth at 250 GeV of protons (Np=1x10^{11}) initially cooled to an rms emittance of 0.8 μm at 27 GeV, with the electron cooler current corresponding to Ne=1x10^{11} in a bunch.

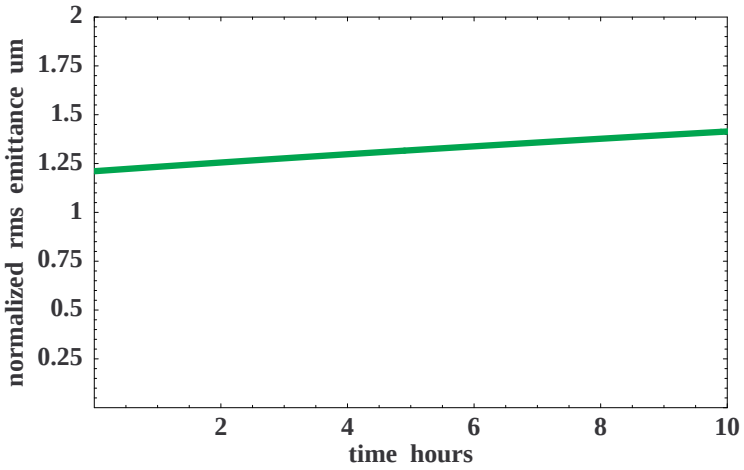

Figure 3.11: BetaCool: Emittance growth at 250 GeV of protons (Np=1x10^{11}) initially cooled to an rms emittance of 1.2 μm at 27 GeV, with the electron cooler current corresponding to Ne=1x10^{11} in a bunch.

In figures from Figure 3.4 to Figure 3.11, time evolution is shown for the rms beam parameters. However, the process of electron cooling results in a rapid cooling of the core of beam distribution. This feature has a unique application to cooling in a collider: even for a relatively weak cooling of rms beam parameters one can get a significant luminosity gain as a result of cooled beam core. This major feature of electron cooling in a collider is shown in Figure 3.12-Figure 3.15. In this example, the parameters of the electron cooler are chosen such that the rms beam emittances stay approximately constant during the cooling time, as shown in Figure 3.12 for the unnormalized transverse rms emittances.

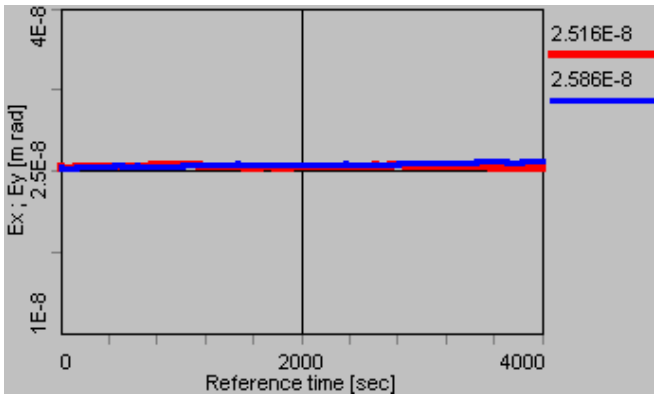

Figure 3.12: BetaCool code: Time evolution of unnormalized rms emittances for Au ions (N_i=1x10^9 in a bunch)at storage energy of 100 GeV for a typical parameters of electron cooler with N_e=6x10^{10}.

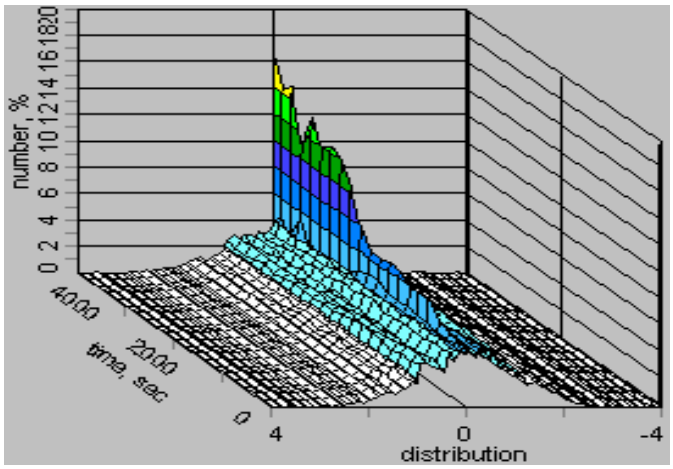

Figure 3.13: BetaCool code: Time evolution of longitudinal beam profile (4 σ) for the same parameters of electron cooler as in Figure 3.12.

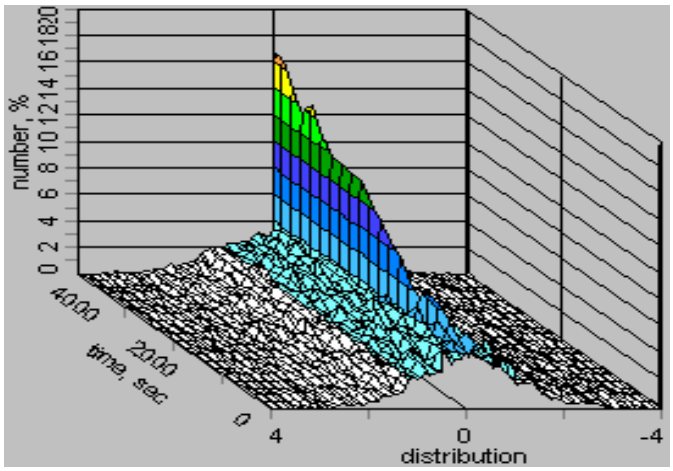

Figure 3.14: BetaCool code: Time evolution of horizontal beam profile (4 σ) for the sameparameters of electron cooler as in Figure 3.12.

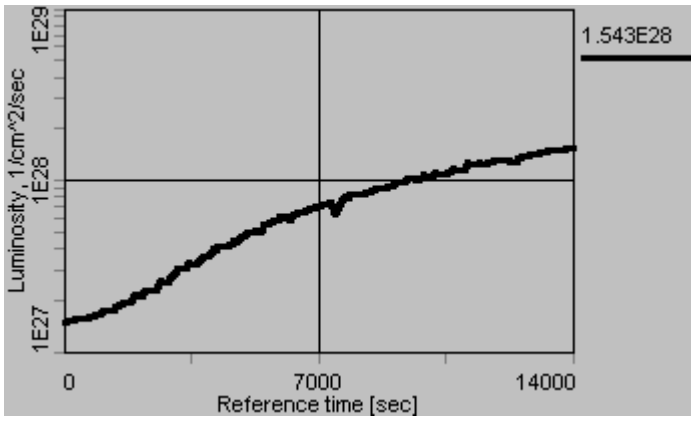

Figure 3.15: BetaCool code: Example of the luminosity increase for Au-Au collisions in RHIC at 100 GeV due to a cooled beam core (Figure 3.14) even for the case when there is no rapid cooling of the rms beam parameters, as shown in Figure 3.12.

A detailed benchmarking of simulation codes is presently in progress.

3.2 Towards 360 Bunches in RHIC

To achieve a high luminosity in eRHIC, the bunch number in the hadron ring of RHIC needs to be maximized while the bunch spacing in the hadron and electron rings needs to be the same. With larger bunch numbers, and consequently larger beam currents, a number of effects must be addressed. Among those are

1. Acceleration of high intensity beams
2. Vacuum breakdown with high intensities
3. Increased heat load to the cryogenic system
4. Instabilities, single and multi-bunch
5. Long-range beam-beam interactions
6. Radiation safety concerns with high intensity beams
7. Injection

3.2.1 360 Bunches Injection

Currently the maximum number of bunches is 112, limited by the injection kicker rise time and the need for an abort gap. After summarizing the current injection scheme, we discuss 3 options to get to larger bunch numbers in RHIC:

1. Very fast injection kickers
2. Long flattop injection kickers
3. Barrier rf stacking and bunching into the current 28 MHz acceleration system

The first and third option has not been demonstrated at another accelerator with beam parameters comparable to those required at RHIC. The second option resembles injection schemes use at HERAp, and foreseen for the LHC.

The existing injection scheme

Bunches are transferred from the AGS to RHIC one-by-one, and placed into one of the RHIC accelerating buckets of harmonic 360. With this scheme the harmonic numbers of the AGS and RHIC are independent. The injection kickers rise for each bunch, and have an integrated strength to provide a 1.5 mrad kick for the beam of 81 Tm rigidity. The kicker flattop to accommodate a single bunch. In this way, the bunch spacing is limited by the injection kicker rise time. A gap is needed to allow for the abort kicker to rise without kicking beam into the superconducting magnets. Injection kicker rise time and abort gap currently limit the number of bunches to 112, with two empty buckets between filled ones. The main parameters of the existing injection system are listed in Table 3.1.

Table 3.1: Main parameters for the current injection system for hadron beams

Parameter	Symbol	Unit	Value
Beam rigidity	$B\rho$	Tm	81
Rf frequency	f_{rf}	MHz	28
Harmonic number	h	…	360
Bucket length	l_{bucket}	ns	36
Total bunch length	l_{bunch}	ns	15
Injection kicker rise time	t_{rise}	ns	95
Revolution time	T_{rev}	μs	12.8
Abort gap	t_{abort}	μs	0.85

Very fast injection kickers

If the injection kicker rise time could be shortened, more bunches could be injected with the existing scheme. With the existing bucket spacing, bunch length, and abort gap (see Table 3.1), the injection kicker rise time would need to be 57 ns or less if every other bucket is filled (allowing for a total of 168 bunches), and 20 ns or less if every bucket is filled (allowing for a total of 336 bunches).

Reducing the injection kicker rise time in RHIC is limited by several conceptual and technological constraints. The present system is well understood and can serve as basis for scaling. The four injection kickers are in a warm space of 5.4 m length, between the flanges to the Q9O and D9O magnets. The physical magnet length is 1.12 m, and the effective ferrite length 80 cm. The magnet is designed as an all-ferrite transmission line with 40 Ω characteristic impedance. The propagation velocity was measured to be 3.3 cm/ns (one ninth the speed of light). The thyratron pulser delivers a pulse with a 33 ns rise time. In order to avoid voltage breakdown, the kicker is presently operated with a mismatched 25 Ω termination, resulting in an effective rise time of 95 ns.

The design concept for the present kicker system can accommodate the rise time requirement for a 180 bunch pattern. This can be achieved by operating the kicker fully matched, leading to a pulse transit time of 24 ns which together with the pulser rise time of 33 ns leads to the required 57 ns. Necessary changes must address the voltage limitation in the kicker:

- Currently only 60% of the available warm space is filled with ferrite, and a fifth magnet may be fitted in. The additional magnet can serve to sufficiently reduce the operating voltage while retaining the present kicker constructions. Alternatively, the transit time in a shortened magnet leads to gains of about 5 ns in rise time.

- Another solution would be to adopt conventional plate kickers designed for 25 Ω to match the present Blumlein pulser. However, the transit time would be increased to an unacceptable 38ns. By accepting the reflections at the kicker input, which the present system tolerates, one can design the plate kicker for 40 Ω, or even 50 Ω, and operate it with matched termination.

Whereas a solution for the 180 bunch pattern is plausible within presently available technology, the requirements for a single bunch injection with 20 ns rise time in the 360 pattern are extreme. An advanced R&D program at the Lawrence Livermore National Laboratory (LLNL) has the goal of achieving 10 ns rise times in pulsers using solid state Metal Oxide Semiconductor Field Effect Transistors (MOSFET) and Insulated Gate Bipolar Transistors (IGBT). Assuming that 10 ns can be obtained at the current/voltage level required, only 10 ns remains for the transit time in the kicker. Thus, the effective kicker length is limited to 33 cm provided by 10 units. Although in principle possible, this solution would require a completely new injection system, kicker magnets and pulsers, as well as dramatic technology breakthroughs and corresponding R&D efforts.

Long flattop injection kickers

With a long flattop of the injection kickers, a whole AGS fill could be transferred at once.
This would require a new rf system in the AGS and a completely new injection system. With about 6 such transfers, RHIC would be filled. For this the bucket length in the AGS and RHIC must be the same. That could be achieved by having a 28 MHz system in the AGS. The circumference of RHIC is 19/4 of the AGS circumference. If the RHIC harmonic number remains unchained, the AGS extraction would need to be performed at a non-integer harmonic. Furthermore, about 20 times more intensity would need to be accelerated in AGS than with the current scheme, while preserving the transverse and longitudinal emittances. With 20 times more booster cycles needed to fill the AGS, some part of the beam would stay significantly longer at AGS injection, subjecting it to space charge and possibly intra-beam scattering effects. The large number of Booster cycles needed to fill the AGS may also raise issue with the local electricity utility. In this scheme, however, the rise time is a less critical issue since a few gaps in the bunch train would have only a small effect on the luminosity.

Barrier rf stacking

By employing a barrier bucket system in RHIC it is, in principle, possible to inject a large number of bunches without constraints from the injection kicker rise time. A barrier bucket system creates only a few rf wave forms per turn. In this way, beam can be held in a large part of the circumference, and new bunches injected in buckets that are then merged into the long bunch (see Figure 3.16). After injection of all bunches, the beam can be bunched with the 28 MHz acceleration system, and accelerated to the store energy.
First consider the rf gymnastics that was used in an AGS experiments. A schematic plot of the net voltage per turn for injection above transition is shown below. Note that the time scale is very different from what would actually occur so as to make details clear.

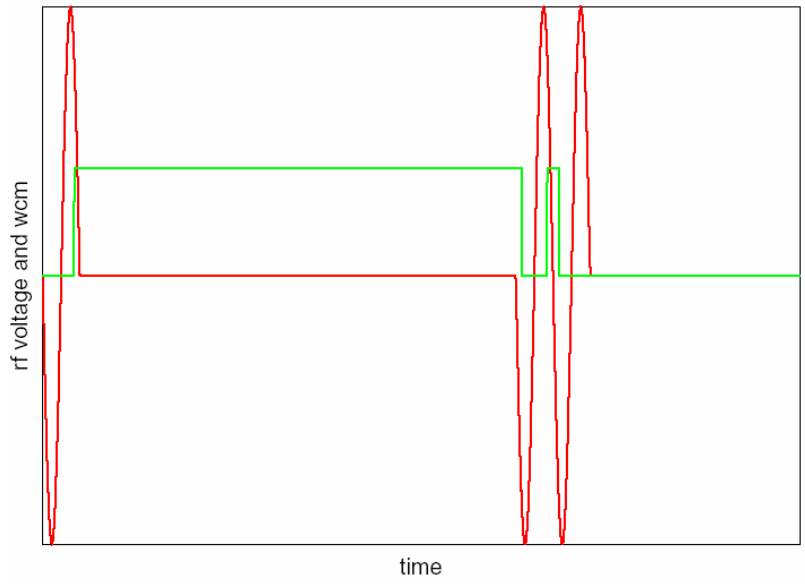

Figure 3.16: Rf voltage (red) and beam current (green) over one turn.

The rf waveform is shown in red, and wall current monitor signal in green. A bunch has just been injected between the closely spaced barrier waveforms, while beam is held in a large part of the circumference. The next step is to adiabatically lower the barrier between the freshly injected bunch and the long bunch. The voltage waveform confining the right side of the injected bunch would need to be tuned so that the merge conserves emittance. Naively, the relevant time scale for the merge to conserve emittance is the time it takes a particle to perform one oscillation in the long bunch, $T_{ad} = T_{rev} f/\Delta f$. For an rms momentum spread of $\delta p/p = 0.001$ one finds $T_{ad} = 29$ s for $\gamma = 25.9$, which is far too long to be practical.

The time required for the merge can be shortened with a technique that does not require a change in the momentum spread of the stored bunch. One way to accomplish this is to shift both the amplitude and the timing of the waveforms that confine the injected bunch as the merge proceeds.

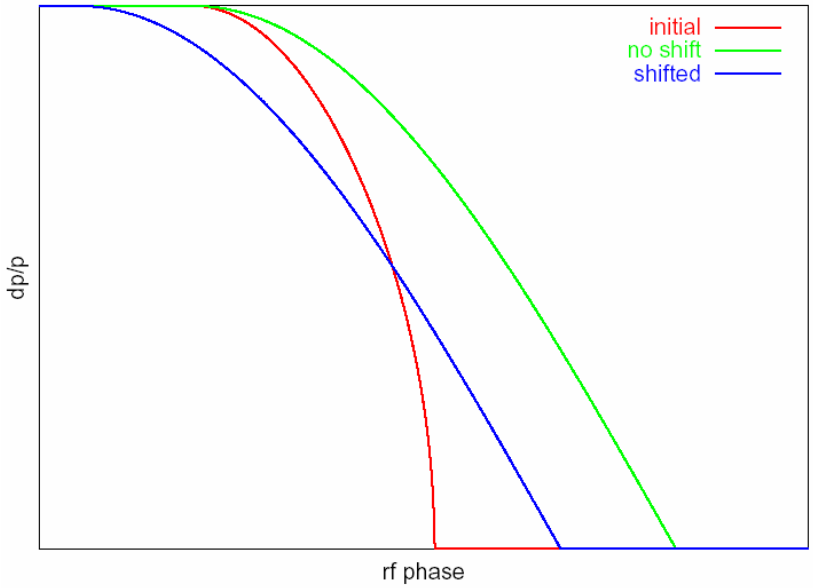

Figure 3.17: Phase space distribution of the long bunch, before and after a merge without and with shifted barrier voltage.

Figure 3.17 shows the longitudinal phase space area before and after a bunch merge. The red curve shows the initial phase space boundary of the stored bunch. If the voltage of the barrier between the stored and injected bunches is simply lowered the green curve results. If the process were completely adiabatic the green curve would have a smaller peak value than shown. However, if the barrier voltage is simultaneously shifted and lowered, the blue curve could be obtained. The areas under the blue and red curves are the same. The adiabatic time in this case is reduced by the ratio of the barrier length to the machine circumference, of order 0.01 in our case. This would allow for bunch transfers every 300 ms.
Another option is a technique described by K.Y. Ng in [10], which employs barrier voltage waveforms that do not change sign in the merging region. The bunch is injected off momentum, and accelerated through the barrier into the stored bunch. This is likely to result in an emittance growth of about 50%.

Summary

To increase the bunch number in RHIC beyond the current value, a number of problems need to be considered. One of the most severe problems is the injection scheme. We considered very fast injection kickers, long flattop injection kickers, and barrier rf stacking, to fill close to 360 bunches in RHIC. The parameters of all three options are beyond the operating conditions of any existing machine. Thus, significant research and development is needed for either option.

3.2.2 Pressure Rise and Electron Cloud

This section reviews presently existing limitations on ion beam intensity due to pressure rise and electron cloud effects. Plans to overcome the limitations in order to increase the number of bunches, ultimately to 360, are considered.

Injection pressure rise

Pressure rise at the injection has been observed for gold, deuteron, and proton operations in the RHIC. This pressure rise limits operation of 112 bunches with bunch intensity of 10^9 gold ions, and 10^{11} for protons [11].
It has been diagnosed that the injection pressure rise is due to the electron multipacting, i.e. electron cloud. The evidences include,

1. Electron detector signals are very closely related with the pressure rise, at onset, saturation, and drooping.
2. Pressure rise and electron signal are very sensitive to the bunch spacing, 112 bunch mode is much worse than 56 bunch mode. Note that the sensitivity to bunch spacing is an important characteristic of the electron cloud.
3. Bunch gap helps.
4. Solenoid field at 5 to 50 Gauss can suppress both pressure rise and electron signal, but not completely.
5. Beam scrubbing has been demonstrated helpful in reducing pressure rise.

On the other hand, the electron cloud observed at the RHIC is different from other machines. For example, the RHIC electron cloud takes place at the bunch spacing of 108 ns or even 216 ns. All other machines have much smaller bunch spacing.

1. The B factories, KEKB and PEP II, have bunch spacing of 4 ns to 8ns.

2. Electron cloud was peaked at 20 ns of bunch spacing at the APS of Argonne.
3. SPS observed electron cloud at 25 ns bunch spacing with the threshold of bunch intensity of 3 to $4x10^{10}$ protons. At the bunch spacing 130 ns, no electron cloud observed at the bunch intensity of $2.5x10^{11}$ protons.
4. Tevatron observed electron cloud at 18.9 ns bunch spacing with the bunch intensity of $4x10^{10}$ protons. The situation is very similar to SPS. The Tevatron Run II plan calls for 132 ns bunch spacing with bunch intensity of $2.7x10^{11}$ protons.

The RHIC pressure rise and electron cloud have several distinguished characteristics from other machines.

1. It only takes place in warm sections, and the pressure rise distribution in the ring is very un-uniform. When pressure rise at certain location(s) is high enough to close the vacuum valve, many locations have none. The worst locations also may change.
2. Given same chambers, the beam intensity threshold at the Q3 to Q4 straight section, 34 meters long, is only 60% of that at the interaction straight section, which is 17 meters long.
3. No noticeable cryogenic heat load has been observed. Together with the absence of electron cloud induced beam instability and emittance growth, it is believed there is no electron multipacting at the RHIC cold region.
4. RHIC pressure rise decreases at the ramp, and it is non-existent at the store. In SPS, the electron activity was stronger at the store than at the injection [12].

It is suspected that the beam halo scraping at the wall, which generates mostly positive ions, may have helped the secondary electron to survive long bunch gaps, and makes electron multipacting possible. If this is the case, then most RHIC injection pressure rise observations can be explained.

During the 2003 polarized proton run, a beam scrubbing was studied. Total high intensity beam scrubbing time was less than 1 hour. However, beam scrubbing effect was observed not only in the locations with highest pressure rise, but also in others with non-trivial pressure rise. The feasibility of applying the beam scrubbing in RHIC to allow for higher beam intensities has been confirmed.

In Figure 3.18, it is shown that for locations with high pressure rise at about $5x10^{-6}$ Torr, the pressure rise kept about the same for 3 fills. For locations with medium pressure rise of about $5x10^{-7}$ Torr, the pressure rise increased. For locations with low pressure rise at less than $5x10^{-8}$ Torr, the pressure rise of 3rd fill is about 2.5 times higher than the first fill, which is approximately reflecting the beam strength in terms of exciting electron multipacting.

In Figure 3.19, the scrubbing effect at all locations in the ring is displayed against the dose. Note that the dose is defined as the pressure rise times the beam scrubbing duration.

For RHIC operation, the complete elimination of the injection pressure rise is not necessary. Therefore, a limited time of high intensity beam run might be sufficient to allow beam injection with higher intensity.

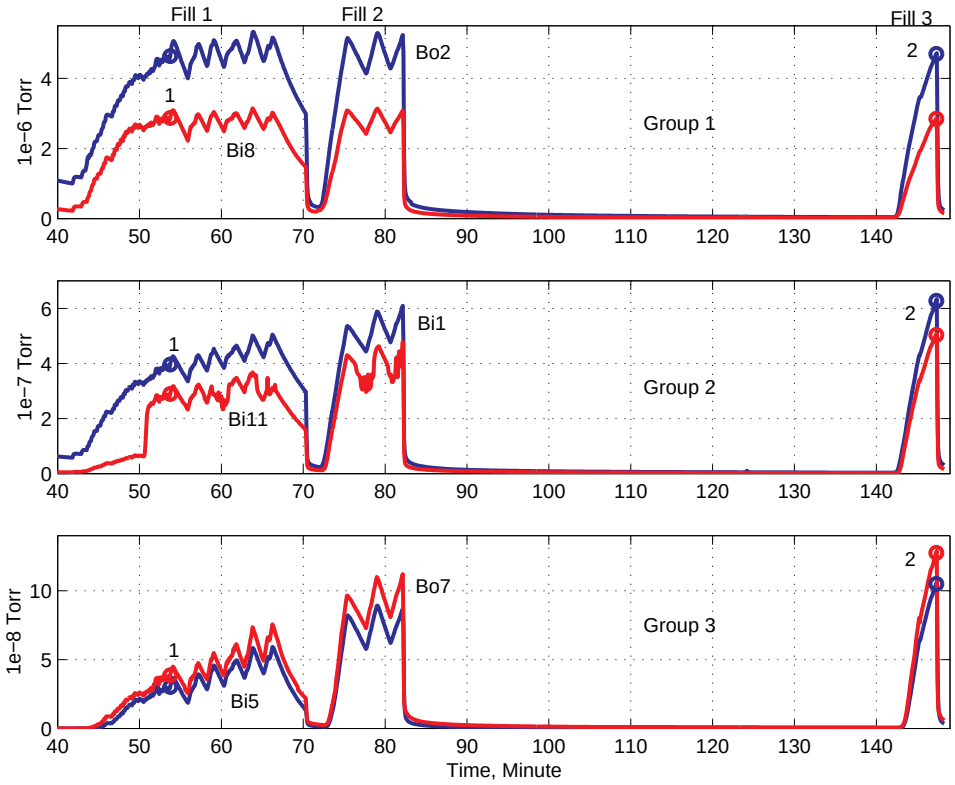

Figure 3.18: Typical pressure rise pattern for three different groups, with the high, medium, and low pressure rises.

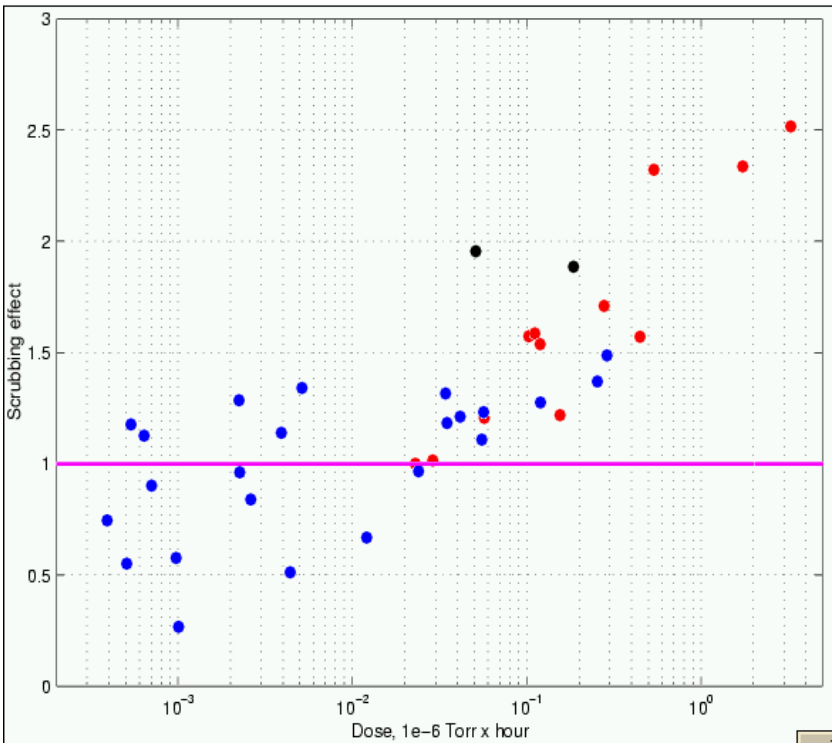

Figure 3.19: Beam scrubbing effect. Unit 1 means no scrubbing effect. Red dots are for the Q3-Q4 single beam straight sections. Black dots are special ones in sections 4 and 10. Blue dots are for interaction regions.

Transition pressure rise

The beam transition pressure rise for heavy ion operations is another intensity limit for the RHIC. In Figure 3.20, the transition pressure rises in the deuteron-gold (d-Au) run at IR2(BRAHMS), IR10(PHOBOS), and IR12 are shown against the total beam intensity. Intensity unit is charge equivalent to 1e9 Au ions.

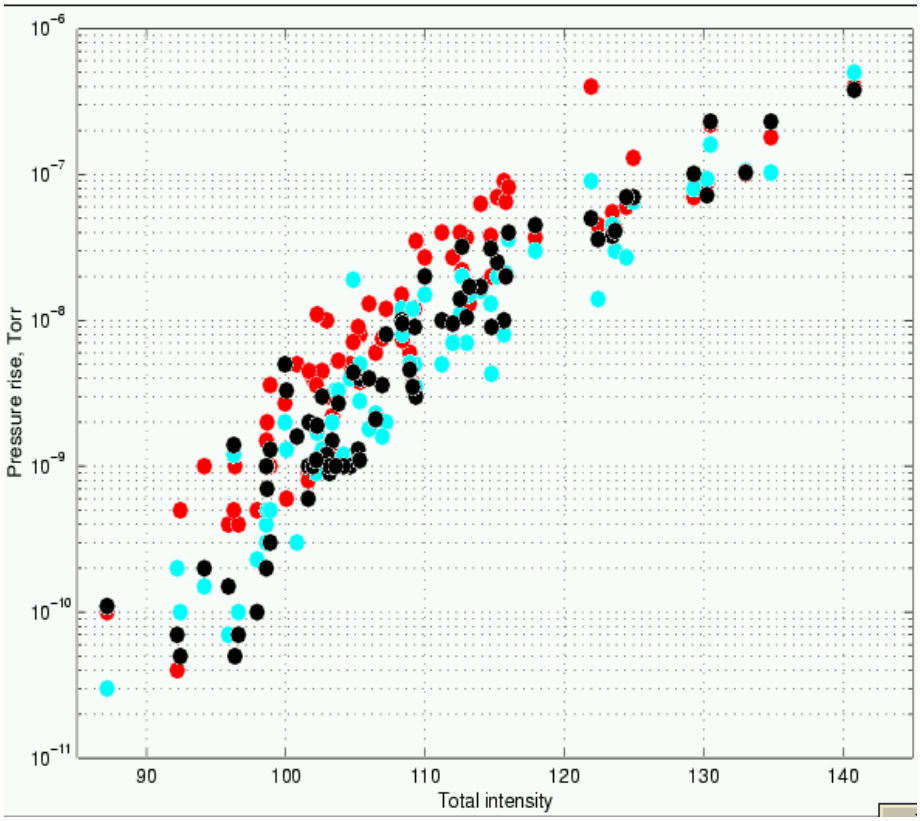

Figure 3.20: Transition pressure rise at IR2 (red), IR10 (cyan), IR12 (black).

The characteristics of this pressure rise are as follows:

1. The pressure rise is quasi-exponentially proportional to the total beam (charge) intensity.
2. For same intensity, no difference between 56 bunch and 112 bunch modes can be identified. The absence of bunch spacing efect indicates that the transition pressure rise is not dominated by the electron cloud. Another evidence is that no electron multipacting signal has been detected at the transition.
3. In Figure 3.20, most high intensity ramps are included, where the beam loss at the transition varies from less than 1% to larger than 10%. The reasonably narrow band in the pressure rise distribution indicates that the beam loss is not a dominant factor.
4. The pressure rise is not related to the ion species. The gold beam intensity was considerably higher than the deuteron in early run. After the deuteron bunch merge in the AGS Booster, the deuteron intensity was much higher than gold beam. No difference can be identified regarding to these different beams. Since the gold ion gas desorption cross section is about 79 times larger than the deuteron ion, this indicates that the gas desorption is not a dominant factor in the transition pressure rise.

It is found that the transition pressure rise is, on the other hand, related to the beam momentum spread:
The beam momentum spread is 0.17% at the injection, it is peaked at 0.3% at the transition, and decreases afterwards. The pressure rise follows this pattern. In proton run, the beam momentum spread decreases in the acceleration, and the pressure rise decreases as well.
The bunch length seems not a dominant factor in the transition pressure rise. At the beam rebucketing, where the bunch was captured in 200 MHz storage cavity, the bunch length reduces to 5 ns, the same as that at the transition (the beam potential at the rebucketing is actually 37% higher than that at the transition due to the smaller transverse size), yet no rebucketing pressure rise observed in the d-Au run.
The total storage cavity voltage was 2.5 MV in d-Au run. At the rebucketing, the beam momentum spread was 0.17%, the same as that at the injection, and much lower than 0.3% at the transition. This may explain the absence of the pressure rise at the rebucketing.
In Run 4, two more common cavities have been commissioned to increase the total rebucketing voltage to 4 MV. The beam momentum spread at the rebucketing becomes larger than 0.19%. The pressure rise was observed at several interaction regions. Much higher storage voltage and the better rebucketing imply higher beam peak current and beam potential. Accordingly, some electron multipacting may have been observed at the rebucketing in Run 4.
The transition pressure rise had caused serious experiment background problem in d-Au run. For same luminosity, 56 bunch mode requires 30% less total intensity than the 112 bunch mode. Switching from 112 bunch mode to 56 bunch, the experiment background was significantly improved. One might expect that the background problem will be relevant again at higher beam intensity, since given 56 bunch mode, the luminosity increases at the square of the bunch intensity, whereas the transition pressure rise is quasi-exponential to that.
Some NEG (non-evaporable-getter) pipes have been installed in the RHIC rings for test. Very rough surface of the activated NEG coating is essential for better pumping. As by-products, the SEY (secondary electron yield) and electron desorption reductions have been measured for the NEG coating, where the rough surface may have contributed. To alleviate the transition pressure rise, ion desorption reduction might be more important. The data on this aspect is, however, less than sufficient. The NEG pipes in RHIC have made possible for the evaluation on ion desorption, and also other issues, such as the activation condition, the saturation effect, the aging, venting effect, possible dust, and impedance problem, etc.
For same purpose, a test stand has been built at the Tandem Van de Graaff. Different activations will be tested, and also the ion desorption on the shallow angle ion beam scraping on stainless steel and NEG surface will be compared.

Scenario of 360 bunches in RHIC

In the scenario of 360 bunches in the RHIC, not only the injection and transition pressure rises, but also a usual electron cloud may take place for both proton and heavy ion beams. With the bunch spacing of 35 ns, eRHIC is very similar to SPS and LHC in terms of electron multipacting. In Table 3.2, the eRHIC heavy ion and proton parameters are compared with the SPS and LHC, where $\langle \Delta E \rangle$ is the energy gain per bunch passing.

Table 3.2. Parameters defining electron multipacting for eRHIC, SPS and LHC

Injection/store	eRHIC, Au	eRHIC, p	SPS	LHC
Kinetic energy, E_k, *GeV/u*	8.9/100	24/250	26/450	450/7000
Charge per bunch,N_{bh} ,10^{11}	0.79	1	1	1
Bunch spacing, t_{bs}, *ns*	35	35	25	25
Chamber radius, *b*, *cm*	3.45	3.45	2.5	1.74
Beam radius, *a*, *mm*	3.0/0.93	1.9/0.59	3.2/0.78	1.15/0.293
Energy gain, $\langle \Delta E \rangle$, *eV*	104/154	198/277	267/450	728/1095

The bunch spacing is one of the most important parameters. In general, larger the bunch spacing, less the secondary electrons survive the bunch gap, and higher SEY is needed for electron multipacting. The 35 ns bunch spacing at the eRHIC is only a little larger than the 25 ns at the SPS and LHC.
The second most important parameter is the energy the electrons gained during the one bunch passing, which is

$$\langle E \rangle = \frac{e}{2m_e}\left(\frac{N_{bh} e Z_0}{2\pi b}\right)^2 \ln\left(\frac{b}{a}\right) \qquad (3.1)$$

where $Z_0 = 377\,\Omega$ is the impedance in free space, and m_e is the mass of electron. Most important factor affecting $\langle \Delta E \rangle$ is the bunch intensity.

The intensity threshold at the SPS was considerably lower than the LHC beam requirement. It was 5 to 6 10^{10} at the straight sections, and 3 to 4×10^{10} at the dipoles. Only after several days of beam scrubbing, the LHC beam requirement was achieved.
For normal electron cloud, eRHIC have several new issues to deal with.

1. Electron multipacting in cold region. The chamber radius at the cold region is 3.46 cm, compared with 6.1 cm at warm sections. The multipacting threshold at the cold region is, therefore, lower. Once electron cloud built up, the cryogenic heat load will be of concern. Experiment data at the CERN SPS shows that the heat load is larger than 1.2 W/m under electron multipacting, which is not acceptable for RHIC cryogenic system [13].
2. Since the cold region consists 3/4 of the RHIC ring, the electron cloud induced beam instability and beam emittance will be of concern.
3. Electron cloud will present not only at the injection, but also at the ramp and storage.
4. Electron activity in dipole and quadrupole becomes relevant. The multipacting threshold at the dipoles is lower than that at the straight sections. Moreover, since the electron dose stripes in dipoles vary according to the bending field and beam intensity, the scrubbing is more difficult. As for quadrupole field, it is suspected the electrons are trapped there and stay for a long time.

The pressure rise at the cold region is probably not a problem, thanks to the cryogenic pumping.

Plans

RHIC pressure rise
Active study is undergoing at the RHIC in searching for the pressure rise and electron cloud remedies. Collaboration items with the eRHIC effort include,

1. Beam scrubbing, which has been demonstrated in principle, but further study is needed for incorporating it to the operation. First for proton beam, then for heavy ion beam.

2. Beam scraping study of ion desorption. The ion desorption of high energy particle at glancing angles is still a pending issue. At the RHIC Run 4, warm dipoles will be used to actually scraping ions at the wall to measure the ion desorption rate. Measurement will take place for both stainless steel and NEG pipes for comparison.
3. The relation between the beam momentum spread and the transition pressure rise remains to be clarified. By changing the RF voltage at the transition, this can be studied. The approach has a potential to provide a remedy for this pressure rise.

The RHIC effort in reducing the beam induced pressure rise is past two years has already gained much better understanding and the machine improvement. These efforts, such as baking, solenoid, beam scrubbing, beam injection pattern, and NEG coating will likely to take effect and gradually improve the RHIC performance.

Electron cloud

The 360 bunches mode cannot be studied at the RHIC, due to the lack of beam injection apparatus. Since the situation will be very similar to the LHC, a collaboration should be pushed forward. Fortunately the intense studies have been undergoing for several years in the CERN, including numerous beam experiments at the SPS, simulation, and theoretical efort. Suggested collaboration items include,

1. Heat load problem. Experiments at the SPS, during the 2003 run, have shown that the heat load is significant enough to be treated seriously. Further data are of interest.
2. Electron activity at dipoles and quadrupoles.
3. Beam scrubbing efect at the cold region. Also in 2003 SPS experiment, it was found that the cold region scrubbing was much less effective than that at the warm region [13]. According to these results, the current LHC plan calls for initially using not higher than 4 10_{10} protons per bunch for 25 ns bunch spacing, and/or a 75 ns bunch spacing injection. The lengthy scrubbing scenario is under study, which is pending on several unknowns, such as the possible beam instability during the scrubbing, the maximum heat load can be tolerated, and magnet quenching problem.

The eRHIC-LHC collaboration should be on both experimental and theoretical aspects, and simulation will be an important tool.

180 bunch scenario

Given luminosity unchanged, it is of interest to study the benefit of using larger bunch spacing and higher bunch intensity.

Issues related with the 180 bunch (70 ns bunch spacing), with 40% increase in bunch intensity, include,

1. Electron activity will be reduced compared with the 360 bunch mode. The decrease of the electron activity is more than linearly proportional to the inverse of bunch spacing. The experimental data of the SPS are shown in Table 3.3 [14].

Table 3.3. Bunch intensity threshold versus bunch spacing from SPS experimental data.

Bunch spacing	25	50	75	ns
Bunch intensity threshold	0.3	0.6	1.2	10^{11}

2. In 180 bunch scenario, the total beam intensity is reduced. This will benefit at least the pressure rise in warm sections, perhaps more.
3. Heat load needs to be estimated, including the resistive wall contribution.

4. Beam scrubbing needs to be studied.

3.2.3 Beam Abort Issues

The general issue considered in this section is to what extent an upgrade of the present RHIC beam abort system is required to cope with the eRHIC design level beams. An eRHIC proton beam would contain 360 $1x10^{11}$ proton bunches at an energy of 250 GeV. The specific issue which appears most likely to require some upgrade is the likelihood that beam "punch through" from a well-controlled dumping of a design level eRHIC proton beam would quench the magnet downstream of the dump absorber. In addition the increased heating and stresses in the steel section of the absorber need to be revisited.

For reference the present Accelerator Safety Envelope (ASE) limits beams in RHIC to be less than (120 proton bunches of $2x10^{11}$ particles each at 250 GeV). The ASE also sets maximum numbers for a gold beam, namely (120 gold bunches of $2x10^{9}$ gold ions at 100 GeV/u). The gold situation is relevant here to the extent that we try to learn from gold experience - past or future. The proton and gold ASE limits correspond to machine setups with equal magnetic fields or currents in the RHIC superconducting magnets and hence to magnets running with equal beam-heating margins before quenching. The proton and gold limits also correspond to approximately equal radiation "dose" creation outside the machine shielding for a loss of the same fraction of the entire beam. The two ASE limits do not necessarily correspond to equal risks for beam induced quenches. That the present proton ASE would be exceeded by 50% for the eRHIC design is not the subject here, but of course this dose production is a major ASE issue, which will need to be reconsidered. Also any proposed near-term beam tests toward understanding the dump absorber behavior during an eRHIC size beam dump must still cope with the RHIC ASE.

Present experience with dumping high intensity beams is given (approximately) by gold beams at 100 GeV/u and with 60 x $1x10^{9}$ ions and by proton beams at 100 GeV and with 60 x $1x10^{11}$ protons. The 100 GeV proton experience teaches us little since the magnets are powered with only 40% of the current required for eRHIC. The quench margin is large. The gold experience is with the right RHIC magnet currents – the right quench margin. The total beam energy is lower that eRHIC by a factor of six. As will be mentioned again below, this is not the only trouble with gaining relevant information from gold dumps.. Simulations have indicated that for gold and proton beams with equal energy the magnet heating from beam escaping the dump absorber is not equal, and unfortunately higher by a factor of 2 -3 for the proton beam.

Experience with the present abort system reliability has not been satisfactory in that the system has "prefired" too frequently. A prefire means that one out of the abort system's five PFN–magnet modules has triggered spontaneously causing the loss of the circulating beam. The prefire starts with a very weak kick given to some of the beam and with the rise of the abort magnet currents not synchronized to the "abort gap" present in the circulating beam. A fast "retrigger" circuit greatly reduces the damage from such events (at least at past intensities) to the RHIC experiments, but has not prevented many magnet quenches (and lost beam time). The damage from prefires would scale with the intensity of circulating beam. With a factor of six more beam in the machine, losses marginally tolerable now would probably be intolerable. This situation is already not acceptable and so the problem will be solved or at least greatly improved independent of eRHIC.

The beam energy available for deposit into the dump absorber is larger than our present experience by the factor of six. As a result the heating in the absorber will increase significantly. For the RHIC design this general subject was studied and reported on by A.J.Stevens in [15]. The initial energy

deposition as the beam enters the dump absorber is predicted to be not as severe for eRHIC as for even our present running conditions with gold due to the "Z^2 " dependence of the initial ionization energy loss. The maximum stresses in the downstream steel section will increase, and need to be revisited. For the geometry studies in the '92 note, they were shown to be acceptable with RHIC design intensity. Stevens' work was done with an absorber design somewhat different from what was actually built several years later. In particular he is working with an upstream carbon section 1.5 meters long while the constructed absorber has 3.2 meters of carbon [16]. The longer carbon section will reduce the peak stress in the steel. Another upgrade to attack this problem is suggested in the introduction section of [17], namely to add a vertical sweeping magnet upstream of the absorber to further spread the incoming beam over the absorber face. Temperature issues with a longer time constant are also relevant. The Beam Dump section of the RHIC Design Manual states that a system to actively cool the absorber is unnecessary for beams up to four times RHIC design and bumped once per hour. The eRHIC design intensity would require revisiting this aspect of the situation.

Now the "punch through" issue is discussed. The question is: will the magnet (Q4) just downstream of the dump absorber quench if an eRHIC design intensity beam is dumped in a well-controlled way? Two RHIC reports by A.J. Stevens [18],[19] deal with this subject. The earlier report uses a less specific model for the vacuum chamber and magnet geometry. The second is fairly close to what was actually built.

Some of the conclusions from these reports are summarized here. For a geometry close to that built, and with several conservative assumptions described in the reports, there is no margin for quenching at the RHIC design proton running conditions – at 60 bunches each with 10^{11} protons and at 250 GeV. This at face value implies that the eRHIC condition would push Q4 over the quenching limit by the factor of six. Also in these notes, and as mentioned above, Stevens reports that simulations suggest 10^9 gold ions at 100GeV/u creates a lower hot spot in the magnet coil than 10^{11} protons at 250Gev by a factor of 2 to 3. Stevens simulated one possible modification from what became the as-built geometry, namely using a beam pipe for the beam circulating just beside the primary dump absorber with a 3mm wall thickness vs the "as-built" 1.25mm. This change increased the predicted quench margin by a factor between 2.5 and 5. Stevens also suggested adding a shielding "collar" at the upstream end of Q4, (the design manual speaks of adding a Q4 liner), and magnetizing the steel of the dump absorber as potentially effective modifications. He notes but does not quantify, that the amount of punch through is sensitive to the size of the abort kick – so a stronger kicker would also decrease the heating in Q4. Clearly there needs to be additional simulation work with the present geometry to see how significant a redesign is required to satisfy eRHIC, and the work by Stevens points in some reasonable directions.

Can any information be deduced from the fact that RHIC is no longer just a paper machine? Q4 has not quenched during dumps. This is a necessary condition to believe the past simulations, but not useful beyond that. Gold at 100 GeV/u and at the ASE intensity limit would be interesting, but again not sufficient since it is expected that gold is less effective in generating the quench conditions. Protons only get interesting at 250 GeV, which is not a planned running configuration for a few years. If this condition were available, then dumping at the proton ASE is certainly interesting, since that condition is only 50% away from the eRHIC design. The injector is not a limit for proton intensity, so doing such a test is not completely crazy, though obviously RHIC must be able to accelerate the beam.

3.2.4 Cryogenic Load Limit

RHIC is a superconducting machine and all its magnets, dipoles and quadrupoles, are superconducting magnets. Because of this most of the RHIC beam pipe is at cryogenic temperature. The limit on allowable heat load on the walls of the cold vacuum chamber provides a serious limitation on the total beam intensity which can be stored in ion rings. The capacity of the present refrigerator of the RHIC cryogenic system defines the maximum allowable heat load at the level of 0.5-1 W/m. Two dominating sources of the vacuum pipe heat load are pipe heating by the image current of the beam due to finite wall conductance and heating produced by the electron cloud.

The vacuum pipe used at the RHIC is made from stainless steel with the conductivity of $\sigma = 2\,\mu\Omega^{-1}\mathrm{m}^{-1}$ at 4.2K. Heat load produced in the resistive walls of the vacuum pipe depends on bunch intensity N_b, number of bunches M in the beam and on the rms length σ_l of individual bunch. To evaluate the power P of the resistive heat load the expression derived in the paper [20] has been used:

$$P = 2I_{ave}^2 \sum_{n=1}^{\infty} R_c \left(\frac{n}{n_c}\right)^{\frac{1}{2}} \exp\left(-n^2\alpha^2\right) \qquad (3.2)$$

where I_{ave} is the average beam current, $\alpha = M\sigma_l / R_0$ and R_0 is the average ring radius. The parameters of critical resistance R_c and critical harmonic number n_c are defined by properties of the vacuum pipe such as the conductivity, mean free path length for electrons and the pipe radius. For the RHIC stainless steel vacuum pipe at 4.2K temperature these parameters are equal to:

$$R_c = 6.04\times10^6\ \Omega, \qquad n_c = \frac{8.0\times10^{11}}{M}$$

Due to very large value of n_c the anomalous skin effect is not important for the RHIC vacuum pipe and is not taken into account in the expression (3.2). Figure 3.21 shows results of resistive heat load calculations versus rms bunch length for different number of bunches with 10^{11} proton bunch intensity . At 360 bunches the heat load limit of 0.5 W/m is reached at $\sigma_l \approx 12cm$. The rms bunch length value for eRHIC operation, 20cm, stays by more than factor 2 below the cryogenic limit, thus providing necessary safety margin.

Since the result of the infinite summation in the equation (3.2) is approximately proportional to $M^{-1}\sigma_l^{-3/2}$ the resistive heat load power is proportional to $M \cdot N_b^2$. Then for the eRHIC luminosity in cryogenic load limit $P_{\lim}$, at fixed bunch length, one gets dependence: $L \sim P_{\lim}/N_b$. It shows that at the same total proton current increasing the number of particles per bunch effectively leads to lower luminosity. Increasing the number of bunches while decreasing the bunch intensity would be a way to go to higher luminosity. But it will require the serious upgrade of RHIC RF system.

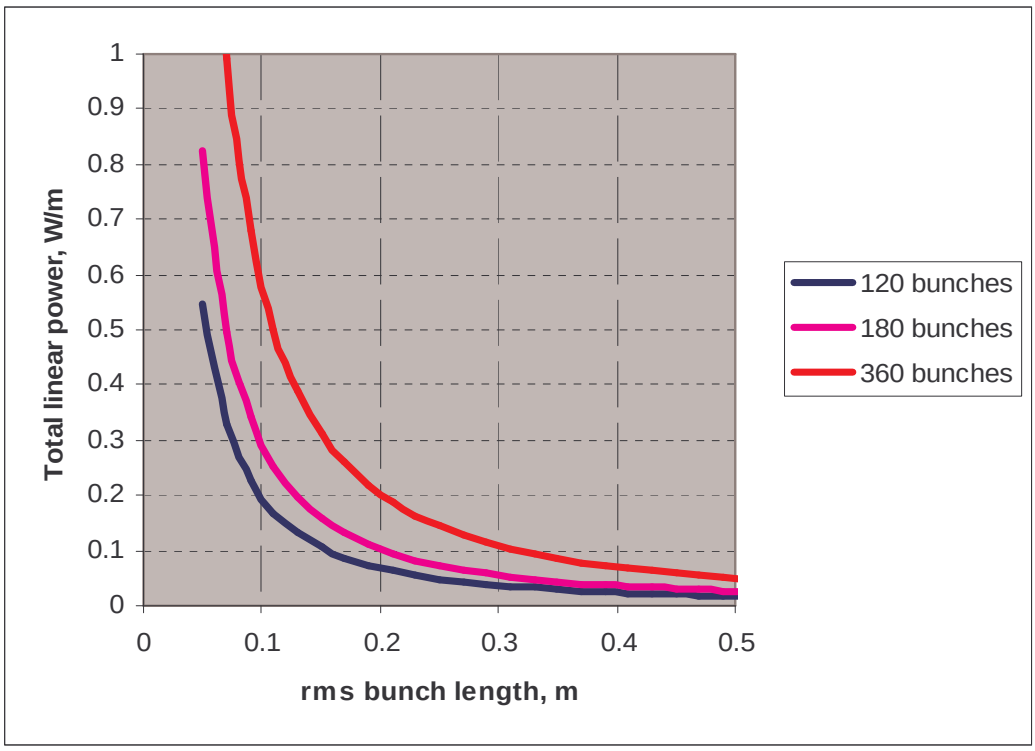

Figure 3.21:The resistive heat load power per unit length versus rms bunch length for different number of bunches with the intensity of 10^{11} protons per bunch. The maximum allowable load defined by RHIC cryogenics is about 0.5 W/m.

The heat load contribution from electron cloud might be very important as demonstrated by experiments done at SPS accelerator at CERN. Heat load more than 1 W/m has been observed there at similar to RHIC bunch intensities but with smaller distance (25ns) between bunches [13]. The subject will require careful studies to evaluate a contribution from this source of heat load for eRHIC parameters.

3.3 Instabilities

At present we are most troubled by single bunch transverse instabilities near transition. The transverse impedance model is low by about a factor of 3 [21],[22] , so we will scale the most extreme conditions from the last run to obtain threshold estimates.

For a short range transverse wake field, the rigid mode betatron tune shift is $\Delta Q = K_0 Z I_p / A\gamma,$ where K_0 is a constant that depends only on the lattice and machine impedance, Z and A are the atomic number and mass of the ion, I_p is the peak beam current, and γ is the Lorentz factor. When the rigid mode tune shift becomes too large, instabilities can result.

The fast head tail, or transverse mode coupling , instability threshold is reached when the rigid mode tune shift becomes comparable to the synchrotron tune. This threshold also depends on the relative length scales of the bunch and the wake field [23],[24]. For a general wakefield the dependence is fairly complicated but since the instability is due to coupling between low lying snychro-betatron modes a pessimistic estimate can be made by assuming that the wakefield is a step function. In this

case the instability threshold for a rectangular bunch is given by $\Delta Q = Q_s / 2$. For a 2 particle model one gets $\Delta Q = Q_s / \pi$, suggesting that the estimate is fairly robust.

For unstable transverse microwave modes the threshold is $\Delta Q = K_1 |\xi + n\eta| \delta + q$, where K_1 is a constant of order unity, ξ is the un-normalized chromaticy, $n = f / f_0$ is the ratio of the instability carrier frequency to the revolution frequency, η is the frequency slip factor, δ is the fractional, rms momentum spread, and q is the rms detuning with betatron amplitude. For $\xi = q = 0$, and $1/f$ equal to the bunch length, the transverse microwave threshold is similar to the fast head-tail threshold. Direct addition of the detuning and momentum dependent damping terms is a rough approximation and more accurate formulas will be considered in the future.

A high intensity study from May 30, 2003 sets strong limits on the various thresholds.

Six bunches of 2×10^{11} protons with $I_p = 5.5A$ were stored with $\gamma = 25$. The rms bunch length was $\sigma_t = 2.3ns$, so $c\sigma_t = 70cm$. The synchrotron frequency was about $25Hz$ and the 95% normalized transverse emittance was between 15 and 25 mm-mrad.

The rms detuning with amplitude was calculated from a model to be $q = 2\times10^{-4}$. Since the synchrotron tune was $\approx 3\times10^{-4}$, the damping from each source is comparable. For eRHIC operations the synchrotron tunes will be no smaller than those during the study. If we assume that the octupoles can always be tuned to give the same rms tune spread then thresholds during eRHIC operation can be estimated by demanding that the rigid mode tune shift be no larger than it was during this study. Take $c\sigma_t = 15cm$, which is the nominal bunch length during collision for eRHIC. The maximum bunch intensities calculated by this method are shown in the third column of the Table 3.4.

Table 3.4: Estimated bunch intensity thresholds for different species and energies.

gamma	Species	Threshold, same ΔQ
25	Protons	4.3E10
107	Protons	1.8e11
250	Protons	4.3e11
107	Gold	5.8e9

As one can see from the Table 3.4 the low and medium energy protons are the most worrisome. However, by demanding the same tune shift we have neglected a significant benefit from the shorter eRHIC bunches. Since the eRHIC bunches are less than half as long as the bunches during the study , the synchrotron frequency in eRHIC can be more than double the value during the study without increasing the momentum spread of the bunch. Also, the octupoles were off during the study and operations with gold beams have shown that an octupole induced tune shift of comparable magnitude to the tune shift from the bare lattice can be tolerated. Therefore, it is likely that careful tuning will allow for double the intensities in the third column of the table.

With the exception of transition, single bunch longitudinal instabilities have not been observed in RHIC. These instabilities occur only when the coherent synchrotron tune shift becomes comparable to the synchrotron tune. This is equivalent to demanding that the induced voltage from the machine impedance be comparable to the rf voltage. Setting these equal gives $|Z/n| I_p = h\omega_0^2 \sigma_t^2 V_{rf}$, where |Z/n| is the broad band impedance, h is the rf harmonic number, and V_{rf} is the amplitude of the rf voltage. The most stringent condition occurs for protons with $\gamma = 25$ since the proximity to transition reduces the allowed rf voltage. If we take the conservative value of $Z/n = 3j\Omega$ and the

same momentum spread as was obtained during the study one finds a threshold intensity of 1.8×10^{11} protons per bunch. The actual impedance near transition is about half of the conservative estimate so no longitudinal single bunch instabilities are expected in eRHIC.

With short bunch spacing and large average current, coupled bunch instabilities are a concern. Both short and long range wakefields along with the sources and amounts of collisionless damping available are key points. Since both longitudinal and transverse single bunch instabilities are not expected the short range wakefields are not large enough to overcome the collisionless damping. Therefore, we expect coupled bunch instabilities only if the tune shifts due to long range wakefields are larger than the tune shifts due to short range wakefields. The transverse impedance due to resistive wall, abort kickers and unshielded bellows is shown in Figure 3.22: Transverse resistance (red) and reactance (blue) from the RHIC impedance model. Figure 3.22 and the resulting rigid mode coupled bunch tune shifts are shown in Figure 3.23.

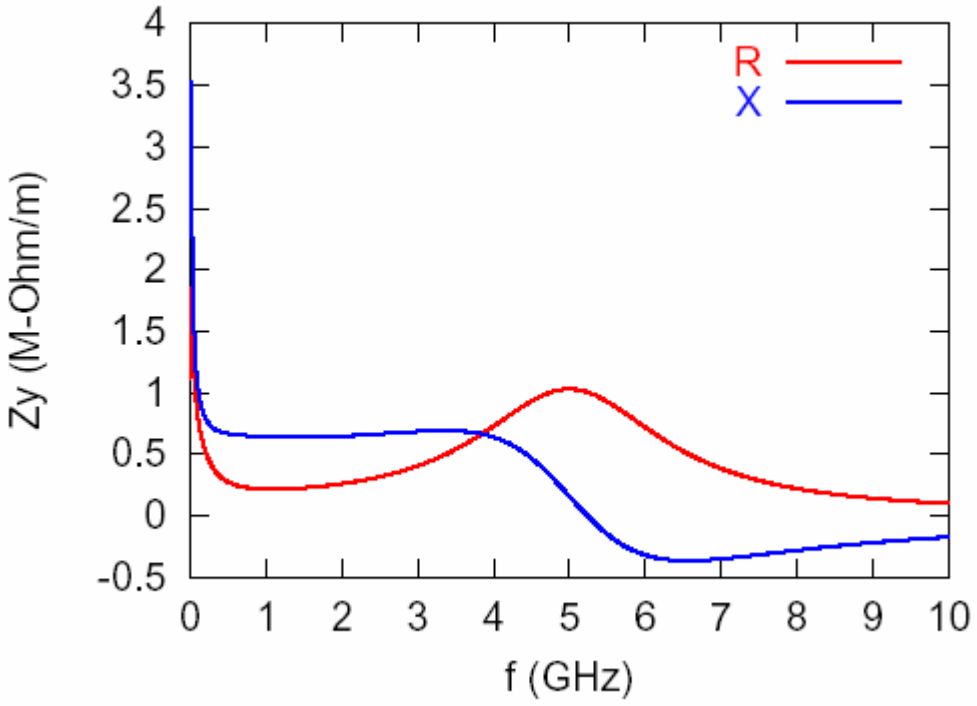

Figure 3.22: Transverse resistance (red) and reactance (blue) from the RHIC impedance model.

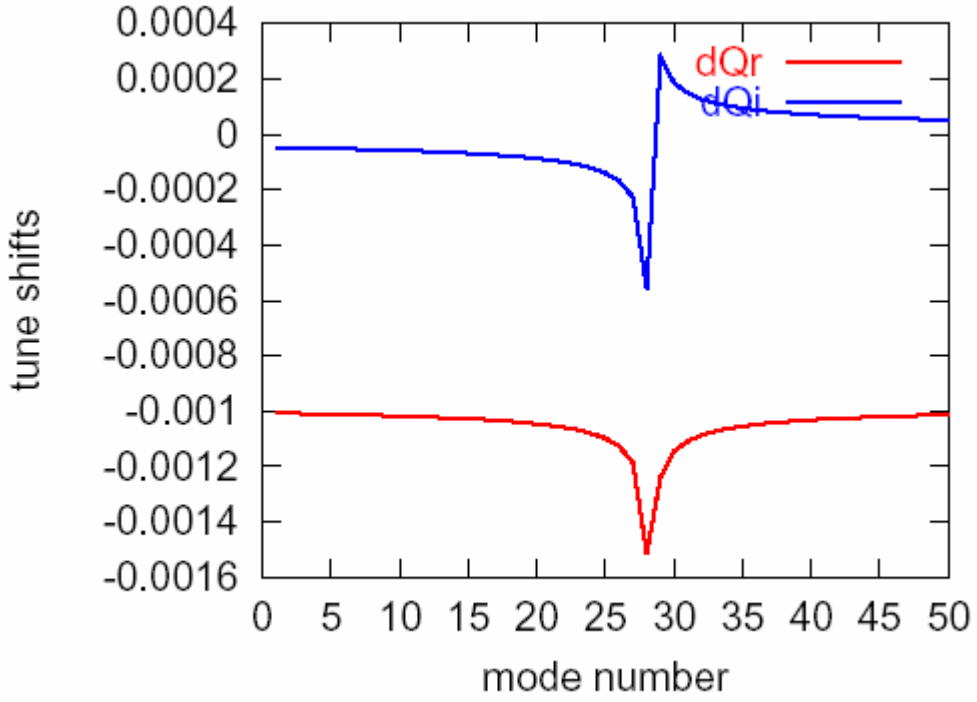

Figure 3.23: Real (red) and imaginary (blue) tune shifts for the rigid coupled bunch modes of protons with eRHIC parameters at $\gamma = 25$. All Landau damping is neglected.

Near the peak of the resistive wall growth rate, at mode number 29, the magnitude of the coherent tune shift is about 50% larger than the value for small mode numbers.
This is not too great a difference so if single bunch instabilities are absent we expect no problems from transverse coupled bunch modes. If there are problems then the maximum growth rate in figure 2 corresponds to an e-folding time of 5 milliseconds, which should be fairly easy to damp. Once the beams are brought into collision the nonlinear beam-beam forces will enhance the tune shift with amplitude providing even more transverse damping.
Longitudinal coupled bunch modes have not been studied in detail, but no serious problems are expected.

3.4 Beam Polarization Issues

Motion without snakes or spin rotators

To achieve a high energy polarized proton beam requires an understanding of the evolution of spin during acceleration and the tools to control it. The evolution of the spin direction of a beam of polarized protons in external magnetic fields such as exist in a circular accelerator is governed by the Thomas-BMT equation[26],

$$\frac{d\vec{P}}{dt} = -\left(\frac{e}{\gamma m}\right)\left[G\gamma\vec{B}_{\perp} + (1+G)\,\vec{B}_{\parallel}\right]\times\vec{P} \qquad (3.3)$$

where the polarization vector $\vec{P}$ is expressed in the frame that moves with the particle. Here $G=(g-2)/2$ is the anomalous magnetic moment coefficient, and $B_{\parallel}$ and $B_{\perp}$ are the respective longitudinal and perpendicular components of the magnetic induction in the laboratory frame. This simple precession equation is very similar to the Lorentz force equation which governs the evolution of the orbital motion in an external magnetic field:

$$\frac{d\vec{\mathrm{v}}}{dt}=-\left(\frac{e}{\gamma m}\right)\left[\vec{B}_{\perp}\right]\times\vec{\mathrm{v}}, \qquad (3.4)$$

where $\vec{\mathrm{v}}$ is the proton's velocity. From comparing these two equations it can readily be seen that, in a pure vertical field, the spin rotates $G\gamma$ times faster than the orbital motion. Here $G=1.7928$ is the anomalous magnetic moment coefficient of the proton and γ is the Lorentz factor. In this case the factor $G\gamma$ then gives the number of full spin precessions for every full revolution, a number which is also called the spin tune ν_{sp}. At top RHIC energy (250 GeV) this number reaches 478. Parameters for protons as well as a few other ion species are given in Table 3.5. The Thomas-BMT equation also shows that at low energies ($\gamma\approx 1$) longitudinal fields $\vec{B}_{\parallel}$ can be quite effective in manipulating the spin motion, but at high energies transverse fields $\vec{B}_{\perp}$ need to be used to have any effect beyond the always present vertical holding field.

Table 3.5. . Parameters for various polarized species. While deuterons and tritium ions are not presently being considered, they are included for reference. Parameters for electrons at 10 GeV are also shown for comparison.

	p	$^2\mathrm{H}^+$	$^3\mathrm{H}^+$	$^3\mathrm{He}^{+2}$	e^-
m [GeV/c^2]	0.9382720	1.8756127	2.80892823	2.8083912	0.0005109989
$G=(g-2)/2$	1.79284734	-0.1426177	7.918194	-4.18396	0.001159652
mc^2/G [MeV]	523.3418	13156.49	354.7435	-671.2216	440.6485
$R_{\mathrm{inj}}=p_{\mathrm{inj}}/q$ [Tm]	81.113	81.113	81.113	81.027	
U_{inj} [GeV]	24.335	24.364	24.479	48.664	
U_{inj}/n [GeV]	24.335	12.182	8.160	16.221	
γ_{inj}	25.9362	13.0034	8.7146	17.3280	
$G\gamma_{\mathrm{inj}}$	46.500	-1.854	69.004	-72.500	
$R_{\mathrm{store}}=p_{\mathrm{store}}/q$ [Tm]	833.904	833.904	833.904	833.904	33.356
U_{store} [GeV]	250.000	250.005	250.014	500.004	10
U_{store}/n [GeV]	250.000	125.003	83.338	166.668	10
γ_{store}	266.4473	133.2926	89.0069	178.0394	19569.54
$G\gamma_{\mathrm{store}}$	477.699	-19.062	704.774	-744.917	22.6938

The acceleration of polarized beams in circular accelerators is complicated by the presence of numerous depolarizing resonances. During acceleration, a depolarizing resonance is crossed whenever the spin precession frequency equals the frequency with which spin-perturbing magnetic fields are encountered. There are two main types of depolarizing resonances corresponding to the possible sources of such fields: *imperfection resonances*, which are driven by magnet errors and misalignments, and *intrinsic resonances*, driven by the focusing fields.

The resonance conditions are usually expressed in terms of the spin tune ν_{sp}. For an ideal planar accelerator, where orbiting particles experience only the vertical guide field, the spin tune is equal to $G\gamma$, as stated earlier. The resonance condition for imperfection depolarizing resonances arises when $\nu_{sp} = G\gamma = n$, where n is an integer. Imperfection resonances for protons are therefore separated by only 523 MeV energy steps. The condition for intrinsic resonances is $\nu_{sp} = G\gamma = kP \pm \nu_y$, where k is an integer, ν_y is the vertical betatron tune and P is the superperiodicity. For example at the Brookhaven AGS, $P = 12$ and $\nu_y \approx 8.8$. For most of the time during the acceleration cycle, the precession axis, or stable spin direction, coincides with the main vertical magnetic field. Close to a resonance, the stable spin direction is perturbed away from the vertical direction by the resonance driving fields. When a polarized beam is accelerated through an isolated resonance, the final polarization can be calculated analytically[28] and is given by

$$P_f / P_i = 2e^{-\frac{\pi|\varepsilon|^2}{2\alpha}} - 1, \tag{3.5}$$

where P_i and P_f are the polarizations before and after the resonance crossing, respectively, ε is the resonance strength obtained from the spin rotation of the driving fields, and α is the change of the spin tune per radian of the orbit angle. When the beam is slowly ($\alpha \ll |\varepsilon|^2$) accelerated through the resonance, the spin vector will adiabatically follow the stable spin direction resulting in spin flip. However, for a faster acceleration rate partial depolarization or partial spin flip will occur. Traditionally, the intrinsic resonances are overcome by using a betatron tune jump, which effectively makes α large, and the imperfection resonances are overcome with the harmonic corrections of the vertical orbit to reduce the resonance strength ε [29]. At high energy, these traditional methods become difficult and tedious.

Effect of Siberian snakes

By introducing a 'Siberian snake' [30], which generates a 180° spin rotation about an axis in the horizontal plane, the stable spin direction remains unperturbed at all times as long as the spin rotation from the Siberian snake is much larger than the spin rotation due to the resonance driving fields. Therefore the beam polarization is preserved during acceleration. An alternative way to describe the effect of the Siberian snake comes from the observation that the spin tune with the snake is a half-integer and energy independent. Therefore, neither imperfection nor intrinsic resonance conditions can ever be met as long as the betatron tune is different from a half-integer.

Such a spin rotator is traditionally constructed by using either solenoidal magnets or a sequence of interleaved horizontal and vertical dipole magnets producing only a local orbit distortion. Since the orbit distortion is inversely proportional to the momentum of the particle, such a dipole snake is particularly effective for high-energy accelerators, e.g. energies above about 30 GeV. For lower-energy synchrotrons, such as the Brookhaven AGS with weaker depolarizing resonances, a partial

snake[31], which rotates the spin by less than 180°, is sufficient to keep the stable spin direction unperturbed at the imperfection resonances.

Acceleration of polarized protons

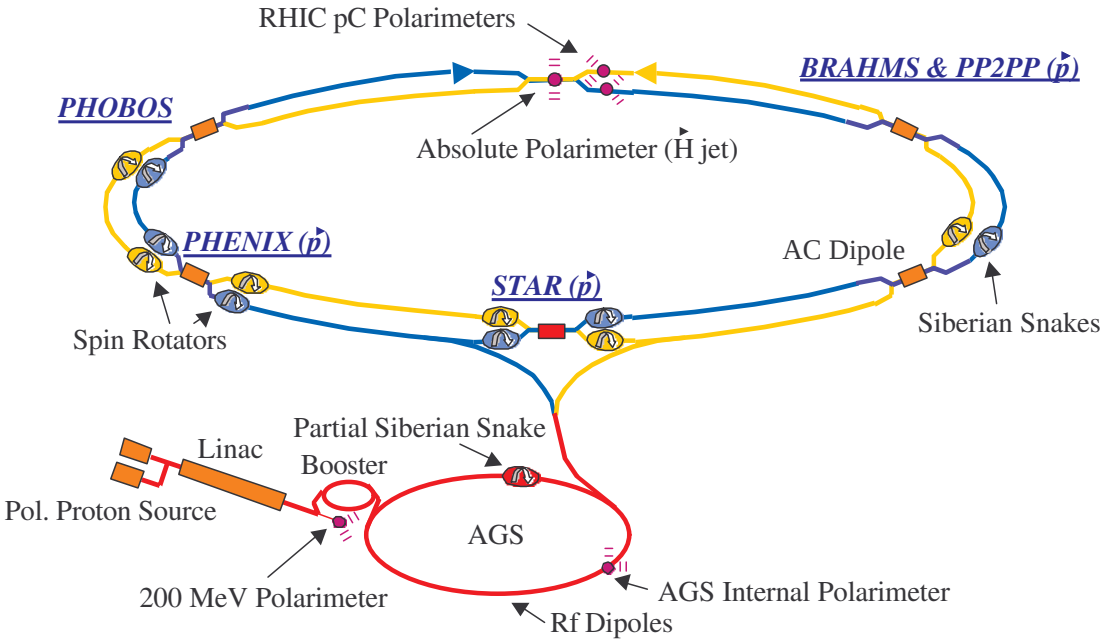

Figure 3.24. Present layout of RHIC accelerator complex for polarized protons.

Each snake and rotator is composed of four helical dipole magnets[32]. Helical field magnets have some distinctive advantages over more conventional transverse snakes or rotators: (i) the maximum orbit excursion is smaller, (ii) the orbit excursion is independent of the separation between adjacent magnets, and (iii) they allow an easier control of the spin rotation and the orientation of the spin precession axis.

In an ideal helical dipole magnet to be used for our purposes, the central dipole field should rotate through a complete 360° from one end of the magnet to the other. In a real magnet, of course, the fields at the ends of the magnet will also contribute to the particle dynamics. We require that the integrals $\int B_x d\ell$ and $\int B_y d\ell$ are both less than 0.05 Tm. The maximum body field will thus rotate through an angle less than 360° along the axis of the magnet. Moreover, in order to simplify the construction of the snakes/rotators, a solution has been found with all magnetic modules identical in both devices. For the snakes each helix is right handed with the field at the end being vertical. For the rotators, the helices alternate between right and left handedness with the field at the end of each helix being horizontal.

The orbit though an ideal helix will have the incoming and outgoing rays parallel but transversely displaced. In order to have a net displacement of zero through a snake we require that the offset be canceled by powering in pairs with opposite fields. The inner pair are wired in series with opposite polarity and powered by a common power supply. The outer pair are also wired in series with opposite polarity to a second supply. Figure 3.25 shows the field components, design orbit, and spin

rotation through a snake at injection energy. At 250 GeV the required fields are almost the same, but the orbit displacement in the middle of the snake is only about 3 mm.

By operating the helices at different currents it is possible to adjust both the amount of spin rotation (angle μ) and axis of rotation. With the helices wired as described above, the axis of rotation for the snake is in the horizontal plane at an angle ϕ from the longitudinal direction. Figure 3.26 shows the dependence of μ and ϕ on the two field settings – B_1 for the outer pair of helices, and B_2 for the inner pair.

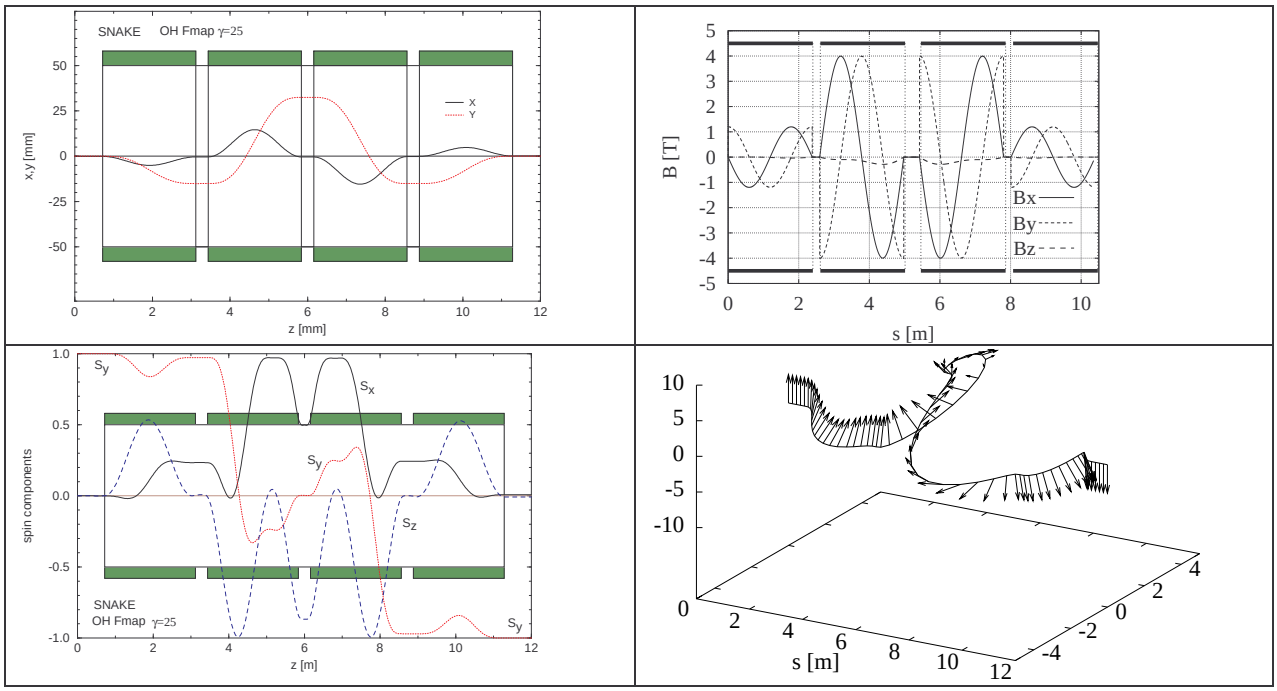

Figure 3.25: Field, orbit, and spin tracking through the four helical magnets of a Siberian snake at $\gamma = 25$. The spin tracking shows the reversal of the vertical polarization.

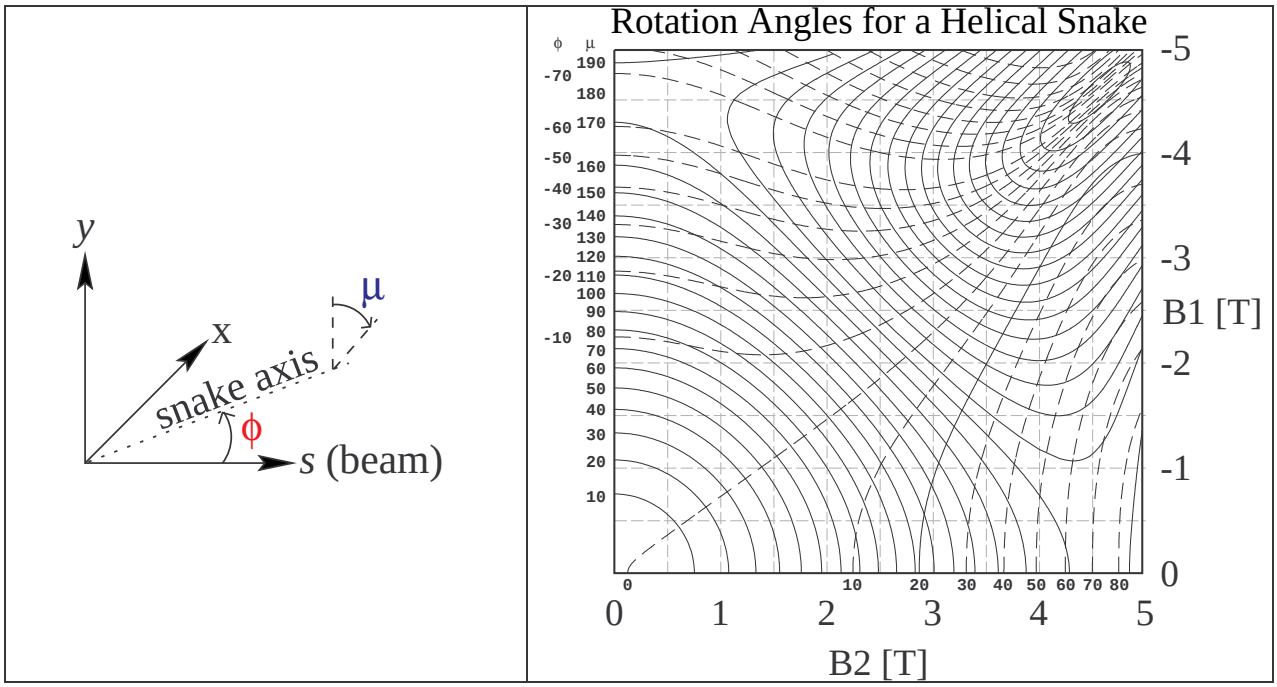

Figure 3.26: Change of the direction of the snake rotation axis as a function of magnet excitation. This calculation uses a simplified analytical expression for the snake magnetic field. The rotation axis of the snake is ϕ (dashed), and μ (solid) is the rotation angle. B_1 is the field strength of the outer pair of helices, and B_2 is the field strength of the inner pair.

For the ion beam in the electron-ion interaction region, a pair of spin rotators identical to the existing rotators around STAR and PHENIX may be used. Spin rotator parameters are listed in Table 3.6. The result of the orbit and spin tracking is shown in Figure 3.27. At STAR and PHENIX, the direction of the spin rotator beam line is at a horizontal angle $\theta = 3.674\,\text{mrad}$ with the direction of the adjacent insertion, the spin should emerge from the rotator in the horizontal plane and at an angle $G\gamma\theta$ with the rotator axis in order to obtain a longitudinal polarization through the insertion region. The needed rotation is therefore dependent on the beam energy. The values of the field needed to provide a longitudinal polarization at different energies are shown in Figure 3.28. The rotators will be turned on only after accelerating the beam to the desired storage energy.

In the electron-ion interaction region, the incoming and outgoing rotators are parallel to the beam at the interaction point. In this case, there is no net precession between the rotators and the collision point, so to obtain longitudinal polarization the rotators will be set with fields corresponding to the intersection of the $\theta = 0^\circ$ and $\mu = 90^\circ$ contours of Figure 3.28. With no extra precession from beam splitter magnets, there is no need to change values for different energies.

Table 3.6. Parameters for the spin rotator magnets. Helical magnets alternate right-handed and left-handed, and all begin and end with horizontal fields. The central field strengths were optimized to include end effects of the magnets, and are calculated for longitudinal polarization at the beam collision point.

Number of helical magnets				4	
Total length				10.56 m	
Magnet bore				100 mm	
Helical Magnets					
	Length (effective)	Field helicity	Field orientation at entrance/exit	Field (25 GeV)	Field (250 GeV)
1	2.40 m	right-handed	Horizontal	2.1 T	3.5 T
2	2.40 m	left-handed	Horizontal	2.8 T	3.1 T
3	2.40 m	right-handed	Horizontal	2.8 T	3.1 T
4	2.40 m	left-handed	Horizontal	2.1 T	3.5 T
Max. orbit excursion (hor./ver.) (25 GeV)				25 mm / 10 mm	
Total field integral				23 T-m	
Orbit lengthening (25 GeV)				1.4 mm	

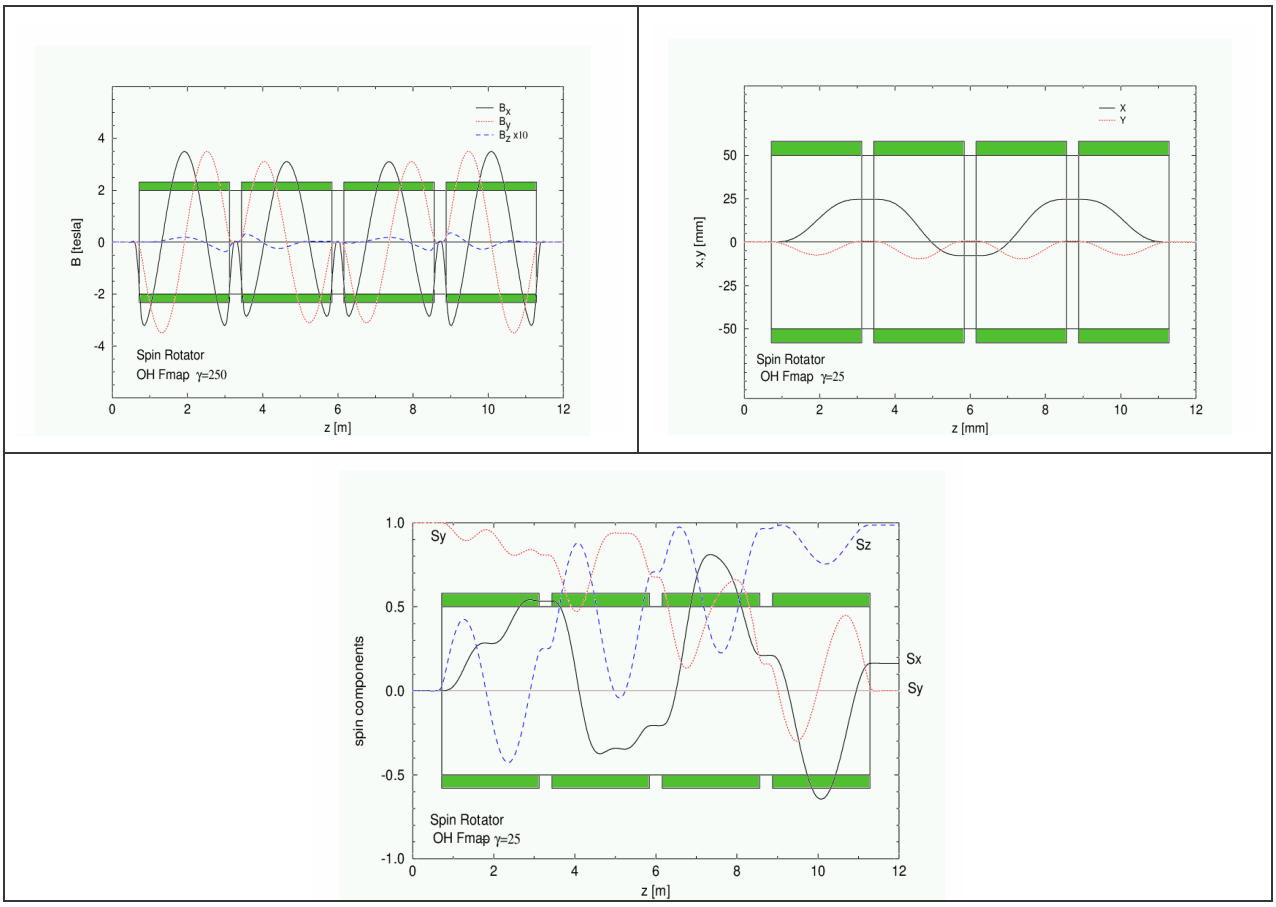

Figure 3.27: Field, orbit, and spin tracking through the four helical magnets of a spin rotator at $\gamma = 25$. In this example, the spin tracking shows how the polarization is brought from vertical to horizontal.

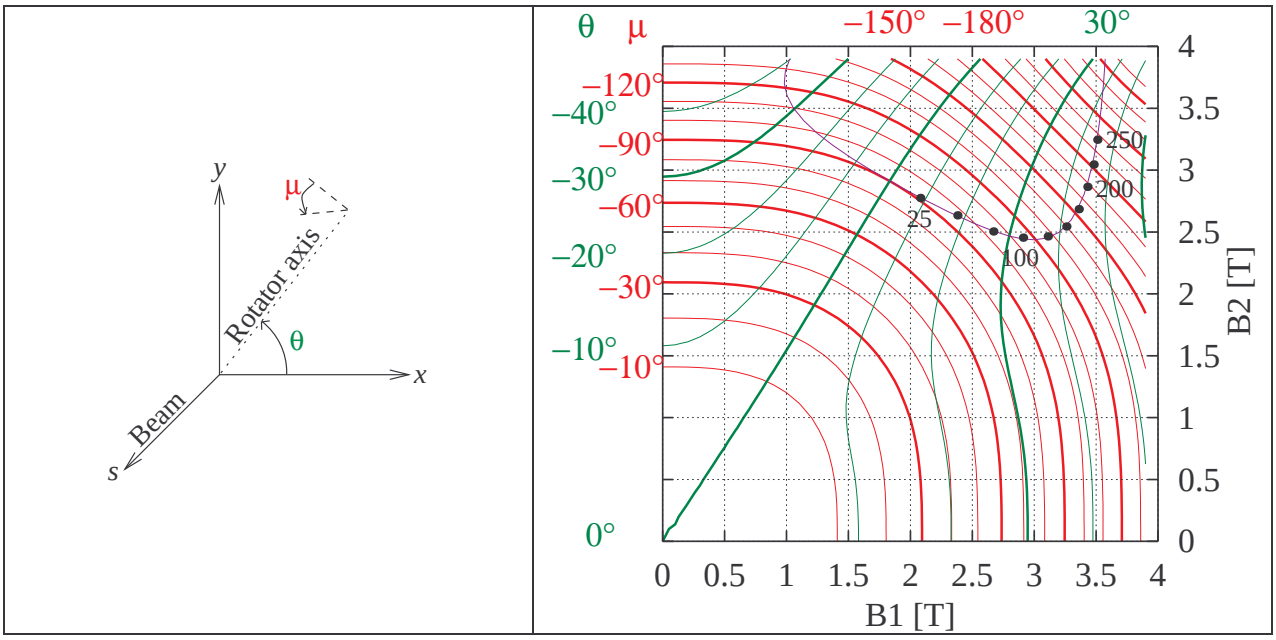

Figure 3.28: Excitation of the two pairs of helical magnets in the rotator to achieve longitudinal polarization in the insertion of RHIC, for various beam energies. The large dots indicate settings for the rotators around the STAR and PHENIX detector. For the eRHIC collision point, there is no net rotation between the collision point and the adjacent rotators, so the desired setting for longitudinal polarization corresponds to $\theta = 0^\circ$ and $\mu = 90^\circ$.

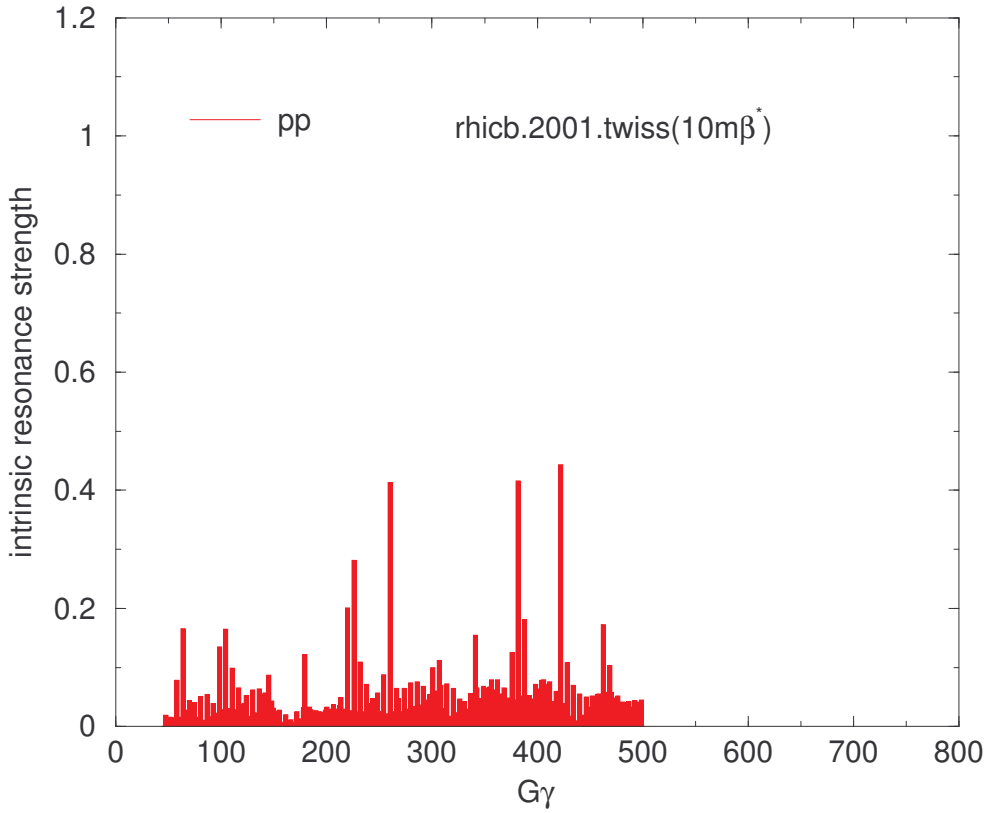

Figure 3.29: DEPOL calculation of intrinsic resonance strengths for polarized protons in RHIC without snakes.

Acceleration of polarized $^3He^{+2}$ ions

In order to scale to a different ion species such as $^3He^{+2}$, we should examine the parameters for a single RHIC rotator helix. The pitch is given by

$$k = \frac{2\pi}{\lambda}, \tag{3.6}$$

where $\lambda = 2.41\text{m}$ is positive for a right-handed and negative for a left-handed helix. The rotation axis is given by

$$\hat{n} = \frac{k\hat{z} + \kappa\hat{x}}{\sqrt{\kappa^2 + k^2}} \tag{3.7}$$

where

$$\kappa = \frac{q}{p}(1 + G\gamma)B \tag{3.8}$$

with a precession angle of

$$\alpha = 2\pi\left[\sqrt{1 + \left(\frac{\kappa}{k}\right)^2} - 1\right]. \tag{3.9}$$

The transverse step of the trajectory is

$$\Delta x = \frac{q}{p}\frac{B\lambda}{k} = \frac{q}{p}\frac{\lambda^2}{2\pi}B. \tag{3.10}$$

The Lorentz factor for a given rigidity is

$$\gamma = \sqrt{1 + \left(\frac{ZeR}{mc}\right)^2}, \tag{3.11}$$

for an ion with with rigidity $R = p/q$, charge Ze and mass m. We want to have the same spin precession in snakes and rotators for other ions as for protons. Keeping the rigidity constant for different ion species, we should scale the fields as

$$B_i = \frac{1 + G_p\sqrt{1 + \left(\frac{eR}{m_p c}\right)^2}}{1 + G_i\sqrt{1 + \left(\frac{eR}{m_i c}\right)^2}}B_p \tag{3.12}$$

from protons to ions, where the i-subscript indicates parameters for the ion.

Assuming that the maximum energy at storage corresponds to a rigidity of $R = 834\text{Tm}$, then the maximum value of Lorentz factor for $^3He^{+2}$ would be 178.039. Values for injection and storage energy are given in Table 3.5. It should be noted that there are about 56% more precessions for $^3He^{+2}$ than protons at the same rigidity. Since the precessions for $^3He^{+2}$ are larger, we should expect more depolarizing resonances. The resonances will also be stronger. This can be seen by comparing DEPOL calculations with no snakes for protons in Figure 3.29 and $^3He^{+2}$ in Figure 3.30. In principle with snakes, acceleration of $^3He^{+2}$ should be possible to full energy, but the closed orbit and tune requirements will be more severe for $^3He^{+2}$. The scaling to $^3He^{+2}$ for the rotators actually lowers the required fields to obtain longitudinal polarization. Table 3.7 gives rough values of field settings for the snakes and rotator settings (electron-ion experiment). Since the transverse excursions in scale

with field (See Eq.(3.10)), the beam excursions for $^3He^{+2}$ in snakes and rotators will be about 65% of the size of those for protons at the same rigidity.

Table 3.7. Approximate field settings for snakes (outer: $B_{1,s}$, inner: $B_{2,s}$) and rotators (outer: $B_{1,r}$, inner: $B_{2,r}$ at full energy. Note that even though G has opposite signs for protons and $^3He^{+2}$, the snakes power supplies do not need to be reversed, since we only require that the snake axes be at 90° to each other. Similarly the rotator supplies at the electron-ion experiment do not need to be reversed, since the precession is about the radial $\hat{x}$-axis in the rotators.

	p	$^3He^{+2}$
$B_{1,s}$ [T]	1.2	0.77
$B_{2,s}$ [T]	4.0	2.57
$B_{1,r}$ [T]	1.8	1.16
$B_{2,r}$ [T]	2.9	1.87

Other possible species

Acceleration of tritium ions would probably be similar to $^3He^{+2}$. Deuterons have a considerably smaller anomalous magnetic moment coefficient which would require much higher field magnets for full snakes. It might be possible to deal with deuterons by operating a single snake as a partial snake. Scaling a 100% snake for protons to deuterium makes about an 8% snake. With only a single snake, the snake axis could be in any direction, so we might consider ramping the snake to a higher strength up the ramp. Strong intrinsic resonances might be handled by an ac dipole as we have done in the past with polarized protons in the AGS.

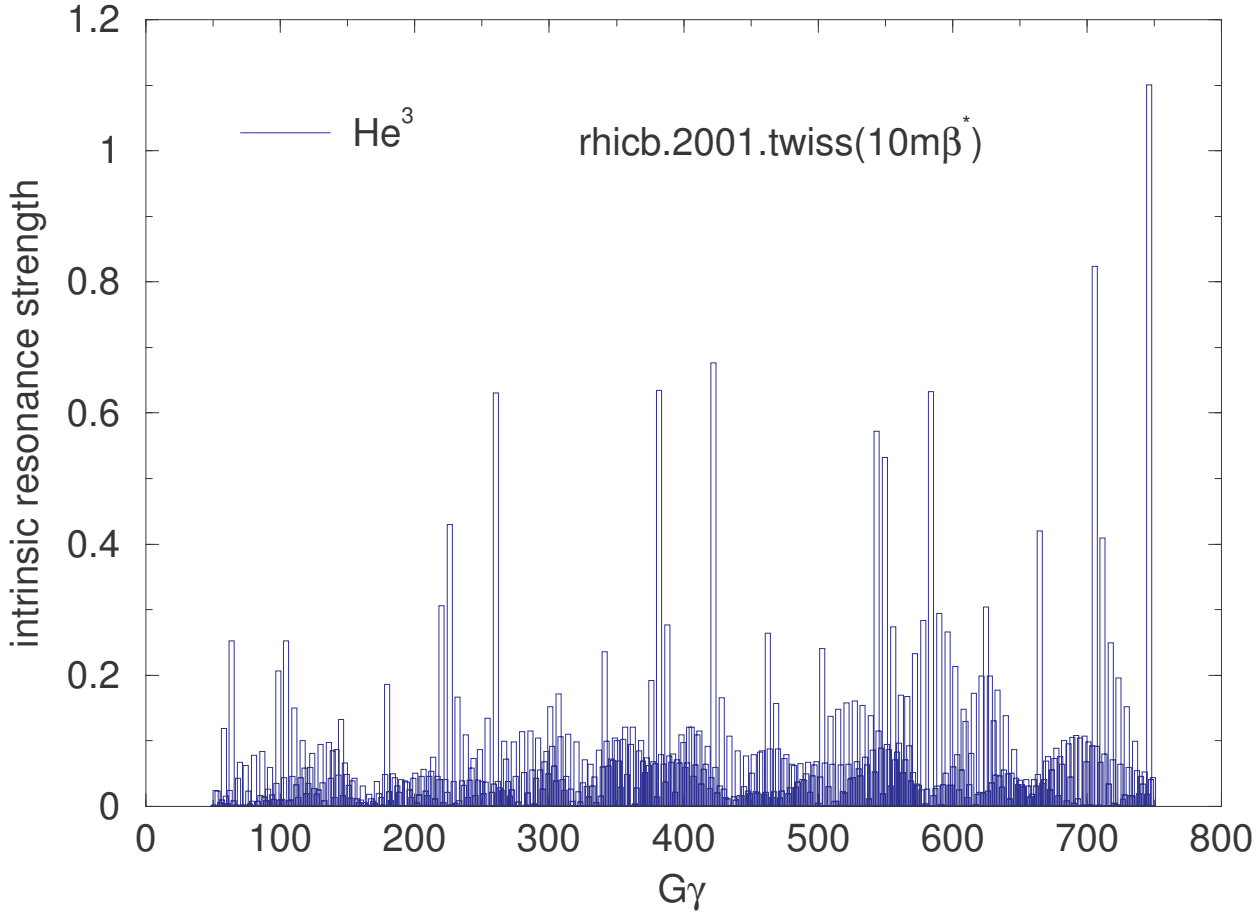

Figure 3.30: DEPOL calculation of intrinsic resonance strengths for polarized He^3 ions in RHIC without snakes. Compare this with Figure 3.29. Here there are more resonances, and they are stronger than for protons.

References:

1. V.V. Parkhomchuk and I. Ben-Zvi, Electron Cooling for RHIC, Design Report 2001.
2. I. Ben-Zvi et al., R&D towards cooling of RHIC collider, COOL'03, May 2003, Japan.
3. D. Wang et al., Proc. PAC'03, Portland, Oregon. USA 2003.
4. J. Kewisch et al., Proc. PAC'03, Portland, Oregon. USA 2003.
5. W.W. Zhang et al., PRST-AB **3**, 122401 (2000).
6. D.L. Bruhwiler et al., Proc. PAC'03, Portland, Oregon USA 2003.
7. Code SimCool was originally written in BINP (Russia) and is now being developed at BNL.
8. I.N. Meshkov et al., Proc. Beam Cooling and Related Topics, Bad Honnef, Germany, 2001.
9. Ya. Derbenev, Proceedings of EPAC'00 (Vienna, Austria), p.8, 2000.
10. K.Y. Ng , PRSTAB 061002 (2002)
11. S.Y. Zhang et al, PAC, 2003, Portland, Oregon.
12. J.M. Jimenez, Pressure rise workshop. Dec. 2003, BNL.
13. F. Ruggiero, Pressure rise workshop. Dec. 2003, BNL.
14. G. Arduini, Chamonix XIII, Jan. 2004

15. A.J.Stevens ,“Maximum Energy Deposition Densities in the Internal Dump”, AD/RHIC/RD-41, June, 1992.
16. Beam Absorber section of the RHIC Design Manual.
17. The Beam Dump System in the RHIC Design Manual.
18. A.J.Stevens, “Preliminary Study of Energy Deposition Downstream of the Internal Dump”, AD/RHIC/RD-33, January, 1992.
19. A.J.Stevens, Energy Deposition Downstream of the Internal Dump”, AD/RHIC/RD-97, December, 1995.
20. A.Ruggiero, S.Peggs, RHIC/AP/46, November 1994.
21. S.Y. Zhang, et all, EPAC02, Paris, p.1112, 2002.
22. M. Blaskiewicz, et all, PAC03, Portland, p.3026, 2003.
23. B.Zotter CERN/ISR-TH/82-10, 1982.
24. M. Blaskiewicz prstab 1, 044201, 1998.
25. “RHIC Design Manual”, Brookhaven National Laboratory; *Nucl. Inst. and Meth.*, **A499** (2003).
26. L.H. Thomas, Phil. Mag. , 1 (1927); J. Frenkel, Z. Phys. , 243 (1926); V. Bargmann, L. Michel, V.L. Telegdi, Phys. Rev. Lett. , 435 (1959).
27. I. Alekseev et al., “Polarized proton collider at RHIC”, *Nucl. Inst. and Meth.*, **A499** 392 (2003); I. Alekseev et al., *Design Manual Polarized Proton Collider at RHIC*, Brookhaven National Laboratory (1998).
28. M. Froissart and R. Stora, Nucl. Instr. Meth., , 297 (1960).
29. T. Khoe et al., Part. Accel. , 213 (1975); J.L. Laclare et al., J. Phys. (Paris), Colloq. , C2-499 (1985); H. Sato et al., Nucl. Inst. Meth., Phys. Res. Sec A, 617 (1988); F.Z. Khiari, et al., Phys. Rev. D, 45 (1989).
30. Ya.S. Derbenev et al., Part. Accel. , 115 (1978).
31. T. Roser, AIP Conf. Proc. No. 187, ed. K.J. Heller p.1442 (AIP, New York, 1988).
32. V.I.Ptitsin and Yu.M.Shatunov, Helical Spin Rotators and Snakes, Proc. Third Workshop on Siberian Snakes and Spin Rotators (A.Luccio and Th.Roser Eds.) Upton, NY, Sept. 12-13,1994, Brookhaven National Laboratory Report BNL-52453, p.15.
33. A.U.Luccio, Program SNIG, unpublished, and SNIG Formalism Proc. Third Workshop on Siberian Snakes, loc. cit., p. 193. Also: “Numerical Optimization of Siberian Snakes and Spin Rotators for RHIC”, Proc. Adriatico Conf. Trieste, Italy, Dec. 1995, World Scientific, and: Spin Note AGS/RHIC/SN008.
34. A.U.Luccio, “Optimization of Spin Angles from a Helix Field Map”, Spin Note AGS/RHIC/SN042, Upton, Nov.5, 1996.
35. E.D.Courant, “Possibilities of Accelerating Polarized D, ^{3}He and other ions in RHIC”, AGS/RHIC/SN No. 066 (1997).
36. W.W. MacKay, et al., Superconducting Helical Snake Magnets: Design and Construction, p.163, DESY-PROC-1999-03.

4. INTERACTION REGION STRAIGHT

The interaction straight of eRHIC has to serve various purposes. First of all, it contains the actual interaction region where beams are colliding inside the eRHIC detector. While it is necessary to provide head-on collisions, beams must be separated as close as possible to the IP to allow low-β magnets for both individual beams to be installed as close as possible to the IP without interfering with the other beam. Furthermore, since eRHIC is designed to collide longitudinally polarized beams, spin rotators are required to rotate the polarization direction of both beams from the vertical to the longitudinal direction. To measure the amount of resulting longitudinal polarization, polarimeters have to be embedded in the IR straight as well. The following sections present the IR design, the detector interface and the design of the spin rotators.

4.1 IR design

A preliminary design for the interaction region of the e-p collider eRHIC has been developed, which provides a luminosity of $4.4 \cdot 10^{32}\,\mathrm{cm}^{-2}\mathrm{sec}^{-1}$ (see Table 1.1). This design has evolved from an earlier version [1] to provide sufficient space for focusing elements in both rings in spite of the fact that beam separation is less than some $20\,\mathrm{cm}$. Figure 4.1 shows a 3D view of the interaction region.

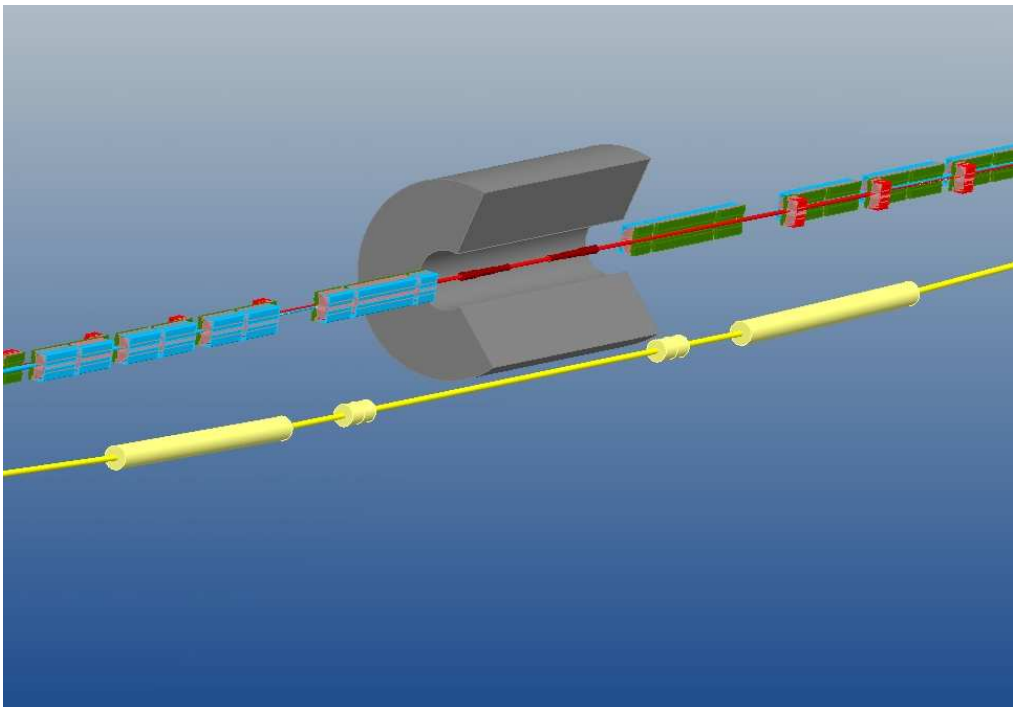

Figure 4.1: 3D view of the interaction region.

4.1.1 Electron IR Optics

Since electron β functions at the interaction point are almost equal, $\beta_x = 0.19\,\text{m}$, $\beta_y = 0.27\,\text{m}$, focusing is provided by a superconducting quadrupole triplet inside the detector solenoid. With the horizontal emittance being about five times larger than the vertical one, the first and last magnet of that triplet are chosen to be focusing in the horizontal plane to keep the horizontal beam size small. The smaller vertical emittance in turn allows for a larger β function in the vertical plane, as it occurs inside the second, vertically focusing quadrupole. Figure 4.2 shows the quadrupole arrangement and β functions, while Table 4.1 lists some key parameters of the magnets.

With the first electron quadrupole, QE1, starting at a distance of $1.0\,\text{m}$ from the interaction point, this configuration provides a free section of $\pm 1.0\,\text{m}$ around the IP to be used by detector components.

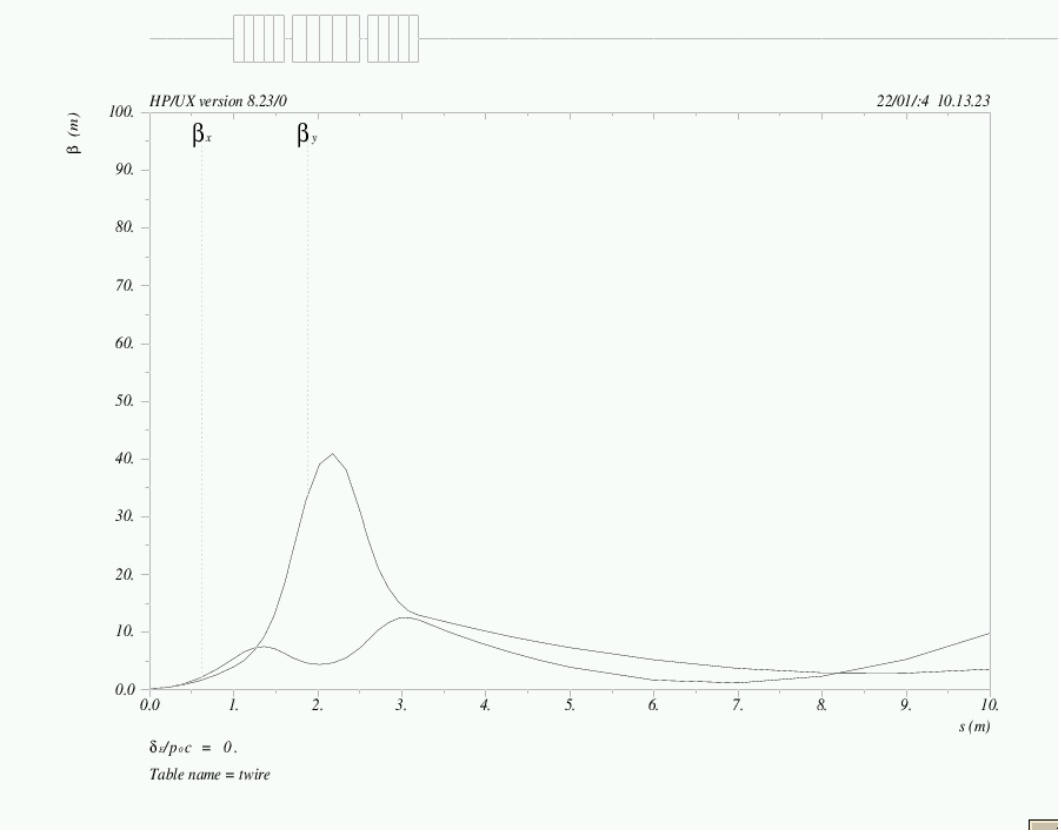

Figure 4.2: Electron IR lattice of the electron-ion collider eRHIC

The required minimum beam pipe radius is determined by the width of the synchrotron radiation fan that has to be passed safely through these magnets, as well as by the dimensions of the electron beam itself. For the latter, a minimum aperture of $20\sigma_e$ has been used throughout the entire design of the interaction region, thus ensuring sufficient aperture even in the presence of orbit distortions.

Matching into the regular FODO lattice of the arcs is provided by septum quadrupoles which can be placed in-between the hadron low-β quadrupoles, starting at a distance of $12.2\,\text{m}$ from the IP.

Table 4.1: Magnet parameters for the electron triplets.

	QE1	QE2	QE3
length [m]	0.6	0.8	0.6
gradient [T/m]	83.3	76.7	56.7
radius [mm]	24	26	35
bending angle left/right [mrad]	2.50/-2.74	5.30/-2.02	0.0/-4.19
shift w.r.t. detector axis left/right [mm]	0/-10	0/-10	0/-10
tilt w.r.t. detector axis left/right [mrad]	1.25/-1.37	3.90/-2.38	3.90/-4.48
synchrotron radiation power left/right [W]	735/882	2475/360	0/2063
synchr. rad. power on septum left/right [W]	466/360	0/360	0/0
critical photon energy left/right [keV]	9.3/10.1	14.7/5.6	0/15.5

4.1.2 Hadron IR Optics

Hadron focussing is provided by a normal-conducting quadrupole doublet, starting $5m$ from the IP (Figure 4.3).

Septum quadrupoles are foreseen for both doublet lenses to keep the necessary separation between electron and hadron beam small, thus minimizing the width as well as the power of the resulting synchrotron radiation fan. Dedicated gaps in the hadron low-β magnet string provide sufficient space for the septum quadrupoles in the electron ring.

Both lenses are split up into different individual magnets, with pole tip radii tailored according to the varying beam sizes. Pole tip fields are limited to 1.0 Tesla in all magnets to avoid saturation effects at the edges of the magnet poles. Table 4.2 lists the main parameters of these magnets.

Table 4.2. Parameter list of the hadron low-β septum quadrupoles

	Q1	Q1B	Q1C	Q2	Q2B	Q2C	Q2D	Q2F	Q2G
length [m]	0.8	2.8	1.2	1.5	1.5	1.5	1.5	1.5	1.5
gradient [T/m]	58.3	41.7	33.3	20.2	17.0	16.2	16.2	16.2	17.0
pole tip radius [mm]	17.1	24.0	30.0	49.4	58.9	61.8	61.8	61.8	58.9
pole tip field [T]	1.0	1.0	1.0	1.0	1.0	1.0	1.0	1.0	1.0

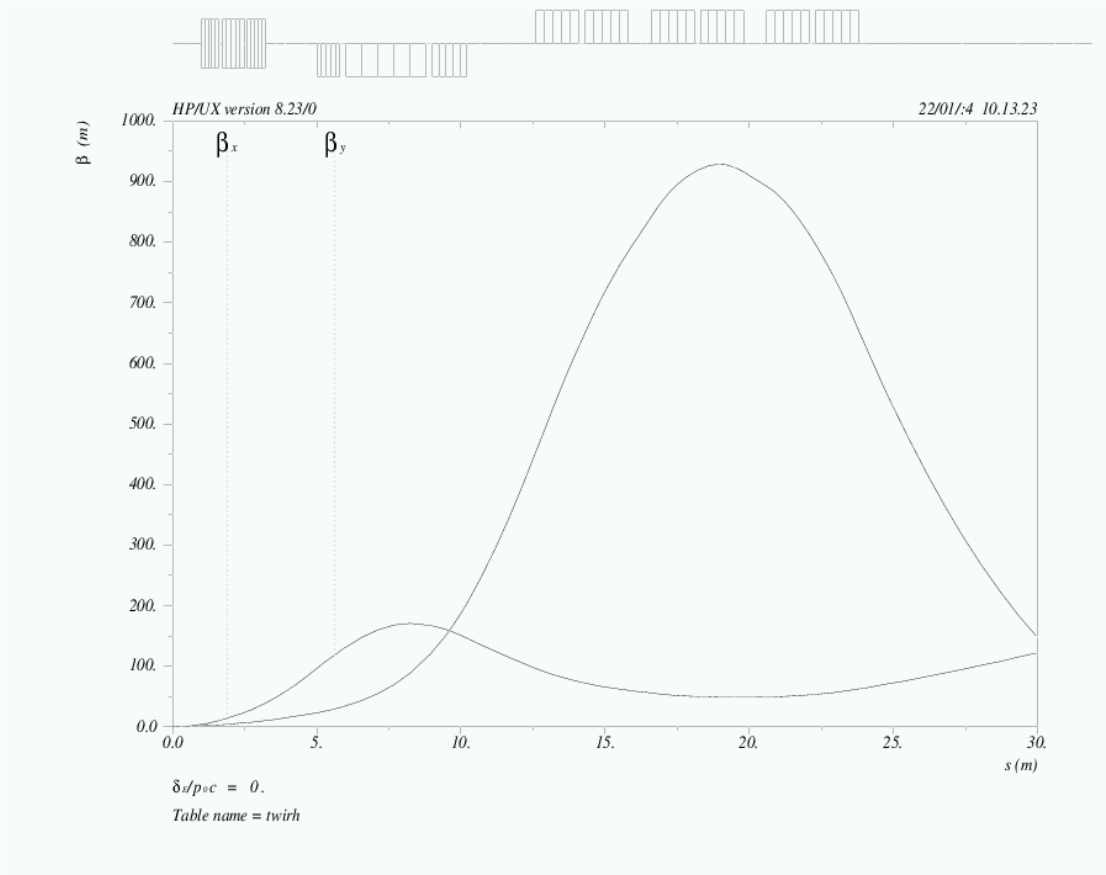

Figure 4.3: Hadron IR lattice of the electron-ion collider eRHIC.

4.1.3 Synchrotron Radiation Issues

The electron quadrupole triplet inside the detector volume is shared by the hadron beam. The focusing effect on the hadron beam is marginal due to the large energy difference - 10 GeV electrons compared to 250 GeV protons. This large energy difference in turn requires the beams to be separated such that the electrons do not experience the much stronger focusing fields of the hadron low-β quadrupoles. This separation is provided by dipole windings in the superconducting electron low-β quadrupoles. To minimize the necessary beam separation, the first hadron magnet is realized as a septum quadrupole, with a septum thickness of $d_{\text{septum}} = 10\,\text{mm}$, including beam pipes. Since the design apertures for the two beams are $20\sigma_{x,e}$ for the electrons and $12\sigma_{x,p}$ for the hadron beam, the required total separation between the orbits of the two beams at the location of the septum is therefore

$$\Delta x = 12\sigma_{x,p} + 20\sigma_{x,e} + d_{\text{septum}}. \qquad (4.1)$$

Taking into account the β functions shown in Figure 4.2 and Figure 4.3, together with the respective emittances according to Table 1, the required beam separation is

$$\Delta x = 12 \cdot \sqrt{\beta_{x,p}\varepsilon_p} + 20 \cdot \sqrt{\beta_{x,e}\varepsilon_e} + d_{\text{septum}} = 12 \cdot 0.48\,\text{mm} + 20 \cdot 0.45\,\text{mm} + 10\,\text{mm} = 24.8\,\text{mm}. \qquad (4.2)$$

When providing this separation using the dipole windings of the superconducting electron low-β quadrupoles, this produces a synchrotron radiation fan that has to be passed safely through the detector beam pipe. Since some fraction of this synchrotron radiation fan unavoidably hits the septum on the electron downstream side (right side) of the detector, it was attempted to minimize the power and critical photon energy hitting the septum by distributing the bending angles in the individual dipole coils accordingly.

On the right side, this minimization is accomplished by a soft bend provided by the dipole coils in QE1 and QE2, which produce the part of the synchrotron radiation fan actually hitting the septum, and a strong bend in the QE3 that provides the required remaining separation angle to achieve sufficient separation at the septum.

This scheme cannot be adopted for the left side since a bend in the QE3 there would result in a very wide synchrotron radiation fan further downstream, where it would require large aperture magnets to be passed through. Since large aperture magnets would cover a significant fraction of the detector volume, this is therefore not desirable. Instead, a soft bend is provided by the QE1 alone, resulting in a synchrotron radiation fan that is just wide enough to cover the angle between the hadron beam orbit and the inner edge of the septum. The remaining beam separation is then provided by the QE2 dipole coil.

To further minimize the required magnet aperture, all quadrupoles on the right side are shifted towards the inside of the RHIC ring, resulting in an off-center electron orbit through these quadrupoles. The effect of this shift on the electron beam orbit is to be compensated by the dipole coils.

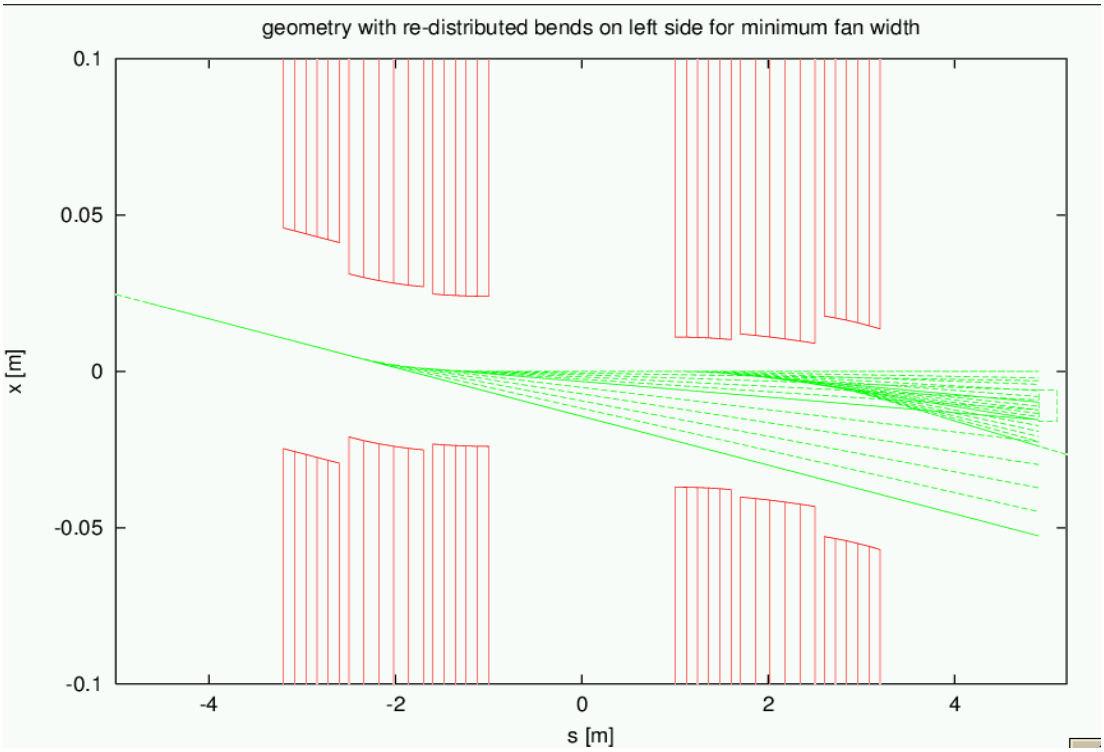

Figure 4.4: IR geometry and synchrotron radiation fan.

4.2 Hadron Insertion

A plan for the RHIC insertion is to remove the crossing dipoles at the eRHIC IP. This leads to the geometry shown in Figure 4.5 below:

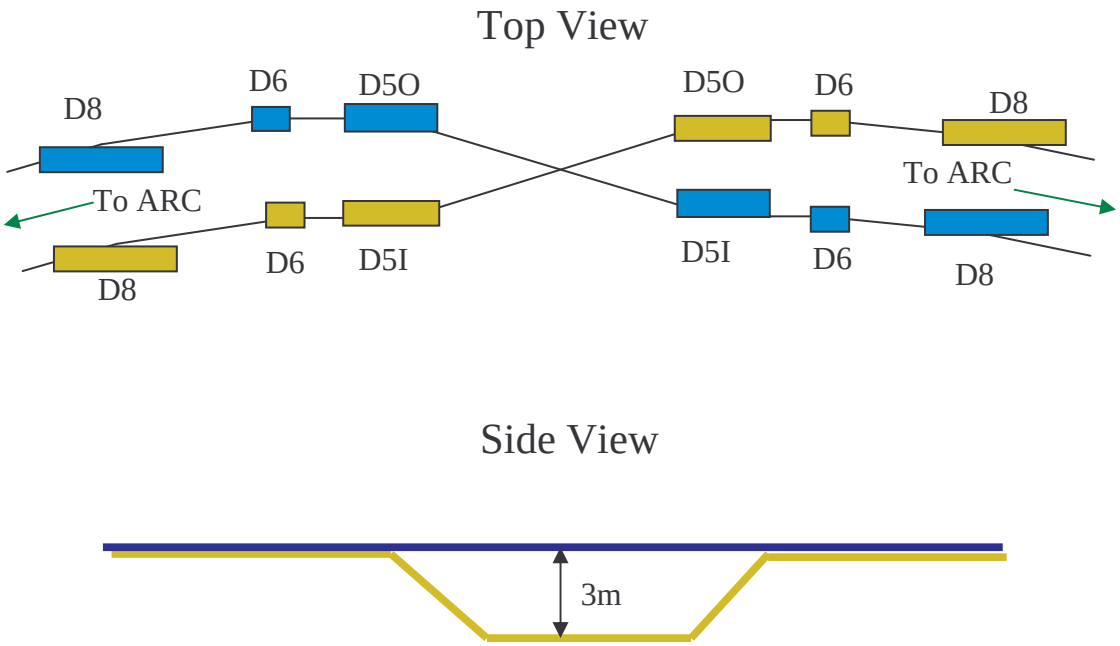

Figure 4.5: The top view and side view of the insertion. The electron beam collides with the Blue ring and the Yellow ring is moved out of the way.

Furthermore, the dipoles D5O are increased in bend angle by 1.32*mrad* and D5I is decreased by 1.32*mrad*. Both these changes will cause a path length change to the RHIC optics. We plan to change the horizontal bends, moving the beam line towards the center to adjust the path lengths.
For the Yellow ring, we will use a simple FODO cell design. The vertical bends will be placed such that the vertical dispersion is canceled. Additionally, there are no horizontal bends between the vertical bends so that the polarization is preserved. Figure 4.6 shows a design for the Yellow ring optics. The superconducting dipole bends are 8.058*m* long with a 32.22*mrad* bend angle. Thus, at Bρ = 831*Tm* the dipole field is 3.43*T*, which is near the standard arc dipole of about 3.6*T*. Furthermore, the length of this insertion is increased by 15.8*cm* over the standard RHIC insertion.
The magnet parameters of the Yellow insertion are listed in Table 4.3

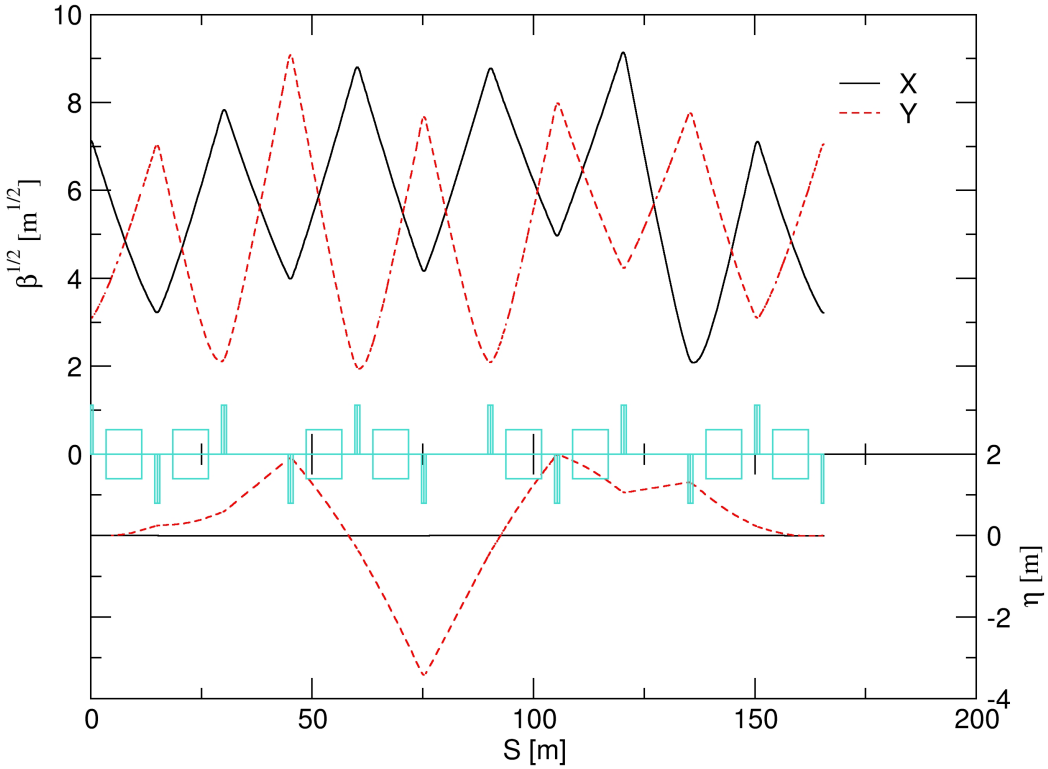

Figure 4.6: The insertion optics for the yellow ring. The fit was not perfect and there is a small residual vertical dispersion of about 0.5*mm*. The trade off of larger beta functions, will allow the vertical dispersion matching to be further improved.

The electron beam will collide with the hadron beam in the blue ring. This insertion will produce a flat beam with β^*'s of (0.27, 1.08)*m* at the interaction point (IP). In order to produce a flat beam, a symmetric insertion design is used. Since, RHIC insertions are anti-symmetric, an additional half cell had to be added. This shifts the IP by about 7.5*m* from original RHIC IP.
The triplet was designed to minimize the background from the electrons. This required using specialized quadrupoles with 1*T* pole tip fields (non-superconducting). The strength is dependent on the allowable aperture. Furthermore, these triplet positions were adjusted so that they do not interfere with the electron ring magnets. This triplet design leads to β_{max} of 1.4*km*.
The Blue ring IR insertion optics is shown in Figure 4.7. The magnet parameters of the Blue insertion are listed in Table 4.4

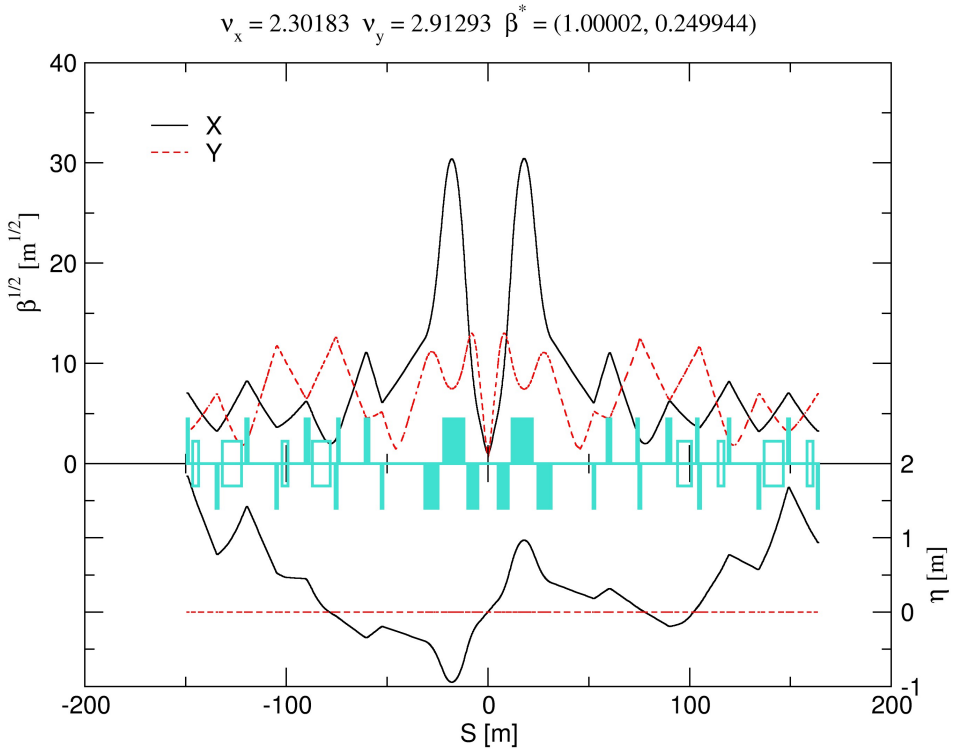

Figure 4.7: The insertion optics for the blue ring. This insertion is 2.127*mm* shorter than the standard RHIC insertion. Note, the extra half cell on the right side, needed in order to convert this insertion to use symmetric optics.

Alternative hadron insertion scheme

Here we describe an alternative approach[3] to the eRHIC insertion. In this case we remove the crossing dipoles for two insertions: 12 o'clock and 4 o'clock. Instead of having the connecting beam lines cross, they continue straight from blue to yellow at 12 o'clock and then return from yellow to blue at 4 o'clock, vice versa for the other ring. These two changes cancel leaving the other 4 insertions unchanged. Yellow ring does not need to make vertical excursion at this scheme and path lengths for Yellow and Blue ring circumferences are naturally equal. But there is a serious question as to whether breaking this symmetry will affect normal RHIC behavior. More studies are needed for this scheme.

3 W. MacKay, private communication

Table 4.3. Yellow ring insertion magnet parameters.

Device	***Coil Radius [cm]***	***Length [m]***	***Field (250GeV protons) [T]***	***Gradient (250GeV protons) [T/m]***	***Drift space [m]***	
QF	4	1.110		67.59		2.941
V1	4	8.058	3.43		QF - V1	2.941
QD1	4	1.110		83.46	V1 - QD1	2.941
V1	4	8.058	3.43		QD1 - V1	2.941
QF1	4	1.110		62.90	V1 - QF1	2.941
QD2	4	1.110		88.17	QF1 - QD2	11.249
V2	4	8.058	3.43		QD2 - V2	2.941
QF2	4	1.110		59.74	V2 - QF2	2.941
V2	4	8.058	3.43		QF2 - V2	2.941
QD3	4	1.110		94.92	V2 - QD3	2.941
QF3	4	1.110		53.50	QD3 - QF3	11.249
V3	4	8.058	3.43		QF3 - V3	2.941
QD4	4	1.110		85.02	V3 - QD4	2.941
V3	4	8.058	3.43		QD4 - V3	2.941
QF4	4	1.110		68.56	V3 - QF4	2.941
QD5	4	1.110		61.77	QF4 - QD5	11.249
V4	4	8.058	3.43		QD5 - V4	2.941
QF5	4	1.110		82.65	V4 - QF5	2.941
V4	4	8.058	3.43		QF5 - V4	2.941
QD	4	1.110		69.76	V4 - QD	2.941

Table 4.4. Blue ring IR insertion magnet parameters. (Parameters of Q1,Q2 septum quadrupoles are listed in Table 4.2)

Device	*Name*	*Pole Tip or Coil Radius [cm]*	*Length [m]*	*Gradient (250GeV protons) [T/m]*	*Drift Space [m]*	
Q3	Q3a	5.98	1.5	16.72	Q2f - Q3a	2.745
	Q3b	5.98	1.5	16.72	Q3a - Q3b	0.200
	Q3c	5.98	1.5	16.72	Q3b - Q3c	0.200
	Q3d	5.98	1.5	16.72	Q3c - Q3d	0.200
Q4	Q4OT	4	0.75	66.52	Q3d - Q4OT	20.841
	Q4IT	4	0.75	66.52	Q3d - Q4IT	20.841
Q5	Q5Ob	4	1.11	75.08	Q5OTb - Q5Ob	0.131
	Q5OTb	4	0.75	32.85	Q4OT - Q5OTb	6.100
	Q5Ib	4	1.11	75.08	Q5ITb - Q5Ib	0.131
	Q5Ic	4	1.11	75.08	Q5ITc - Q5Ic	0.131
	Q5ITb	4	0.75	52.81	Q5Ic – Q5ITb	12.821
	Q5ITc	4	0.75	32.85	Q4IT - Q5ITc	6.100

4.3 Considerations on the Machine / Detector interface

4.3.1 Outline of the eRHIC Detector Design

The following discussion will be restricted to the nominal eRHIC collider mode operation of a 10GeV electron/positron beam colliding with a 250GeV proton beam. Simple four vector kinematics in e-p collisions which involves an electron and a proton in the initial state and a scattered electron along with a hadronic final state in the final state can be used to study analytically the energy and angular acceptance of the scattered electron and hadronic final state as a function of the main kinematic quantities in deep-inelastic scattering (DIS), x and Q^2 [1]. This provides a first understanding of the final state topology. Q^2 is the negative square of the momentum transfer between the incoming and scattered electron. The Bjorken scaling variable x is interpreted in the Quark-Parton model as the fraction of the proton momentum carried by the struck quark.

The hadronic final state consists of the current jet which emerges from the struck quark characterized by its polar angle and energy.

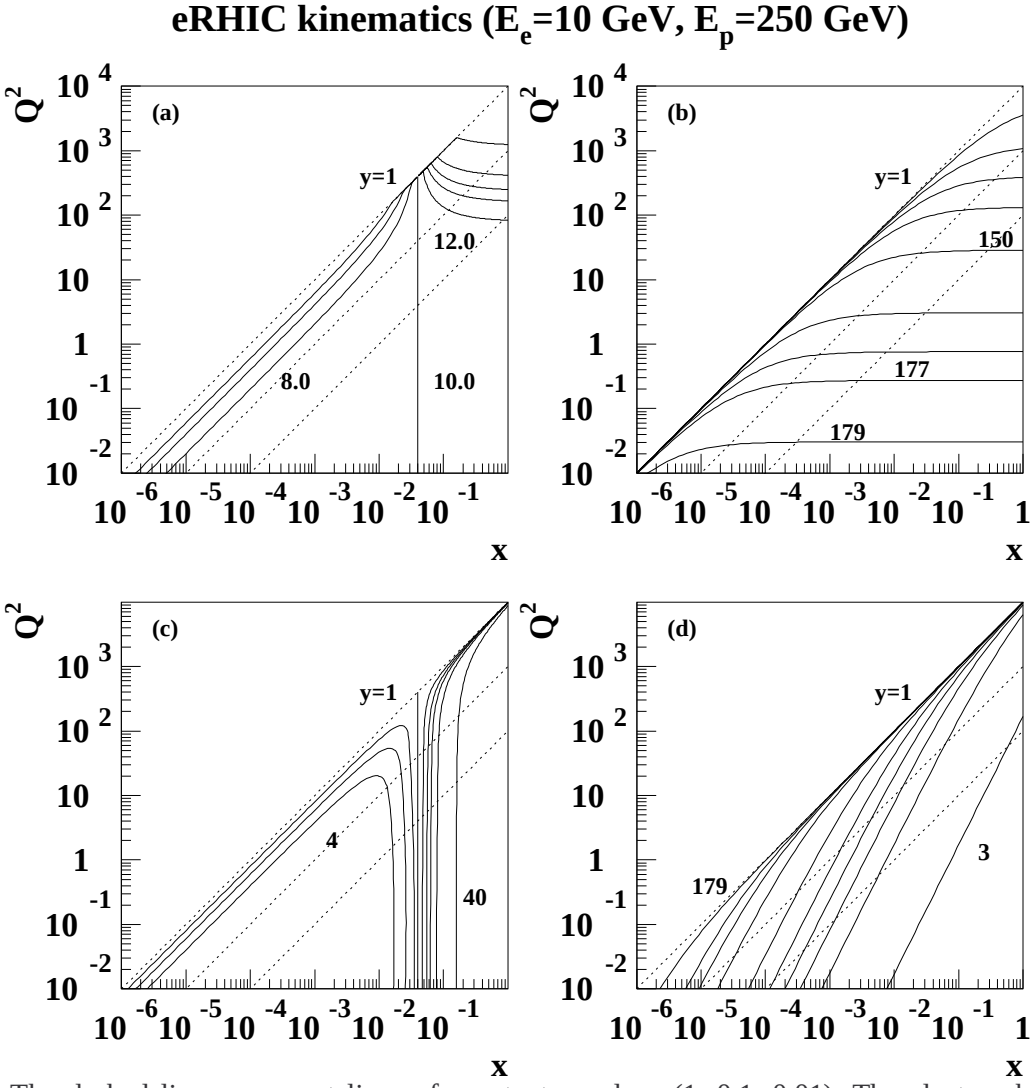

Figure 4.8: The dashed lines represent lines of constant y values (1, 0.1, 0.01). The electron beam energy amounts to 10GeV whereas the proton beam energy is 250GeV. Isolines of constant electron energies (4, 6, 8, 10, 12, 14, 16, 20 and 40GeV) (a), electron scattering angles (30º - 150º in steps of 30º and 170º, 175º, 177º and 179º) (b), current jet energies (4, 6, 8, 10, 12, 14, 16, 20 and 40GeV) (c) and current jet angles (3º, 30º - 150º in steps of 30º and 170º, 175º, 177º and 179º) (d).

Figure 4.8 shows isolines of constant electron energy (a) and constant scattering angles (b) as well as lines of constant y values (1, 0.1, 0.01). The kinematic variable y is given in terms of x and Q^2 ($y = Q^2 / sx$) and refers to the inelasticity in the rest frame of the proton. The kinematic limit is given by y=1. The scattering angle is measured with respect to incoming proton beam which defines the positive z axis. Electron tagging acceptance down to at least 177º will be necessary to provide acceptance in Q^2 below $1GeV^2$. The energy of the scattered electron is less than 10GeV and is in particularly small in the region of low x and medium to low values in Q^2. This sets stringent requirements on trigger and reconstruction efficiencies.

Figure 4.8 shows isolines of constant current jet energy (c) and angle (d). The energy of the current jet is rather small in the low x and medium to low Q^2 region and overlaps to some extend with the scattered electron. The current jet energy increases towards the forward direction in the region of high x and Q^2 values. This will require e/h separation capabilities in particular in the rear direction (incoming electron direction) and increasing jet energy measurement capabilities in the forward direction (incoming proton direction).

The following minimal requirements on a future eRHIC detector can be made:

- Measure precisely the energy and angle of the scattered electron (Kinematics of DIS reaction)
- Measure hadronic final state (Kinematics, jet studies, flavor tagging, fragmentation studies, particle ID)
- Missing E_T measurement for events involving neutrinos in the final state (Electroweak physics)

In addition to those demands on a central detector, the following forward and rear detector systems are crucial:

- Zero-degree photon detector to control radiative corrections, measure Bremsstrahlung photons for luminosity measurements and in e-A physics to tag nuclear de-excitation
- Tag electrons under small angles (Study of the non-perturbative/perturbative QCD transition region and luminosity measurement from Bremsstrahlung ep events)
- Tagging of forward particles (Diffraction and nuclear fragments)

Figure 4.9 show the first conceptual GEANT detector implementation of the above requirements on a central detector. The hermetic inner and outer tracking system is surrounded by an axial magnetic field on the order of 1-2T. The tracking volume is surrounded by a hermetic calorimeter system in the rear, barrel and forward direction. The calorimeter system is subdivided into electromagnetic and hadronic sections which are then in-turn subdivided into certain size towers. The inner most double functioning dipole and quadrupole magnets at a distance of 1m to the interaction region are also shown. The detailed design is under preparation.

The stringent requirements on the high-rate capability of the tracking system make a silicon-type detector for the inner tracking system (forward and rear silicon disks together with several silicon barrel layers) together with a GEM-type detector for the outer tracking system (forward and rear GEM-type tracking disks with several barrel GEM-type tracking layers) a natural choice.

The forward and rear detector systems have not been considered so far. The design and location of those detector systems has to be worked out in close collaboration to accelerator physicists since machine magnets will be employed as spectrometer magnets and thus determine the actual detector acceptance and ultimately the final location. It is understood that demands on optimizing the rear/forward detector acceptance might have consequences on the machine layout and is therefore an iterative process.

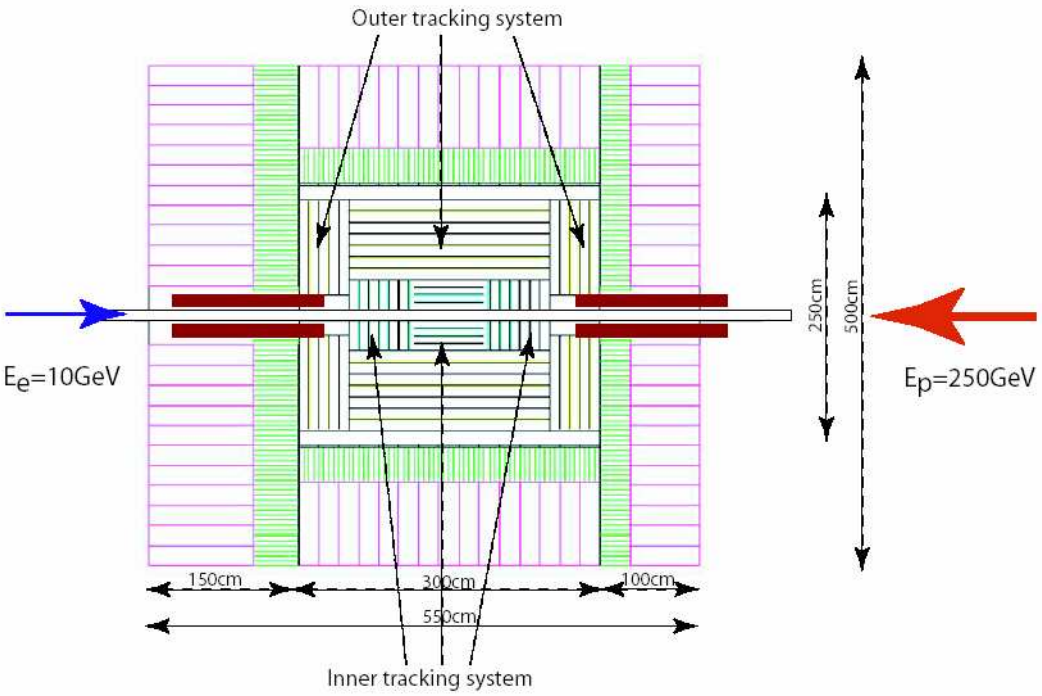

Figure 4.9: Conceptual GEANT detector implementation of the main central eRHIC detector components. The inner and outer hermetic tracking system is surrounded by an axial magnetic field on the order of 1-2T. The tracking volume is surrounded by a hermetic calorimeter system in the rear, barrel and forward direction.

4.3.2 Considerations on the Detector/Machine Interface

The following section provides an overview of some aspects on the detector/machine interface. The specification of those items has only recently been started.

- **Synchrotron radiation**

The location of the direct synchrotron radiation fan has been previously discussed. The direct synchrotron radiation has to pass through the entire interaction region before hitting a rear absorber system. This requires that the geometry of the beam pipe is designed appropriately with changing shape along the longitudinal beam direction which includes besides a simulation of the mechanical stress also the simulation of a cooling system of the inner beam pipe. The distribution of backscattered synchrotron radiation into the actual detector volume has to be carefully evaluated. An installation of a collimator system has to be worked. Those items have been started in close contact to previous experience at HERA.

- **Location of inner machine elements**

The demand of a high luminosity ep/eA collider facility requires the installation of focusing machine elements inside the actual detector volume. Such a scenario has been carried out as part of the HERA II luminosity upgrade with the installation of superconducting low beta quadrupole magnets. The inner most double functioning magnet as part of the electron lattice has an inner distance to the nominal interaction region of 80cm. Assuming an outer dimensions of 20cm in diameter, would restrict the Q^2 acceptance to $0.5GeV^2$. A careful design of the inner tracking system to optimize the

tracking system is crucial. The optimization in acceptance will require a close collaboration between the actual detector design and the location of inner most machine elements which includes also the design of the inner beam pipe. The GEANT simulation on those aspects has been started. A first conceptual implementation is shown in Figure 4.9.

- **Rear electron tagging system**

The need for acceptance of scattered electrons below the central detector acceptance is driven by the need for luminosity measurement through e-p/e-A Bremsstrahlung and photo-production physics. Besides that a calorimeter setup to tag radiated photons from initial-state radiation and Bremsstrahlung will be necessary. The scattered electrons will pass through the machine elements and leave the pipe through special exit windows. The simulation of various small-angle calorimeters has only been started. This will require a close collaboration with the eRHIC machine design efforts to aim for an optimal detector setup.

- **Forward tagging system**

The forward tagging system beyond the central detector will play a crucial role in diffractive ep/eA physics and in eA physics in general. A significant fraction of the hadronic final state is produced in the forward direction.

The design of a forward tagger system based on forward calorimetry and Roman pot station is foreseen. Charged particles will be deflected by forward machine elements. This effort will require as well a close collaboration with the eRHIC machine design efforts to ensure the best possible forward detector acceptance.

4.4 Electron Spin Rotator Design

A spin rotation from vertical direction in the arcs to longitudinal one in the IPs will be performed in two steps: at first, by a solenoidal spin rotator to horizontal plane and then by dipoles. The $\pm 90^{\circ}$ spin rotator consists of two superconducting solenoids, each 3 m long, and with the field of 8.7 T. Between solenoids is placed a focusing structure, which cancels the betatron coupling and also creates the spin transparency. On the opposite side of the interaction straight, spin is restored to vertical direction by the negative spin rotator. As a result, the spin tune is undisturbed by the interaction region insertion, and the polarization behavior is mainly the same as without the spin rotators.

The equilibrium polarization direction (vector $\mathbf{n_0}$) is vertical in the main part of the ring and therefore one can expect a relatively low depolarization rate of the electron beam. Moreover, the Sokolov-Ternov polarization mechanism should provide a high enough beam polarization.

Still there are some requirements, which should be satisfied by the insertion optics, where the spin vector $\mathbf{n_0}$ lies in the horizontal plane. To minimize the negative effect from a spin perturbation $\mathbf{w}$ over the whole straight section, we should fulfill the so called spin transparency condition, namely, the integral of the perturbation through the insertion azimuth θ:

$$I = \int_{\theta_1}^{\theta_2} \mathbf{w}\,\boldsymbol{\eta}\, d\theta$$

should be made zero or, at least, small. Here $\boldsymbol{\eta} = \boldsymbol{\eta}_1 - i\boldsymbol{\eta}_2$ is a complex vector, which is composed from the unity vectors $\boldsymbol{\eta}_1$ and $\boldsymbol{\eta}_2$, which in turn are the two orthogonal solutions of the spin motion equation for the equilibrium particle. The spin perturbation components are:

$$w_x = \nu_0 z'' + K_x \frac{\Delta\gamma}{\gamma}$$

$$w_z = -\nu_0 x'' + K_z \frac{\Delta\gamma}{\gamma}$$

$$w_y = K_y \frac{\Delta\gamma}{\gamma}$$

where $\nu_0 = \gamma a$ is the dimensionless spin tune, z'' and x'' are the second derivatives of the vertical or horizontal displacements over the azimuth θ, $K_{x,y,z}$ are respectively the normalized horizontal, longitudinal or vertical magnetic fields.

Careful analysis shows that the spin transparency condition for the interaction region straight section, which contains the discussed above spin rotators, can be fulfilled, and a small decrease of the equilibrium polarization degree is caused only by bending magnets in the straight between two spin rotators.

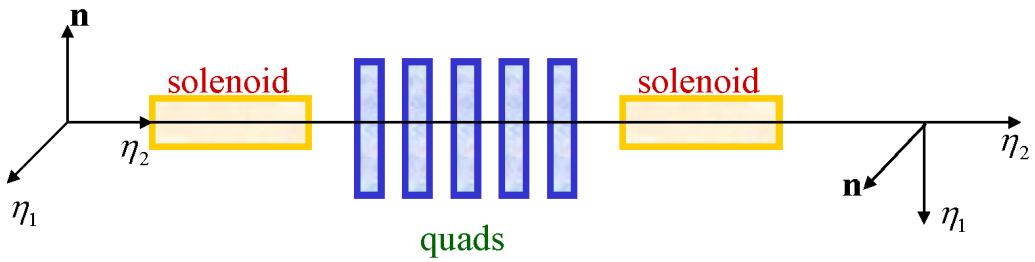

Figure 4.10: Scheme of the solenoidal spin rotator in the electron ring.

The scheme of the focusing structure has been found (see Figure 4.10), that contains only regular quadrupoles inside the solenoidal spin rotator and cancels the betatron coupling as well as creates the spin transparency. Transfer matrices of a full insertion (from the first solenoid edge to the second solenoid edge):

$$T_x = \begin{pmatrix} 0 & -2r \\ (2r)^{-1} & 0 \end{pmatrix}, \qquad T_z = \begin{pmatrix} 0 & 2r \\ -(2r)^{-1} & 0 \end{pmatrix}$$

Here r is a curvature radius in the solenoidal field B_y:

$$r = B\rho / B_y$$

Table 4.5. Main parameters of the rotator insertion.

Parameter	**Value**
Solenoid length	3 m
Solenoidal field	8.7 T
Quadrupole length	0.4 m
Maximal quad's gradient	28 T/m

In proposed design the condition on transparency is fulfilled, thus, all spin rotators as well as the horizontal wiggle between them are spin transparent against the betatron motion deviations. An inevitable spin-orbit coupling for the energy-off particles is excited by the first spin rotator and then compensated by the second one. In result the spin-orbit coupling vector $\mathbf{d} = \gamma \frac{\partial \mathbf{n}}{\partial \gamma}$ is exactly equal to zero in arcs (see Figure 4.11).

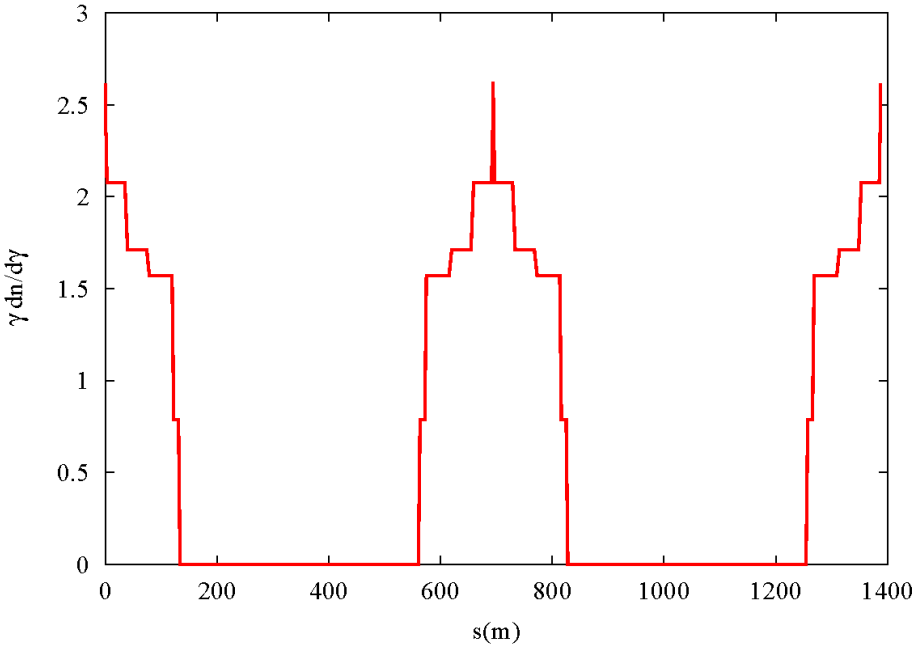

Figure 4.11: Spin-orbit coupling along the ring.

References:

1 C. Montag et al., Proceedings of the 30th Advanced ICFA Beam Dynamics Workshop on High Luminosity e+e- Collisions, Stanford, (2003)

2 B. Surrow, 'Measurement of the Proton Structure Function F2 at Low Q2 and Very Low x with the ZEUS Beam Pipe Calorimeter at HERA', *EPJdirect* **C2** (1999)

Linac-Ring eRHIC.

Daniel Anderson, Ilan Ben-Zvi[1], Rama Calaga[1], Xiangyun Chang[1], Manouchehr Farkhondeh[2], Alexei Fedotov[1], Jörg Kewisch[1], Vladimir Litvinenko[1], William Mackay[1], Christoph Montag[1], Thomas Roser[1], Vitaly Yakimenko[3]

[(1)] C-AD, BNL [(2)] Bates, MIT [(3)] Physics Department, BNL

Content **page**

1. Introduction to the Linac-Ring collider

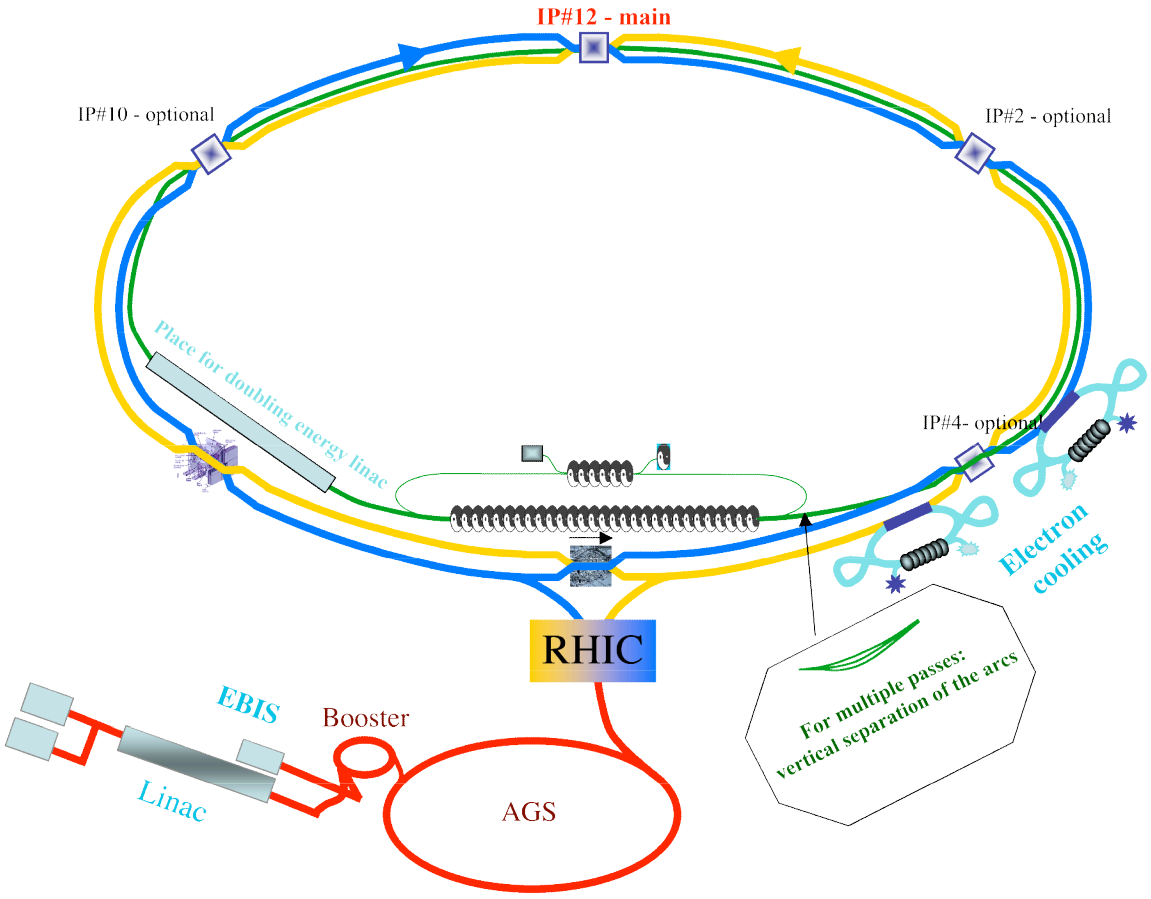

Figure 1.1.a. The most natural linac-ring eRHIC with multiple IP(s) with the arcs are located in the RHIC tunnel. A polarized electron beam generated in a photo-injector is accelerated to the energy of the experiment in the ERL. After colliding with the hadron RHIC beam in as many as four IP(s), the electron beam is decelerated to energy of few MeV and damped. The energy thus recovered is used for accelerating subsequent bunches to the energy of the experiment. Electrons by-pass both the Star and Phenix experimental halls. The main 5 GeV superconducting linac, which electron beam passes twice during acceleration and twice during deceleration, the injection and the beam damp are located north of the Star experimental hall. The by-pass around the Phenix experimental hall is the natural place for a future linac, which extends the electron beam energy to and above 20 GeV *(see section 6 for detail)*.

The Linac-Ring eRHIC has a large number of unique features, which make it a perfect match for versatile nuclear physics program at Brookhaven National Laboratory by:

- ✓ providing luminosity up to 10^{34} cm^{-2} s^{-1} in electron-hadron collisions [1];
- ✓ providing full polarization transparency at all energies [2] ;
- ✓ providing multiple electron-hadron interaction points (IPs) and detectors [3];
- ✓ providing very long "element-free" straight section(s) for detector(s);
- ✓ taking full advantage of electron cooling of the RHIC II hadron beams;
- ✓ being perfectly compatible with RHIC operations and hadron-hadron collisions[4];
- ✓ providing full range of C-M energies required for the physics program;
- ✓ being directly upgradeable to electron energies of 20 GeV and above.

The choices of the IPs or/and the exact layout of the electron accelerator in the linac-ring configuration are completely flexible. Figures 1.1 a,b and c give a flavor of possible schematic layouts of the Linac-Ring $\vec{e} \square \vec{p}$ and e-Au^{79}_{197} collider based on an energy-recovery linac (ERL) and the RHIC facility. These figures *are not drawn to scale*.

In all these schemes a high-brightness polarized electron beam generated in a photo-injector is accelerated to the energy of experiment 2 GeV – 10 GeV (*and possibly to 20+ GeV in future*) in the super-conducting energy recovery linac (ERL). After the collision(s) with proton/ion beam in the IP(s), the electron beam is decelerated to energy of few MeV in the same ERL and damped. By this process the energy of the electrons is recovered and is used for accelerating subsequent bunches to the collision point.

The simple fact that linac-ring eRHIC uses fresh electron beam for each collision is of the foremost significance for all attractive features of this scheme. Most importantly, the use of fresh beam removes the tune shift limit on electron beam and opens the range of collider parameter-space inaccessible by ring-ring scheme. As the result, the linac-ring eRHIC provides for higher luminosity at any given level of RHIC performance, compared with the ring-ring case. This scheme meets or exceeds the requirements for the collider specified in the physics program for eRHIC [1]:

- ✓ Electron beams colliding with beams of protons or light and heavy nuclei
- ✓ Wide range of collision energies (E_{cm}/nucleon from 15 GeV to 100 GeV)
- ✓ High luminosity L > 10^{33} cm^{-2} s^{-1} per nucleon
- ✓ Polarization of electron and proton spins
- ✓ Preferably, two interaction regions with dedicated detectors.

---

[1] Luminosity is quoted $\vec{e} \square \vec{p}$ collisions. This number is also correct for e - Au^{79}_{197} , when luminosity is calculated *per nucleon*. Quoted luminosity assumes that eRHIC runs in a dedicated mode – see discussion below.

[2] In contrast with ring-ring option, the linac-ring eRHIC does not have prohibited energies where beam polarization vanishes.

[3] In the case of multiple IPs, the total luminosity is ~ 10^{34} cm^{-2} s^{-1}

[4] In this mode of operation the eRHIC luminosity will be limited by a total beam-beam tune shift for hadron beam, i.e. to a portion of 10^{34} cm^{-2} s^{-1}.

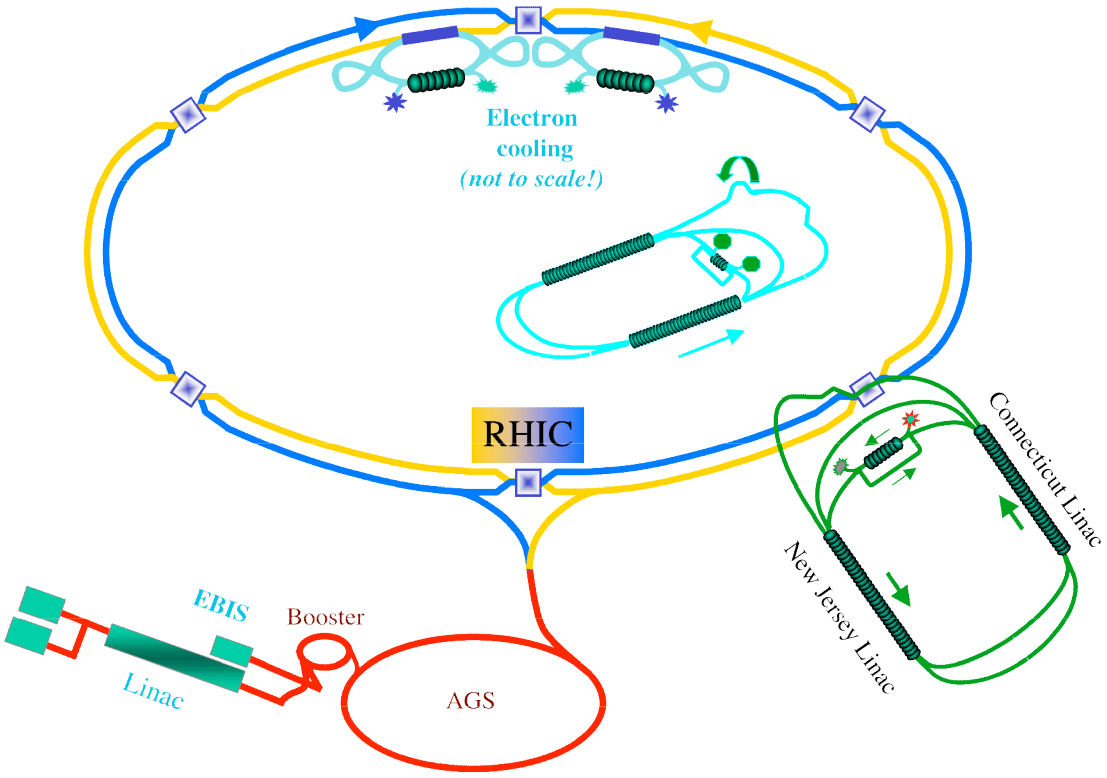

Figure 1.1.b. Linac-ring eRHIC with a separate tunnel and an IP at 4 o'clock. A polarized electron beam generated in a photo-injector is accelerated to the energy of the experiment in the ERL. After colliding with the hadron RHIC beam in the IP, the electron beam crosses over both blue and yellow RHIC rings and is decelerated to energy of few MeV in the same ERL and damped. The energy thus recovered is used for accelerating subsequent bunches to the energy of the experiment. Both Blue and Yellow ring (hence the colors of the lines) of the RHIC as well its injector (red lines) operate in standard conditions for hadron collisions, while the electrons (green lines) collide with hadron beam in the Yellow ring at 4 o'clock. Both hadron beams are cooled by electron beam coolers (light blue lines) located at 12 o'clock. Note, that both electron cooling and ERL can be relocated to an IP at 10, 12 and 2 o'clock.

The first feature *(Electron beams colliding with beams of protons or light and heavy nuclei)* is satisfied by having a variety of nuclei (*p, D, Au, He*…) accelerated by the blue and yellow ring of the RHIC, and by ERL's polarized e-beam with continuously tunable energy.

The ERL-based eRHIC has very large tunability range of c.m. energies while maintaining very high luminosity (*14.4 - 100 GeV per nucleon in e-p collisions and 20 - 63 GeV in e-Au collisions – see Tables 1.1 and 1.2 for details; the possibilities of extending this range further are discussed in chapter 6*).

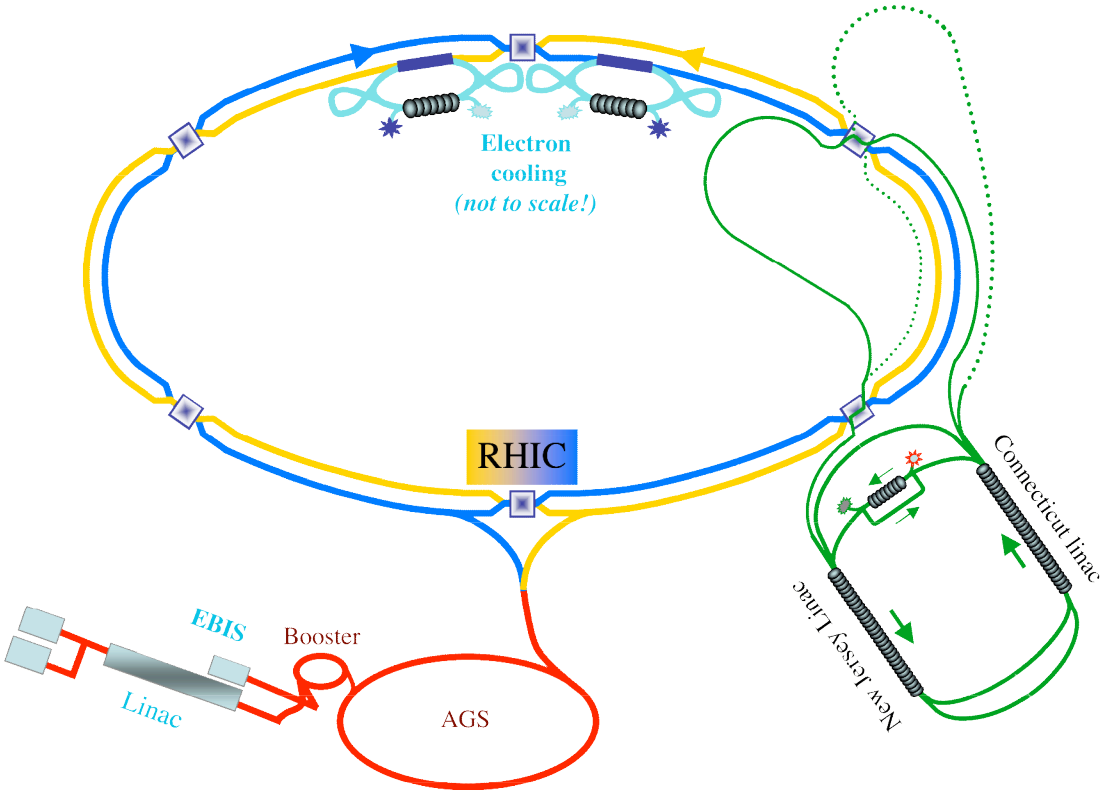

Figure 1.1.c. eRHIC (based on stand-along ERL) with two IPs.

Table 1.1 Center of mass energy per nucleon (GeV, green) in *e-p* collisions in eRHIC vs. energy of protons (red) and ERL (blue)

Energy, GeV **proton** **electrons** c.m.	**26**	**50**	**100**	**250**
2	**14.42**	20.00	28.28	44.72
5	22.80	31.62	44.72	70.71
10	32.25	44.72	63.25	**100.00**

Table 1.2 Center of mass energy per nucleon (GeV, green) in e - $^{79}Au_{197}$ collisions in eRHIC vs. energy of ions per nucleon (red) and ERL (blue)

Energy, GeV **Au/u** **e** c.m.	**50**	**100**
2	**20.00**	28.28
5	31.62	44.72
10	44.72	**63.25**

In the ERL-based eRHIC we collide two round beams of equal size (see section 3.f) to maximize the luminosity. The main distinctive feature here is that the attainable luminosity is defined in practice by the energy and intensity of the proton or ion beam in RHIC:

$$L = f_c \cdot \square_h \cdot \frac{\square_h}{\square_h^*} \cdot \frac{Z \cdot N_h}{r_h} \tag{1}$$

i.e., by the intensity N_h (number of hadrons per bunch), repetition rate f_c, the energy of the ion or proton beam, $\square_h = E_h / Mc^2$, its charge $q = Ze$, its classical radius $r_h = Z^2 e^2 / Mc^2$, and the allowable beam-beam tune shift $\square_h$ in the eRHIC IP(s) (*see explanation in the next section*). The linac-ring eRHIC's luminosity is independent of the electron beam's energy and linearly proportional to the energy of the proton or ion beam. This means that that the same center of mass energy, (*given that there is no preferred energy ratio*), can be reached using higher energy protons (ions) and lower energy electrons; hence, the high luminosity.

There are two possible modes of eRHIC operation:

a) A parallel with the normal RHIC collider where hadrons are colliding with hadrons in 2 detectors. This mode is considered to be typical for eRHIC;

b) A dedicated mode when hadrons collide only with electrons.

In any mode of operation, the total allowable beam-beam tune shift for hardons in RHIC is limited to $\sum_{IPs} \square_h \square 0.024$ [2]. It is considered that with three beam-beam interaction points, two for hadron-hadron and one for electron-hadron collisions, the beam-beam parameter per interaction point should not exceed $\square_h = 0.007$ [3]. The hadron beam-beam tune shift in the linac-ring eRHIC IP is given by following formula:

$$\square_h = \frac{N_e}{\square_h} \cdot \frac{r_h / Z}{4 \square \square_h} \tag{2}$$

where N_e is number of electrons per bunch and $\square_h$ RMS emittance of hadron beam. Therefore, for a given energy and species hadron beam and for given intensity of electron beam in ERL we will control the hadron beam-beam parameter by changing the hadron beam emittance via electron cooling [5] (see section 3.e). This is an additional advantage of the linac-ring eRHIC – the betterment of electron cooling allows the reduction of the hadron beam emittance with a proportional reduction of the electron beam intensity (and the related to it synchrotron radiation back-ground in the detectors) while keeping the luminosity (1) constant.

The other parameter which influence the eRHIC luminosity is the hadron beam intensity:

$$I_h = Ze \cdot f_c \cdot N_h . \tag{3}$$

[5] We plan to cool gold ions energy of operation, while pre-cool protons at energy of 27 GeV before accelerating them to 250 GeV – see section 3.e.

The number of hadrons per bunch is limited by the single bunch stability [4]. With present parameters of RHIC, the hadron bunches with intensities following intensities will be stable [4]:

□h	Species	Threshold, same □Q
250	Protons	4.3e11
107	Gold	5.8e9

The collision rep-rate is determined by the revolution frequency $f_o \square 78\ kHz$ and number of hadron bunches in RHIC N_b:

$$f_c = f_o \cdot N_b .$$

Presently RHIC operates up to 60 bunches with $N_p \sim 10^{11}$, $N_{Au} \sim 10^9$ per bunch. Doubling the number of hadron bunches to 120 while keeping the bunch intensity at present level is considered as the main stream goal for RHIC II luminosity up-grade, which employs electron cooling of hadron beams [2]. The hadron beam parameters RHIC II are considered to be realistic and should reached many years before commissioning of the eRHIC.

The ring-ring eRHIC requires 6-fold increase of the hadron beam intensity compared with the present level of performance of RHIC. Specifically [3], it suggests using 360 hadron bunches in RHIC for eRHIC operation. The intensity of the hadron beam can be limited by a number of factors such as development of electron cloud or by exceeding the cryogenic load in the RHIC super-conducting magnets, to mention few. These issues as well as their technical and financial implications for RHIC require further detailed studies.

For simplicity, we show here the linac-ring eRHIC luminosities two cases:

- the most optimistic:
  - 360 bunches (as in ring-ring case [3]) with $N_p = 2 \cdot 10^{11}$, $N_{Au} = 2.5 \cdot 10^9$ per bunch;
- the most realistic [6]:
  - 120 bunches (as in RHIC II) with $N_p \sim 10^{11}$, $N_{Au} \sim 10^9$ per bunch.

The maximum luminosity of the linac-ring eRHIC for both the proton-electron and the gold-electron collisions is given in Tables 1.3 and 1.4. Note that luminosities at the level of **10^{34} cm^{-2}sec^{-1}** per nucleon can be reached in linac-ring eRHIC independently from the energy of electrons used. The ratio of luminosity between the parallel and dedicated modes of operation is approximately 3.4.

[6] 120 bunch mode was tested at RHIC but with reduced intensity per bunch. Note using 120 bunches instead of 360 reduces luminosity by a factor of 3 for both linac-ring and ring-ring eRHIC.

Table 1.3 Luminosities for e-p collisions for various energies *in the ERL- based eRHIC: 360 bunches with* $2 \cdot 10^{11}$ *protons per bunch.*

Luminosity 10^{33} **cm**$^{-2}$**sec**$^{-1}$	*Protons 26 GeV*	*Protons 50 GeV*	*Protons 100 GeV*	**Protons 250 GeV**
Parallel mode	**0.285**	**0.548**	**1.097**	**2.74**
Dedicated mode	**0.978**	**1.88**	**3.76**	**9.40**

Table 1.4 Luminosities for e-Au collisions for various energies *in the ERL- based eRHIC*: *360 bunches with* $2.5 \cdot 10^{9}$ *gold-ions per bunch.*

Luminosity (per nucleus) 10^{31} **cm**$^{-2}$**sec**$^{-1}$	*Au 50 GeV/u*	*Au 100 GeV/u*
Parallel mode	**1.71**	**3.42**
Dedicated mode	**5.86**	**11.7**

What is quite remarkable, is that the linac-ring eRHIC can reach luminosities at the level of $\mathbf{10^{33}}$ **cm**$^{-2}$**sec**$^{-1}$ per nucleon with beam parameters which are currently attainable at RHIC: 120 bunches with intensities of $Z \cdot N_h \sim 10^{11}$. These parameters are shown in Table 1.5 and Table 1.6.

Table 1.5 Luminosities for e-p collisions with intensities of proton beam for RHIC II: *120 bunches with* 10^{11} *protons per bunch.*

Luminosity 10^{33} cm^{-2}sec^{-1}	*Protons 26 GeV*	*Protons 50 GeV*	*Protons 100 GeV*	Protons 250 GeV
Parallel mode	.0456	0.0914	0.183	0.457
Dedicated mode	0.156	0.313	0.627	1.57

Table 1.6 Luminosities for e-p collisions with intensities of gold-ion beam for RHIC II*: 120 bunches with 10^9 ions per bunch..*

Luminosity (per nucleus) 10^{31} $cm^{-2}sec^{-1}$	*Au 50 GeV/u*	*Au 100 GeV/u*
Parallel mode	0.228	0.456
Dedicated mode	0.781	1.56

It worth noting that eRHIC parameters in the last two tables are reachable with one third of the electron beam current required for ring-ring operations and, therefore, one third of the back-ground from the synchrotron radiation in the detectors.

Overall, the eRHIC based on the emerging technology of superconducting RF ERL promises to deliver the extremely high luminosity required for the eRHIC physics program. It will also provide several very important features that are not possible or likely impossible with other collider technologies.

1.1 Advantages of the ERL-based eRHIC

- Usage of a fresh electron beam and absence of the memory in the e-beam
  - waives in practice the limitation on the tune shift in the IP, and
    - increase in the density of the proton/ion beam
    - **10 fold increase in the luminosity**
    - larger β_e^* for the e-beam and simplified IP geometry
      - smaller e-beam emittance
      - smaller angular divergence in IP
      - smaller aperture for e-beam
      - **no-need for e-beam quads in the detector area**
      - possibility of focusing the e-beam after separating it for protons/ions
      - **simplified IP geometry**
  - reduces the number of coupled-bunch instability modes
  - secures spin-transparency of the system at all energies
  - provides a high (80%+) degree of e-beam polarization at all energies
  - eliminates "prohibited" energies for the e-beam
  - precludes the need to preserve beam qualities (polarization, emittance…) after the IP(s)
    - simple geometry of the return pass
    - absence of spin-resonances
    - possible multiple collisions (IPs)
- Usage of the linac (ERL) geometry
  - ensures easy adjustment the e-beam repetition rate to that of the beam in the RHIC, which significantly depends on the ion energy (equivalent change in circumference is ~ 30m);
  - allows straightforward upgrades of the e-beam's energy
  - opens possibility of using multiple energy collisions
  - offers possibility of employing an γ-ion collider with an ERL-based Compton source of γ-rays

There are some limitations for ERL-based eRHIC that include

- No positron-ion collisions;
- Need for intense R&D program on
  - High-intensity, high-current polarized electron source
  - High current ERLs

[1] "The Electron Ion Collider", A white paper summarizing the scientific opportunities and the preliminary detector and accelerator design options, February 2002, http://www.phenix.bnl.gov/WWW/publish/abhay/Home_of_EIC/Whitepaper/Final/

[2] "Upgrading RHIC for Higher Luminosity", W. MacKay, I. Ben-Zvi, J.M. Brennan, M. Harrison, J. Kewisch, S. Peggs, T. Roser, D. Trbojevic, V. Parkhomchuk, Proc. Of PAC'2001, Chicago, Illinois U.S.A. June 18-22, 2001

[3] General accelerator concept and parameters, V.Ptitsyn, T.Roser, F.Wang, eRHIC ZDR, Chapter 1.1, http://www.agsrhichome.bnl.gov/eRHIC/eRHIC_ZDR.htm

[4] "Instabilities in RHIC", M.Blaskiewicz, W. Fischer, eRHIC ZDR, Chapter 3.2.5, http://www.agsrhichome.bnl.gov/eRHIC/eRHIC_ZDR.htm

2. Main beam parameters and Luminosity

In contrast with ring-ring eRHIC [3], the IP of the ERL-based eRHIC has round beam geometry in the IP (i.e., *its horizontal and vertical emittances as well as β* are equal*), which is optimal for attaining maximum luminosity. The sizes of the electron and hadron beams are chosen to be equal

$$\varepsilon_e^* \beta_e = \varepsilon_h^* \beta_h \qquad (2.1)$$

by selecting β^* of the electron beam to be $\beta_e^* = \varepsilon_h^* \beta_h / \varepsilon_e$.

For operating the ERL-based eRHIC, we propose using the same number of hadron bunches (360 bunches, rep-rate ~28 MHz) in the RHIC-ring as in the main part of the ZDR [2.1]. Because of the lifting of limitations on the electron beam's tune shift in the ERL case, the number of hadrons per bunch is set to the present limit in RHIC: $2 \cdot 10^{11}$ of protons or $2 \cdot 10^9$ gold-ions.

Table 2.1. Main parameters of the beams and the IP in ERL-based eRHIC.

RHIC	
Ring circumference [m]	3834
Number of bunches	120-360
Beam rep-rate [MHz]	28.15
Protons:	
Beam energy [GeV]	26 - 250
Protons per bunch	$1.0 - 2.0 \cdot 10^{11}$
Normalized 96% emittance [μm]	4-14.5
β^* [m]	0.26
RMS Bunch length [m]	0.2
Beam-beam tune shift in eRHIC	0.005
Synchrotron tune, Qs	0.0028 (see [2.4])
Gold ions:	
Beam energy [GeV/u]	50 - 100
Ions per bunch (max)	$1.0 - 2.5 \cdot 10^9$
Normalized 96% emittance [μm]	1.5-6
β^* [m]	0.25
RMS Bunch length [m]	0.2
Beam-beam tune shift	0.005
Synchrotron tune, Qs	0.0026
Electrons:	
Beam rep-rate [MHz]	9.38 - 28.15
Beam energy [GeV]	2 - 10
RMS normalized emittance [μm]	1- 50 *for $N_e = 10^{10}$ / 10^{11} e^- per bunch*
β^* [m]	0.3-1m, *to fit beam-size of hadron beam*
RMS Bunch length [m]	0.01
Electrons per bunch	$0.1 - 1.0 \cdot 10^{11}$
Charge per bunch [nC]	1.6 – 16*(see below)*
Average e-beam current [A]	0.015 – 0.45

The intensity of the electron beam is limited by the allowable tune shift for hadrons in the eRHIC IP:

$$\Delta_h = \frac{N_e}{\gamma_h}\frac{\beta_h^*}{4\pi}\cdot\frac{r_h/Z}{\varepsilon_e^*\beta_e^*} \quad .$$

With the matching condition present (2.1), it obtains a simpler form that depends only on the number of electrons and the hadron beam's parameters:

$$\varepsilon_e^*\beta_e^* = \varepsilon_h^*\beta_h^* \quad \Rightarrow \quad \Delta_h = \frac{N_e}{\gamma_h}\frac{r_h}{4\pi Z\varepsilon_h} \tag{2.2}$$

Thus, limit for the hadron tune shift (2.2) limits the number of electron per bunch to

$$N_e = \gamma_h\cdot\Delta_{h\ \max}\cdot\frac{4\pi Z\varepsilon_h}{r_h} \quad \approx 1\cdot 10^{11} \quad \text{for 250 GeV p \& 100 GeV/u Au ions} \tag{2.3}$$

In this document we consider that condition (2.2) is satisfied and the hadron beam is stable under such collisions.

- **Luminosity limitations**

For round beam geometry with equal beam sizes, the luminosity formula is very simple :

$$L = f_c\frac{N_e N_h}{4\pi\varepsilon_h^*\beta_h^*}. \tag{2.4}$$

where f_c is the collision repetition rate.

The strongest limitation of eRHIC luminosity in the linac/ring configuration arises from the limitation on the beam-beam tune shift for hadrons (2.2):

$$L = f_c\cdot\gamma_h\cdot N_h\cdot\frac{\Delta_h\cdot Z_h}{\beta_h^*\cdot r_h}, \tag{2.5}$$

that defines the dependence of maximum attainable luminosity through the hadron beam's parameters. It worth noting that the maximum attainable luminosity is directly proportional to the energy of hadron (ion) beam. For the linac-ring collider, the beam-beam effect on the electron beam is better described not by a tune shift but by a disruption parameter:

$$D = \frac{Z_h N_h}{\gamma_e}\frac{r_e}{\sigma^2_{r(h)}}\sigma_{s(h)}$$

Our studies of the electron beam dynamics in the IP (see section 3.f.2) showed that disruption parameters (attainable within parameter-range in Table 2.1) do not limit the eRHIC luminosity. In the ERL configuration, the growth of the beam's emittance in the IP is acceptable for full energy recovery. Thus for, for the parameters listed in Table 2.1, the ERL operation will be stable.

An additional limitation on luminosity may come from the so-called "kink hard head-tail" instability, i.e., the transverse coupled mode instability of ion beam [2.2]. This effect is similar for the linac-ring and for the ring-ring collisions: the head of hadron

bunch can affect its tail by altering the position of the electron beam propagating through the ion beam in the IP. According to a rather conservative analysis[7] [2.3], the beams are stable when

$$\Box = \frac{D \cdot \Box_h}{Q_s} < 2\Box. \qquad (2.6)$$

This stability criterion is satisfied for the most[8], but not all, of the parameter range we did considered above. The stability criteria (2.6) can be exceed in parallel mode of operation for electron energies below 5 GeV as well as for 10 GeV electrons in the dedicated mode of eRHIC operation.

We plan to use a simple feedback system for stabilizing this potential instability. The idea of the feedback is based on the fact that electron bunches are very short (~ 1 cm) and do oscillate a whole in the kink-instability. Thus, using a detector of the transverse position of the electron beam after the IP and applying the transverse kick to a fresh electron bunch, which will interact with the same hadron bunch on a consecutive turn about the RHIC, will suppress the instability. This feedback system, requiring a very decent bandwidth ~ 56 MHz, has many precedents in the accelerator technology. Again, the use of fresh electron bunch for the ERL makes the concept of the feedback very straight-forward and transparent.

- **Luminosity constraints**

Other luminosity constraints can come from the limitation of the detector's DAQ-speed or from the background created by synchrotron radiation from the electron beam. The latter is very unlikely to occur in the linac-ring version of eRHIC. Using a low emittance electron beam and a large $\Box_e^*$ in the linac-ring version of eRHIC very significantly reduces the angular spread of the synchrotron radiation (8-to-10 fold vertically), which can leave the interaction region with relative ease (see section 3.f for details).

References:

[2.1] ZDR's section 1.2: V.Ptitsyn, General accelerator concept and parameters http://www.agsrhichome.bnl.gov/eRHIC/

[2.2] R.Li, B.C.Yunn, V.Lebedev, J.J.Bisognano, Proceedings of PAC 2001 (2001) p.2014

E.A. Perevedentsev, A.A.Valishev, Phys. Rev. ST-AB **4**, 024403 (2001)

[2.3] R.Li, B.C.Yunn, ICFA Beam Dynamics Newsletter No. 30, April 2003, p.69

[2.4] Synchrotron frequencies are taken from Instability limit on ion bunch length, M.Blaskiewicz, eRHIC, Meeting: July 15, 2003www.agsrhichome.bnl.gov/eRHIC/

[7] This analysis does not take into account the tune spread induced in the ions at the IP. It is known that tune spread can cause Landau damping and, hence, large stability range of the beams. Simple arguments of the phase mixing lead to a slightly different stability criteria $D < 2\Pi$.

[8] A 10 GeV electron beam colliding with 2 10^9 Au ions in parallel mode gives $\Pi = 3.5$, and a 10 GeV electron beam colliding with 2 10^{11} proton in parallel mode gives $\Pi = 4.09$.

3. Layout of the linac-ring eRHIC

Main components of the ling-ring eRHIC are show in the following figure:(one of several possible configurations – not in scale, see layouts in the Section 1.)

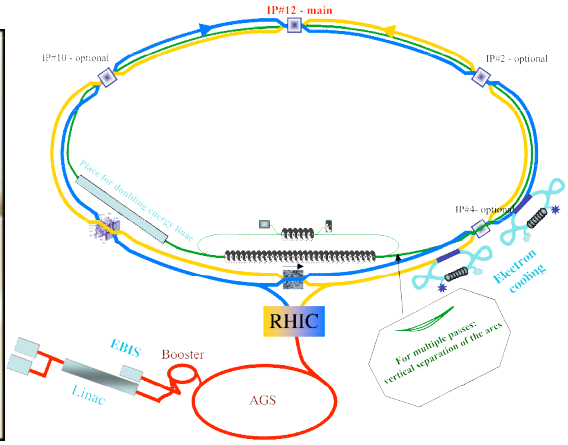

- RHIC – remains practically unchanged with exception of one IP http://www.bnl.gov/RHIC
- Electron cooling – as described in section 3.e

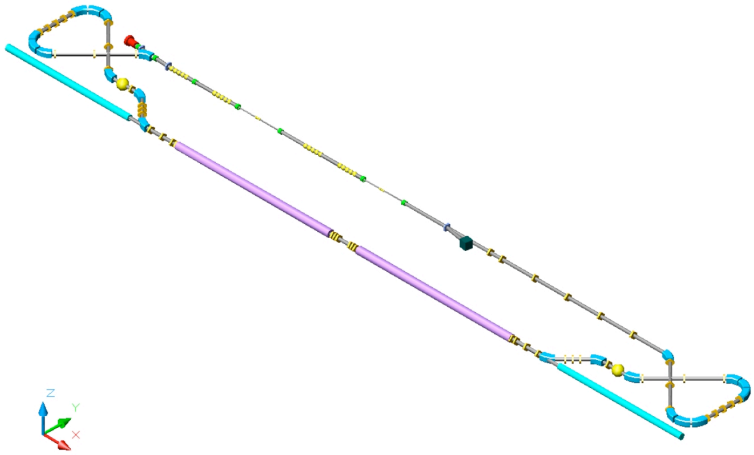

- Polarized electron gun - – as described in sections 3b and 3c
- Accelerating super-conducting linacs – see following section

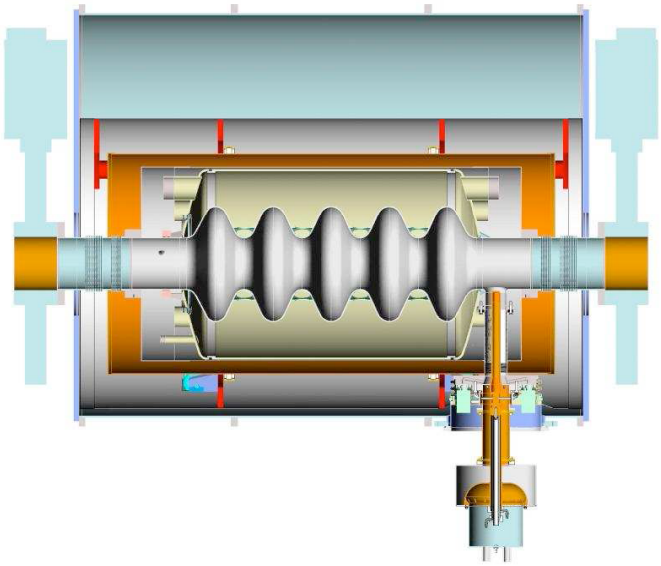

- Arcs and turns – The ERL has four major and two minor arcs. Arcs are comprised of a rather simple FODO lattice with high density, but low field dipoles (for reducing synchrotron radiation losses to about 5 MeV for the entire cycle from the gun to the damp). The arc with the largest energy of electrons incorporates the IP. Issues related to spin transparency are described in section 3.d.
- Interaction region – see section 3.f
- Returning pass and beam dump – It is not necessary to preserve the high quality of the e-beam and its polarization after the collision. Accordingly, a returning half-arc can be designed after the IP with a vertical chicane for avoiding a second crossing with the RHIC rings (see section 2.2 and 2.5 in the main part of ZDR). The returning pass serves the rather *simple but critical role* of recovering energy from the decelerating beam into the superconducting RF system. With the exception of the first half-arc, the decelerating beam reuses the same arcs. Finally, at the end of the deceleration process, the electron beam's residual energy, which is well below 10 MeV, is damped. Using damping energy below 10 MeV is a very critical environmental issue – it avoids residual radioactivity in the damp.

The following additional major systems are required for the linac-ring eRHIC, but are not shown in the above schematic:

- $2K^{o}$ helium refrigerator for superconducting RF cavities
- 700 MHz RF power system
- Power supplies for ERL's and arc's magnets
- Auxiliary RF system for compensating synchrotron radiation losses

3.a Energy recovery linac

Figure 3.a.1.is a schematic of the proposed two-stage 10-GeV energy-recovery linac based on 703.75 MHz super-conducting RF-linacs for the eRHIC.

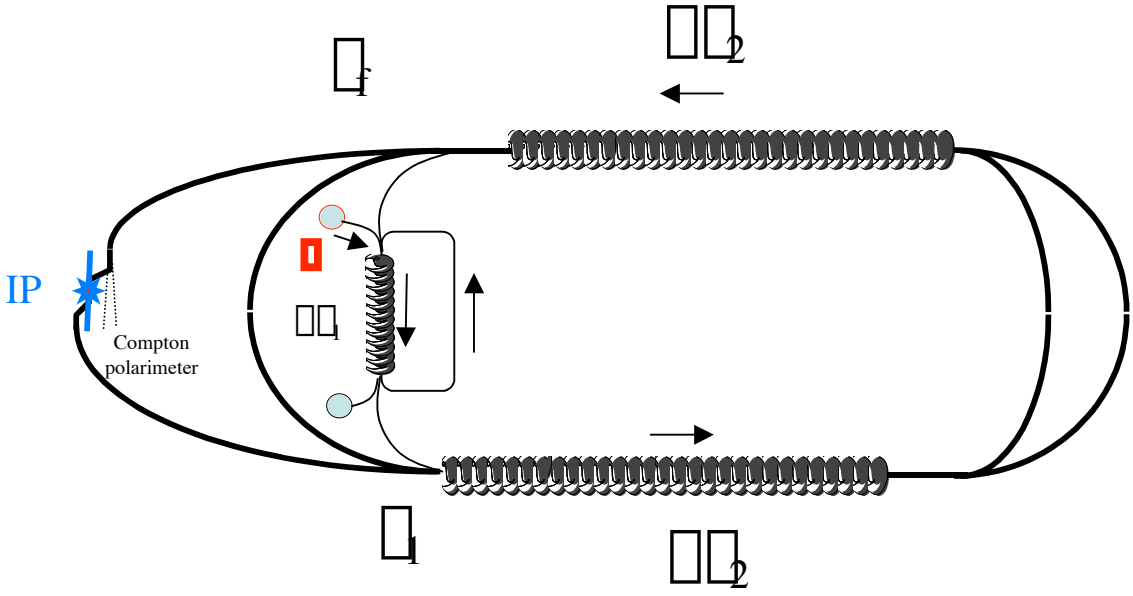

Fig. 3.a.1 Schematic of the two-stage ERL.

In this section we give bulk values for energies of electron beam for the maximal 10-GeV e-beam energy in the IP. Section 3.d details the choice of the linac settings required for spin transparency.

Polarized electrons with initial energy of 5 MeV are injected into the first ERL with a 500-MeV superconducting linac. They pass twice through this linac before entering the main ERL.

Table 3.a.1 Energy and relativistic parameters of electrons in the low energy ERL: $\gamma\gamma_1 = 965.75$

Pass	E in, MeV	E out, MeV	γ	γ
1	5	498.5	9.78	975.53
2	498.5	1000	975.53	1956.93

Table 3.a.2 Energy and relativistic parameters of electrons in the main ERL: $\gamma\gamma_2 = 4403.10$

Pass	E in, MeV	E out, MeV	γ	γ
1 – linac 1	1000	3250	1956.93	6360.04
2– linac 2	3250	5500	6360.04	10763.14
3– linac 1	5500	7750	10763.14	15166.24
4– linac 2	7750	10000	15166.24	19569.34
eRHIC IP	**10000**		**19569.34**	

The main ERL has two linacs with a nominal energy gain of 2250 MeV per linac. Passing twice through each linac, the e-beam reaches maximum energy of 10 GeV. During the process of acceleration in the ERL, the electron beam passes through the arcs where it loses about 2.5 MeV of its energy in the form of synchrotron radiation.

At full energy, the e-beam passes through a half arc towards the IP. A Compton laser polarimeter installed in the dogleg just before this acquires final measurements of the e-beam's polarization in the IP (note that the dogleg does not affect the polarization, see section 3.d).

Each normal arc or transfer line of the ERL ensures a delay in e-beam time equal to an integer number of RF cycles. In this case, all linacs will synchronously accelerate (or decelerate) electrons. The last arc with the IP and vertical chicane is a special one – it provides for a delay in the e-beam time equal to an integer number plus a half of RF cycles to change the accelerating sequence into a decelerating one. It also incorporates a special cavity to compensate for the synchrotron radiation losses. Section 3.h addresses details of the synchronization, RF cavity phasing and collision frequency adjustment.

The decelerating schedule for the e-beam is just the inverse of that in Tables 3.a.1 and 3.a.2. The electrons pass twice through the same linacs and arcs in the main ERL to decelerate to 1 GeV:

Pass - decelerating	E in, MeV	E out, MeV
1 – linac 1	10000	7750
2– linac 2	7750	5500
3– linac 1	5500	3250
4– linac 2	3250	1000

This sequence matches the e-beam energy in each arc in both accelerating and decelerating processes; hence, there is a significant reduction in the cost of magnetic lattice of the ERL.

Finally, the 1 GeV e-beam decelerates in a low energy ERL to an energy of about 5 MeV and is damped. A damping energy of about 5 MeV insures the absence of residual radiation in the damp, i.e., the damp looks like a "simple" but shielded 2 MW heat source.

Standard cell

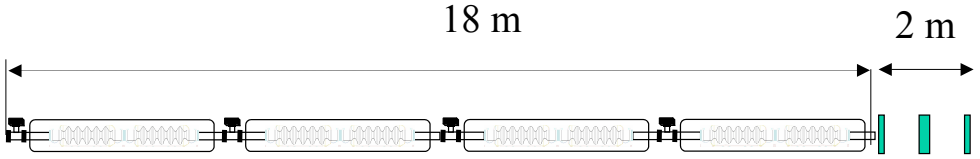

Fig. 3.a.2. Standard basic cell of the ERL linac

Each linacs of the main ERL is comprised of fifteen standard basic cells. Each standard cell (shown in Fig. 3.a.2) contains 4 super-cavity structures and a set of magnetic quadrupoles with constant gradients (leading to and for a linearly growing □-

function [3.a.12]). Each superstructure consists of two 5-cell superconducting accelerating cavities sharing one helium tank and high-efficiency ferrite high-order mode (HOM) - absorbers (the cavity is described below). The use of large aperture RF structure [3.a.1] with effective HOM absorbers is unique to BNL's approach to the ERL. These arrangements assure both a reasonable average accelerating gradient (of about 9-10 MeV/m) and very high stability of the re-circulating e-beam.

The low energy linac, which determines the ultimate stability of the e-beam , has a similar structure but has quadrupoles filling each gap between the helium tanks thereby obtaining lower values of the □-function without significant beating In addition, the first few of low energy accelerating cavities (i.e., those accelerating and decelerating the e-beam between 5-100 MeV) have individual HOM tuners to further increase the e-beam's stability.

Main components of ERL linac

- Five-cell high-current superconducting accelerating cavity
- standard design, normal temperature quadrupoles in linac
- standard design, normal temperature quadrupoles and dipoles in FODO lattice arcs

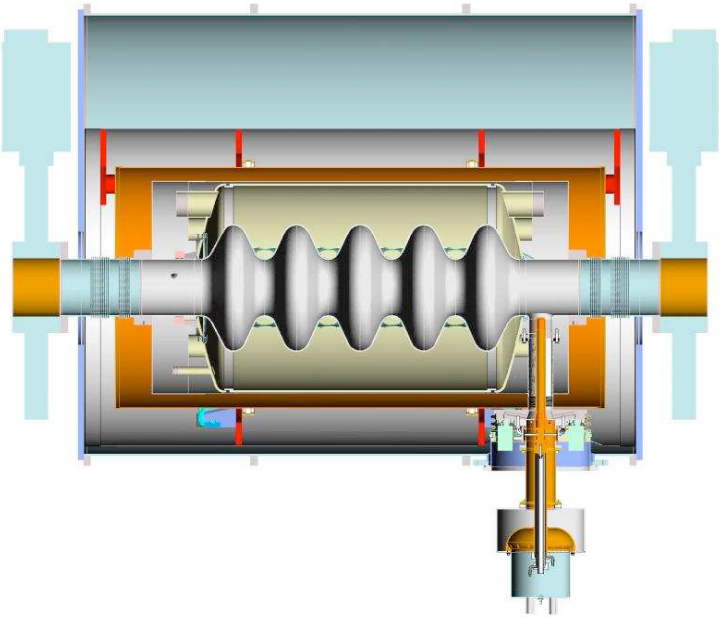

Fig. 3.a.3 A 3-D computer-generated model of the prototype five -cell 703.75 MHz superconducting cavity [3.a.1].

The most important individual component of the ERL is the five-cell superconducting RF (SRF) cavity – a first SRF cavity designed specifically for high-current ERLs [3.a.1]. Its unique features are the key for the proposed eRHIC scheme.

Several factors influenced the choice of key parameters of the cavity.

1. A frequency of 703.75 MHz was chosen due to both physics and engineering issues. This is the 25th harmonic of the RHIC bunch repetition frequency with 360 buckets. A small loss factor from HOMs and the possibility of a larger aperture were important criteria. Also, engineering issues such as the availability of high-power CW klystrons and chemical-cleaning facilities played an important role. A potential future use of this cavity in a linac-ring version of eRHIC (electron-ion collider) also was considered.
2. A five-cell structure with a large aperture of 19 cm was selected in the original design [3.a.2] to optimize the cavity for the best possible damping of higher-order modes. However, further investigation revealed that a 17 cm aperture gave higher acceleration efficiency while effectively damping all HOMs.
3. Ferrite absorbers have proven successful in single-cell cavities (CESR & KEK-B). Following the Cornell design, we adopted them in a five-cell linac cavity.

   The HOM absorbers adequately damp all modes in the cavity that might lead to beam instabilities. Using two ferrite absorbers located along the beam pipe at room temperature simplifies the design. Additional HOM couplers installed in the cavity may prove useful for tuning HOMs in individual cavities to further increase the beam's stability.

The cavity geometry was constructed using "Build Cavity code" "[3.a.4], a graphics interface software to Superfish. It allows the user to specify multi-cell cavity parameters and optimizes the cavity's geometry through a series of Superfish runs. Figure 3.a.4 shows the cavity design with 17 cm aperture and a 24cm beam pipe.

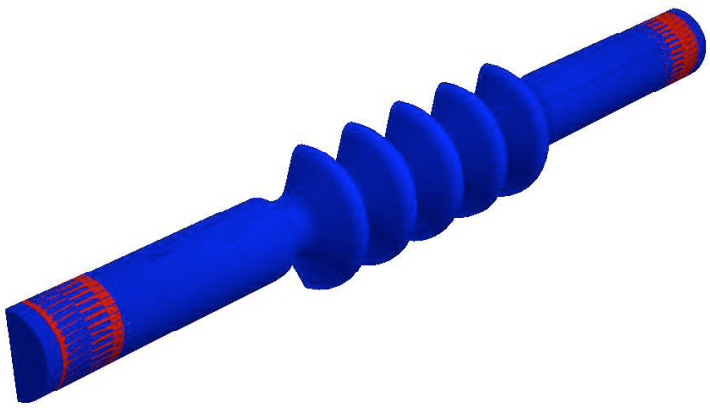

Fig. 3.a.4 Mafia-generated 3D geometry of cavity with enlarged beam pipe and ferrites.

The ferrite absorbers, 24 cm in diameter and 20 cm long, are located outside the cryostat at room temperature. The ferrite material used is Ferrite-50 and is manufactured by ACCEL according to the Cornell design. Various parameters of the five-cell cavity are shown in Table 3.a.3. The optimum iris diameter of 17 cm is compared to an earlier choice of 19 cm.

Table 3.a.3: Cavity Characteristics

Iris Diameter (cm)	17	19
Frequency (MHz)	703.75	703.75
G (Ω)	225	200
R/Q (Ω)	807	710
Q @ 2k	4.5×10^{10}	4×10^{10}
E_p/E_a	1.97	2.10
H_p/E_a (mT/MV/m)	5.78	5.94
cell to cell coupling	3%	4.8%

For the calculation of Q at 2K, we assumed $R_{BCS} = 3n\Omega$ *, and* $R_{residual} = 2\ n\Omega$.

Field flatness and surface fields for the fundamental modes, calculated using 2D FEM code [3.a.5], is similar to the Mafia results shown in Fig. 3.a.5.

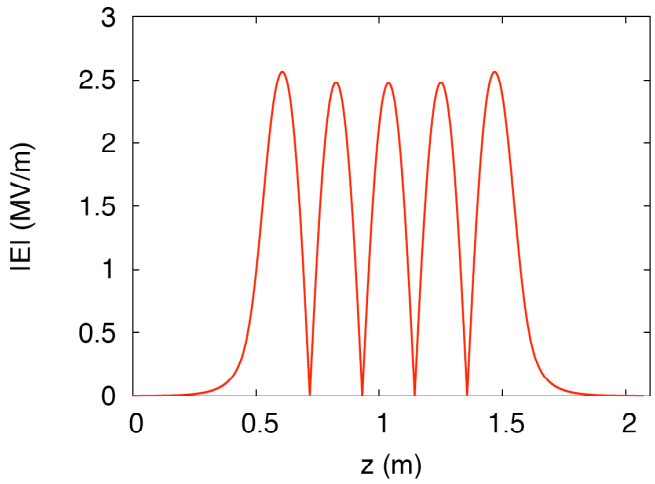

Fig. 3.a.5. Field flatness of the fundamental mode peak-peak 96.5%.

The complex structure of multi-cell cavities often cause modes to be trapped inside the cavity, thus limiting the beam's performance due to instabilities. There are two main reasons for HOMs to become trapped inside the cavity structure:

1. The geometry of the end cell differs from that of the middle cells. This may result in poor cell-to-cell coupling and thereby trap HOMs.

2. Some HOMs may occur below the cutoff frequency of the beam pipe, so preventing the mode from propagating out of the structure. These modes exponentially decay in the beam pipe before they reach the ferrite absorbers.

It is very important to carefully analyze such trapped modes and to modify the cavity structure accordingly to propagate them. It is common practice to use HOM couplers to couple out some harmful modes that exist in these complex structures. A preliminary design for couplers is underway at BNL. However, we propose a cavity design that will demonstrate the possibility of a high current operation with just ferrite absorbers placed in the warm section, thus minimizing cryogenic losses and simplifying critical engineering issues.

The cavity's geometry was optimized for higher-order modes using Mafia's e-module with inverse solver[9]. An initial geometry using a 19cm iris was proven to have three trapped dipole modes (TM1xx) causing the beam to break up at when operating at high current. Analysis of several combinations of cavity iris and beam-pipe radius showed that an iris of 17cm and beam radius of 12cm was an optimized design for both fundamental efficiency and preventing the trapping of harmful dipole modes. The Q values of the dipole modes can directly indicate possible trapped modes. Fig. 3.a.6 shows dipole Qs as a function of frequency for different beam-pipe diameters. A different method exploiting boundary conditions to calculate the coupling of cavity dipole modes to the beam pipe's diameter yield similar conclusions that all modes couple to the beam pipe and will be adequately damped by ferrite absorbers. The factor k shown in Fig. 3.a.6 is a measure of relative field strength between the middle cells and end cell. Fig. 3.a.7 shows a similar calculation for monopole modes.

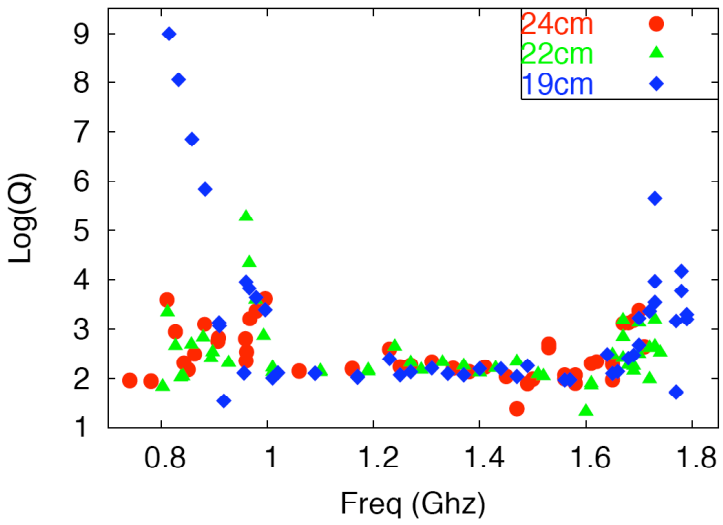

Figure 3.a.6: Dipole Q dependence for 17 cm iris and various biam-pipe diameter geometry.

[9] complex eigenvalue solver

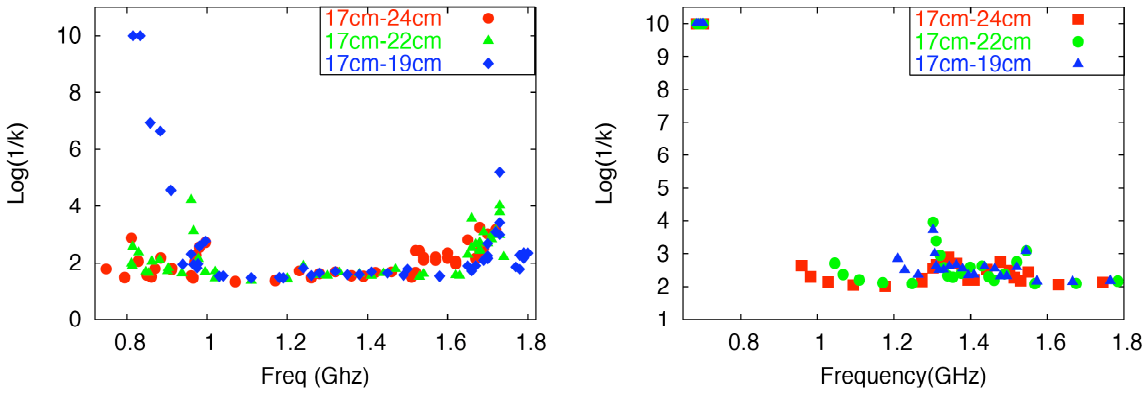

Figure 3.a.7: Analysis of trapped modes in loss-free case. A. Dipole, B. Monopole

The R/Q values for the cavity modes can be easily computed using perturbation methods in MAFIA. It is most desirable to design a cavity with a high fundamental R/Q while keeping the R/Q for dipole modes as low as possible. We find that the R/Q values for dipole modes are quite small for our geometry. Table 3.a.4. shows a few modes with the highest R/Q.

Table 3.a.4 : R/Q and Q Values for Six Dipole Modes of Interest

Frequency (MHz)	R/Q (Ω)	Q
862.6	30.1592	623.266
882.2	54.6518	2499.858
906.9	41.719	1133.058
967.1	3.5272	3212.957
979.2	3.7425	4608.0
995.7	1.7205	8088.546

The MAFIA results were crosschecked using HFSS [6]. Since HFSS only computes in 3D, the exact input used in MAFIA was replicated in 3D in HFSS and dipole Qs were computed. We were able to extract the dipole Qs of particular modes of interest. Fig. 3.a.8 shows that the MAFIA values agree well with those of HFSS. This is additional proof that our cavity structure is indeed HOM free. Spell out HFSS

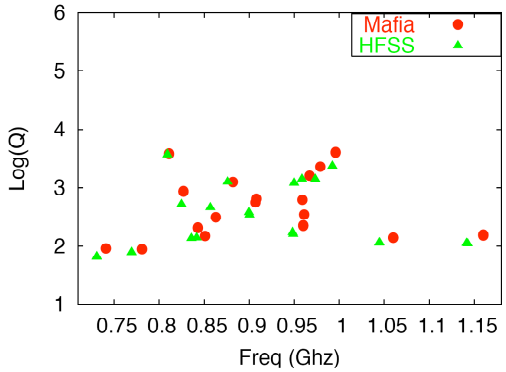

Figure 3.a.8: Dipole Qs from MAFIA and HFSS for the 17 cm geometry

Multi-bunch instabilities are an important issues for any ERL. The energy recovery mode, and high currents contribute strongly to coupled bunch instabilities due to the poorly damped higher modes that limit the cavity's performance. The low frequency dipole modes are particularly dangerous and cause breakup of the beam. We find most dipole Qs to be small with a few of the order of 10^3, but still they do not pose any significant threat. This feature remains to be checked in the high-frequency range (above 2 GHz), but contributions from high-frequency modes to the break up of the beam usually are small. Also, we find that R=Q values are small for all modes which indicate that the threshold currents for such breakup are high. We used the TDBBU simulation code developed in Jefferson Laboratory [3.a.7] to calculate these breakup thresholds from R=Q, Q, and corresponding frequencies, along with other beam parameters as input. We simulated each cavity as two drifts with an energy gain of 13.5 MeV with the HOMs placed inbetween the drifts. Using each dipole mode in both polarizations with a 15 MHz Gaussian distribution, we obtained a threshold current of 1.8 A. Work is underway to accurately build a cavity matrix and optics for the beam to propagate around the ring. In principle, this approach should increase the threshold currents. A sister simulation software called MATBBU [3.a.8] was recently acquired from Jefferson Laboratory that solves an eigenvalue problem to determine the threshold limits; the results give a threshold current of 1.85 A. Fig. 3.a.9 shows the transverse beam's position as a function of time calculated by TDBBU for a current of 1.8 A. The initial (artificial) transverse kick decays, showing that 1.8 A is a stable operational current.

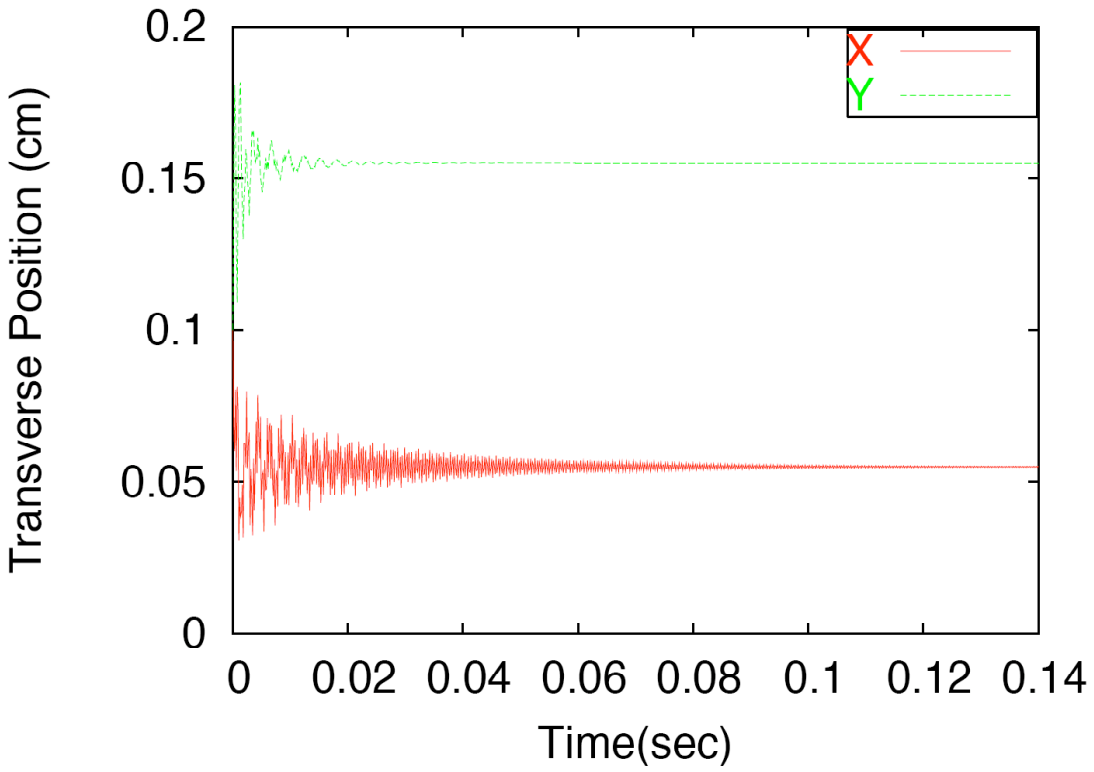

Figure 3.a.9: Simulation of beam breakup in TDBBU with a threshold current of 1.8 A.

One of the major issues in SRF cavity design is power dissipated in the HOMs. High current and high bunch charge implies a huge HOM power that has to be absorbed by the ferrite absorbers or extracted through HOM couplers. When this power is large it becomes a major cryogenic challenge, so it is imperative to keep HOM power loss to a minimum. The HOM power is given by

$$P_{HOM} = f_{beam} k_{loss} q^2$$

where f_{beam} is the beam-repetition frequency at a bunch charge q, and k_{loss} is the loss factor which is given by

$$k_{loss} = \frac{1}{2\pi} \int_0^{\infty} Z_r(\omega) d\omega .$$

In the neighborhood of the resonance frequency, the integral simplifies to the following expression: use normal size type

$$k_{loss} = \frac{\omega_n R_n}{4 Q_n}$$

where loss factor was calculated with ABCI, using a single bunch with a 1cm RMS length. The loss factor results are displayed below in Fig. 3.a.10.

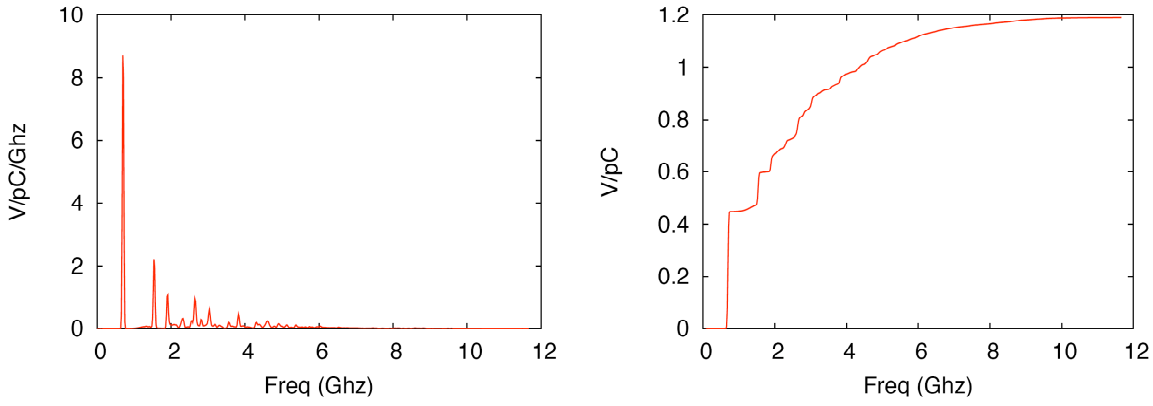

Figure 3.a.10: Loss Factor and integrated loss factor for 17-24cm geometry

Another important factor to consider is wall losses due to the fundamental mode in the beam pipe. Since part of the beam pipe is at 2K, it becomes crucial to minimize this loss so that CW operation becomes feasible. Preliminary calculations from BNL's cryogenic group [3.a.13] indicate a maximum loss of 25 watts will be tolerable for a sustained CW operation. This power loss can be calculated with MAFIA. Thus, for a beam pipe 20-cm long made of copper after the end cell with our present configuration shows a total wall loss less than 10 watts on both sides of the cavity. We expect to intercept this power at liquid nitrogen temperature. The copper tube, also serving as a shielding for the stainless-steel bellows, will be anchored to the radiation shield and thermally isolated from the niobium pipe. The electrical path for HOM power and beam image currents will be

provided by a small capacitive element.

Simulations for a low energy prototype of the ERL showed that *threshold current for the transverse beam breakup is as high as 1.85 A for a single pass (i.e., ~ 0.9 A for two passes)*. The main reason for this very impressive result is strong damping of the HOM in the advanced five-cell cavity design described above with large sized irises and ferrite absorbers.

The PERL design studies [3.a.11] demonstrated that choosing a focusing optics in the linacs with β-function proportional to the e-beam energy sets conditions for improved beam stability, assuming that arcs properly match β-function and the phase advance is proper. The above conditions allow element M_{12} to come very close to zero for all individual cavities.[10]

Presently, detailed designs are underway for

- Lattice for the linacs
- Lattice for the arcs
- Longitudinal dynamics in the ERL
    - Including Polarization effects (see also section 3.d)
- Losses for synchrotron radiation
- Energy recovery and beam dump

Layout and Optics of the linac – on of the options for ERL [3.a.14]

The linac recirculates the beams to reduce the number of cavities needed to reach the final beam energy. A recirculating energy-recovery linac consists of three distinct building blocks:

- The linacs that accelerate and decelerate the beam. Beams of different energies can be in the linac simultaneously.
- The arcs that bend the beams around to reinject them into the linacs. A separate arc must be used for each beam energy.
- The spreader/recombiner sections that distribute bunches from the linac into the arcs according to their energy.

Since the number of arc beam lines increases proportionally to the number of passes through the linacs, and the current threshold for multibunch instability decreases with the number of passes, only two passes are used in the eRHIC.

The focusing in the linacs is determined by the lowest beam energy. Overfocussing must be avoided. For that reason, a two-stage scheme is used (Fig. 3.a.11). The beam is generated by an RF gun and accelerated to about 10 MeV. It is injected into the first-stage linac with 12 cryo modules and accelerated to 1.018 GeV using one recirculation. The second stage uses a racetrack layout, similar to the CEBAF accelerator, that minimizes the tunnel's length.

[10] Detailed studies of theoretical aspects of ERL beam dynamics also are in progress

The two linacs are parallel. Accordingly, the linacs can be lengthened in future upgrades with a minimum amount of concrete work. A triangular layout also could be adopted , that would lower synchrotron-radiation power, but at the cost of a longer tunnel.

Each of the two linacs has 60 cryo modules for an energy gain of 2.268 GeV per pass. The beams are focused by quadrupoles in a F0D0 arrangement. In contrast to the CEBAF accelerator where the field gradient increases with the beam's energy, the quadrupole field is fixed. In such a lattice, the beta functions oscillate around an average value, which increases with the beam's energy. Since the linacs are optically symmetric, a mismatch and large beta beat is avoided. Small beta functions increase the threshold for the multi-bunch beam breakup. Fig. 3.a.12 shows the beta functions for all passes of the second-stage linac.

The arc length is given by the allowed synchrotron radiation power that must not exceed 7 kW/m in the highest energy arc. This requires a bending radius of 155 m in the arc dipoles. The arcs must be isochronous so that the initial energy spread of the beam does not cause bunch lengthening in the first arc which would increase the energy spread in the next linac, and so on. The arc dipoles are 5 meters long with a field of 2 kG at 10 GeV. The arc cell, consisting of twelve dipoles (Fig. 3.a.13), has a fill factor of 68% (integrated dipole length over total length). The average radius of the arc is 250 m. The dispersion function is zero at both ends of the cell, thereby allowing the insertion of the interaction region in the 10 GeV arc and of dogleg dipole magnets for variation in path length in the lower energy arcs.

The spreaders/recombiners separate the beams horizontally. Since there are only two beam lines in the arc tunnels this does not make the magnets inaccessible as it would in the CEBAF with five beam lines. Further, there is no need to match the vertical dispersion. The horizontal dispersion can easily be matched by modifying the quadrupole strength in the first arc cell. Figs. 4 and 5 show the spreader for the north end and the south end of the linacs, respectively.

To protect the superconducting cavities from the synchrotron radiation, the first dipole of the spreader has a low field of 200 Gauss, resulting in a bending radius of 1500 m at 10 GeV. The total radiated power from this dipole is 70 Watts. Half of this power can be removed with a collimator in front of the first cryomodule. Since the inner diameter of the cavities is 17 cm, the remaining radiation will go through the cavities without hitting the walls. A second collimator (and maybe third) inside the linac will remove this radiation.

The optics of the interaction region optics are similar to those used for the ring-ring version (Fig. 6). However, since the beta function in the interaction point is much larger (92 cm), the beta function in the focusing quadrupoles is much smaller. Figure 7 shows the fan of synchrotron radiation created in the interaction region; it must not hit the beam pipe inside the interaction region. Fig. 7 shows that the IR must be antisymmetric to accomplish this. A detailed layout of the arcs and interaction region is being developed.

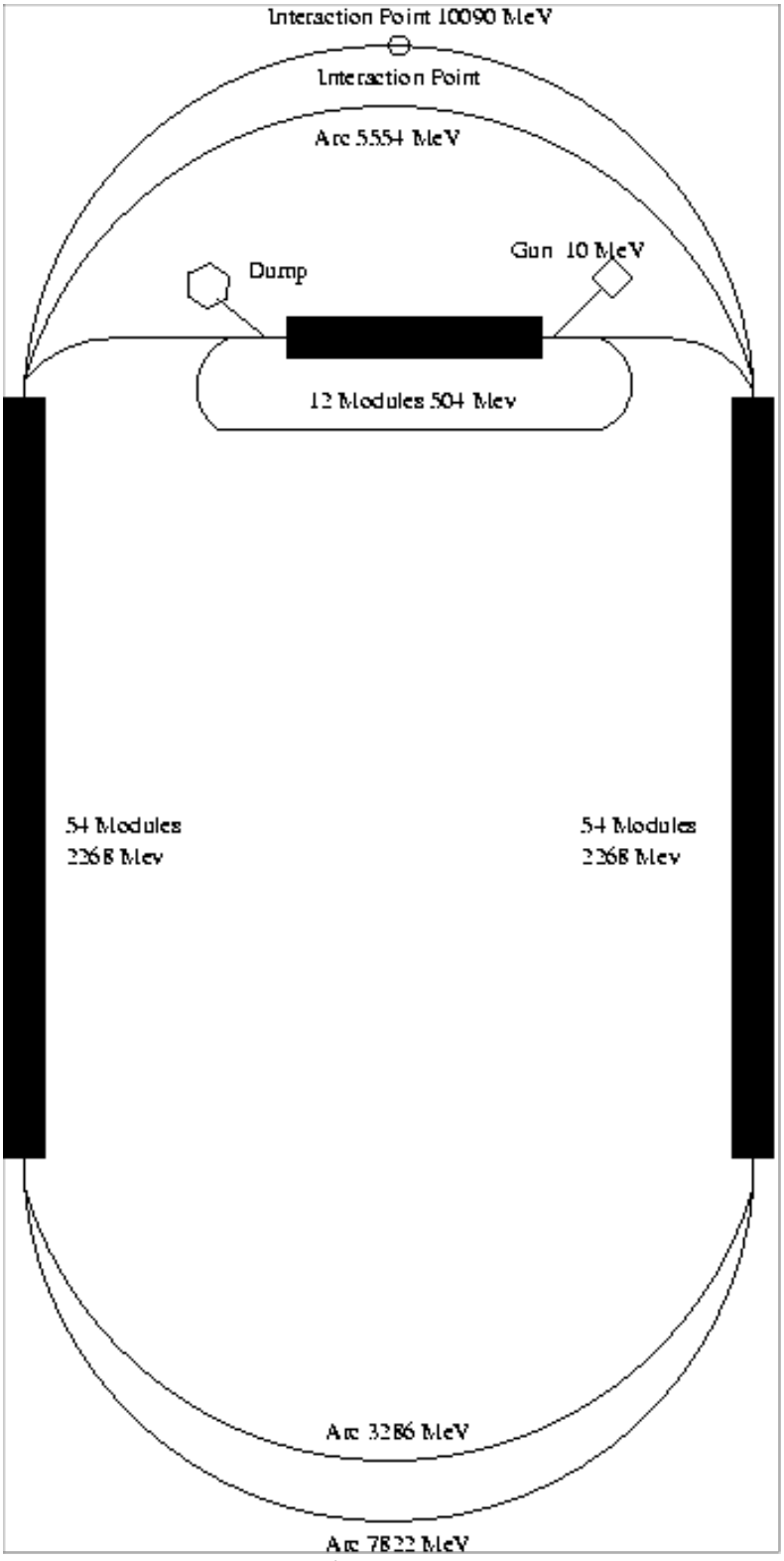
Interaction Point 10090 MeV
Interaction Point
Arc 5554 MeV
Gun 10 MeV
Dump
12 Modules 504 Mev
54 Modules
2268 Mev
54 Modules
2268 Mev
Arc 3286 MeV
Arc 7822 MeV
Figure 3.a.11

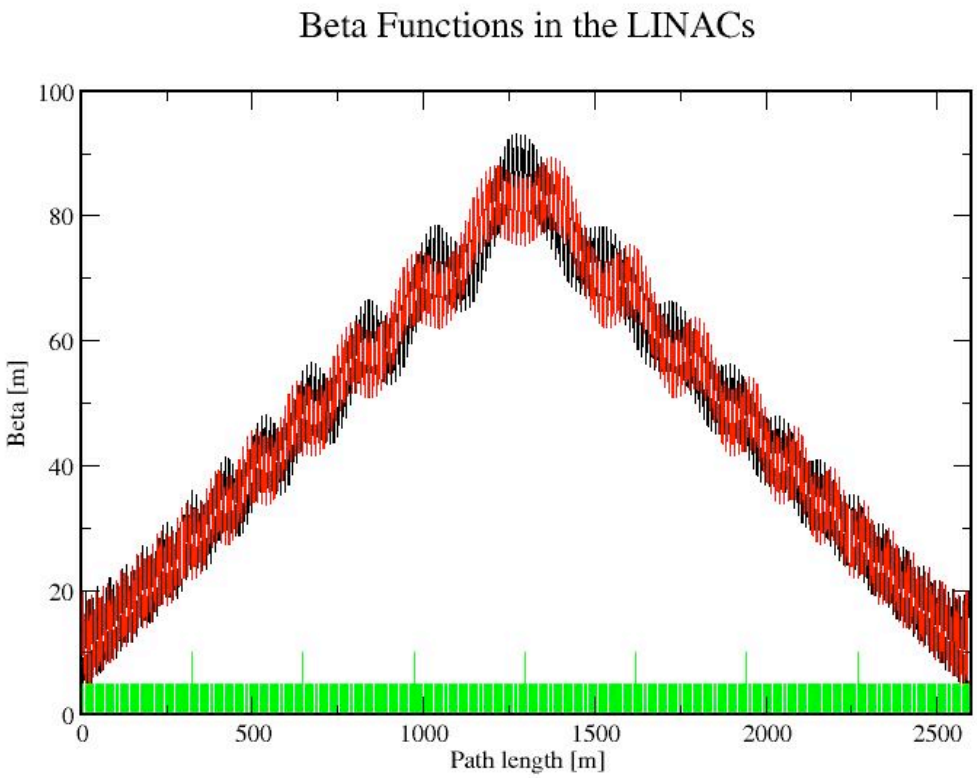

Figure 3.a.12 Beta functions (black horizontal, red vertical) of all Linac passes. The arcs are represented as thin matrix elements, shown as tall green lines.

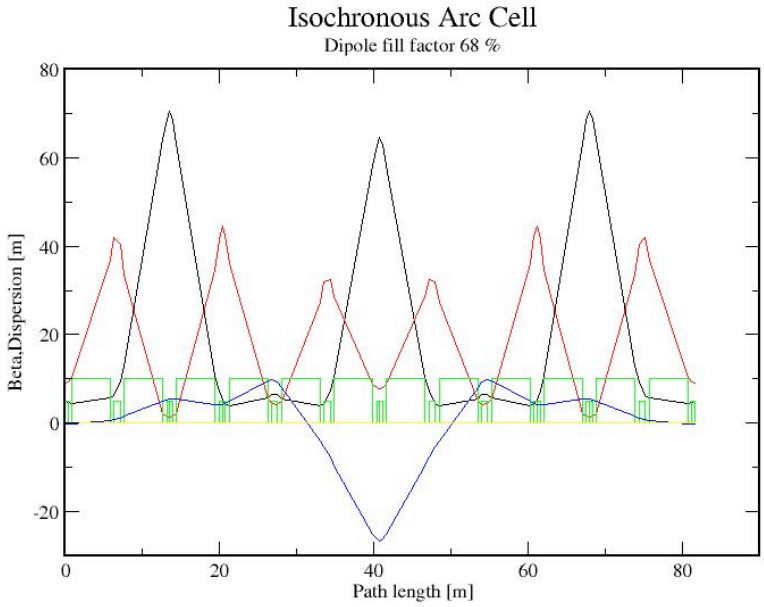

Figure 3.a.13. Arc cell

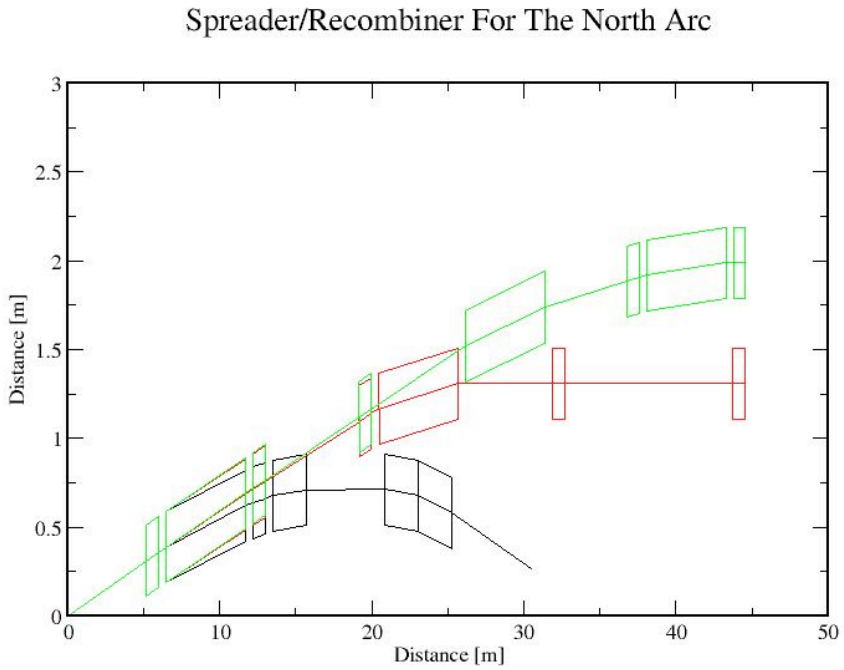

Fig. 3.a.14: Beam spreader/recombiner for the north end of the linac for the injection/extraction line (black), the 5.5 GeV line (red), and the 10 GeV line (green).

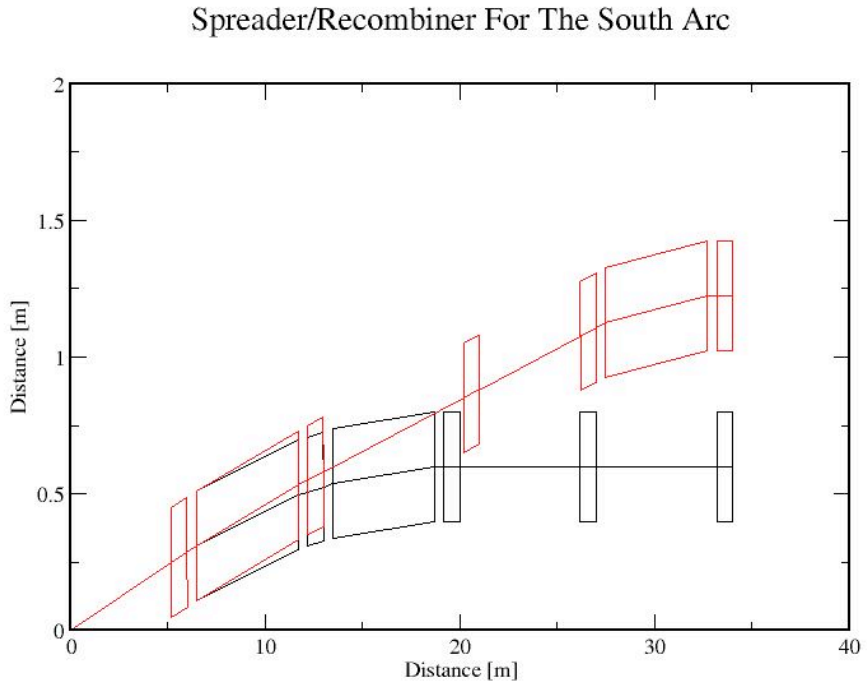

Fig. 3.a.15: Beam spreader/recombiner for the south end of the linac for the 2.25 GeV line (black) and the 7.75 GeV line (red).

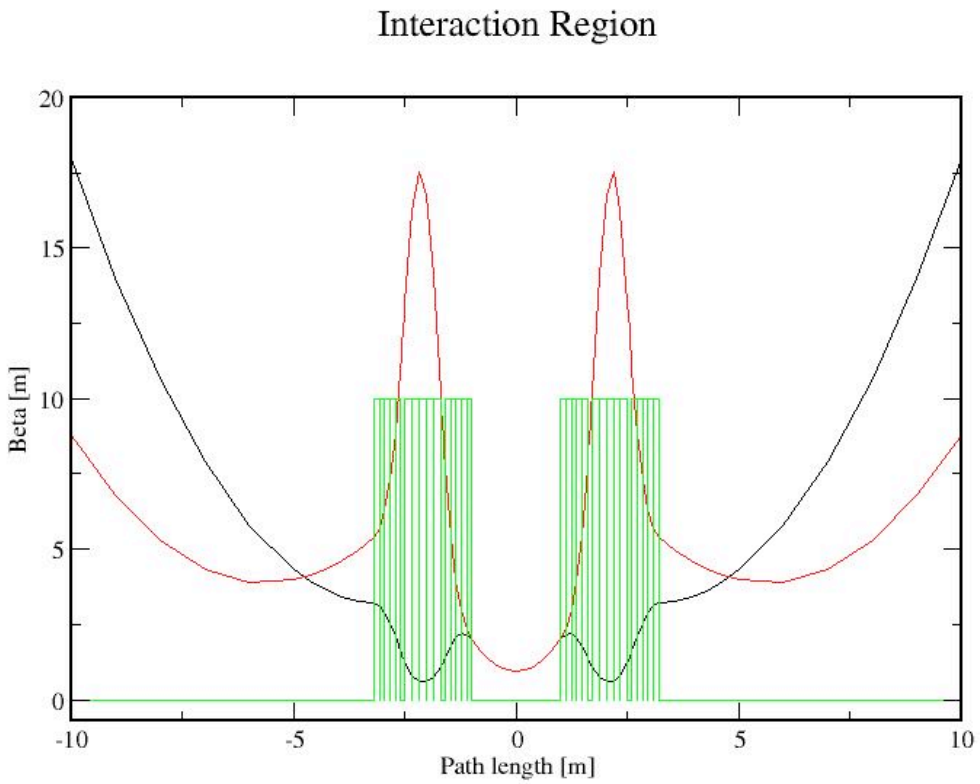

Fig. 3.a.16: Interaction region optics

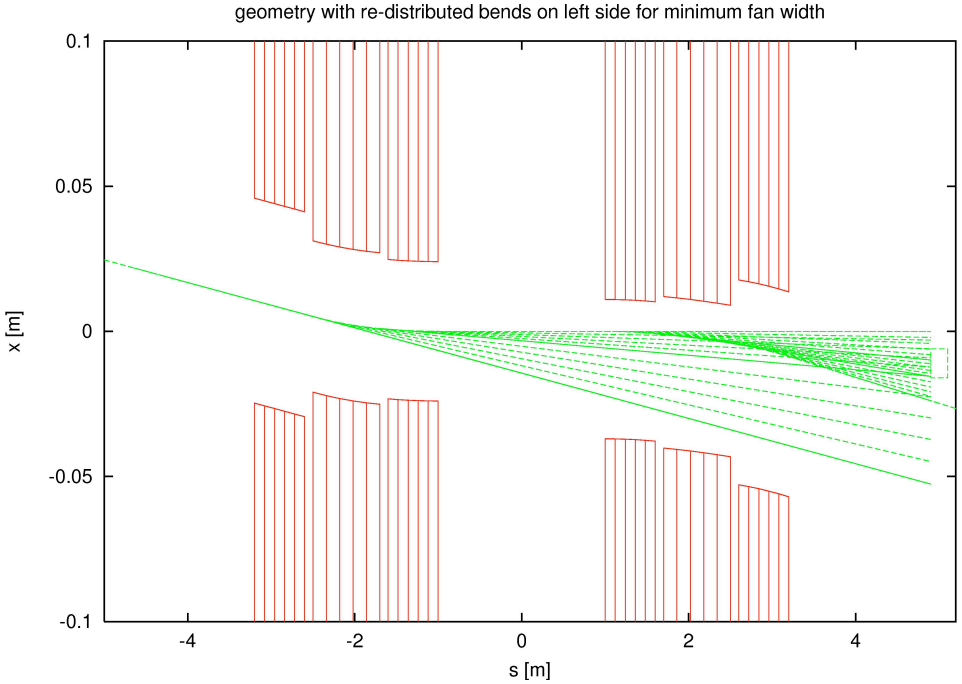

Fig. 3.a.17: Radiation fan in the interaction region. The radiation created in the interaction region must be absorbed outside the beam pipe.

References

[3.a.1] R. Calaga et. al., Proceedings of SRF2003, Travemünde/Luubeck, September 2003.
[3.a.2] Dong Wang et. al., PAC 2003, Portland, May 2003.
[3.a.3] The MAFIA Collaboration, MAFIA Version 4.0, CST, GmbH, Darmstadt, Germany.
[3.a.4] Paolo Pierini, Build Cavity Manual, Milan, Italy.
[3.a.5] J. Sekutowicz, Proceedings of Linear Accelerators Conference, Tsukuba, Japan, 1994.
[3.a.6] High Frequency Structure Simulation (HFSS), ANSOFT Co., Pittsburgh, PA, USA.
[3.a.7] TDBBU was written by G.A. Krafft at Jefferson Laboratory.
[3.a.8] MATBBU was written by G.A. Kraft at Jefferson Laboratory.
[3.a.9] Advanced Energy Systems, USA.
[3.a.10] E. Chojnacki et. al., Proceedings of the Particle Accelerator Conference, 1997
[3.a.11] V.Yakimenko et al., PERL design paper
[3.a.12] V.Litvinenko, eCooling group, Internal Note, August 2003
[3.a.13] Mike Iarocci, Private Communication
[3.a.14] Jörg Kewisch, Vladimir Litvinenko, Christoph Montag, Daniel Anderson, C-AD, Working material, BNL, January 14, 2004

3.b Polarized electron gun

The following description highlights the common part with a description of the main requirements and parameters of the polarized gun in the main section of the ZDR (Sec. 2.3.1, Polarized Electron Photoinjector by M. Farkhondeh and W. Franklin), as well as focusing on issues specific for the ERL-based eRHIC.

Introduction: The advancement in the polarized electron source technology over the past decade at nuclear and particle physics accelerator centers have been substantial [3.b.1-3]. Highly polarized electron beams of diverse peak currents, time structures and duty cycles including CW beams are now routinely produced at Jefferson Lab, SLAC, HERA, MIT-Bates, Mainz and Bon [3.b.1-5]. These polarized injectors are based on photoemission process from strained GaAs based photocathodes illuminated by laser radiations at 800-850 nm followed by an extraction process with high gradient electric field. At MIT-Bates, long pulses with 2 mA currents of highly polarized electron are now routinely achieved.

High polarization photocathodes: Polarized electron beams for accelerators are generated by photoemission process using longitudinally polarized laser lights at 750-850 nm from the surface of GaAs based photocathodes under UHV conditions. The electrons are extracted from the surface using high gradient field present between the anode and cathode electrodes. The maximum theoretical limit for degree of polarization from a bulk GaAs surface is 50% and ~40% in practice due to depolarization effects in the bulk. The photoemission process in bulk GaAs is the simultaneous excitation of electrons in degenerate states in the valance band to the conduction band. To the degree that this degeneracy in the valance band is removed, higher degree of polarization can be achieved. A common technique to remove the existing degeneracy is to introduce strain in the lattice by growing GaAsP layers on substrate GaAs. The lattice mismatch between GaAs and GaAsP produces mechanical strain near the boundary surface [3.b.6]. The active layer must be very thin of the order few hundred nm to keep the strain present near the surface of the photocathode. The reduced depth in the active layer causes a substantial reduction in the Quantum Efficiency (QE) of the photocathode. QE is the fractional number of electrons generated by a single photon. QE for bulk GaAs photocathodes with pol~30-40% is of the order of 1-10 % and 0.01-0.1% for high polarization strained GaAsP, smaller by two decades. The high polarization photocathodes therefore, have the inherent problem of low QE's. With a laser radiation of wavelength λ and power P, the maximum peak current generated from a photocathode of appropriate band gap structure is given by

$$I(mA) = \frac{QE \times P(mW)\lambda(nm)}{1239}$$

For instance, with P=1kW, QE=0.1% at λ=800 nm, a current of ~0.64 A can be generated. As shown in Figure 3.b.1, the QE and polarization are strong functions of λ.

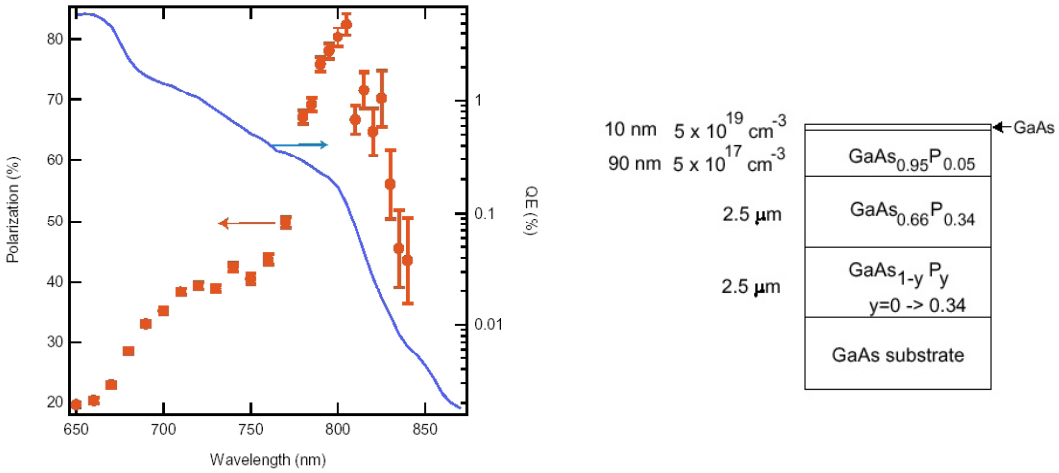

Figure 3.b.1. (Left) Photoemission data on a GaAsP from SLAC [3.b.7] showing Polarization and QE as a function of wavelength. (Right) A schematic diagram of the lattice structure of a high polarization high gradient doped strained GaAsP photocathode [3.b.8] now in use at SLAC and MIT-Bates. The peak polarization for this sample is near 800 nm where commercial high power lasers are more readily available The 10 nm thick layer is highly doped to reduce the surface charge limit effect.

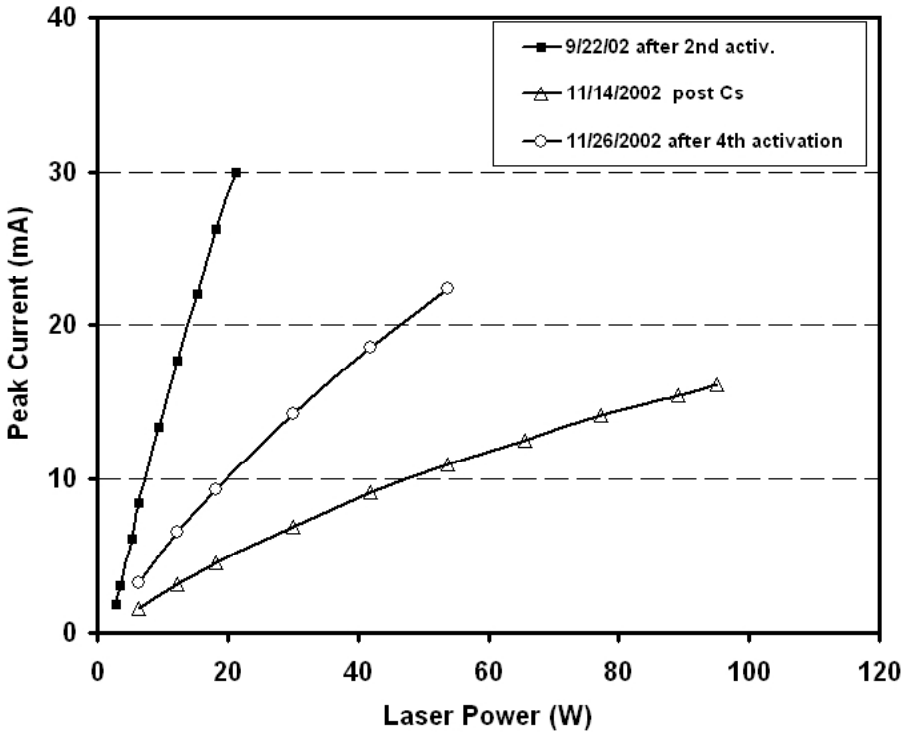

Figure 3.b.2. Peak current vs. laser power shown after several heat cleaning and activations for a two months period for the MIT-bates polarized injector. Due to surface charge limit effect the slope of the current vs. laser power decreased between 9/22 and 11/26 (squares and triangles). A heat cleaning and activation on 11/26 partially restored the slope (circles).

Surface Charge Saturation effect: In a perfectly atomically clean and freshly activated photocathode, the extracted charge is proportional to the incident laser power. However, as the QE of the photocathode decreases due to surface pollution, the relationship between the laser power and the extracted charge begins to deviate from linear. This is particularly pronounced at high laser power densities where due to an abundance of negative charges on the surface, the effective work function near the surface is increased causing a reduction in the extracted charge per bunch. This effect has been observed at SLAC and at MIT-Bates and studied in great detail at SLAC [3.b.8]. Figure 3.b.2 shows data from the MIT-Bates polarized injector that clearly indicates the deviation from linear as the photocathode is aged over the course of many months. As charge saturation effect increases more laser power is required for producing the current required. To reduce the surface charge limit in the high gradient doped sample currently used at SLAC and MIT-Bates, the top 10 nm GaAs layer is heavily doped. However, this thin layer is evaporated after several heat cleaning at near 600 C. Cares must be taken to reduce the number of heat cleaning for as long as possible. There are potentially several other methods to reduce the surface charge limit for high polarization photocathodes. These include cathode biasing, higher gun voltage, higher QE and the use of superlattice structures [3.b.9]. These methods have been tested in various photocathode and gun R&D programs mainly at SLAC and Nagoya but further R&D is required to make them practical.

Issues specific to linac-ring based eRHIC: The 0.5 A average current of highly polarized beam from a polarized electron source for injection into an ERL linac is a demanding task and has not yet been accomplished. At 28.1 MHz eRHIC collider frequency and bunch lengths of 100 ps, bunch charges of 18 nC are needed from the polarized source. Usage of longer bunch combined with bunch compression should help to ease the current requirements. Using a simple linear scaling extrapolation of results achieved at J-Lab and elsewhere, it may be possible to produce such high average currents assuming that sufficient laser power is available. For instance, the polarize source at J-Lab with a laser spot size of ~ 0.2 mm diameter, routinely produces ~100 μA current at 500 MHz and is beginning to produce ~40 μA for the G0 experiment at ~30 MHz [3.b.1]. With the same laser power density as J-Lab, to produce 0.5 A at 30 MHz, a laser spot size and illuminated photocathode area of 14 mm in diameter is needed. In this case, the required laser power for a high polarization GaAs based photocathode with QE of ~5×10^{-4} would be in the kW range, a level that may only be produced with a future ERL-based free electron laser linac as discussed later in this section. It may also be possible to reach this high level of laser power using an array of high power diode array laser systems used for the MIT-Bates polarized injector. It should however be emphasized that this is a simple scaling extrapolation and the required current of 0.5 A is about three orders of magnitude over the current produced with a CW linac today. It should also be noted that to date unpolarized currents as high as 5-10 mA have been produced from a 3-5 mm laser spot on a bulk GaAs photocathode at the J-Lab's ERL-FEL [3.b.11].

An important issue that requires R&D is the surface charge limit effect described [3.b.7] in detail in the eRHIC ZDR section 2.4. This phenomenon can often place a severe limit on the maximum amount of charge that can be extracted from the photocathode regardless of the level of laser power. Charge limit effects often appear when the QE of the photocathode becomes very small and the surface condition of the photocathode

deteriorates. The beam emittance from a large area photocathode needs to be studied with computer simulation to ensure that it can be brought under control before injection to the linac. A detailed computer simulation with software packages like PARMELA needs to be made of this polarized injector to ensure that proper optics solution can be obtained. Also high average and high peak current photoemission tests need to be carried out in the next few years to ensure that the simple scaling law discussed above is valid. The MIT-Bates polarized injector group has the expertise and a test stand that can carry R&D in high peak and high average current photoemission tests. The test stand at MIT-Bates includes an electron gun, laser systems, beam transport system and a Mott polarimeter that can be used for these R&D efforts if proper level of funding is available.

Another critical issue for a high average current polarized electron source is the lifetime of the photocathode. It is very difficult to study and estimate the lifetime without building an actual gun and beam line. The lifetime of a photocathode is defined as the total time a desired level of electron current can be maintained before the surface of the photocathode needs a heat cleaning and activation. Any additional laser power would prolong this period unless severe charge limit effect is present. At these very high average currents there is no experimental data on lifetime issues of photoemission guns. At high average currents, the lifetime of photocathode is severely shortened by desorption caused by any slight beam loss near the gun chamber. Therefore it is extremely critical that beam optics in the gun chamber and its vicinity are designed very carefully and relative beam losses are $1x10^{-5}$ or better. Beam losses can be further reduced by keeping the laser light clear of the periphery of the photocathode to prevent electrons with extreme trajectories. It is prudent to have a photocathode diameter of at least a factor of two larger than the diameter of the laser spot.

In addition, the heat generated by a kW laser power must be removed from the photocathode assembly that is under UHV condition. Any increase of the photocathode surface would seriously reduce the quantum efficiency by an increase in the rate at which the surface Cs is evaporated at elevated temperatures. The design of the photocathode assembly and the gun should accommodate this heat load.

Requirements for the laser driver for the gun: The latter are defined by the electron beam's parameters, as well as by the photocathode used for generating polarized electrons [3.b.12]. The degree of polarization is the most important parameter for the eRHIC and hence, the wavelength should be chosen at which polarization is maximum, i.e., λ=815 nm where polarization reaches 82% for a strained GaAs photocathodes (see Fig. 3.b.1), or even 90% for super-lattice photocathodes. A high degree of polarization occurs at the wavelengths where the quantum efficiency of the photocathode is rather low, ~ 10^{-3}, hence, the power requirements for the laser-driver are high.

The eRHIC requirements (the maximum electron beam current of 0.45 A) combined with feasible parameters of AsGa strained photo-cathodes give following requirements for the laser source:

○ Wavelength [nm]	815 ± 5	
○ Photon energy [eV]	1.52	
○ Polarization	circular (left/right)	
○ Laser power [W]	475	for 0.15% QE
	2,283	for 0.03% QE
○ Mode of operation	CW	
○ Rep-rate	28.15 MHz	
○ Energy per pulse [□J]	17 - 844	
○ -□Pulse duration [psec]	100 - 200	
○ Peak power [kW]	170 – 8,440	
○ Stability		
▪ Pulse-to-pulse	< 0.1%	
▪ Long term	< 1%	

References:

3.b.1. "*Status of the Jefferson Lab Polarized beam*", J. Grames, AIP proceeding of SPIN2002 Vol. 675 p1047.

3.b.2. "*The SLAC Polarized Electron Source"*, J. E. Clendenin, AIP proceeding of SPIN2002 Vol. 675 p.1042

3.b.3. *"MIT-Bates Polarized Source*", M. Farkhondeh, PESP2002 workshop, Danvers, MA, AIP proceeding of SPIN2002 Vol. 675 p.1098.

3.b.4. "*Status of the polarized source at MAMI"*, K. Aulenbacher, AIP proceeding of SPIN2002 Vol. 675 p1088.

3.b.5. "*The polarized Electron Source at ELSA*", W. v. Drachenfels, AIP proceeding of SPIN2002 Vol. 675 p1053.

3.b.6. T. Maruyama, et. al., Phys. Rev. Lett. **66** (1991) 2376.

3.b.7. T. Maruyama et. al., NIM A492, 199(2002)

3.b.8. Bandwidth Semiconductor Inc., Bedford, NH.

3.b.9. "Suppression *of the Surface Charge Limit in Strained GaAs Photocathodes*", T. Maruyama, AIP proceeding of SPIN2002 Vol. 675 p1083.

3.b.10. Spectra-Physics Opto Power diode laser model OPC-DO60-mmm-FC. Also" *High power Diode Laser System for SHR*", E. Tsentalovich, AIP proceeding of SPIN2002 Vol. 675 p1019.

3.b.11 B. C. Yun, et al., Proc.1999 IEEE Particle Accelerator Conference (1999PAC), P2453.

3.b.12 P. Hartman et al., "Polarized Electron Linac Sources", In Proc. Of The 2nd eRHIC workshop, Yale, CN, April 6-8, 2000, p.120
T. Zwart et al., "Polarized Electron at Bates: Source to Storage Ring", Proc. Of Second EPIC Workshop, Cambridge, MA, 14-15 September 2000, p.343

3.c Laser source for the polarized gun

The requirements of the laser source for the polarized electron gun naturally match those of a FEL driven by a small energy-recovery linac (ERL). The ERL for the FEL should be based on exactly the same technology as the main 10 GeV ERL (but with dramatically lower energy and with much smaller scale). First, the FEL wavelength is continuously tunable and can be chosen to maximize polarization of the e-beam. Second, the time structure and repetition rate of the FEL laser beam, 28.15 MHz, coincides with that of the e-beam, which is the 25th sub-harmonic of the ERL's RF frequency. Third, a FEL based on a helical wiggler generates 100% circular polarization in a single-mode laser beam. Fourth, the power requirements of 0.5 kW to 2.5 kW range match with modern ERL-based FELs [3.c.1]

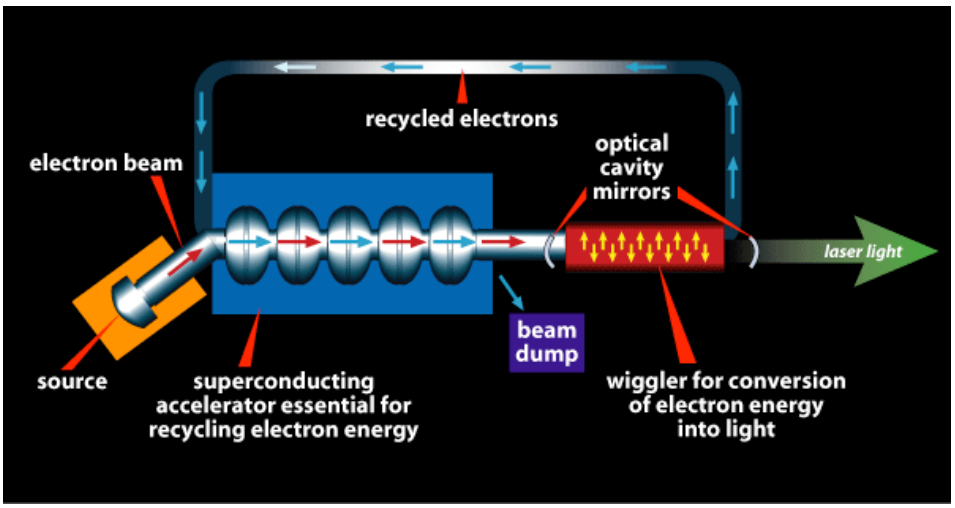

Fig. 3.c.1 Scheme of an ERL-based FEL

Table 3.c.1 gives examples of parameters for the state-of-the-art ERL FEL.

Table 3.c.1. System Parameters of the JLab FELs [3.c.2]

	Achieved	IR 2003
Energy (MeV)	20-48	80-210
Beam current (mA)	5	10
Beam Power (kW)	**240**	**2000**
FEL ext. efficiency	**>0.75%**	**1%**
FEL power (kW)	**2.1**	**>10**
Charge/bunch (pC)	135	135
Rep. Rate (MHz)	18.75-75	4.7-75
Bunch Length* (psec)	0.4 (60 pC)	0.2

The FEL parameters chosen for the eRHIC's polarized gun (see below) are relatively conservative, keeping them well within or very close to demonstrated technology. The relatively high energy of the electron beam allows for both a lower value of the electron beam's current and its better quality. This factor simplifies the propagation of the beam in the FEL and in the ERL.

Table 3.c.2. Parameters of FEL for eRHIC's polarized gun

Electron beam	
Energy [MeV]	**160**
Beam current (mA)	**5**
Beam Power (kW)	800
FEL ext. efficiency	up to 0.75%
FEL power (kW)	**up to 6, nominal - 2**
Charge/bunch (pC)	180
Rep. Rate (MHz)	28.15
Wiggler	
Type	helical with switchable helicity
Length [m]	2 x 0.9
Period, λ_w [cm]	6
Aperture [cm]	1
Wiggler parameter, K_w	1.29 - nominal (tunable within 0-1.5)
Peak magnetic field [T]	0.230 (tunable within 0-0.265)
Laser light	
Wavelength, λ [nm]	815, nominal, (tunable within 400 – 1000 nm)
Chirp [nm/psec]	5
Polarization	100% circular (left/right)
Spot-size in FEL[cm^2]	0.0020
that the mirror [cm^2]	2.08
τ-Pulse duration [psec]	5 (chirped)
Optical cavity	
Length [m]	31.8926
Radius of curvature [m]	15.962
Rayleigh range [m]	0.5
Out-coupling	10%
Intracavity power [kW]	60
CW Power density [kW/cm^2]	30 at the mirror
Peak Power density [MW/cm^2]	205 at the mirror
Laser pulse stretcher	
Input pulse duration [psec]	5, chirp 5 nm/psec
Wavelength [nm]	*815*
Chrip [nm/psec]	*5*
Dispersion section [psec/nm]	20 –40
Input pulse duration [psec]	100 -200

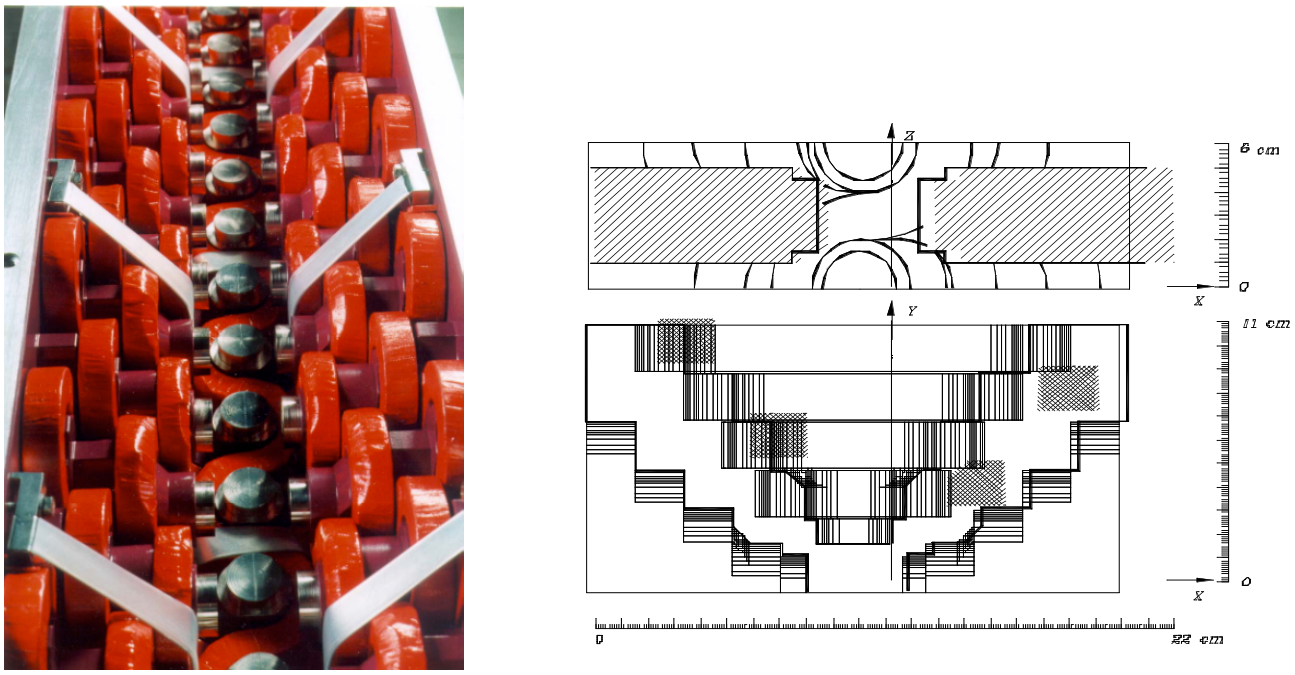

Fig. 3.c.2 Electromagnetic pseudo-helical wiggler with switchable helicity [3.c.3]: On the left, a photograph with the top quarter of the wiggler removed. On the right, there is a drawing of its half-period.

Even though most of these FEL parameters are typical for modern high power FELs, some special features are specifically required for a polarized gun with a low-emittance electron beam:

- Switchable helicity of the FEL photons;
- Wide range of the power control to compensate for degradation of the photo-cathode's quantum efficiency and to extend the time between cathode changes;
- About 2x excess of optical power for giving the laser beam a flat top profile at the surface of the photocathode to maintain low emittance of the e-beam;
- Feed-back on both the FEL power and time-profile of optical pulses;
- Matching the FEL pulse's duration ~ 5 psec with the pulse duration at the gun ~ 100 psec requires a laser pulse stretcher and, therefore, a wavelength chirp in the FEL pulse.

The polarization of the FEL wigglers determines that of the FEL photons [11] – i.e., a planar wiggler imprints linear polarization into the FEL photons, while a helical wiggler imprints circular polarization into them. The need to switch the helicity of circular polarization requires this feature to be incorporated into helical wiggler of the FEL. One possibility of doing so is to use a pseudo-helical electromagnetic wiggler as that shown in Fig. 3.c.2. In this case, the magnetic field is generated by a horizontal- and a vertical-

[11] Assuming that the mirrors of the optical cavity are optically inactive, i.e., do not rotate the polarization.

array of poles with independent controlled strengths via their coil's currents. Horizontal poles are shifted for a quarter of the period with respect to the vertical ones. When both currents are equal, the field has helical structure with *cos*-like dependence of vertical magnetic field and *sin*-like dependence of horizontal one, i.e., the electron's trajectory in this wiggler is helical. The helicity sign can be easily flipped by the changing the sign of the current in one of the coils (for example, the horizontal one). This excellent approach guarantees 100% helical polarization of FEL photons [3.c.4].

The other possibility is to use permanent magnet wigglers, in which horizontal array of magnets can be moved with respect to the vertical [3.c.5]. These wigglers perform reasonably well, but the sign of helicity is switched by slow mechanical movements, and cannot be performed as rapidly and reliably as with an electromagnetic wiggler.

The other required feature is a smooth and wide-ranging control of the FEL power. A scheme of an optical klystron (OK, [3.c.5]) for the FEL can provide this feature. Employing a buncher in the scheme of the optical klystron ensures smooth control of the power limitation by a simple control of the current in the buncher's coil. This feature will be used for maintaining constant electron-beam current when the quantum efficiency drops, as well as for stabilizing the FEL power.

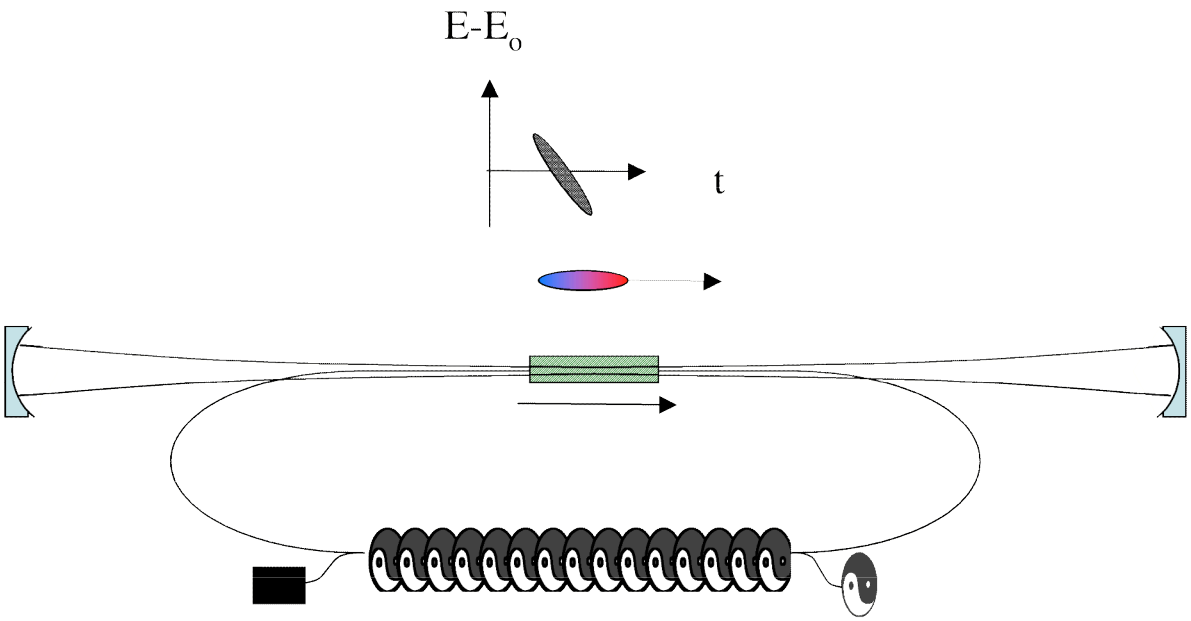

Fig. 3.c.2 Scheme of 6 kW CW FEL for eRHIC polarized gun. The electron beam, injected into the ERL at energy of 6 MeV, accelerated to 160 MeV with an energy chirp of 1.5% per 5 psec, is used in the FEL (where it loses ~ 1 MeV of energy), then decelerated to 5 MeV and damped. *Damping the electron beam at energies below 10 MeV is environmentally preferable because it does not create residual radioactivity.*

The driving electron beam determines the time structure of the laser pulses in the FEL. FEL-gain requirements lead to a high peak current resulting in a rather short laser micropulses (~ 5 psec). Following a well-known FEL technique, we will extend laser

pulses to the required 100-200 ps using wavelength chirp in FEL and the laser pulse stretcher. The wavelength of the FEL photons, defined by well-known FEL formula for a helical wiggler with wiggler period λ_w

$$\lambda = \frac{\lambda_w}{2\gamma^2}\left(1 + K_w^2\right) \qquad (3.c.1)$$

can be controlled either by changing the electron beam's energy or by thewiggler's parameters

$$K_w = \frac{eB_w\lambda_w}{2\pi mc^2}.$$

In our case, we will use both dependencies: K_w will be used to tune FEL to the optimal wavelength, and the dependence of the resonant FEL wavelength on the energy of electrons $E = \gamma mc^2$ will be used to chirp the energy of FEL photons (see Fig.3.c.2 below). By accelerating electrons slightly off-phase, we will imprint the energy chirp into the electron beam. In response to this chirp, the wavelength of the photons has the chirp from the head to the tail of the FEL pulse. Using a dispersive system (i.e., a system with an index of refraction and time of pass depending on the wavelength, which is schematically out-lined below) we will extend the chirped pulse from 5 psec to the desirable duration of 100-200 psec.

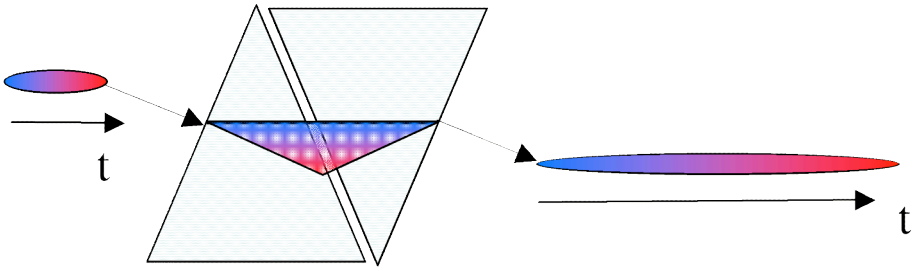

Fig. 3.c.3 A chirped FEL pulse can be extended using an optical system with a pass-time depending on the wavelength.

Overall, the ERL-based FEL can meet all requirements for the driver of a polarized electron gun with average current of 0.5 A. Being based on exactly the same elements as those used for 10 GeV ERL, this laser source can be build within a very modest budget.

References:

[3.c.1] G.Neil et al., Phys. Rev. Letts. **84**, 662 (2000)
[3.c.2] http://www.cebaf.gov/FEL/feldescrip.html
[3.c.3] V.N.Litvinenko et al., NIM **A 475** (2001) 247-252
[3.c.4] V.N.Litvinenko et al., NIM **A 475** (2001) 407-416
[3.c.5] H.Hama et al., NIM **A 393** (1997) 23
[3.c.6] N.A.Vinokurov, A.N.Skrinsky, Preprint 77-59, BINP, Novosibirsk (1977)
[3.c.7] V.N.Litvinenko et al., NIM **A 475** (2001) 65-73

3.d e-beam polarization and polarization transparency of the ERL lattice

In remarkable contrast with many other schemes, the ERL option for the eRHIC does not have any forbidden energy ranges[12], and a desirable polarization of electrons can be maintained at any energy of electrons without using spin-matching sections or "snakes".

This flexibility and the spin-transparency of the ERL are most evident in the present ERL scheme shown in Fig. 3.d.1. By design, the electron trajectory stays in the horizontal plane from the gun to the IP and, therefore, the spin also stays in the horizontal plane, x-z.

Electrons are generated in a photo-injector with longitudinal polarization exceeding 80% (see section 3.b) and the energy of $E_i = \gamma_i mc^2$. Helicity (projection of spin on the momentum, i.e., the z-axis) is controlled by choosing the helicity of the photons, and can be switched from positive to negative. The electron beam is turned for the angle $\theta_i = \pi/12$, and is injected into first stage of the ERL. This stage has one linac. The electron beam passes twice through it gaining $\Delta E_1 = \Delta\gamma mc^2$ at each pass, and then makes one 360° turn before reaching transfer energy $E_1 = \gamma_1 mc^2$ in the second section of the ERL. The e-beam makes $\theta_t = \pi/2$ turn before reaching the first main acceleration section.

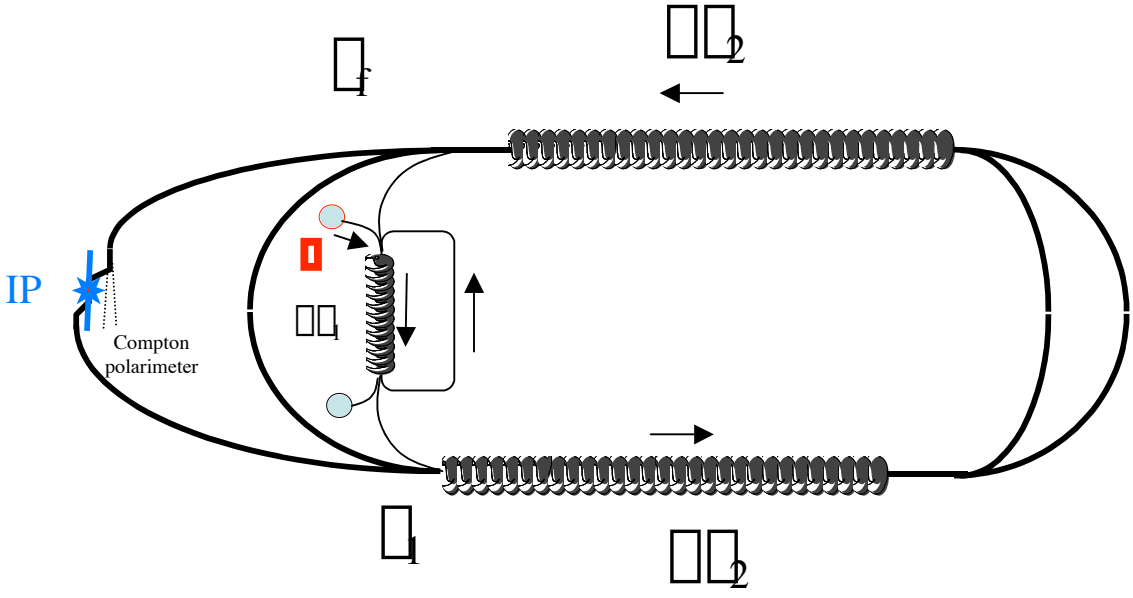

Fig.3.d.1. Acceleration scheme for eRHIC with a two-pass ERL

[12] To be exact, it is correct for all energies of interest for eRHIC. This scheme would not work for very low energies of electrons $E_f < 0.22$ GeV.

The second stage of the ERL is comprised of two linacs, and electron beam passes twice through each of them gaining $\Delta E_2 = \Delta\gamma_2 mc^2$ at each pass, and makes three180 turns before reaching final energy $E_f = \gamma_f mc^2$. The e-beam makes its last $\Delta\gamma_t = \gamma/2$ turn before reaching its goal in the IP.

After the IP, polarization of the electrons in no longer important and downstream of it, the lattice does not need to be "spin-transparent".

It is important to notice that acceleration along z-axis does not affect the particles' spin[13]. Therefore, spin rotation occurs only in the bending magnets. The vertical magnetic field in the arcs turns the trajectory of the electrons and rotates their spin about the y-axis for an angle, $\Delta\Theta$, proportional the angle of trajectory rotation, $\Delta\theta$, electron energy $E_e = \gamma mc^2$, and the anomalous magnetic moment, $a = g/2 - 1 = 1.1596521884 \cdot 10^{-3}$:

$$\Omega = \frac{g}{2}\frac{e}{m_o}\hat{s} = (1+a)\frac{e}{m_o}\hat{s}; \qquad \gamma_{spin} = a\cdot\gamma = \frac{E_e}{0.44065[GeV]}$$

$$\Delta\Theta = \Delta\theta\cdot\gamma\cdot a. \tag{3.d.1}$$

Therefore, the total angle of spin rotation is a direct sum of the individual turns (see below):

$\Delta\theta/\pi$	γ
-1/12	γ_i
2	$\gamma_i + \Delta\gamma_1$
1/2	$\gamma_i + 2\Delta\gamma_1$
1	$\gamma_i + 2\Delta\gamma_1 + 1\Delta\gamma_2$
1	$\gamma_i + 2\Delta\gamma_1 + 2\Delta\gamma_2$
1	$\gamma_i + 2\Delta\gamma_1 + 3\Delta\gamma_2$
1/2	$\gamma_i + 2\Delta\gamma_1 + 4\Delta\gamma_2$

and for the entire pass from one can easily calculate the total angle of the spin rotation:

$$\gamma = a\sum_k \Delta\gamma_k\theta_k = \pi a\{(6-1/12)\gamma_i + 10\Delta\gamma_1 + 8\Delta\gamma_2\}. \tag{3.d.2}$$

The final energy of electrons

$$\gamma_f = \frac{E_f}{mc^2} \equiv \gamma_i + 2\Delta\gamma_1 + 4\Delta\gamma_2; \tag{3.d.3}$$

---

[13] According to Bargman, Mitchel, and Telegdi's equation, in the absence of magnetic field

$$\frac{d\hat{s}}{dt} = \frac{e}{mc}\hat{s}\times\left[\left(\frac{g}{2}-1+\frac{1}{\gamma}\right)\vec{B} - \frac{\gamma}{\gamma+1}\left(\frac{g}{2}-1\right)\hat{\beta}\left(\hat{\beta}\cdot\vec{B}\right) - \left(\frac{g}{2}-\frac{\gamma}{\gamma+1}\right)\vec{\beta}\times\vec{E}\right]$$

particle spin is preserved for a particle moving along electric field $\vec{\beta}\,//\,\vec{E}$.

is defined by the experiment. Usually fixing the injection energy is required by conditions for generating very bright electron beam. These make the choice of energy gains in the ERL linac unique for longitudinal polarization in the IP[14]:

$$\Delta\mathcal{E}_2 = \frac{\mathcal{E}_f - \mathcal{E}_i}{4} - \frac{\Delta\mathcal{E}_1}{2}$$
$$\frac{\nu}{\gamma} = a \cdot \left[\frac{47}{12}\mathcal{E}_i + 2\mathcal{E}_f + 6\Delta\mathcal{E}_1\right] = N \qquad (3.d.4)$$

where N here is an integer number. Chousing N to be nearest integer to the nominal energy gains (required for reaching the final energy)

$$N = \text{nearest\_integer}\left[a\left(\frac{47}{12}\mathcal{E}_i + 2\mathcal{E}_f + 6\Delta\mathcal{E}_{1\,nominal}\right)\right]$$

and using a small adjustment of $\Delta\mathcal{E}_1$

$$\Delta\mathcal{E}_1 = \frac{1}{6a}\left(\frac{\nu}{\gamma} - N\right) \approx 143.7 \cdot \left(\frac{\nu}{\gamma} - N\right)$$

provide for integer number of π-rotation for electron spin. In the above scheme, a very small adjustments of the linacs in two sections in the range of

$$\Delta\mathcal{E}_1 \in \{-71.9, 71.9\}; \quad \Delta E_{linac1}[MeV] \in \{-36.72, 36.72\}$$
$$\Delta\mathcal{E}_2 = -\Delta\mathcal{E}_1/2; \quad \Delta E_{linac2} = -\Delta E_{linac1}/2$$

do provide for attainment of complete spin transparency[15]. It is advantageous for the beam stability to operate fist section of ERL close to nominal accelerating gradients. Presently the nominal ranges for the ERL with two passes[16] are shown in next table:

Injection energy	5	MeV
E_1	1000	MeV
Final	2-10	GeV
Nominal ΔElinac1	497.5	MeV
Nominal ΔElinac2	1000 - 2250	MeV
Nominal $\Delta\mathcal{E}_1$	973.58	π
Nominal $\Delta\mathcal{E}_2$	489 - 4403	π

[14] First, capability of spin flip at the source side allows us to have integer number of 180° turns of spin. Proper helicity is chosen at the gun. Conditions similar to (3.d.4) can be derived for any plane ERL [3.d.1].

[15] It is important to note that initial energy spread of electrons is very small $\sigma_\delta << 1$. The energy spread is kept small $\sigma_\delta < 1$ (see section 3.a) also during the acceleration process. Therefore, the spread of the spin rotation angle caused by the energy deviation stays very small $\sigma_\theta < 7a\sigma_\delta \approx 0.025$ *rad*, $\cos\sigma_\theta \approx 0.9997$ and high degree of e-beam polarization is preserved.

[16] Energies of electron beam from 2 GeV to 5.5 GeV can be reached with a single pass through the ERL linacs, which is a preferable choice.

The process of making the lattice spin-transparent at *any energy of operation* is as simple as following:

- ✓ Energy gain in the first and second linac are slightly adjusted (for less than 40 MeV) to satisfy criteria (3.d.4) while keeping final energy fixed.

An example of the choice for accelerating gains of two linacs for e-beam energy range from 5 to 10 GeV is shown in Fig.3.d.2

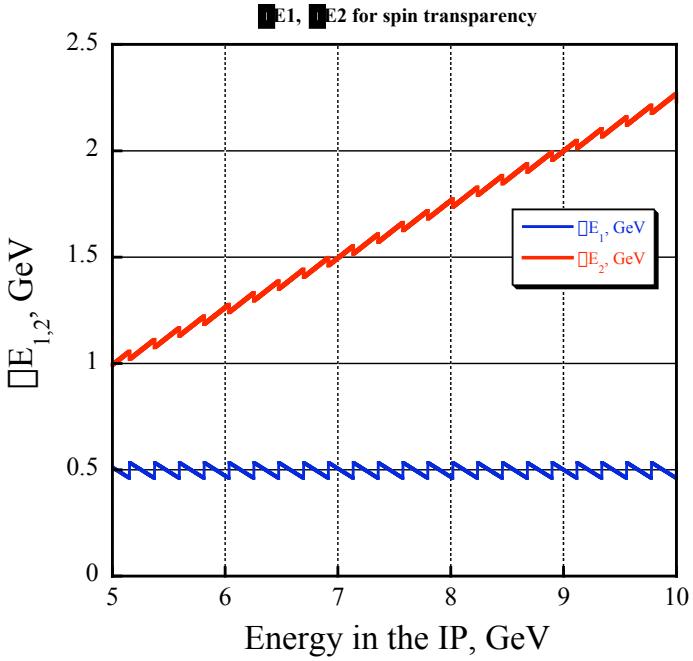

Fig. 3.d. Required energy gains for spin transparency vs. the e-beam energy in the IP.

Similarly the spin transparency can be kept with a single pass ERL (see Fig. below).

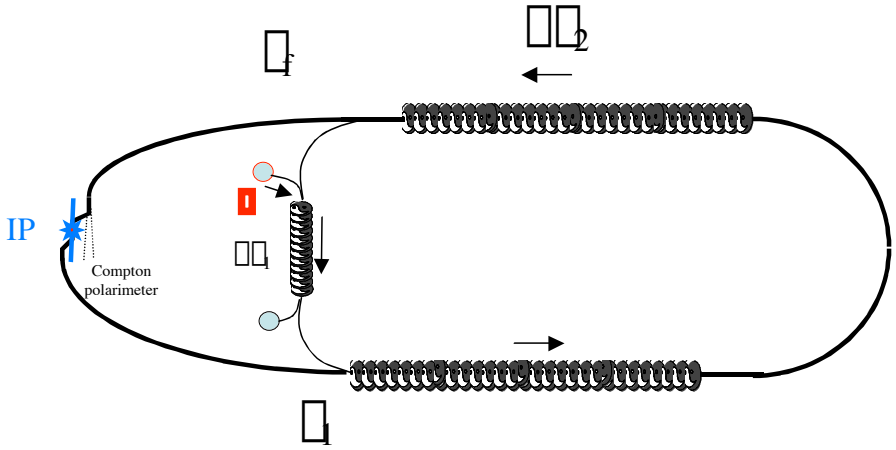

Fig.3.d.3. Scheme for low energy eRHIC operation with a single-pass through ERL.

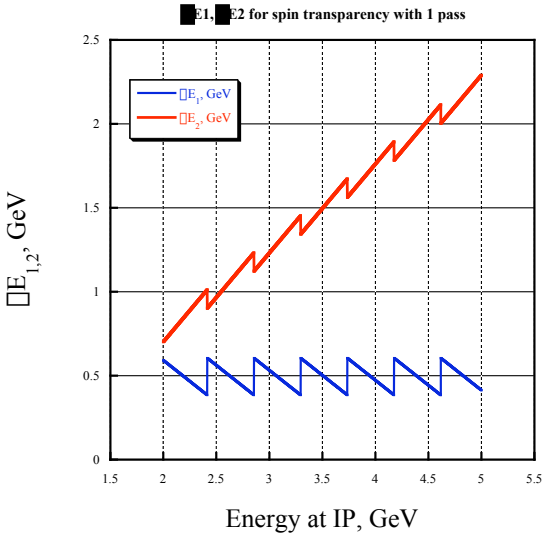

Fig.3.d.4. The choice of the energy gains for linacs for a single - pass through the ERL

In addition to longitudinal polarization by a properly selecting energy gains in two linacs of ERL, e spin can be oriented horizontally in the IP, if required. Overall, the ERL-based eRHIC has full capability of controlling the polarization of electrons in the IP while preserving a very high degree of polarization attained at the photo-cathode. Most importantly, there are several schemes with ERL-based eRHIC that allow *any desirable polarization at the IP at any desirable energy of electrons*. The scheme described in this section is one of them.

References:

[3.d.1] V.N. Litvinenko, W.W. Mackay, I.Ben-Zvi, "Spin Transparency of ERL lattice", C-AD internal note

3.e Electron cooling

In this section, we focus on issues specific for the ERL-based eRHIC, which allows operation with double the intensities of both the ion- and proton-beams compared with ring-ring option [3.e.2]. Electron cooling plays as important a role in the ERL-based eRHIC as it does in the ring-ring case.

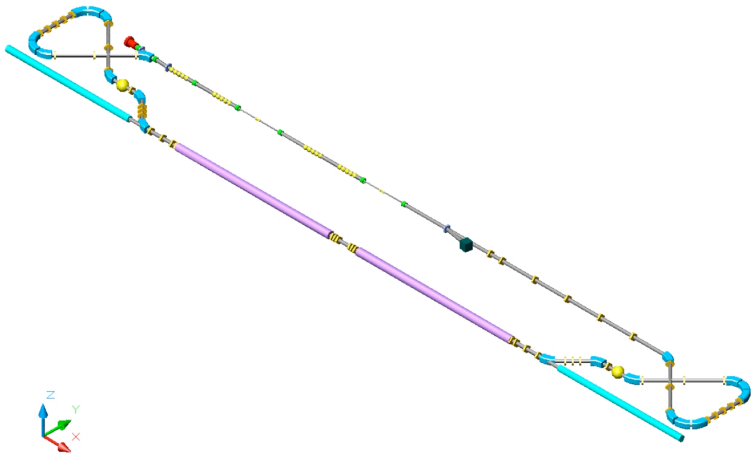

Fig. 3.e.1. eRHIC electron-cooler system comprises a photoinjector (red), a superconducting energy-recovery linac, and a cooling RHIC section with 30-m long solenoid (purple).

The detailed description of electron-cooling scheme (fig.3.e.1) and its aspects specific for eRHIC operation are shown in Section 3.2.1 in the main body of ZDR [3.e.1]. To achieve the design luminosity of eRHIC, an ion beam must be continuously cooled while colliding with the electron beam. The needs for electron cooling in eRHIC can be summarized as the following:

1. The RHIC gold-beam evolution is dominated by Intra-Beam Scattering (IBS) that leads to the growth of emittance and beam loss and/or de-bunching. Electron cooling is planned during the storage phase of the machine to control IBS and reduce emittance to the required values (limited by the beam-beam parameters).
2. For high-energy 250 GeV protons, electron cooling is ineffective. This suggests a staged cooling for such protons: they are initially cooled at injection energy with a subsequent acceleration to higher energy. At low proton energies in the range of 25-50 GeV, using cooling reduces transverse-beam emittance to the required values.
3. Cooling the longitudinal emittance causes bunch shortening at both low- and high-energies, and, hence, provides the match with a low β^* in the IPs.

Initial simulations indicate that all the major tasks described above can be achieved with the electron cooler presently under design for the RHIC II upgrade. Section 3.2.1 presents the simulations of cooling times for the current eRHIC baseline intensities

of protons (Np=1x10^{11}) and Au ions (Ni=1x10^{9}). Here we offer some examples for upgraded intensities of the RHIC beams to N_p=2x10^{11} and N_i=2x10^{9} for protons and Au ions per bunch.

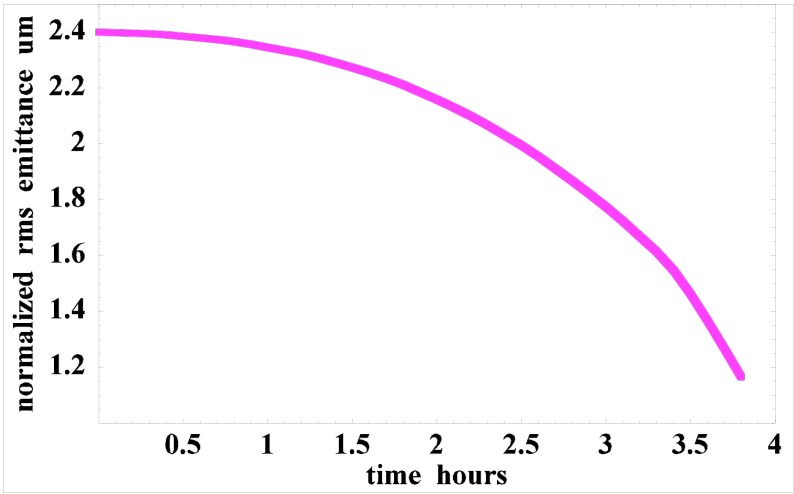

Fig.3.e.2 BetaCool simulation code: Cooling of a proton bunch with N_p=2x10^{11} 27 GeV protons to a normalized rms emittance of 1.2 □m.

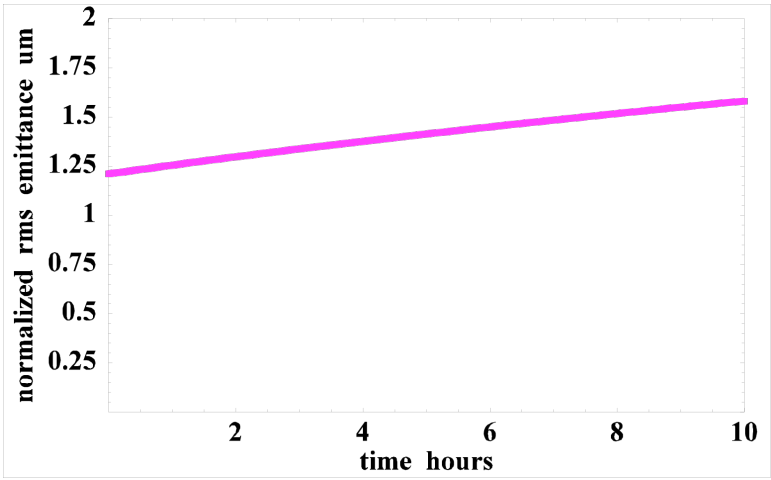

Fig.3.e.3. . BetaCool simulation code: Emittance growth of the cold proton bunch with N_p=2x10^{11} particles stored at 250 GeV.

For high-intensity protons, staged cooling is employed. The protons are first cooled at energy of 27 GeV, and then accelerated to the energy of experiment. Figure 3.e.2 shows cooling of protons (N_p=2x10^{11}) using a current of electron cooler corresponding to the number of electrons in a bunch Ne=1x10^{11} (16 nC per bunch). Figure 3.e.3 shows emittance growth via IBS of the cold proton beam accelerated and stored at 250 GeV for 10 hours. Overall, the simulations support the possibility of

maintaining the beam's quality of intense protons required for attaining $2x10^{33}sec^{-1}cm^{-2}$ luminosity in theERL-based eRHIC.

Electron cooling also is essential for reaching the design luminosity of $2x10^{31}$ sec^{-1} cm^{-2} in e-Au collisions with 100 GeV/u golden ions. As discussed previously, this requires an intense ion beam with $2x10^{9}$ ions per bunch. Without cooling, both the transverse and longitudinal emittance of such a beam will increase very rapidly because of IBS. This would cause the luminosity to decline, and/or particle loss from the bucket due to bunch lengthening. Fig.3.e.4. is a simulation of this scenario (no-cooling!).

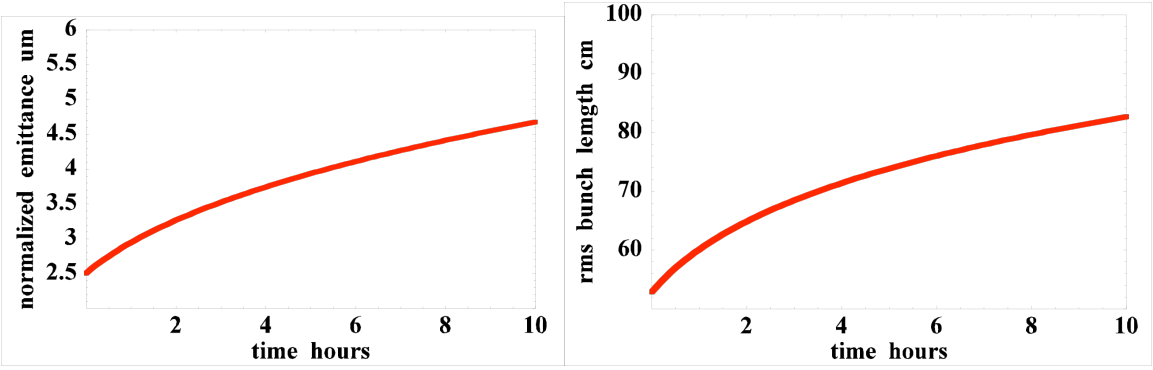

Fig.3.e.4. BetaCool code- WITHOUT COOLING!: Growth of transverse normalized rms emittance (left) and rms bunch length due to the IBS for 100 GeV/u Au ions beam with $2x10^{9}$ particles per bunch.

Electron cooling changes the situation rather dramatically: with $2x10^{9}$ ions per bunch, it cools down the longitudinal emittance while maintaining the transverse emittance required for $2x10^{31}$ $sec^{-1}cm^{-2}$ luminosity. It is noteworthy that this result is based on typical cooler parameters (see Section 3.2.1). Figs. 3.e.5 and 3.e.6 illustrate this mode of eRHIC operation.

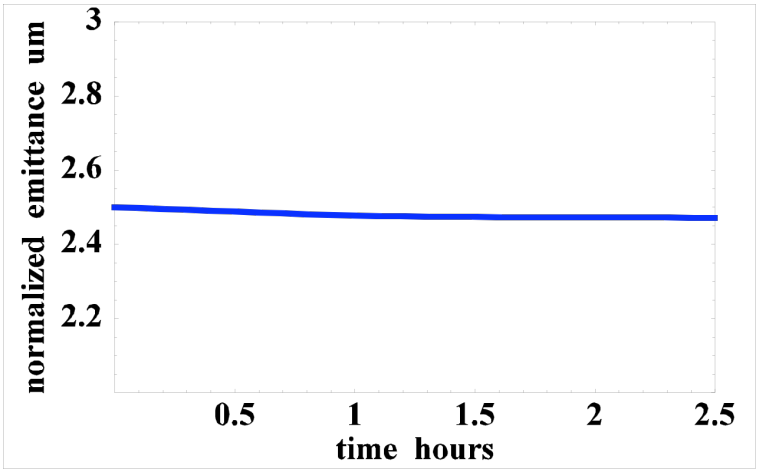

Fig.3.e.5. BetaCool code: Time evolution of rms emittance for a 100 GeV/u Au ions beam with $N_i=2x10^{9}$ particles per bunch. The electron current of the electron cooler corresponds to $N_e=1x10^{11}$ per bunch.

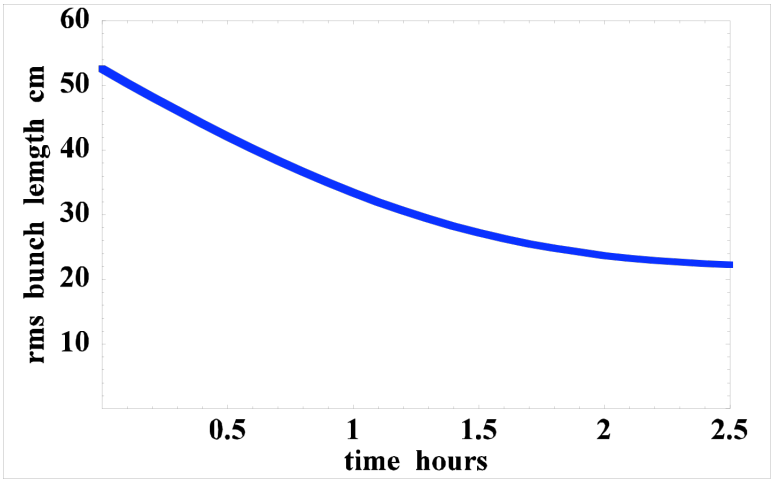

Fig.3.e.6. BetaCool code: Time evolution of the rms bunch length of a 100 GeV/u Au ions bunch with $N_i=2x10^9$ particles. The electron cooler's parameters are the same as in Fig. 3.e.5.

Overall, the simulations provide confidence in the feasibility of high luminosity levels for eRHIC ($2x10^{33}sec^{-1}cm^{-2}$ and $2x10^{11}sec^{-1}cm^{-2}$ for e-beam collision with 250 GeV protons and 100 GeV/u gold ions, correspondingly).. In addition, there is an opportunity to further "luminosity-relevant" electron cooling by fast cooling of ion-beam core by adjusting the size of the transverse electron beam in the cooling section.

As the part of preparing for electron cooling of RHIC beams, R&D on a several systems relevant to the eRHIC is underway: the photoinjector (including its laser and photocathode deposition system), a high-current superconducting cavity for the ERL of the cooler, beam dynamics of the complete system, electron cooling simulation codes, and the high-precision superconducting solenoid.

Electron cooling is important integral part of the linac-ring eRHIC. It provides for the attainment of low emittances required for high luminosity of the linac-ring eRHIC. In addition it provides flexibility of further reducing emittance of hadron beams for extending luminosity towards $10^{34}sec^{-1}cm^{-2}$ per nucleon or for compensating for reduced intensity of the hadron beam.

References:

[3.e.1] ZDR section 3.2.1: Electron Cooling for eRHIC, I. Ben-Zvi, A. Fedotov, J. Kewisch, V.Litvinenko
[3.e.2] ZDR section 1.2: General accelerator concept and parameters V.Ptitsyn, T.Roser et al.

3.f Integration with IP

The interaction region of eRHIC collider serves several purposes. Firstly, both the hadron- and electron-beam should be focused into an optimally equal size at the IP(s) to maximize luminosity. Secondly, there should be sufficient convenient space and volume for the detector to conduct the physics experiments. Thirdly, the apertures and the environment for the beams should provide both for the low experimental background and long luminosity lifetime.

The ERL-based eRHIC has a number of significant advantages for integrating the IP(s):

- ✓ Round-beam collision geometry to maximize luminosity
- ✓ Smaller e-beam emittance resulting in 10-fold smaller aperture requirements for the electron beam
- ✓ Possibility of moving the focusing quadrupoles for the e-beam outside the detector and the IP region, while leaving the dipoles used for separating the beam.
- ✓ Possibility of further reducing the background of synchrotron radiation.

Within this scheme, the first hadron low-β quadrupole, Q1, is installed at 5m from the IP. This requires deflecting the electrons sufficiently to guide them through a field-free region outside this magnet. Since this separation generates synchrotron radiation, it is mandatory to keep it as small as possible by installing septum quadrupoles for the hadron beam.

To minimize the actual volume of the detector occupied by the separation magnets, superconducting dipole magnets are foreseen, similar to those in the HERA luminosity upgrade design [3.f.4]. These dipoles deflect the electron beam while leaving the higher-energy hadron beam's orbit practically unchanged.

3.f.2 Electron beam in the IP [3.f.2]

The tune-shift limitations and the aperture requirements for hadron beams in the ERL-based eRHIC are identical to those in the ring-ring scenario [3.f.1]. At the same time, for the ERL-based eRHIC, the tune shift for electrons can be very large $\Delta Q_e \sim 1$ compared with the ring-ring case. The effect of the collision on the electron beam is better described by disruption parameter (see chapter 2):

$$D = \frac{Z_h N_h}{\sigma_e} \frac{r_e}{\sigma^2_{r(h)}} \sigma_{s(h)};$$

that essentially is a betatron phase advance in the e-beam caused by the hadron beam.

Our studies [3.f.2] revealed that with proper matching in the ERL case, tune shifts up to $\Delta Q_e = 1$ (i.e., disruption parameters up to ~2π) only modestly increase the beam's emittance by ≤ 20%. An electron beam with such emittance can be easily re-circulated in the ERL down to the beam damp.

Fig. 3.f.1(a,b) illustrates one example of the effect of an intense hadron beam on the electron beam. The RMS emittance of the hadron beam (100 GeV/u golden ions) is intentionally reduced from 9.4 nm.rad to 5 nm.rad (RMS normal emittance!) to increase the effect on the electron beam by a factor of ~ 1.9. This is also the reason for the reduced e-beam betatron function in the IP, which is required for fitting the e-beam and ion beam sizes in the center of the IP (z=0 in Fig/ 3.f.1b). The situation is even better for luminosity of $4 \cdot 10^{33}$ cm^{-2} s^{-1} per nucleon (i.e., 9.4 nm.rad RMS emittance of hadron beam).

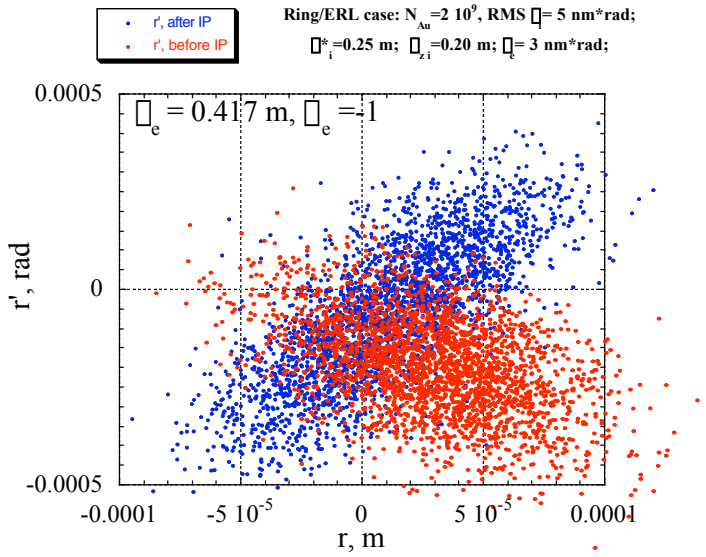

Fig. 3.f.1a Round 10 GeV electron beam from ERL with initial transverse RMS emittance of 3 nm·rad passes through the IP with the disruption parameter 3.61 (tune shift $\Delta Q_e = 0.6$). Figure shows Poincare plots for e-beam distribution before (red) and after (blue) the IP. After removing the *r-r'* correlations, the emittance growth is only 11%.

Another effect, which is of concern for the hadron beam, is a modulation of the size of the electron beam during the collision. Our simulation showed that these variations can be controlled at least for luminosity ~10^{34} cm^{-2} s^{-1} per nucleon for gold-electron collisions (see figure below). For the parameters listed in Table 2.1, the beam-modulation effect is lowered by an additional factor of 4 compared with this figure.

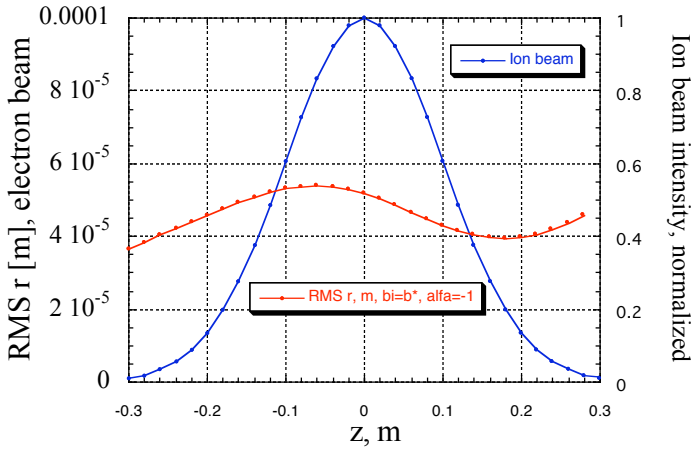

Fig. 3.f.2 Round electron beam from ERL with an initial transverse RMS emittance of 3 nm*rad passes through the IP with the disruption parameter 3.61 (tune shift ξ_e = 0.6). Matching the beam's size with the ion beam and a negative β=-1 at z=-0.3m, permits a modest variation of the e-beam's size (red line on the right graph) through the interaction region; the e-beam's size does not shrink below the matched value. In this case, the tune shift for hadrons does not exceed ξ_h = 0.005.

Another effect, the kink head-tail instability of the hadron beam, and its stabilization were considered in section 2.

Overall, there appears to be no problem in using electron beams above 5 GeV in ERL-based eRHIC within the luminosity ranges ~ 10^{34} cm^{-2} s^{-1} per nucleon.

3.f.2 Hadron IR optics [3.f.1]

One of the main advantages of the linac-ring eRHIC vs. ring-ring eRHIC is operating the IP with round beams. The ring-ring case requires hadron optics with flat beams and unequal β^*: β_x =1.04 m, β_y = 0.26m. In the case of the linac-ring , the hadron beam is round with β^*=0.26m in both directions. A normal-conducting quadrupole triplet focuses the hadron beam in the IP region.. The use of septum-quadrupoles for all these magnets minimizes the required beam separation between electrons and hadrons, and affords maximum freedom for installing magnets in the electron beam's line.

The first and second lens of the triplet are split up into various individual magnets, with pole tip radii tailored to the varying beam size. This ensures a sufficient aperture of 12σ_p, while simultaneously minimizing the total length of the low-β system. Figure 3.f.1 illustrates the resulting β functions and magnet positions.. Whenever possible, pole tip fields were limited to 1.0T to avoid degradation in field quality due to saturation. However, in most magnets this limit had to be exceeded slightly to accommodate the 12σ_p beam in the septum quadrupoles. Table 3.f.2 lists the resulting magnet parameters, while cross-sections of the entrance and exit of each magnet with its pole tip radius and the 12σ_p beam ellipse are shown in Figures 3.f.3 and 3.f.4.

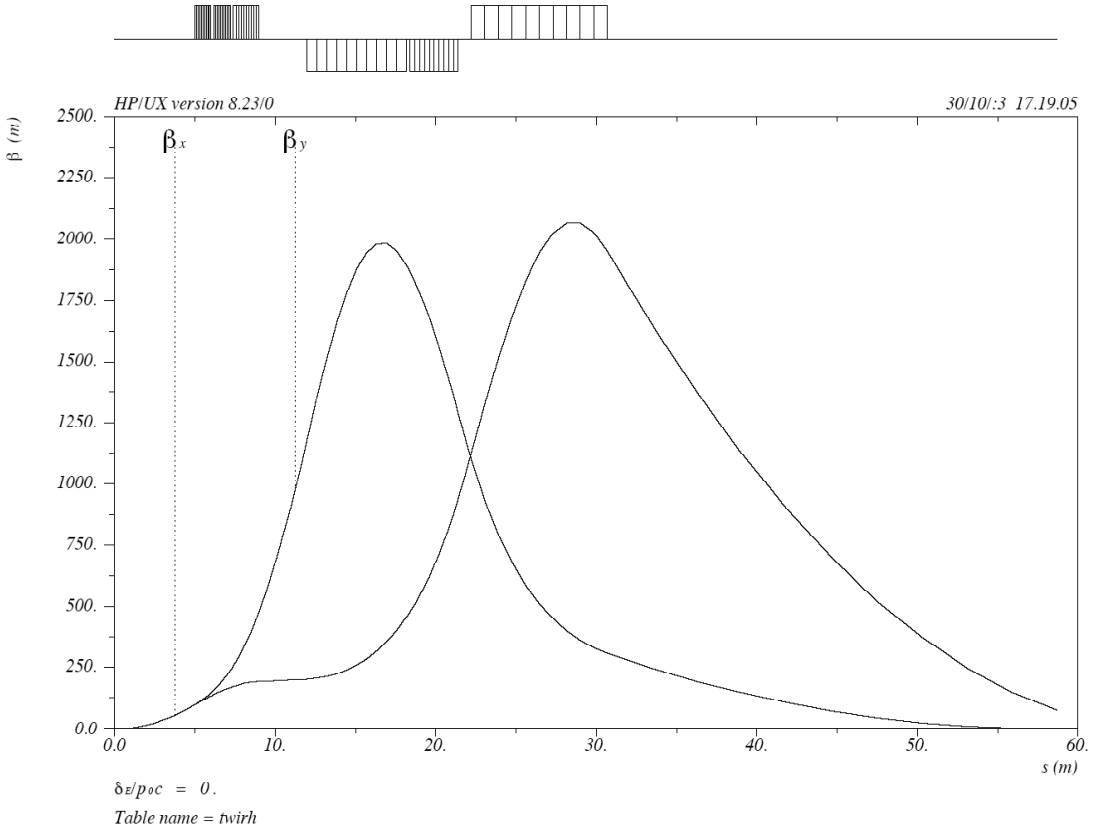

Figure 3.f.2: Hadron IR lattice for the electron-ion collider eRHIC

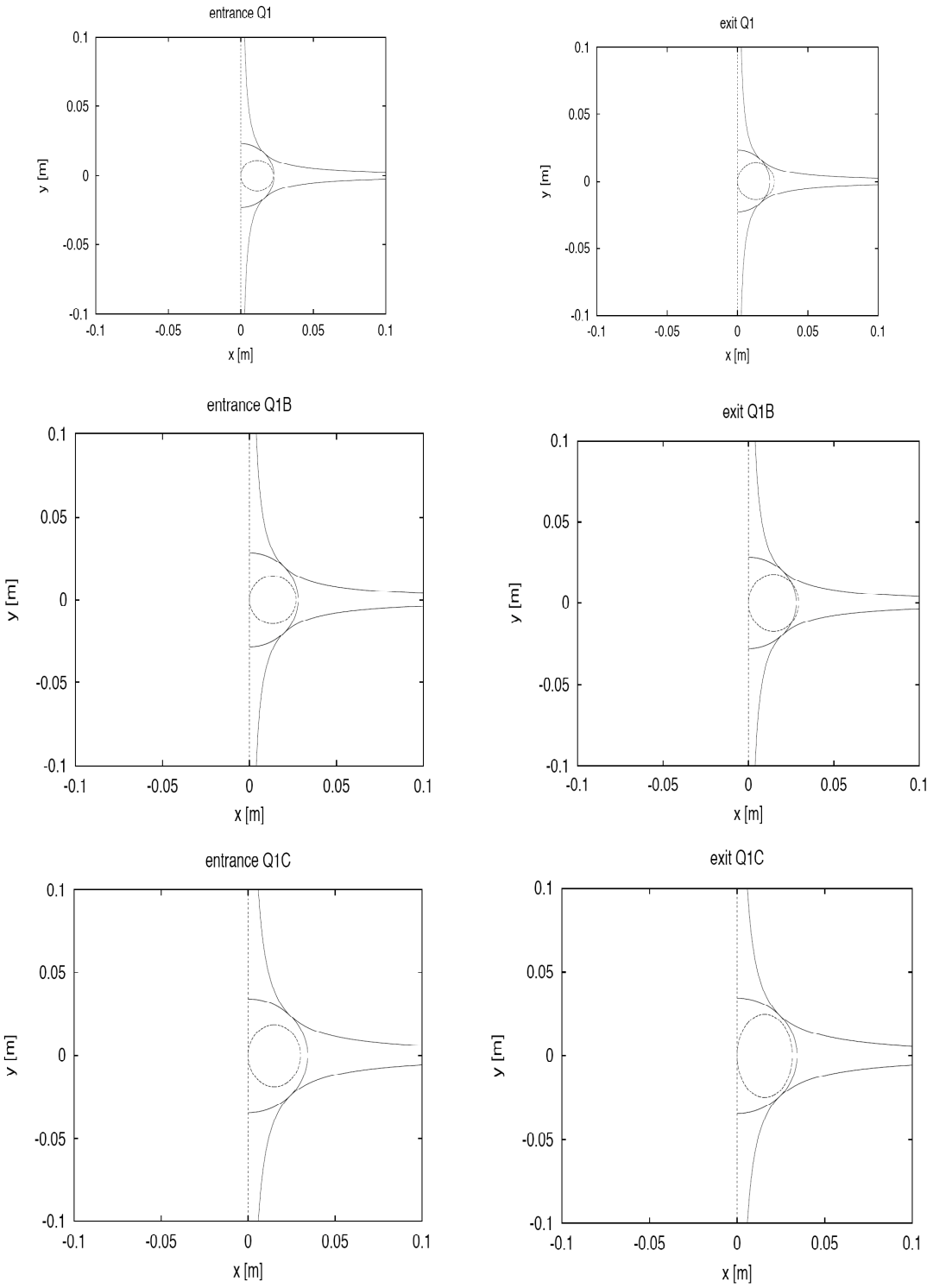

Fig. 3.f.3. Hadron beam envelope, magnet pole-tips, and vacuum chamber in the first hadron magnet Q1 comprising three parts [3.f.3].

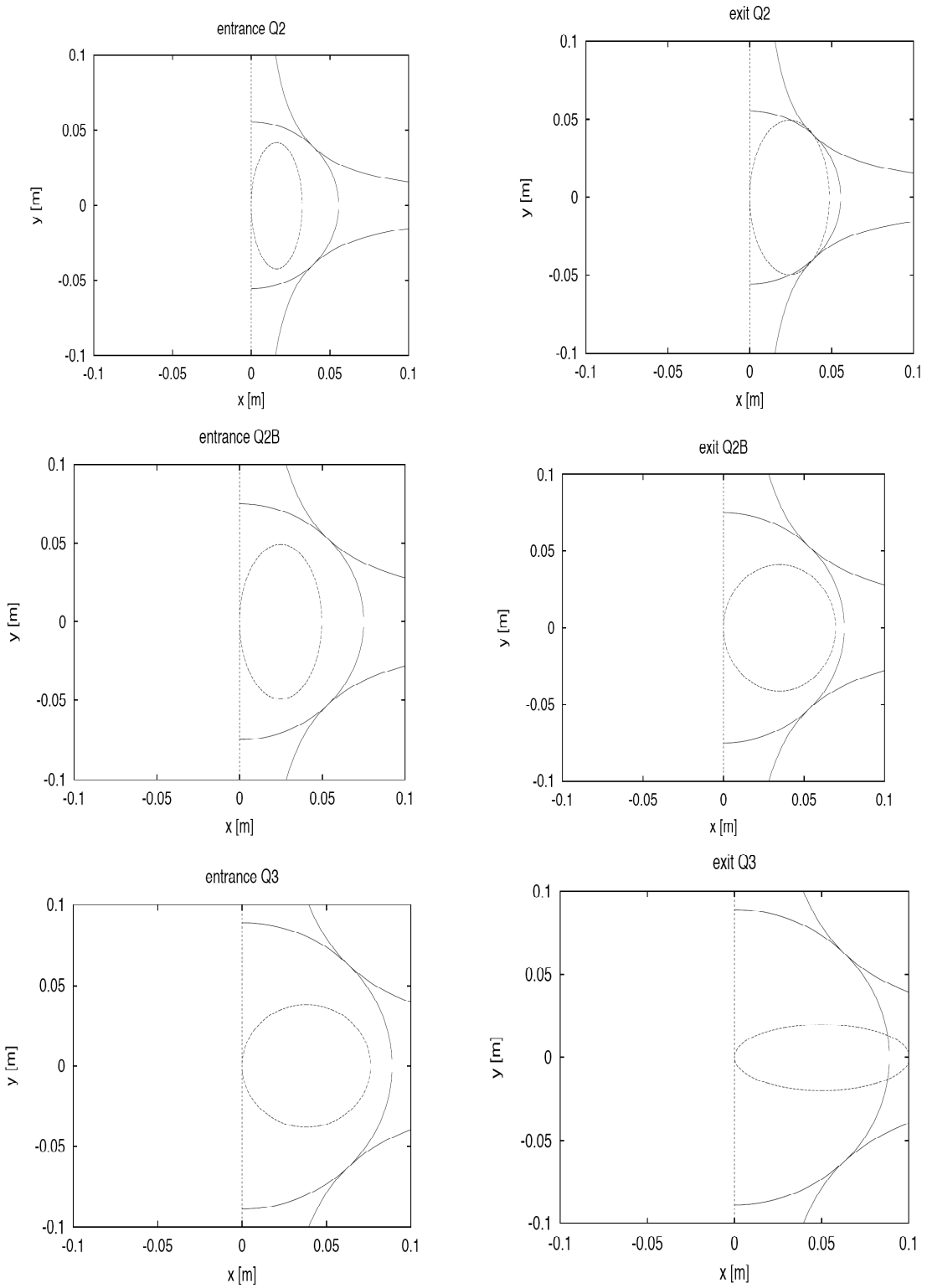

Fig. 3.f.4. Hadron beam envelope, magnet pole-tips, and vacuum chamber in the second and third hadron magnet Q2-Q3 [3.f.3].

Table 3.f.1: Parameter list of the hadron low-□ septum quadrupoles

	Q1	Q1B	Q1C	Q2	Q2B	Q3
length [m]	1.0	1.0	1.6	6.2	3.0	8.5
gradient [T/m]	43.5	35.7	29.2	18.0	13.3	11.3
pole tip radius [mm]	26.4	30.8	37.7	61.1	75.0	88.9
pole tip field [T]	1.15	1.1	1.1	1.1	1.0	1.0

3.f.3 Synchrotron radiation [3.f.3].

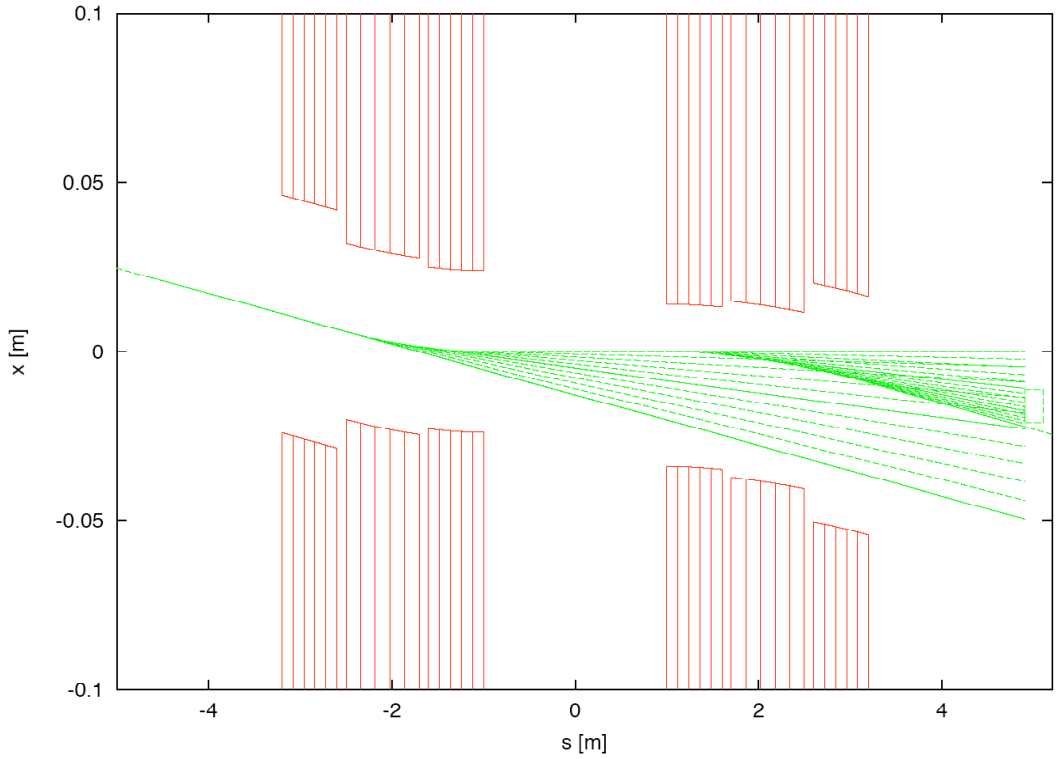

Figure 3.f.5: IR geometry and synchrotron-radiation fan. The electron beam enters the IR from the left. A box on the right indicates the septum of the Q1 magnet.

The synchrotron-radiation fan results from the superconducting dipole windings necessary to separate the beam. At the septum, 5m from the IP, the required separation is given by the $12\Box_{p,x}$ beam size of the hadron beam, plus the thickness d_{septum} = 10mm of the septum itself, plus some sufficient aperture for the electron beam. In contrast to the ring-ring case, where $20\Box_{e,x}$ are mandatory for sufficient lifetime of the electron beam and minimum background conditions, this condition is much more relaxed in the linac-ring approach for two reasons. First , an aperture of 5 $\Box_{e,x}$ is adequate , where the beam passes through the interaction region only once and the halo is absent. Second, the horizontal electron-beam's emittance is more than an order-of-magnitude smaller. Using

the 2.5 nm RMS e-beam emittance the RMS e-beam's size can be less a quarter of mm throughout the IP. Using the β-functions shown in Figures 3.f.2 for the hadron beam with RMS emittance of 9 nm·rad, the required separation is computed as[17]

$$\Delta x = 12\beta_{p,x} + 5\beta_{e,x} + d\text{septum} = 12 \cdot 0.93\text{mm} + 5 \cdot 0.25\text{mm} + 10\text{mm} = 22.4\text{mm}.$$

At the right side of the detector (electron-downstream), some fraction of this fan always hits the septum of the first hadron quadrupole, Q1. To minimize back-scattering of these synchrotron-radiation photons into the detector, the total power as well as the critical photon energy of the synchrotron radiation hitting the septum must be minimized by distributing the required bending angles among the various magnets. The distribution of the synchrotron radiation in and around the IP can be optimized by properly distributing the separating magnetic field. Table below lists some parameters of three separating magnets used for generating the synchrotron radiation fan shown in Fig.3.f.5.

Table 3.f.2: Selected parameter of separating magnets from both sides of the IP

	B1,left/right	B2, left/right	B3, left/right
length [m]	0.6/0.6	0.8/0.8	0.6/0.6
bending angle [mrad]	3.7/-3.0	3.8/-2.4	3.75/-3.6
synchrotron radiation power [W]	1609/1058	1273/508	0/677
synchr. rad. power on septum [W]	800/0	0/508	0/340
critical photon energy [keV]	13.7/11.1	10.5/6.7	0/8.9

The eRHIC interaction region discussed above provides for an e-p luminosity of $2 \cdot 10^{33}$ cm^{-2} sec^{-1} with hadron beam-beam tune shift of $\beta_{x,y} = 0.005$, which is well within values presently achieved at RHIC, and therefore, considered achievable for eRHIC. Minimum apertures of $12\beta_{p,x}$ for the hadrons are possible in this design that is considered sufficient both for safe operation as well as for minimum detector background conditions.

References:

[3.f.1] eRHIC ZDR, Main part, Chapter 3.

[3.f.2] I.Ben-Zvi, J.Kewish, V.N.Litvinenko., ICFA Beam Dynamics Newsletter No. 30, April 2003, p.19

[3.f.3] DESIGN OF AN INTERACTION REGION FOR THE LINAC-RING VERSION OF THE ELECTRON-ION COLLIDER ERHIC, C. Montag, J. Kewisch, I. Ben-Zvi, Internal Technical Note, C-AD

[3.f.4] U. Schneekloth (ed.), The HERA Luminosity Upgrade, DESY HERA 98-05

[17] It might be possible to use a significant vertical separation of the superconducting dipole windings in the detector that would allow the synchrotron-radiation fan to be passed safely outside the system.

3.g Considerations of the experiments

There is a strong desire in the physics community for eRHIC to have at least two IPs and for potential of multiple IPs. The linac-ring eRHIC has such options naturally incorporated into its design. Using the electron form ERL provides for additional experimental possibilities such running two experiments with different energies of electron in different IPs, or for arbitrary split of the luminosity between different detectors[18].

Using low emittance electron beam in linac-ring eRHIC provides for significant simplifications of the final focusing optics (see previous section). Specifically, it provides for possibility of moving all focusing optics for electron beam as far as 10 meters outside of interaction region. This is an advantage for experimental set-up- a detector has a very long straight section free from accelerator elements for its installation. This configuration fits most naturally with a long low-x detector with magnetic field [3.g.1].

According to the HERA experience, synchrotron radiation in the IP can be a main source of background. The linac-ring eRHIC provides the possibility of reducing the intensity of the this background while keeping high luminosity very high (see the introduction).

Overall, very high luminosity added by flexibilities provided in linac-ring eRHIC will be a very significant asset for installation of effective detectors for the most aggressive physics program [1].

References

[3.g.1] "A new detector concept for e-p physics", I. Abt, presented at eRHIC Meeting at BNL January 29-31, 2004

[18] Note that in linac-ring eRHIC luminosity can be split between various detectors and is only limited to a total value ~ 10^{34} sec^{-1} cm^{-2} per nucleon.

3.h Adjustment of collision frequency for variable proton- and ion- energies

Operating the eRHIC requires various energies of hadrons from 26 to 250 GeV/u ($27 < \gamma_h < 267$) that causes a significant variation in the revolution frequency in the RHIC, and hence, variations in the hadron beam's repetition rate in the IP:

$$f_o = \frac{C_{RHIC}}{v_h} \approx \frac{C_{RHIC}}{c}\left(1+\frac{1}{2\gamma_h^2}\right), \quad f_{rep} = N_b \cdot f_o \approx 28\ MHz$$

where C_{RHIC} is the circumference of RHIC ring and $N_b=360$ is the number of hadron bunches in the eRHIC. By definition, the electron beam's repetition rate must be the same as that of the hadrons. Within the entire range of foreseen eRHIC operations, electrons remain ultra-relativistic ($\gamma_e > 4{,}000$) and their velocity is practically constant ($0 < 1-v_e/c < 3.2\cdot10^{-8}$). Covering the 26 - 250 GeV/u hadron-energy range will require adjusting the e-beam rep-rate within

$$\frac{\Delta f_{rep}}{f_{rep}} \approx 0.7\cdot10^{-3}.$$

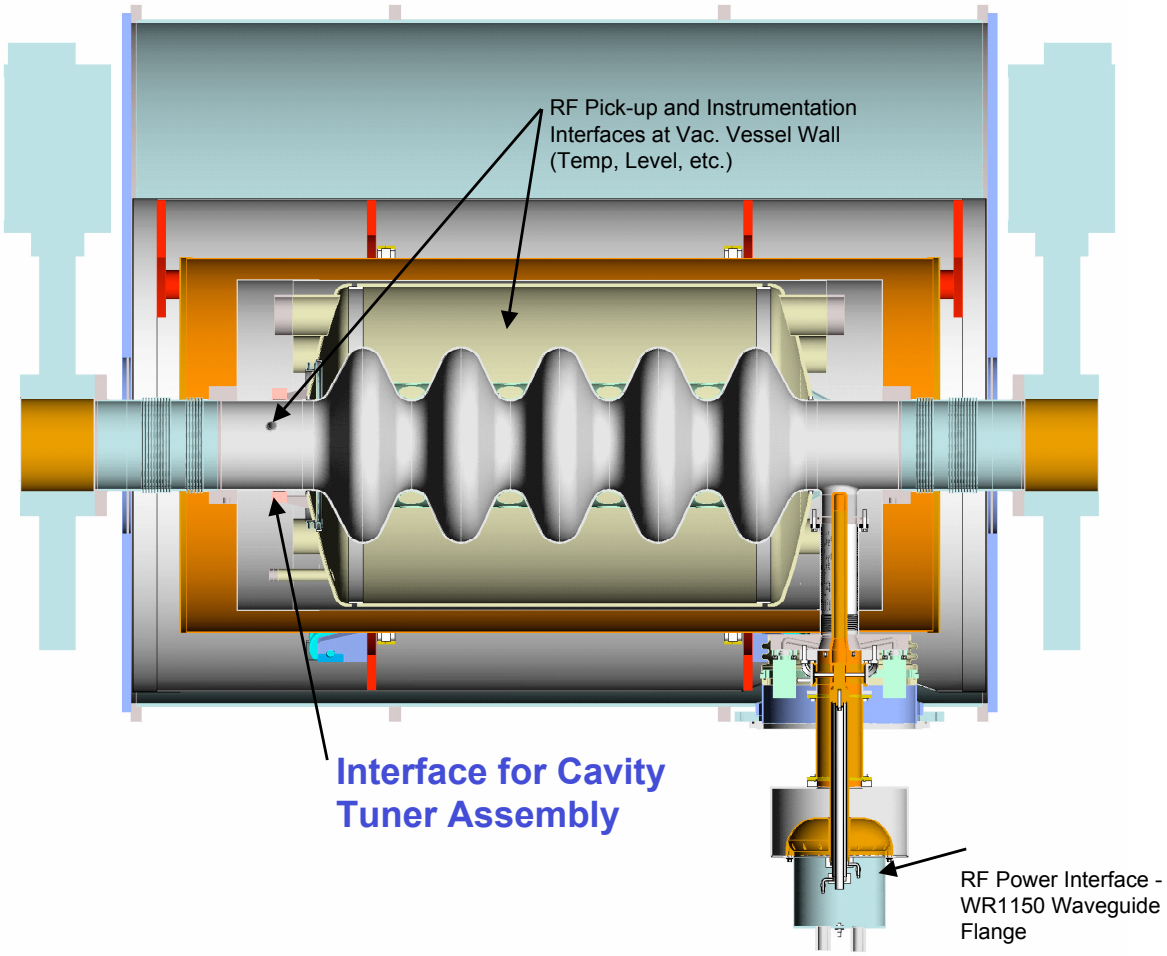

Fig. 3.h.1 A five-cell superconducting cavity with its tuning mechanism.

In contrast to the ring-ring version of eRHIC, where the above requirement is translated into the need for changing the circumference of the electron storage ring by about 0.9 m and causes significant modification of the lattice [3.h.1], in the ERL-based eRHIC it does not raise significant difficulties.

First, in the ERL the repetition rate of the electron beam is controlled by the RF frequency of the superconducting accelerating structure (see below), which operates at 25^{th} harmonic of the beam rep-rate in the eRHIC ($f_{SCC} \sim 705\ MHz$). This cavity is being developed [3.h.2] and is designed to have tunability at least $\Delta f / f \sim 1 \cdot 10^{-3}$, thereby exceeding the above requirement by a wide margin.

The following features of the ERL ensure proper phase matching of the electron beam with each accelerating cavity of the ERL:

- The accelerating structures in each of three linacs will have an individual phase tuner for compensating for the varying RF frequency

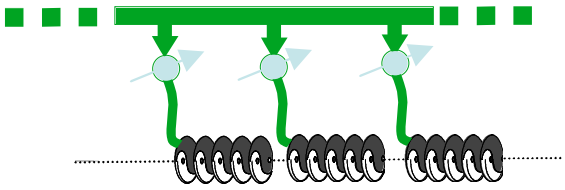

Fig. 3.h.2. A phase tuner controls the phase of each individual cavity.

- The phases of three individual linacs will be individually controlled in conjunction with five chicanes in the arcs and turns;
- The lattice of the ERL arcs is very relaxed and they need to be adjusted by less than a half RF wavelength (λ_{RF}=0.425m, i.e., ΔL<0.215m) using low- and medium-energy chicanes installed in the straight section with large R.
- There is no chicane in arcs at the maximum energy – the phasing is provided by the linacs.

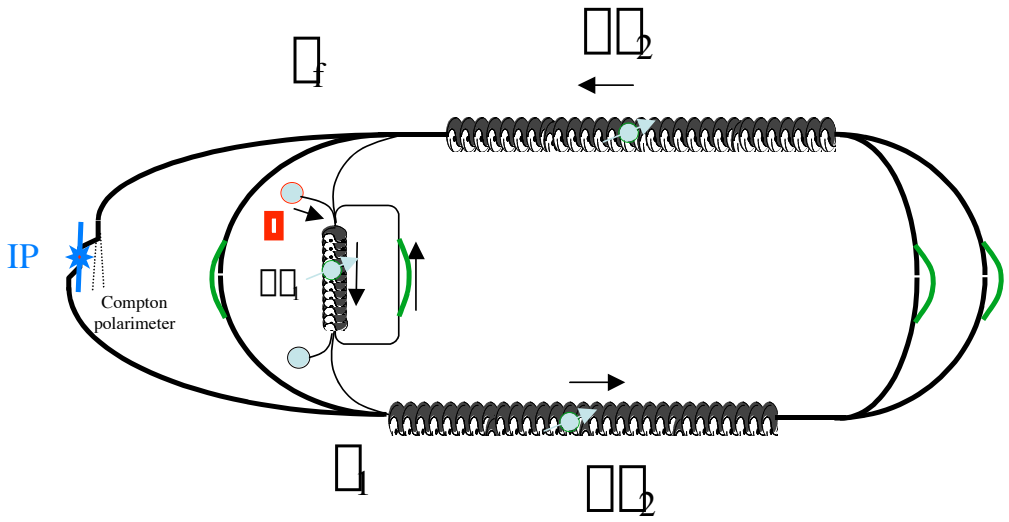

Fig. 3.h.2. The phase matching of the entire ERL system is assured by the phase control of three linacs and four chicanes (depicted by green lines) at intermediate energies.

Overall, the ERL-based eRHIC can comfortably adjust the e-beam repetition rate to any of designed energies of the hadron beam.

References:

[3.h.1] C. Tschalaer, Ring path length adjustment, Presentation at eRHIC Collaboration Meeting, August 19-20, 2003 , BNL, http://www.agsrhichome.bnl.gov/eRHIC/

[3.h.2] I. Ben-Zvi et al., High current SCC

4. Cost

The cost of the ERL-based eRHIC should be close to that of the superconducting linac injector for the ring-ring eRHIC. The main differences will be in following components

- 2 K^o refrigerator with higher power
- Higher power of 700 MHz RF system for linac
- Arcs with a slightly more sophisticated lattice
- Polarized e-Gun with high current with FEL-driver

At the same time, an electron ring and its high power RF system is not required. In addition, one of the layout linac-ring eRHIC will take advantage of the existing RHIC tunnel, which will reduce it cost significantly. It also provides for significant (3-fold) reduction of the losses for synchrotron radiation, which will save megawatts of the RF power.

Therefore, the overall cost is likely to be close to, or slightly below the ring-ring design.

5. R&D items

Linac-ring eRHIC scheme is based on new emerging technology of high-current energy recovery superconducting RF linacs. Accordingly, there is a significant list of R&D items, the principal issues being

- High current polarized electron gun
  - Cathode material, lifetime and cooling
  - Peak current
  - Relaxation time
  - Average beam current
  - FEL source for the photocathode
- High current superconducting cavity structures
  - Five-cell single mode RF structure
  - Superstructures with HOM damping

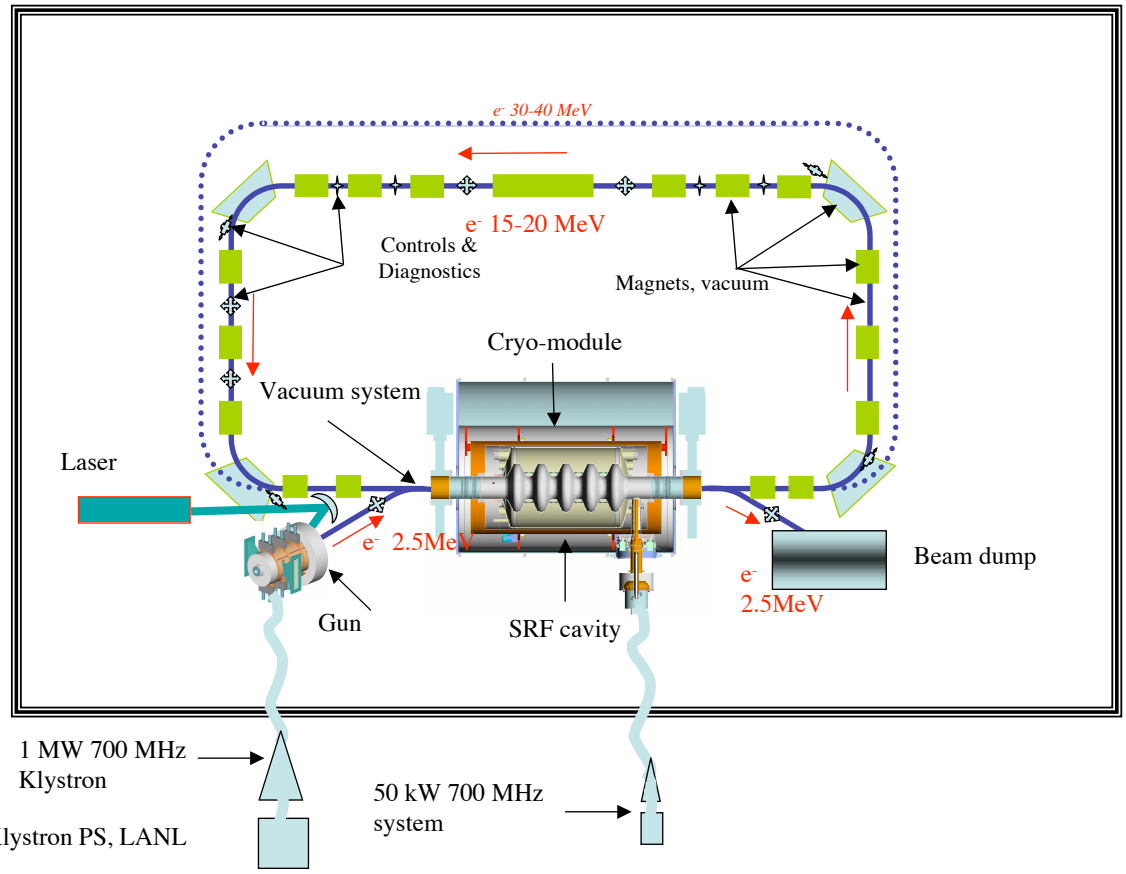

Fig.5.1 Schematic layout of the prototype ERL which is under construction in BNL. This ERL will serve as a test-bed for the concepts of all ERL needed for eRHIC: a) electron cooling, b) FEL for polarized electron gun, and, c) the 10 GeV ERL.

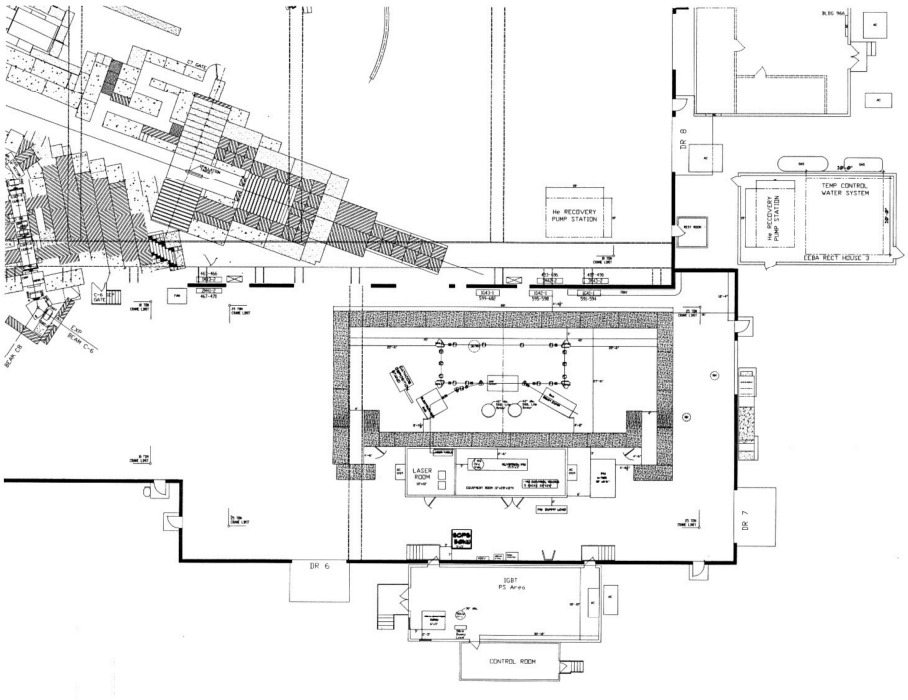

Fig.5.2. Location of the prototype ERL in building 912 at BNL. The experiments are planned to start in mid-2006.

Presently, BNL's accelerator community and others are devoting significant R&D efforts to these issues. They are developing a high-current ERL prototype based on five - cell single-mode SRF structure (planned to be tested in 3-4 years) that will serve as a test bed for both the electron-cooling system and the ERL for eRHIC. In addition, the main centers for SRF technology (Jefferson Laboratory and elsewhere) also are also moving towards developing high-current SRF ERLs. The major technical issues about o the SRF ERL for eRHIC probably will be resolved within 5-10 years. BNL is in excellent position to lead these efforts.

Generating a polarized electron beam with 0.15-0.5 A average current is, and will be, a main R&D item towards the linac-ring eRHIC. Fortunately, an intensive R&D program for linear colliders made several important breakthroughs [5.1-5.3] in such critical areas as surface charge limit and cathode lifetime. Still, there are many problems that must be addressed during feasibility studies for the linac-ring eRHIC. MIT has the relevant expertise to lead these R&D efforts for the eRHIC.

It is also important that polarized electron sources with similar parameters are under development for linear electron-positron colliders [5.3]. Most of beam parameters required for eRHIC electron polarized gun were obtained separately (see Figs 5.3-5), but never in the complete combination. For example, bunches of polarized electrons with charges exceeding by 20-fold that required for the ERL-based eRHIC were demonstrated experimentally (see Figs 5.3), but the duration of the pulses was a few hundreds of nanoseconds [5.2]. Similarly (see Figs 5.4), bunches of polarized electrons with very low normalized emittance were generated [5.4], but with a much smaller charge per bunch.

Therefore, attaining a complete set of parameters requires several very serious developments. Fortunately, many parameters for eRHIC polarized electron gun are close to that of next electron-positron linear collider (see Table 5.1). Therefore, the extensive R&D program for developing such sources for linear colliders [5.5] will address important issues relevant for the ERL-based eRHIC. In any case, developing polarized electron guns is the one of the main R&D for ERL-based eRHIC.

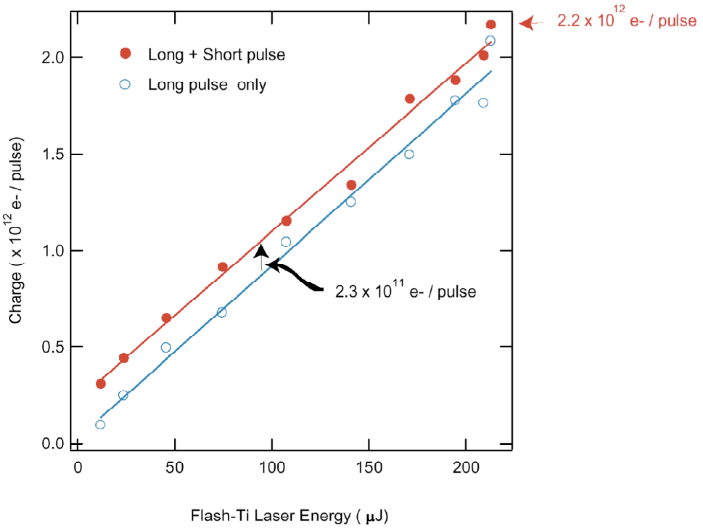

Fig. 5.3. Measured charge per pulse from a ∅14 mm GaAS photocathode [5.2]

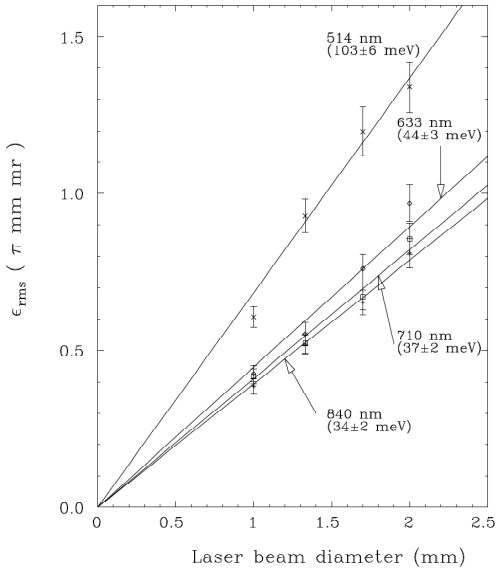

Fig. 5.4. Measured normalized emittance from a polarized e-beam photocathode at CEBAF [5.3]. Simple extrapolation of these measurements to ∅14 mm cathode (i.e., the geometry of the cathode) gives normalized emittance ~ 5 mm x mrad. It supports our assumption that emittance will be dominated by the space-charge effects (see Table 2.1).

Table. 5.1. R&D specifications for polarized electron gun for the next linear collider (a), and for the R&D test gun (b)

	NLC	JLC	TESLA	CLIC
Number of bunches/train	95	95	2820	154
Bunch spacing (ns)	2.8	2.8	337	0.66
DR energy GeV	1.98	1.98	5	1.98
Charge per bunch (nC)	2.56	1.9	3.2	1.0
Injected emittance (mm-mrad)	100	100	10	7
Damped beam emittance (h)	3	2.6	8	.43
Damped beam emittance (v)	0.03	0.004	0.02	0.003
Damped beam bunch length (ps rms)	13.3	16.6	20	10
Damping time (ms)	5.2	3.9	50	21
Damping cycles	4.8	4.8	4	6
Bunch trains per ring	3	3	1	12
Repetition rate (Hz)	120	150	5	100

(a)

Parameter	Symbol	Value	Units
Single Bunch Charge	Q_b	2	nC
Number of Bunches	Nb	1	
Bunch length (FW)	Δt	10	ps
Emittance, normalized	$\gamma\varepsilon$	10	mm-mrad
Energy	E	≈ 5	MeV
Polarization	P	> 80	%
Quantum Efficiency	QE	0.1	%
Repetition Rate	f_{rep}	10	Hertz
Operation Lifetime	τ_{ops}	> 4	Hours

(b)

Smaller but important R&D efforts also will focus on detailed studies and self-consistent simulations of feedback suppressing the kink head-tail instability, the studies of beam-beam effects at low e-beam energies, and the transverse stability of the e-beam in the ERL.

References:

[5.1] P. Hartman et al., "Polarized Electron Linac Sources", In Proc. Of The 2nd eRHIC workshop, Yale, CN, April 6-8, 2000, p.120
T. Zwart et al., "Polarized Electron at Bates: Source to Storage Ring", Proc. Of Second EPIC Workshop, Cambridge, MA, 14-15 September 2000, p.343

[5.2] G. Dugan, "Linear collider: Electron and positron source Potential R&D items", www.lns.cornell.edu/public/LC/MMTI/SourceR&D.pdf

[5.3] ICFA workshop on polarized RF guns for linear colliders, Fermilab, April 18-20, 2001 bc1.lbl.gov/CBP_pages/wim/rfguns_workshop/ RFGuns_workshop.pdf

[5.4] B. M. Dunham, L. S. Cardman, "Emittance Measurements for the Illinois/CEBAF Polarized Electron Source", epaper.kek.jp/p95/ARTICLES/WPC/WPC17.PDF

[5.5] J. Sekutowicz, Proceedings of Linear Accelerators Conference, Tsukuba, Japan, 1994

6. Future energy upgrades and developments

Extending the range of the eRHIC e-beam's energy down to 1 GeV and up or even above 20 GeV is very straight forward with linac-ring eRHIC. It is also for linac-ring eRHIC to have multiple IPs and detectors.

Extending the energy to both into higher and lower range is a natural progression for the ERL-based eRHIC. At low energies, the main problem is the stability of the beams at very high luminosity. An increase in energy principally causes a rise in the intensity of synchrotron radiation in the IP. In principle, an energy of 20-to-25 GeV can be reached in the ERL either by increasing the length of linacs (see Fig.1), or by increase of the number of passes through the system (see Fig.6.1). The most economical choice for the 25 GeV upgrade will be decided by the relative cost of the arcs vs. linac.

Arcs issues

Arcs can be packed on the top of each other for keeping the radii of curvature maximal at all energies[19]. Ultimately, 20+ GeV ERL can utilize RHIC tunnel for the arcs (i.e., maximize the radius of curvature) to keep synchrotron-radiation power under control, i.e. with synchrotron radiation power below ~8 kW/meter presently attained at B-factory.

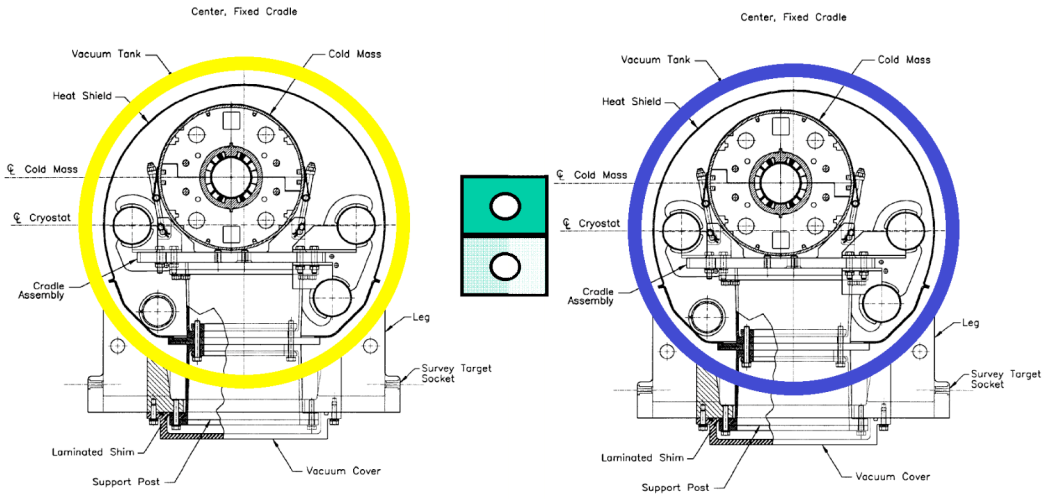

Fig. 6.1. Schematic of the arcs (green rectangle) for the linac-ring eRHIC located in the RHIC tunnel on the top of each other. The nominal number of arcs is two for 20 GeV case, but it can be increased if needed.

Using RHIC tunnel for ERL's arcs significantly increases the radii of curvature and reduces synchrotron radiation losses. Assuming 85% filling factor for the arcs, the 10 GeV ERL will have energy loss of less than 2 MeV per pass and very low linear power

[19] Note that vertical displacements via a dogleg required for this scheme to keep the ERL spin-transparent.

density of synchrotron radiation: 0.22 kW/meter. The linear power density of synchrotron radiation will reach the level of 8.78 kW per meter, which can be considered as attainable, for 25 GeV ERL

IP implications

Increasing electron energy entails growth of the synchrotron-radiation power in the IP. Fortunately, it also reduces the electron beam's emittance and the vertical opening of the synchrotron-radiation fan.

There are two possible solutions for lowering the synchrotron-radiation background in the IP, which are possible only in linac-ring eRHIC:

- First is a further reduction of the ion beam emittance and lowering the electron beam's current (i.e., luminosity stays unchanged)
- Second is to use fewer hadron bunches in RHIC (from 360 to 120*) with the same total intensity of the hadron beam (subject to beam stability studies). This solution reduces the repetition rate of electron bunches, and lowers the synchrotron-radiation background three-fold..
    - This solution has an additional advantage – it is perfectly compatible with present scheme of hadron-hadron collisions; there are no parasitic collisions of hadron beams at both sides of IPs.
    - Additional electron cooling requirements: For the above scheme, an e-cooler is needed with the same average e-beam current but with a three-fold higher charge per bunch.

In addition, ERL created the ideal environment for □-p, □-ion and □-e colliders, where □-beams with energies up to 10 GeV are generated via Compton backscattering. This scheme is prohibited in the ring-ring scenario.

7. Summary

The linac-ring eRHIC naturally fits with the benefits afforded by electron cooling of ion- and proton-beams in the RHIC. It is based on modern rapidly evolving accelerator technology – energy-recovery superconducting linacs. The ERL's configuration of eRHIC takes advantage of lower ion/proton beam emittance and can reach luminosities above 10^{31} for e-Au, and above 10^{33} for e-p collisions.

First, ERL invariably can be optimized to reach maximal luminosity with present and future parameters of the RHIC beams.

Second, ERL offers significant simplification in the final focus, as well as in detector designs.

Third, the ERL's configuration is always compatible with standard and future RHIC beam intensities, independently of the emittance of the ion and proton beam.

Fourth, the ERL's configuration is ideal for flexible e-beam polarization and energy tunability.

Fifth, the ERL's configuration is upgradeable to higher energies, higher luminosities, and multiple IPs.

Sixth, the ERL's configuration can significantly reduce background synchrotron radiation in the IP region by taking maximum advantage of the lowering of emittance via electron cooling.

In a long run, the ten^{+}-fold higher luminosity (compared with best predicted performance of ring-ring option at top energy), flexibility in the IP design, the full compatibility with RHIC operations, and flexible e-beam energy and polarization are probably most important advantages of the ERL configuration.

8. Acknowledgements

We would like to thank Avril Woodhead and Pamela Manning (both BNL) for their indispensable help with making this document readable.

APPENDIX B.
Electron Acceleration for the eRHIC with the Non-Scaling Fixed Field Alternating Synchrotrons

Dejan Trbojevic, Mike Blaskiewicz, Sandro Ruggiero, and Ernest D. Courant

B.1 Introduction

The scaling Fixed Field Alternating Gradient (FFAG) synchrotron has been introduced in 1954 by K. R. Symon [1] and few example electron rings were built at that time. During the last decade, the concept has been revived due to requests for high intensity machines, and has been applied in building the proton and electron FFAG, especially in Japan. The proof of principle proton FFAG was built and commissioned in June 2000 at the KEK, Japan [2]. Presently a 150 MeV proton FFAG synchrotron is being commissioned at the KEK [3].

A principle of the scaling FFAG

The magnetic field in regular synchrotrons varies during acceleration in accordance to the beam momentum such that the average radius and therefore the path length around the machine are constant. A concept of the scaling FFAG lattice is presented in fig. 1.

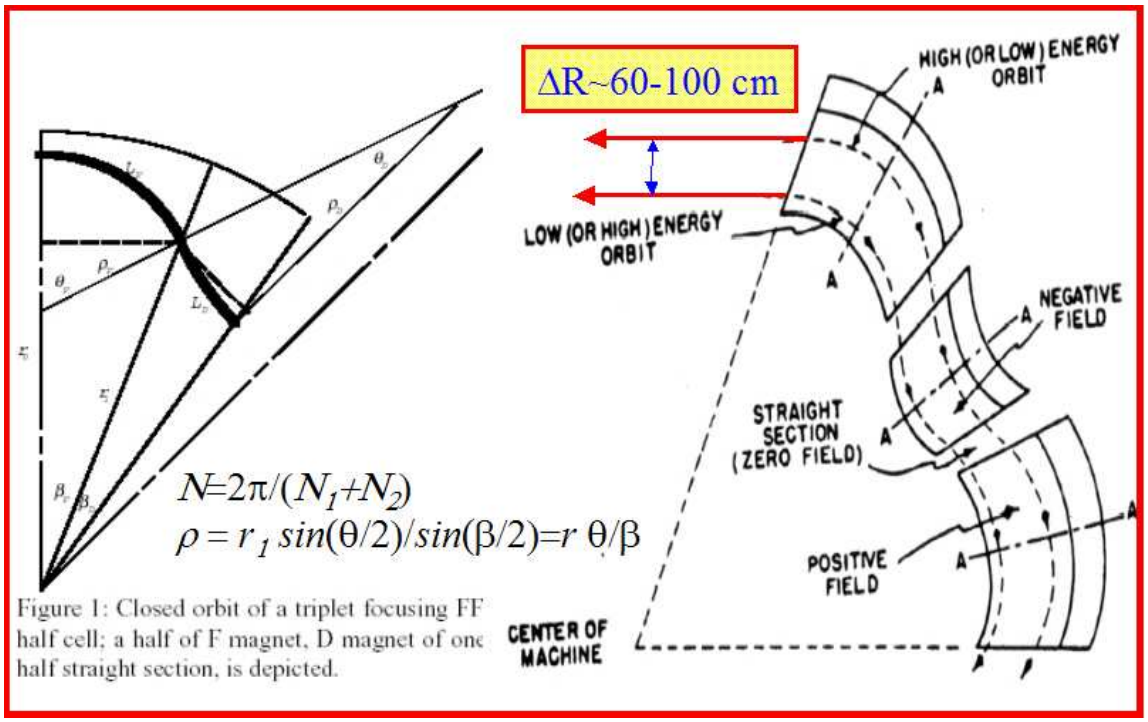

Figure 1. Concept of the scaling FFAG lattice by K. R. Symon.

- The transverse magnetic field in the scaling FFAG is non-linear and fixed:

$$B = B_o \left(\frac{r}{r_o} \right)^k$$

- The radius of particles as they are accelerated, is increasing with momentum: the revolution frequencies vary with momentum, unlike in the cyclotrons where the frequency is constant.
- The scaling FFAG has strong transverse focusing with alternating gradients. The stability of the betatron oscillations is obtained by optimization of betatron tunes. The tunes are constant which makes the chromaticity throughout acceleration equal to zero.
- The momentum acceptance of the FFAG is as large as $\delta p/p \sim +/- 50$ %. The largest momentum offsets in the regular synchrotrons are of the order of few percent. This depends on dispersion function (as the transverse offset is $\Delta x = D_x \delta p/p$, where D_x is the horizontal dispersion function).
- The transition energy is outside of region of energies during acceleration.
- Relatively large apertures are required for the scaling FFAG due to the large radius excursions. The original MARK-I design for the output energy of 10 MeV, required a radius of almost $\Delta x \sim 1$ meter. The present FFAG 10 MeV synchrotron at KEK also has the large variation of radius from $r_o = 4.4$ m to $r_m = 5.3$ m, $\Delta x \sim 0.9$ meter, it requires large aperture magnets.
- A relatively large circumference is required due to large opposite bends.

The non-scaling FFAG

We had introduced the idea of non-scaling FFAG at the Montauk Muon Collider meeting 1999 [4]. The collaboration accepted this concept and a design for the higher energy muon acceleration. We followed the basic idea of the scaling FFAG with a combination of the previously known “minimum emittance lattice” concept for the electron storage rings. Several disadvantages of the original FFAG design: like large aperture requirements, are reduced, the required aperture in the non-scaling FFAG is at least one order of magnitude smaller. The transverse magnetic field in the alternating gradient magnets is linear and particle with different momentum follow orbits oscillating around the ring. The average radius corresponds to the value of the momentum.

The basic lattice cell consists of the **two combined function elements**: the large bending magnet with a defocusing gradient, and a smaller opposite bend with focusing gradient. There is a drift space large enough for the accelerating cavity between two focusing magnets.

The principle of the non-scaling FFAG is based on the basic relation between the radial offset and dispersion function: $\Delta x = D_x \delta p/p$. For example, if the dispersion function were smaller than 10 cm ($D_x < 10$ cm) during acceleration, the orbit offsets for the very large momentum offsets ($\delta p/p = +-50\%$) would not be larger than +-5 cm. The non-scaling design does not have zero chromaticity during acceleration and the betatron tunes change within a range $\nu_{x,y} \sim 0.4 – 0.1$.

B.2 Application of the FFAG Lattice for eRHIC Electron Acceleration

Courant-Snyder functions and magnets in the FFAG non-scaling lattice cell for acceleration from energy of E_o=3.2 GeV up to E_{max}=10 GeV (or in the momentum range of from □p/p = -52% to □p/p = +50%): The basic cell with the betatron functions at the central energy of E_o = 6.7 GeV and magnets is presented in figure 2.

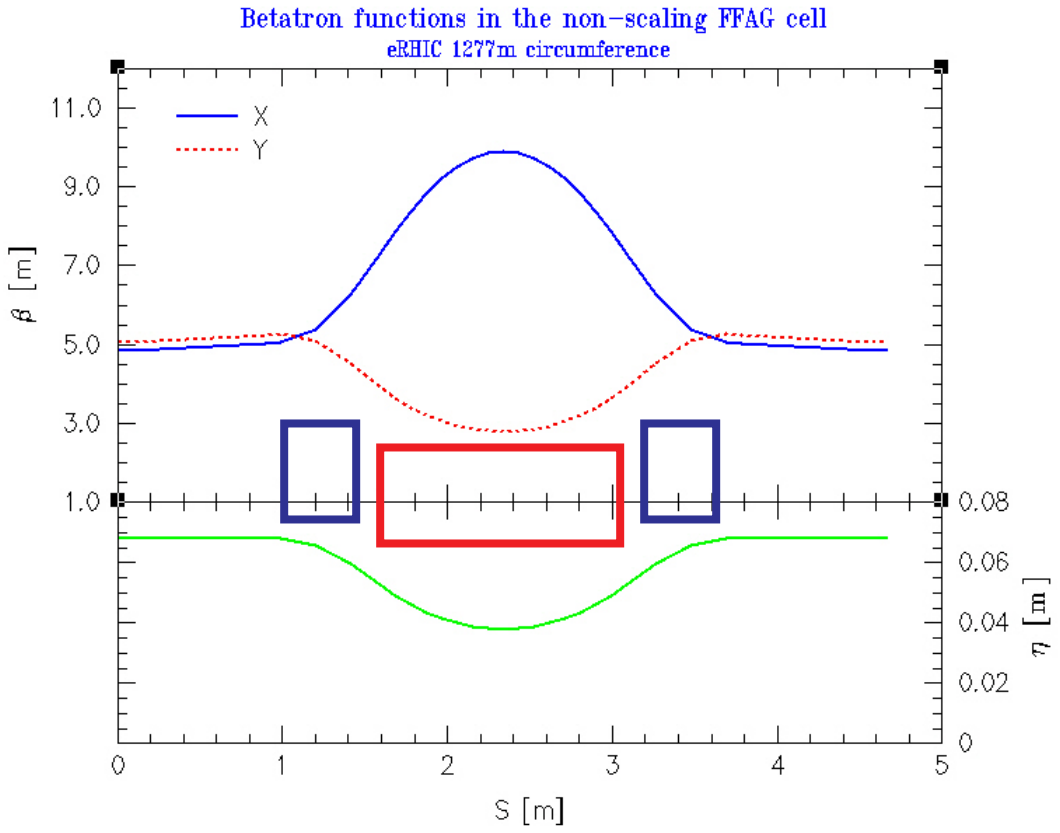

Figure 2. Basic FFAG cell with betatron functions at the central energy of E_o = 6.7 GeV.

The central 1.5 meter long magnet has a bending angle of θ=45.56 mrad, and it is a combined function magnet with a defocusing gradient of G_d =–11.7 *T/m*. The opposite bend is 0.42 meter long with the bending angle of θ=–11.27 *mrad*, with a focusing gradient of G_f = 23 *T/m*. The cell length is 4.678 m. The available drift length for the RF cavity is 2.335 m. There are 273 cells. The required aperture in a transverse direction depends on the orbit offsets during acceleration. The synchrotron radiation from electron depends on the value of the bending angle ($\rho = l/\theta$). The bending angle of the major bend in this example is θ=0.045 *rad*. The bending radius is estimated as $\rho = 1/\theta$ ~33 m.

Orbits During Acceleration: At the start of acceleration, the energy is equal to E_o =3.22 GeV, corresponding momentum offset from the central energy of 6.7 GeV is $\delta p/p$ = –52%. The maximum orbit offset at the beginning of acceleration, as presented in figure 2, is equal to Δx = -15.5 mm. It is passing parallel to the central circular orbit through a drift space assigned to the cavity. As

acceleration proceeds, the orbits move towards the central path. When the momentum offset becomes positive orbits move outside of the central path reaching the maximum value of Δx = +49.27 mm. The aperture of the beam pipe should be wider than ~70 mm. The magnetic field strength of the major bending magnet is B_p=0.679 T while the opposite bending field, of the 42 cm long combined function magnet, is B_{neg} = 0.6 T.

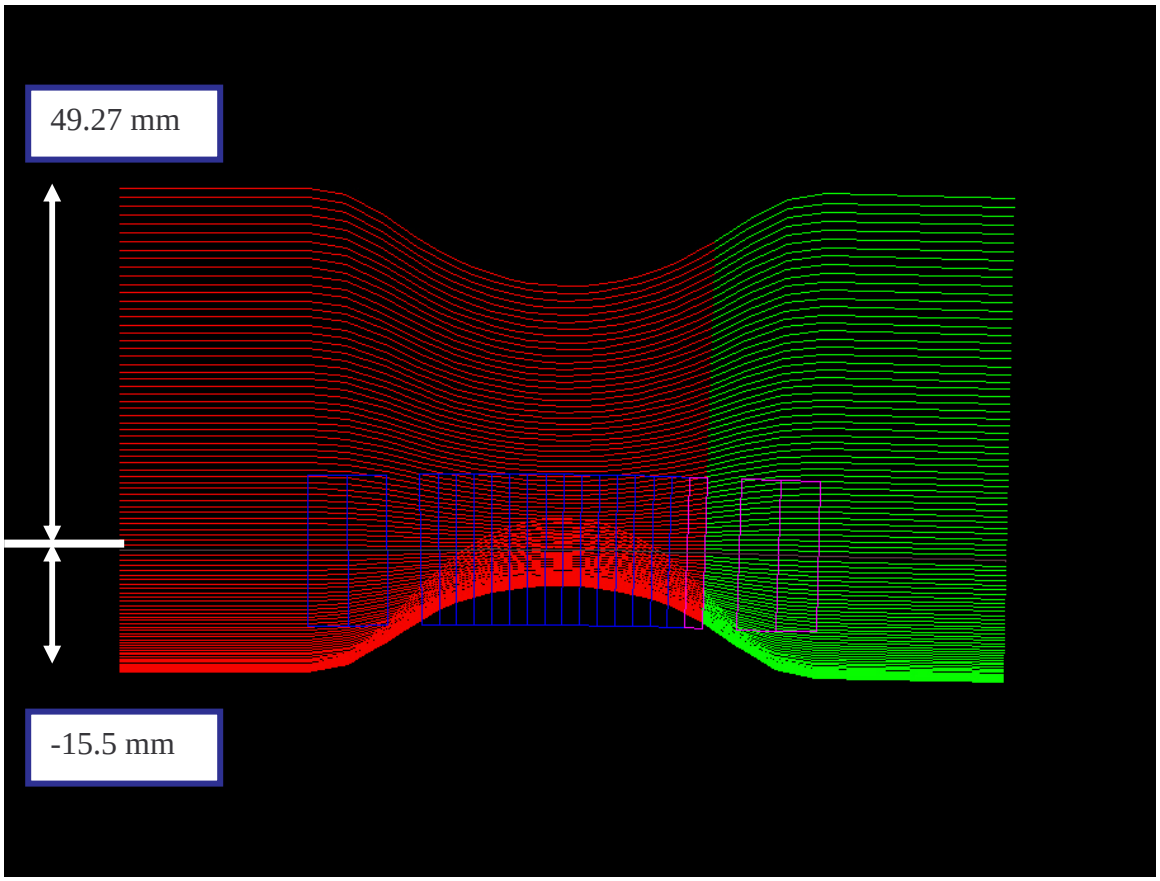

Figure 3. Particle orbits during acceleration. The magnets are presented by the “blue” boxes.

Betatron tunes during acceleration: The betatron tunes in the non-scaling FFAG vary with energy, to the contrary of the scaling FFAG. It is important to avoid half and full integer tunes within the single cell because accelerating particles might be lost due to repetition of the same cells along the circumference path. The vertical and horizontal tune dependence on energy or momentum is presented in figure 4.

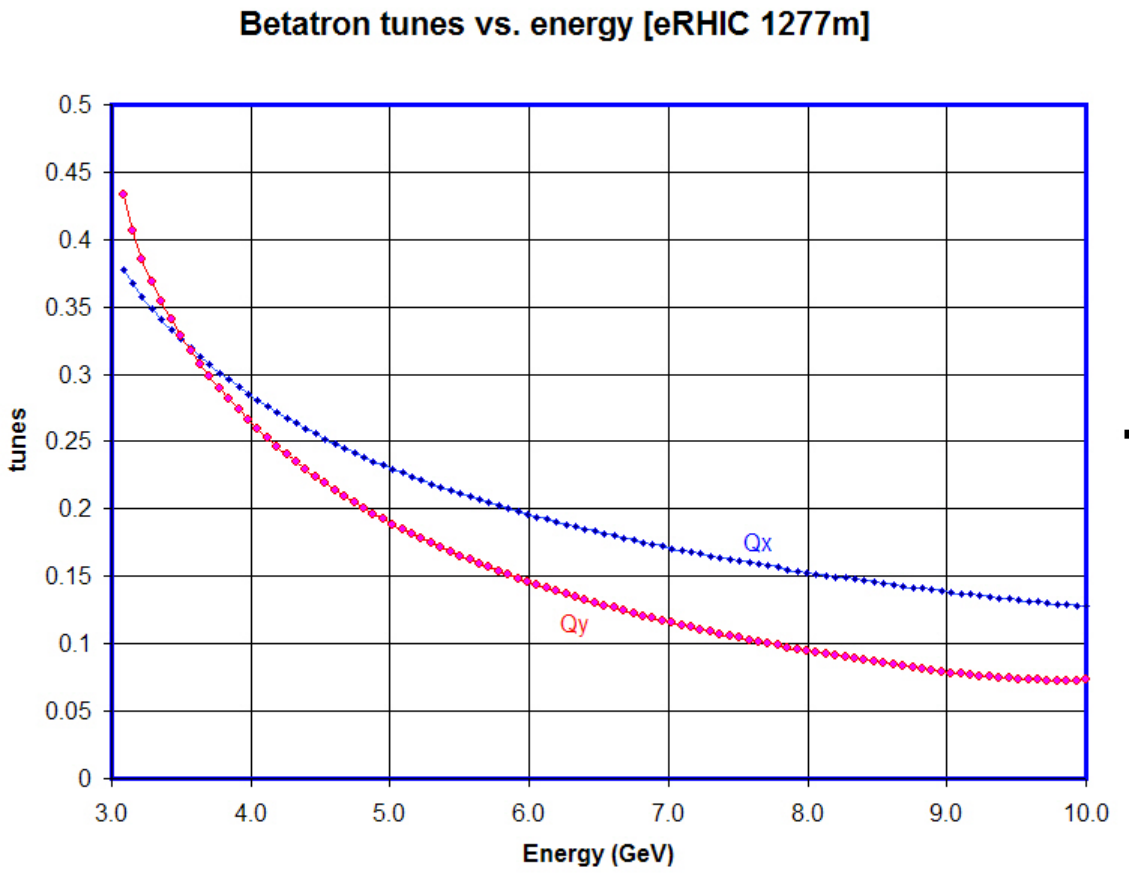

Figure 4. Betatron tunes dependence on energy.

The Path Length and momentum compaction dependence on energy

The path length dependence on energy (fig.5)is very close to a parabolic function. At the lowest energy, α, the momentum-compaction is negative (the transition energy γ_t is an imaginary number). During acceleration from $\delta p/p$ =–52 % up to a value of momentum close to the central value, the absolute value of the transition energy gradually increases. The momentum compaction is also a parabolic function and it crosses the zero value at the same position. The momentum compaction dependence on energy is shown in figure 6.

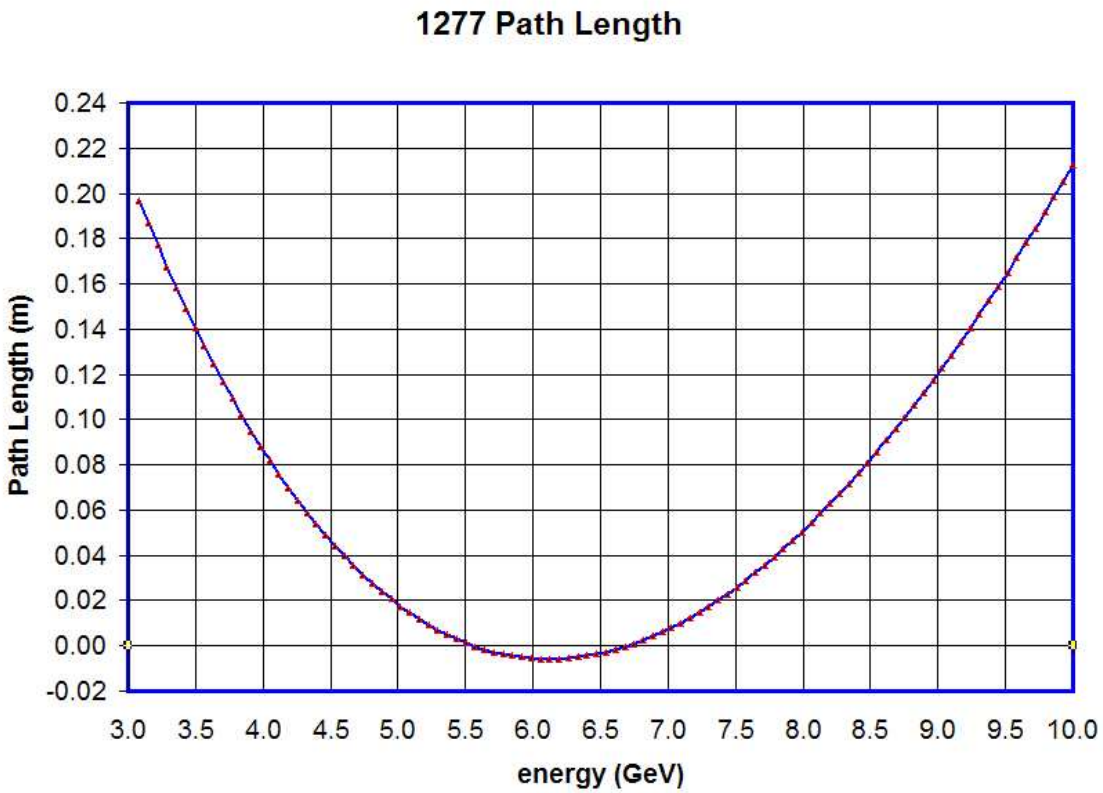

Figure 5. The path length dependence on energy

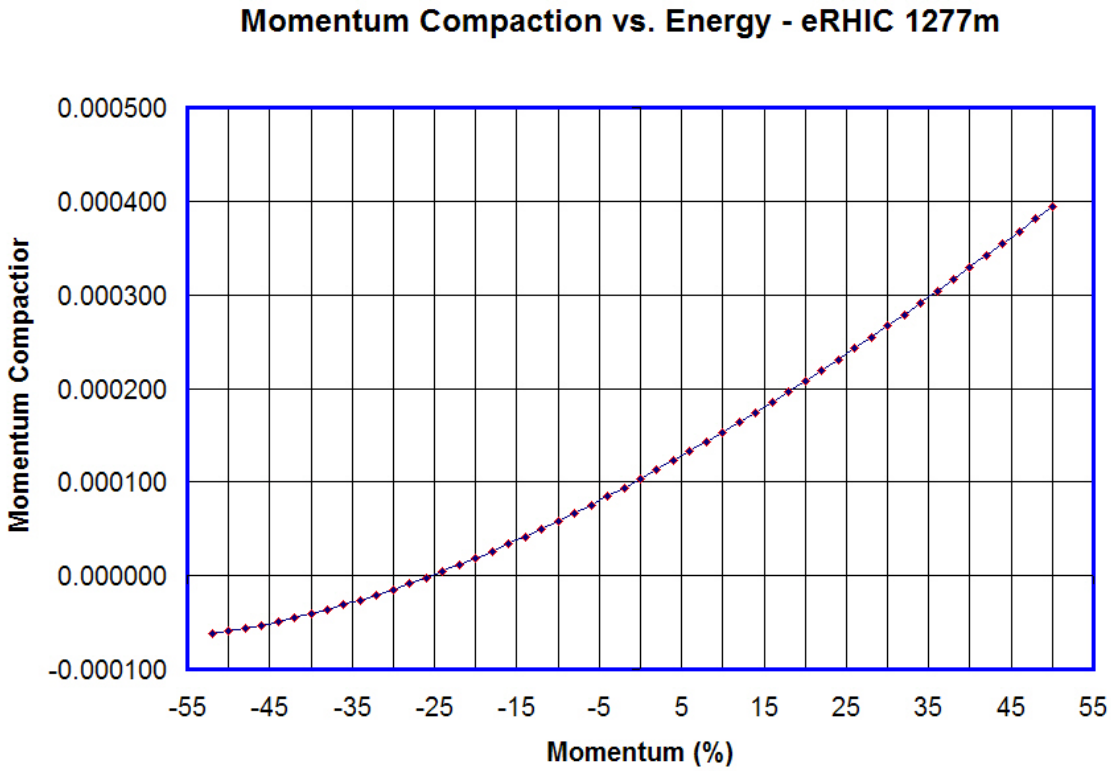

Figure 6. Energy dependence of the momentum compaction factor.

Acceleration

The major problem of applying the FFAG concept for the high electron energy acceleration ***is the loss of energy due to synchrotron radiation***. Energy loss for a single electron per turn in the circular orbit is defined as:

$$\frac{\Delta E}{m_o c^2} = \frac{4\pi}{3}\left(\frac{r_o}{\rho_d}\right)\beta^3\ \gamma^4,$$ r_o is the classical electron radius.

The average radius of the 1/3 of the RHIC circumference is of the order of 200 m, but within the FFAG magnets electrons would be bend much harder even in the opposite way and the radius of curvature is much smaller. The energy loss of electron at the last turn, reaching the highest energy of 10 GeV, is calculated for this example to be 12.891 MeV. This energy needs to be compensated by the RF system. A detail calculation of the synchrotron radiation energy loss is presented in the appendix.

It is assumed that the cavity voltage in the non-scaling FFAG should be at least twice higher at the last turn (energy reaches the largest value equal to 10 GeV). This implies that the total required RF voltage is ~24 MV. If cavities to be used are similar to the RHIC storage cavities, were each reaches a voltage of 2 MV, then twelve cavities are necessary to fulfill the acceleration requirement. This also shows that from 3.2 up to 10 GeV there are required ~560 turns.

The parabolic dependence of the path length difference on momentum requires adjustment of the RF voltage in time. The 20cm path length difference corresponds to a fractional frequency difference of 1.5e-4 or a quality factor of Q=6000 for no cavity tuning. This is a fairly small Q so we will need to tune the cavity. The synchrotron tune with 20MV/turn with a 700MHz cavity frequencies shown in Fig. 7. The large tunes imply adiabaticity except near transition. Figure 8 shows the initial and final longitudinal phase space distributions for an initial (full) emittance of 1.e-3 eV-s per bunch.

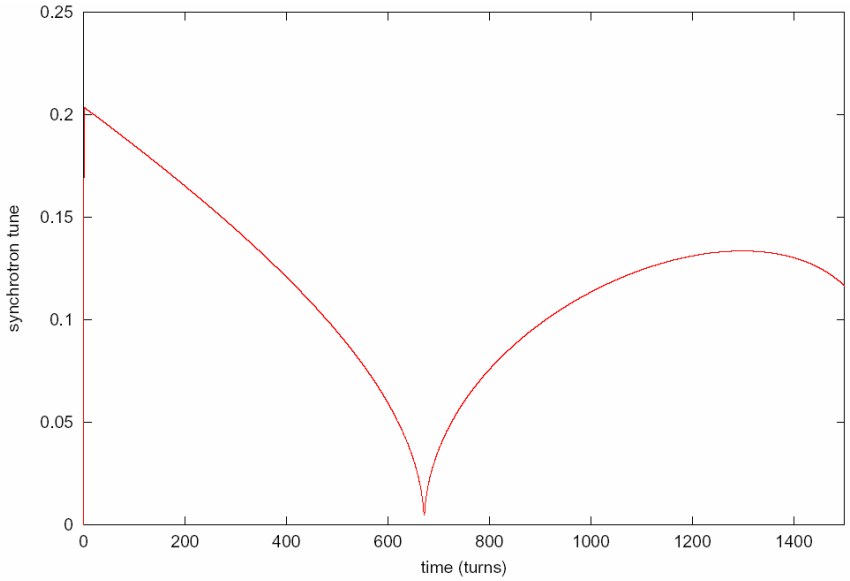

Figure 7. Synchrotron tune versus time for 3-10 GeV acceleration with 20MV/turn and 700MHz cavity frequency

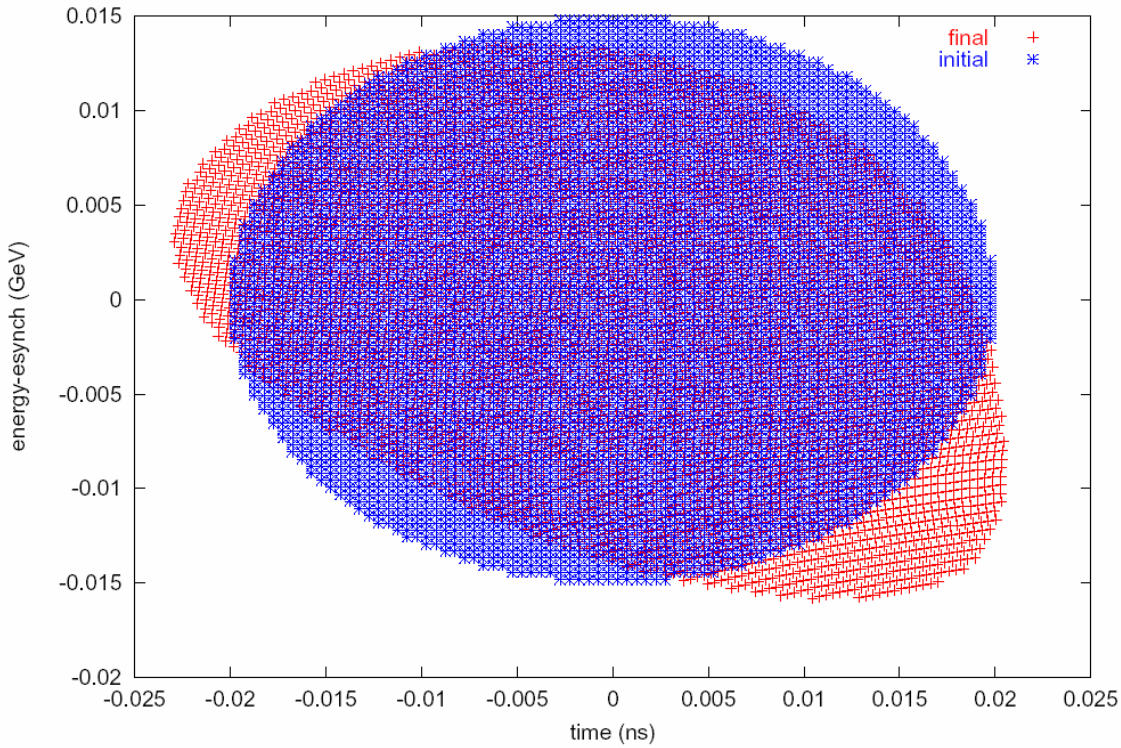

Figure 8. Initial (blue) and final (red) longitudinal phase space for 3-10 GeV acceleration with 20MV/turn and 700MHz cavity frequency.

Energy loss per turn

The energy loss of an electron in this non – scaling FFAG ring during the last turn at the 10 *GeV energy is calculated by separating three part* :

The classical electron radius is : $r_o = 2.817940285\,10^{-15}$ *m*,

$C_1 = m_o c^2 \frac{4\pi}{3} r_o \beta^3 \gamma^4 = 510998.902\ eV\ 4.18879\ r_o\ 1.4666310^{17} = 8.8463\,10^8\ eVm$

A total length in one turn of the major bending magnets : $L_{QD} = 273 \cdot 1.5\,m$

$L_{QD} = 409.5$ *m. A relation to the total circumference* : $k_1 = \frac{L_{qd}}{C_o} = 0.321$

The bending radius : $\rho_d = \frac{l_d}{\theta} = \frac{1.5\,m}{0.045566883} = 32.92\ m$

Energy loss in one turn due to the major bends : $\Delta E_{QD} = \frac{C_1}{\rho_d} k_1 = 8.626\ MeV$

A length in one turn of the opposite bends : $L_{QF} = 273 \cdot 2 \cdot 0.42\ m = 229.32\ m.$

A relation to the total circumference : $k_2 = \frac{L_{QF}}{C_o} = 0.1796$

The opposite bend radius : $\rho_d = \frac{l_d}{\theta} = \frac{0.42\,m}{0.011275776} = 37.25\ m.$

The synchrotron radiation energy loss from the opposite bends in one turn :

$\Delta E_{QF} = 4.265\ MeV$

The total energy loss per turn is equal to $E_{tot} = 8.626 + 4.265 = 12.891$ MeV.

References:

[1] K.R. Symon, “The FFAG Synchrotron – MARK I”, MURA-KRS-6, pp. 1-19, November 12, 1954.

[2] R. Ueno et al, “Multi Orbit Synchrotron with FFAG Focusing For Acceleration of High Intensities Hadron Beams”, PAC 99, New York, 1999, 2271-2273

[3] S. Machida, Y. Mori, A. Muto, J. Nakano, C. Ohmori, I. Sakai et. Al, Status of the 150 MeV FFAG Synchrotron”, PAC 2003, Portland, Oregon, May 12-16, 2003. http://warrior.lbl.gov:7778/pacfiles/papers/FRIDAY/AM_POSTER/FPAB082/FPAB082.PDF.

[4] D. Trbojevic, E.D. Courant, and A.A. Garren, ”FFAG Lattice Without Opposite Bends”, Muon Colliders and Collider Physics at Highest Energies, pp.333-340, Montauk, NY, September 27-October 1, 1999.